The Impact of Mineral Dust Aerosol Particles on Cloud Formation

Dissertation

zur

Erlangung des Doktorgrades (Dr. rer. nat.)

der

Mathematisch-Naturwissenschaftlichen Fakultät

der

Rheinischen Friedrich-Wilhelms-Universität Bonn

vorgelegt von

Khaled Megahed

aus

Benha / Ägypten

Bonn 2006

Angefertigt mit Genehmigung der Mathematisch-Naturwissenschaftlichen Fakultät der Rheinischen Friedrich-Wilhelms-Universität Bonn

Die Arbeit wurde am, Institut für Meteorologie und Klimaforschung, Atmosphärische Aerosolforschung, Forschungszentrum Karlsruhe, durchgeführt

1. Referent: Prof. Dr. A. Bott

2. Referent: Prof. Dr. U. Schurath

Tag der Promotion: 16. 04.07

Diese Dissertation ist auf dem Hochschulschriftenserver der ULB Bonn http://hss.ulb.uni-bonn.de/diss_online/ elektronisch publiziert worden.

Erscheinungsjahr: 2007

To my father who pass away during preparation of this work

and for my sons Mohamed and Mahmoud

Abstract

This investigation examines the role of selected mineral dust samples in heterogeneous ice nucleation. The experiments were done by seeding artificial clouds in the large aerosol chamber AIDA at temperatures between 273 and 190 K. Five different dust samples were collected for this purpose: Two airborne mineral dust samples (denoted Cairo dust 1:CD1 and Cairo dust 2: CD2) were collected during dust storm events at a location about 50 km North of Cairo city. The source regions of these dust samples were identified by altitude-resolved back-trajectory calculations using the FLEXTRA trajectory model and comparing with aerosol index data from the EP/TOMS, MODIS/Terra, and MODIS/Aqua satellite images. The third dust sample (denoted Egyptian Sahara mineral dust: SD) was collected from a hole of 1.5 m depth in the desert 70 km northeast of Cairo city. The fourth dust sample (denoted Asian dust sample: AD) was collected from the ground in the easterly part of the Takla Makan desert in northwest China. The fifth dust sample (denoted Arizona test dust sample: ATD) consists of crushed Arizona desert sand and was purchased from Powder technology Inc. (Minnesota, USA). It is used as a reference material for comparison. All dust samples were analysed on their elemental composition by X-ray fluorescence and on their water soluble ion contents by ion chromatography. The reported data reveals that the fraction of gypsum is the largest in CD1 and CD2, followed by SD. Furthermore, it could be shown that the airborne dust samples (CD1 & CD2) had accumulated soluble coatings during their transportation by interaction with air pollutants.

In addition to the surface-chemical analysis, the mineral dust seed particles were collected during the experiments and analysed on their surface morphology by Scanning Electron Microscopy (SEM). It was found that spherical particles are slightly more efficient ice nuclei than non-spherical particles.

The size distribution of the ice particles was measured by an optical particle counter (OPC, PCS-2000). The output of this instrument was successfully corrected for the evaporation of ice crystals or water droplets in the sampling line. The corrected count median diameters show a good agreement with the values determined from the optical particle counter Welas and FTIR measurements. The measured ice water content is in good agreement between the OPC-based and FTIR-retrieved. Generally, the observed ice water contents compare well with the results from upper tropospheric measurements that were obtained during the INCA campaign (Gayet et al., 2006), although both sets of measurements are totally different.

In the temperature range between 273 and 240 K where mixed clouds form, all dust particles formed liquid water clouds for temperature between 273 and 255 K; very few ice crystals were formed

either by condensation or immersion freezing. Between 255 and 240 K, SD and AD formed liquid water droplets, whereas ATD particles are already efficient ice nuclei by deposition freezing. The airborne Sahara dust samples CD1 and CD2 are also very efficient ice nuclei even in comparison with ATD in the temperature range from 255 to 240 K. Coating ATD particles with sulphuric acid had no significant influence on their ice nucleating ability.

In the temperature range between 240 and 200 K where cirrus clouds form, ATD, SD, and AD show a reduction of the critical ice saturation ratio with decreasing temperature from 1.25 for ATD and 1.35 for SD and AD at 240 K to about 1.1 and less at the lower temperature of the cirrus cloud regime. This is in agreement with critical saturation ratios reported by Bailey and Hallett 2002 and the parameterisation line of cirrus cloud formation by Heymsfield and Miloshevich 1995. Coating ATD with sulphuric acid reduces its ice nucleation efficiency to values predicted for the freezing of haze particles after Koop et al., 2000. Coated SD, on the other hand, shows also reduced nucleation efficiencies, but the effect becomes less important at the lower temperatures.

Finally, the measurements show that the nucleation rates for deposition freezing in the cirrus cloud regime increase as function of the saturation ratio, but decrease towards lower temperatures. The data reported by Archuleta et al. 2005 is in good agreement with our measurement. The results from this work can be used to improve the description of cirrus cloud formation in microphysical cloud models, but there still remain uncertainties about the ice formation in the mixed cloud regime.

Acknowledgments

I would like to thank my supervisor Prof. Ulrich Schurath for many reasons. Firstly, he accepted me as a member in his group at Institut für Meteorologie und Klimaforschung, Atmosphärische Aerosolforschung, Forschungszentrum Karlsruhe GmbH, Karlsruhe. Secondly, for his discussion, developed and improved the style of my dissertation. At the same time, I would like to thank Prof. Andreas Bott who accepted me as a Ph.D postgraduate student at Meteorologisches Institut der Universität Bonn. Many Thanks to Prof. Thomas Leisner a successor of Mr. Schurath who accepted me as a member in his group until the end of my mission.

I would also like to thank the scientist of Institut für Meteorologie und Klimaforschung R. Wagner, H. Saathoff, C. Linke, M. Schnaiter, O. Möhler, S. Benz, and R.Schön for their help in operating AIDA laboratory. My thanks are extending to H. Bunz for helpful discussions and that he allowed me to run his model and Karl-Heinz Naumann for his good personality. My special thanks to the technical staff in the laboratory building, R. Buschbacher, T. Chudy, O. Dombrowski, E. Kranz, G. Scheurig, and S. Vogt for their help with the experimental equipment. Special thanks to M. Koyro for his help in writing program code. My deep thanks to our secretary Mrs. R. Roselieb for her kind personality. Many thanks to Prof. Ulrich Schumann, director of IPA-DLR Oberpfaffenhofen, for allowing me to use the INCA data, and to Andreas Minikin for his help to access the server. I would like to tkank Mrs. S. Merkel, B. Michael, J. Levien and the other contact persons for helping me at the library of Forschungszentrum Karlsruhe. My special thanks to Mrs. M. Hauser at Institut für Technische Chemie, Aerosol-und Partikeltechnologie department for her help to use Imatec image software to analysis the image filter of the collected dust samples.

Finally, I would also like to thank T. Bahr and the staff of CREASO Global Services for helping in data presentation using IDL software, as well as D. Fanning who is the director of Fanning Consulting Services, also for his help in data presentation.

Table of Contents

Table of Contents

Table of Contents

List of Figures

List of Tables

Chapter 1 Introduction

Active weather modification is a scientific and technological challenge. Numerous attempts have been made to enhance precipitation by means of cloud seeding (Wurtele, 1971; Rosenfeld and Nirel, 1996; see also http://rams.atmos.colostate.edu/gkss_node3.html). Many laboratory, modelling, and observational studies in the past were aimed at modifying cloud microstructure in certain simple cloud systems such as fog, thin layer clouds, simple orographic clouds, and small cumulus clouds (Bruinties, 1999; Young, 1993). One of these attempts is based on observations in the atmosphere that precipitation can be developed either by means of the coalescence process in clouds with top temperatures warmer than 0^oC (so-called warm clouds), or via the ice phase by means of the Bergeron-Findeisen process (Eliassen et al., 1978) which is enhanced by riming. The second alternative is important in clouds with top temperatures colder than 0^oC (so-called cold clouds) (Bruinties, 1999), and can be classified further according to the cloud top temperature. It is well known that homogeneous freezing of cloud droplets does not occur above approximately -35^oC (Koop et al., 2000). Therefore, only one of the following natural mechanisms may lead to glaciation of super cooled clouds in the range from 0^oC to about -35^oC:

- Cloud seeding with ice crystals which sediment from higher altitudes where the temperature is low enough for homogenous freezing to occur.
- Heterogeneous ice nucleation on special ice nuclei.

While homogeneous freezing of supercooled water and aqueous solution droplet is now believed to be well understood (Koop et al., 2000), very little is known about the ice nucleating efficiencies of different kinds of refractory aerosol particles. This is the reason why a series of laboratory investigations and modelling studies are being carried out at Forschungszentrum Karlsruhe, Institut für Meteorologie und Klimaforschung, Atmosphärische Aerosolforschung. The goal of this work is to understand the impact of different types of aerosol particles on ice nucleation and thereby on precipitation formation. Experiments were done by seeding artificial clouds (which can be produced in the large aerosol chamber AIDA) with various types of mineral dust (either pristine or aged, e.g. sulphuric acid coated particles) over a wide range of cloud temperatures.

Two modes are believed to contribute to precipitation formation when cold clouds are seeded with suitable ice nuclei (ice particles, solid CO_2 pellets, silver iodide crystals): (a) the “static” mode which is the most efficient when only few ice particles are made by seeding. These grow rapidly via the Bergeron-Findeisen process, which leads to riming and precipitation of graupel (Levi and Rosenfeld, 1996); (b) the “dynamic” mode which requires much larger numbers of ice nucleating seed particles, and arises from the release of latent heat when many supercooled cloud droplets freeze. The

hypothesis (unsupported so far by convincing evidence) is that the resulting increase in buoyancy gives rise to enhanced vertical air motion which triggers strong precipitation (Young, 1993; Bruinties, 1999; Rosenfeld and Woodley, 1993; Dennis and Schock, 1971). Several recent studies have shown that mineral dust plays different roles with respect to cloud seeding in Israel (Rosenfeld and Farbstein, 1992; Rosenfeld and Nirel, 1996; Rosenfeld, 1997).

1.1 The Sources of Mineral (Desert) Dust Particles in the Atmosphere

Atmospheric aerosols are known to impact the climate evolution but they still represent one of the largest uncertainties in climate change studies (Intergovernmental Panel on Climate Change (IPCC), 2001). The aerosols have a direct climate effect in the atmosphere by changing diffuse reflection and absorption of solar radiation and indirect effects by influencing cloud albedo, precipitation development, and cloud life time (Levin et al., 1996; Wurzler et al., 2000; Yin et al., 2002; Rosenfeld et al., 2001; DeMott et al., 2003a; Sassen et al., 2003; Lohmann, 2002).

Among the different aerosol types, the Asian and African dusts are considered the most important types of mineral dust aerosols in the atmosphere. They represent a major factor affecting the Earth's radiation budget (Kishcha et al., 2005), and at the same time they can act as ice nuclei (Rosenfeld and Woodley, 1993; Rosenfeld and Farbstein, 1991; Rosenfeld and Nirel, 1996; Rosenfeld, 1997). The deserts in Mongolia and in Western and Northern China contribute approximately 70% of the total dust emission in Asia and can be considered the principal source of Asian dust (Husar et al., 1997; Zhang and Christopher, 2003; Zhang et al., 2005; Takemi and Seino, 2005; Laurent et al., 2005), which is observed over Japan (Murayama et al., 2001). 10 to 20% of Asian dusts are advected across the Pacific Ocean as far away as the Great Basin of the US (Sassen, 2002; Takemura et al., 2002). These dust particles exhibit hygroscopic growth due to chemical transformations which occurred during long-range transport (Perry et al., 2004). Asian mineral dust was also detectable over Canada although only weakly by a Sun Photometer (Thulasiraman et al., 2002).

The other desert "Sahara" is considered the principal source of African dust having variable emissions from year to year (Moulin and Chiapello, 2004; Yoshioka et al., 2004). Sahara dust is transported to many different zones on Earth's surface (Talbot et al., 1986; Li et al., 1996). It is transported from North Africa across the North Atlantic Ocean into the Caribbean region (Colarco et al., 2003; Reid et al., 2002; Chiapello and Moulin, 2002; Petit et al., 2005) and was observed also in the air masses over Florida (DeMott et al., 2003). The Mediterranean region is the other zone which is affected strongly by the presence of desert dust from the largest global source of desert aerosol: the North African Desert (Levin et al., 1996; Wurzler et al., 2000; Yin et al., 2002; Rosenfeld et al., 2001; Barkan et al., 2005). It is well known that dust from the Sahara is occasionally transported to Central

Europe. Recently a particularly spectacular Saharan dust event has been observed in Switzerland and close to the Bavarian Alps (Waquet et al., 2005) and even northern Europe, reaching the shores of the Baltic Sea (Barkan et al., 2005). The Meteorological Observatory on Hohenpeißenberg reordered a video of the reddish dust cloud which became visible on 21 February 2004 at 9h and disappeared about 3h later (Berresheim, priv. communication).

Very recently, Dentener et al. (2006) have updated inventories of natural and anthropogenic global aerosol emissions which are now recommended for input in global modelling. The inventory distinguishes between dust, sea salt, sulphate, organic matter and soot. According to these authors, the annual flux of mineral dust in 2000 is estimated at 1678 Tg yr^{-1}, topped only by sea salt with an estimated annual flux of 7925 Tg yr^{-1}. They also present global maps of annual dust emission fluxes and dust emissions for January, April, July and October. They show that the Sahara is by far the strongest source, followed by the Asian deserts and minor contributions by others, e.g. in Australia. However, these estimates are rather uncertain. E.g., a global dust source strength of only 662 Tg yr^{-1} has been assumed in the ECJAM5-HAM aerosol climate model by Stier et al. (2005).

Because the largest values of the aerosol index (AI) that has been observed by the TOMS satellite occur along the main trajectories of the mineral dust plumes, Israelevich et al. (2003) have plotted the distribution of the largest aerosol index (AI) that is observed above North Africa and the eastern Mediterranean during the period 1996-2001. They reported African dust aerosol loadings above the eastern Mediterranean with different size distributions and refractive indices during the following three periods: March-May, July-August, and September-November. The differences are attributed to different source regions and desert dust trajectories during these periods. In the first period desert aerosol from the source in Chad is transported to the eastern Mediterranean predominantly along the North African coast, associated with Sharav (Khamsin) cyclones. The aerosols are transported to the eastern Mediterranean via Egypt from the sources near the Red Sea in the second period, while the dust arriving at the eastern Mediterranean during the third period originates from the Libyan coast.

Levin et al. (1980) have measured the aerosol size distribution in a dust storm using a Royco optical counter during and after the passage of a front. They reported that it peaks sharply around 1 µm during the passage of the front and disappears gradually afterwards. On the other hand, Blanco et al. (2003) found that the Total Ozone Mapping Spectrometer (TOMS) aerosol index data was in the range 0.7 - 2.2 over Southern Italy during dust outbreaks from April to June 2002. Also the particle size and shape were analysed using a scanning electron microscope (SEM). It was found that the particle diameter was between 0.3 and 30 µm with median diameters between 1.7 – 2.4 µm and roundness factors varying from 0.8 to 2.5. Barkan et al. (2005) analyzed also TOMS aerosol index data in July

1988 and lidar measurements in Rome in July 2001-2003. They conclude that the Saharan dust plume often reaches Italy. Saharan dust was also observed over eastern Spain where it caused high levels of suspended particulate matter (Escudero et al., 2005).

It has been speculated that a significant proportion of mineral dust in the atmosphere may be the result of anthropogenic activities, and therefore may play an important role in climate change by exerting a significant direct radiative forcing (Tanré et al., 2003). Different authors believe that 20 % (Sokolik and Toon, 1996) or up to 30 and even up to 50 % (Tegen and Fung, 1995) of the total mineral dust in the atmosphere originates from anthropogenic activities. However, more recent work of Tegen (private communication) has reduced this estimate to 10%. As was already mentioned above, mineral dust particles can travel long distances and become coated with soluble sulphates, nitrates and other electrolytes when passing over marine or polluted continental regions (Zhang and Carmichael, 1999; Takemura et al., 2002; Sugimoto et al., 2002, Laskin et al., 2005). These coatings can be due to chemical processes on their surface (Rosenfeld et al., 2001; Laskin et al., 2005), or they may originate from evaporating cloud drops which were originally nucleated on sulphate cloud condensation nuclei and subsequently collected dry interstitial mineral dust particles (Levin et al., 1996).

The radiative forcing using these data was estimated by Tegen et al. (1996) to be -0.25 W m^{-2} in the short-wave and +0.34 W m^{-2} in the long-wave range, resulting in a net radiative forcing of +0.09 W m^{-2}, while it was estimated by Miller and Tegen (1998) to be -0.22 W m^{-2} in the short-wave and +0.16 W m^{-2} in the long-wave range, resulting in a net radiative forcing of -0.06 W m^{-2}.

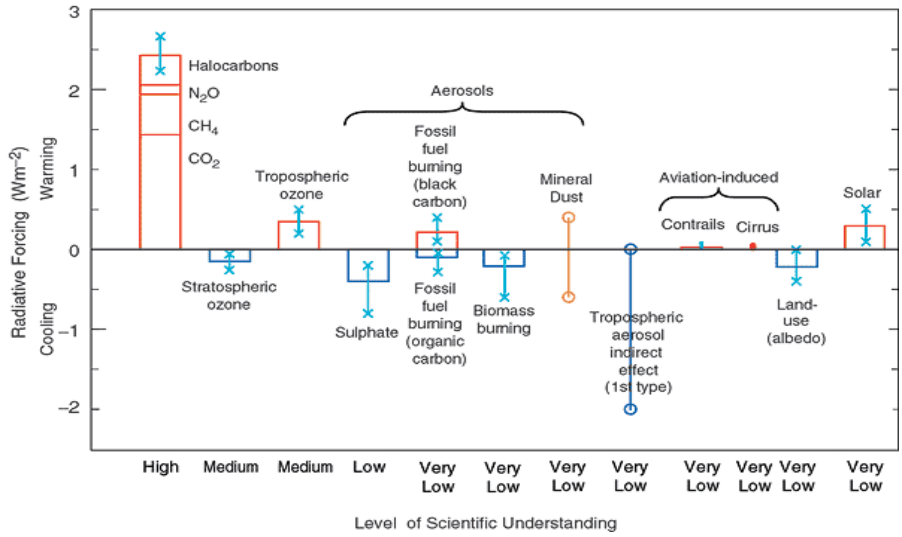

Figure 1.1: Global, annual mean radiative forcing (W m^{-2}) due to a number of agents for the period from pre-industrial to present. After IPCC (2001).

The global annual mean radiative forcings (W m^{-2}) due to a number of agents for the period from pre-industrial to present are shown in Figure 1.1. The height of each rectangular bar denotes a

central or best estimate value while its absence denotes no best estimate is possible. The vertical line about the rectangular bar with "X" delimiters indicates an estimate of the uncertainty range, guided by the spread in the published values of the forcing and physical understanding. A vertical line without a rectangular bar and with "O" delimiters denotes a forcing for which no central estimate can be given owing to large uncertainties. A "level of scientific understanding" (LOSU) index is accorded to each forcing, with H, M, L, and VL denoting high, medium, low and very low levels, respectively (IPCC, 2001). – We note that the next IPCC Report, which will be published in 2007, has recently been made available to scientists on the web. The new Report still considers the scientific understanding of the direct and indirect aerosol effects on climate as low and very low, but does no longer include forcing by mineral dust as a separate item.

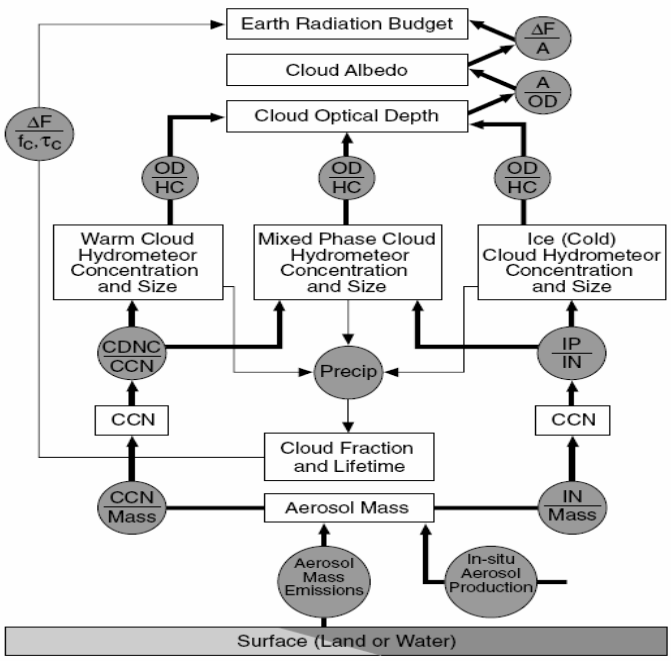

Figure 2.1: Flow chart showing the processes linking aerosol emission or production with changes in cloud optical depth and radiative forcing. Symbols: CCN (Cloud condensation nuclei); CDNC (Cloud droplets number concentration); IP (Ice particles); OD (Optical depth); HC (Hydrometeor concentration); A (Albedo); f_c (Cloud fraction); τ_υ (Cloud optical depth); ΔF (Radiative forcing).

The radiative forcing of mineral dust given by climate models in Figure 1.1 is not yet determined due to the contrast between the results of cooling effect over ocean and land (IPCC, 2001; Ramaswamy et al., 2001), which can be as large as -60 W m^{-2} during important dust outbreaks over ocean under cloud–free conditions (Haywood et al., 2001). It may be positive or negative over land depending on the values of the surface albedo and the aerosol single scattering albedo (Tegen et al., 1996; Hansen et al., 1997) and may have a warming effect over the Saharan desert (Zhang and Christopher, 2003).

Indirect forcing by aerosols is defined broadly as the overall process by which aerosols perturb the Earth-atmosphere radiation balance by modulation of cloud albedo and cloud amount. It can be viewed as a series of processes linking various intermediate variables such as aerosol mass, cloud condensation nuclei (CCN), ice nuclei (IN) concentration, water phase partitioning, cloud optical depth, etc. which connect emissions of aerosols to the top of the atmosphere radiative forcing due to clouds. A schematic of the processes involved in indirect forcing is shown in Figure 2.1 (IPCC, 2001).

The influence of anthropogenic aerosol on cloud optical depth and albedo has recently been analysed by combining satellite measurements with chemical transport modelling (Schwartz et al., 2002).

1.2 Mineral Dust Aerosol and Clouds

Measurements of the ice nucleating ability of aerosol particles in the air masses over Florida having sources in Africa support the potential importance of dust aerosols for indirectly affecting cloud properties and climate (DeMott et al., 2003a). These interactions between aerosols and clouds are the subject of on-going scientific research. Mahowald and Kiehl (2003) have considered the relationship between mineral aerosols and cloud properties over North Africa and the North Atlantic using monthly mean observations of mineral aerosols and clouds and revealed that the mineral aerosols are suppressing precipitation in thin low altitude clouds and changing cloud amounts in ice phase clouds.

In an aircraft campaign of cloud physics measurements over Israel during a dust storm on 16 and 17 March 1998, Rosenfeld et al. (2001) have reported that in the dust-free air the clouds contained large amounts of drizzle and warm rain, which froze at about -7^{o}C and formed high concentrations of frozen drops and graupel with the maximum liquid water content reaching 3 g m^{-3} at -8.5^{o}C. In the heavy dust case the clouds contained only a few drizzle particles over the Sea indicating that coalescence was less effective in the presence of dust. Frozen drops and graupel were formed in the cloud near -8^{o}C with the maximum liquid water content reaching 3 g m^{-3}, much like in the dust-free case. The overall conclusion of this study is that large a mount of mineral dust reduces the mean droplet size and thereby coalescence in warm clouds, although the effect is less pronounced than in biomass burning aerosol plumes or anthropogenic pollution plumes.

The effect of mineral dust on ice formation was studies by Sassen et al. (2003) in a field experiment in southern Florida. The authors used an aircraft and polarization lidar to show that mineral dust particles transported from the Sahara in Africa are effective ice nuclei, apparently capable of glaciating a mildly supercooled (-5.2^{o} to -8.8^{o}C) altocumulus cloud. They concluded that if

these results could be generalised, even small amounts of mineral dust could have an impact on regional climate through the indirect effect on cloud formation in the northern hemisphere.

Gobbi et al. (2004) have analyzed a set of 813 lidar profiles of tropospheric aerosol and cirrus clouds. Extinction and depolarization were measured in Rome, Italy, in the period between February 2001 and February 2002. The data set reveals a meaningful contribution of both cirrus clouds (38%) and Saharan dust (12%) to the total optical thickness of 0.26 at 532 nm. In an aircraft campaign conducted over the Alps, Heintzenberg et al. (1996) found that mineral dust particles were a common constituent in cirrus cloud crystals. Also cirrus clouds associated with Asian dust layers have been observed over Japan (Murayama et al. 2001) and in Western US (Sassen, 2002). This shows that mineral dust from the Sahara and other deserts occurs over large areas of the northern hemisphere, with strong indications that mineral dust particles are involved in ice cloud formation.

Levi and Rosenfeld (1996) found a major fraction of dust in rainwater having its source in the Sahara desert and gave an indication that desert dust plays an important role in cloud seeding over Israel, due to its cloud drop condensing and / or ice nucleating activity. Rosenfeld and Nirel (1996) referred to the action of Saharan dust particles as ice nuclei in attempting to explain impacts on cloud seeding experiments in Israel. These results are strongly suggestive of a cloud seeding effect of mineral dust acting as ice nuclei.

This seems to contrast (but only at first sight) with results of Rudich et al. (2002) who have used NOAA-AVHRR ”Advanced Very High Resoultion Radiometer” retrievals to analyse cases where salt-dust from the Aral Sea interacts with clouds. They reported that large salt-containing dust particles increase cloud drops to sizes that promote precipitation. Their results were in line with the results of microphysical models and recent results from hygroscopic cloud seeding experiments for rain enhancement. Note, however, that mineral dust from the Sahara normally does not contain soluble material and therefore cannot give rise to hygroscopic cloud seeding, in contrast to the salt-dust addressed by Rudich et al. (2002).

1.3 Ice Formation Processes in Clouds

The relation between aerosol and cloud elements is more complex in ice clouds than in warm clouds due to the existences of different modes of ice nucleation: homogeneous and heterogeneous ice nucleation. The relative importance of homogeneous and heterogeneous nucleation during cloud formation is still a matter of discussions. The issue has recently been assessed in a modelling study by Kärcher and Lohmann (2002), and more recently in a laboratory study by Shaw et al. (2005). Which

nucleation mode is thought to dominate under atmospheric conditions is critical to estimates of the aerosol induced anthropogenic impact on cirrus clouds (Seifert et al., 2004).

1.3.1 Homogeneous Freezing Nucleation

Homogeneous freezing nucleation is an important ice-forming mechanism in the absence of significant amounts of solid material which could act as heterogeneous ice nuclei at higher temperatures. It refers to the spontaneous freezing of cloud droplets or haze particles (the latter are solution droplets with water activities less than 1.00 existing in equilibrium with less than 100% RH with respect to super cooled liquid water) below about -35 ^{o}C. This ice nucleation mode requires that soluble particles deliquesce and dilute as they equilibrate with the increasing relative humidity in a rising and therefore adiabatically cooling air parcel. One common basis for quantifying homogeneous ice nucleation in super cooled clouds is classical nucleation theory. The validity of this approach for cloud droplets is supported by numerous laboratory studies on the freezing of pure water and dilute solution drops (Pruppacher and Klett, 1997; Koop et al., 2000; Möhler et al., 2003; Haag et al., 2003; Benz et al., 2005; Duft and Leisner, 2004; Stöckel et al., 2005). However, the extension by Koop et al. (2000) of the homogeneous nucleation rate of pure water to solution droplets with water activities less than unity is still a matter of debate (e.g. Larson and Swanson, 2006). Experiments are under way in the AIDA chamber to find out if ammonium sulphate solution droplets really deviate from the parameterisation published by Koop et al. (2000) of the homogeneous nucleation rate (S. Benz, private communication).

1.3.2 Heterogeneous Ice Nucleation

Heterogeneous nucleation mechanisms are clearly important for ice formation in precipitating clouds warmer than the homogeneous nucleation threshold temperature of -35^{o}C, but there is inferential evidence that it may be important as well for cirrus clouds (Noble and Prather, 1996; DeMott et al., 2003).

At least four mechanisms have been identified for heterogeneous ice nucleation (Vali, 1999):

1. **Deposition freezing** occurs when water vapour at temperatures below 0^{o}C is adsorbed directly from the vapour phase onto the surface of an IN where it grows an ice crystal without passing through the intermediate stage of a bulk aqueous solution.

2. When a partially soluble aerosol particle acts as a CCN below 0^oC forming a drop which freezes at some time during the condensation process, this mode is called **condensation freezing**.
3. In the third mode which is called **immersion freezing**, a partially soluble aerosol particle acts as a CCN below 0^oC, but freezing is initiated at a later time when the temperature of the drop has become significantly lower, making the likelihood of heterogeneous formation of a supercritical embryo progressively greater.
4. In the fourth case, the **contact mode**, the IN initiates the ice phase at the very moment of its contact with a super cooled drop (Young, 1993).

Particles lifted into the atmosphere from the surface of deserts were found to serve as CCN with concentrations up to 10,000 cm^{-3} at supersaturation between 0.3 and 0.8 % during a dust storm south of the Sahara desert (Pruppacher and Klett, 1997). The insoluble dust particles could subsequently act as ice nuclei by immersion freezing if contained in cloud droplets, or by any other of the above heterogeneous freezing modes.

Anthropogenic aerosols can also act as ice nuclei and thereby determine the lifetime of super-cooled water clouds and mixed-phase clouds (Lohmann, 2002; Levin et al., 1996). Zuberi et al. (2002) conclude that mineral dust provides efficient nuclei for ice in H_2SO_4-H_2O aerosols. As a result it can initiate the formation of upper tropospheric ice clouds at warmer temperatures and lower super-saturations in comparison to homogeneous freezing.

Pristine desert dust particles from the Sahara are usually insoluble. However, Saharan dust particles coated with soluble sulphate were observed by Levin et al. (1996) and Noble and Prather (1996). Such coatings may originate from in-cloud scavenging of interstitial dust particles followed by evaporation of the cloud droplets, or by condensation of SO_2 onto the dust particles followed by reaction with ozone or H_2O_2 which converts S(IV) into S(VI), or even by coagulation of mineral dust particles with sulphate particles. The presence of soluble material (which may be of anthropogenic origin) on the desert dust particles converts them into large and effective CCN which may affect the microphysics of clouds. Whether this effect results in a significant climate forcing has not been investigated and cannot presently be quantified.

Hung et al. (2003) studied ice freezing of aqueous sulphate particles containing hematite (α-Fe_2O_3) or corundum (α-Al_2O_3) to mimic mineral dust cores, using an aerosol flow tube combined with infrared spectroscopy (AFT-IR) to detect ice formation. They reported that hematite leads to more rapid ice nucleation when present in aqueous ammonium sulphate particles (i.e., higher freezing temperatures and lower critical ice saturation ratios were observed). Also, the heterogeneous

nucleation rate was found to increase as temperature decreases. These laboratory observations provide an initial quantitative foundation for the consideration of the role of mineral dust particles in the first steps of cirrus cloud formation. In particular, the hematite fraction of mineral dust is expected to initiate cirrus formation much more often than homogeneous ice nucleation alone.

1.4 The Aim of this Work

The injection of refractory aerosol particles, such as mineral dust, into the atmosphere increases the number of ice nuclei in glaciating clouds, while a larger number of smaller droplets are formed in non-glaciating clouds. The formation of ice crystals in the atmosphere depends strongly on temperature, relative humidity, and updraft velocity (Kärcher and Lohmann, 2002). Changes in the cloud droplet spectrum are not only affecting cloud albedo (Schwartz et al., 2002), but are thought to influence cloud life times and thereby the hydrological cycle in the atmosphere as well (Noone et al., 2000; Ackerman et al., 2000).

The current study focuses on the role of insoluble African and Asian desert dust particles as likely heterogeneous ice nuclei in the troposphere. It is based on cloud simulation experiments in the large coolable and evacuable aerosol chamber AIDA with real samples of desert dust which have been collected in different places. Arizona test dust (this is a commercially available kind of mineral dust which is made by milling desert sand) was also studied as a reference aerosol. With the AIDA chamber facility, experiments were carried out over a wide range of temperatures between ± 2 and -78^{o}C. This allowed us to study heterogeneous ice nucleation from warm to cold cloud conditions or from mixed to cirrus clouds. For this purpose the AIDA chamber was used as a large cloud expansion chamber, i.e. high supersaturations with respect to ice were established by expansion cooling with large mechanical vacuum pumps. The critical relative humidity which marks the onset of ice crystal formation was measured as a function of temperature to judge the effect of mineral dust on ice nucleation. Ice particle size distributions which were measured with certain optical particle counters must be corrected for the evaporation of ice crystals in the warmer sampling line. This was done on the basis of a detailed evaporation model. The corrected size distributions are then compared with AIDA box model calculations and under different conditions of temperatures. The corrected size distribution was used to calculate ice water content within cloud under different conditions.

The experimental results of the reported studies can be used to describe the ice nucleation behaviour of mineral dust aerosols under atmospheric conditions. These results will be useful for explaining observations of ice formation in clouds seeded with mineral dust and for quantifying effects of mineral dust in cloud modelling.

Chapter 2 Instrumentation

This chapter describes (a) the AIDA aerosol chamber, (b) the setup which was used for generating aerosol particles with surface coatings of sulphuric acid, and (c) various scientific instruments which were used to analyse the impact of these aerosol particles on ice crystal formation, number concentration, and their size distribution over a wide range of temperatures and relative humidities with respect to the ice phase. Mineral dust aerosols were coated with sulphuric acid, in a tube furnace characterized by a linear temperature gradient. The pristine or coated mineral dust aerosol particles were sent either to a Scanning Mobility Particle Sizer (**SMPS**) or Differential Mobility Analyser (**DMA**) where the aerosol is classified according to electrical mobility, to determine their size distribution, or to the **AIDA** chamber. The latter is equipped with an optical laser system to detect the onset of ice particle formation which gives rise to depolarisation of the laser radiation that is back-scattered by particles from the centre of the AIDA chamber. Ice crystals were also detected and size classified during the experiments with an optical particle counter **PCS-2000** Type 15A, hereafter denoted **PCS-2000**. It was later combined with another optical particle counter, **Welas**. In-situ **F**ourier **T**ransform **I**nfra**R**ed (**FTIR**) extinction spectra were analysed to discriminate unambiguously between liquid solution droplets and ice crystals (Wagner et al., 2005b). Large cloud particles were classified in cooperation with the University of Manchester with a **C**loud **P**article **I**mager (**CPI**) as "spherical" or "non-spherical". 6 different habits of non-spherical particles were distinguished (Connolly et al., 2004; see also http://www.specinc.com/publications/CPIview_Manual.pdf).

The concentrations of interstitial water vapour or of total water (i.e. including particulate water which evaporated before ex-situ detection) were measured by a suite of instruments. Total water was measured redundantly with the following ex-situ instruments: (a) the so-called "**F**ast **I**n-**S**itu **H**ygrometer" **FISH** (Zöger et al., 1999), (b) a commercial frost point hygrometer **MBW 373**, and (c) a **P**hoto **A**coustic **S**pectroscopy (**PAS**) sensor which was developed by the University of Szeged in Hungary (Szakáll et al., 2001; 2004). Interstitial water vapour could be measured in-situ by **T**uneable **D**iode **L**aser **A**bsorption **S**pectrometry (**TDLAS**) in combination with a White-type multi-reflexion cell inside the AIDA chamber (Ebert et al., 2005).

2.1 AIDA

AIDA is an acronym for **A**erosol **I**nteractions and **D**ynamics in the **A**tmosphere. The aerosol chamber AIDA is a big cylindrical vessel, approximately 7.5 m high and 4 m in diameter, with a volume of 84.3 m^3. The vessel is made of 2 cm thick Aluminium (AlMg3 = pure aluminium with traces of Mg and other elements, Zeppelinwerke Friedrichshafen) and mounted vertically at the centre of a

containment with carefully controlled uniform air temperature, as shown schematically in Figure 2.1 a. The chamber can be operated in the pressure range from 0.02 hPa to 1500 hPa and in the temperature range from -90°C to +60°C (Möhler et al. 2003, 2004, 2005; Wagner et al. 2005a). This allows us to simulate the full range tropospheric and lower stratospheric pressures, temperatures and humidities and to study under laboratory conditions ice nucleation processes within different cloud types which occur at all altitudes in the real atmosphere from near the ground up to the lowermost stratosphere.

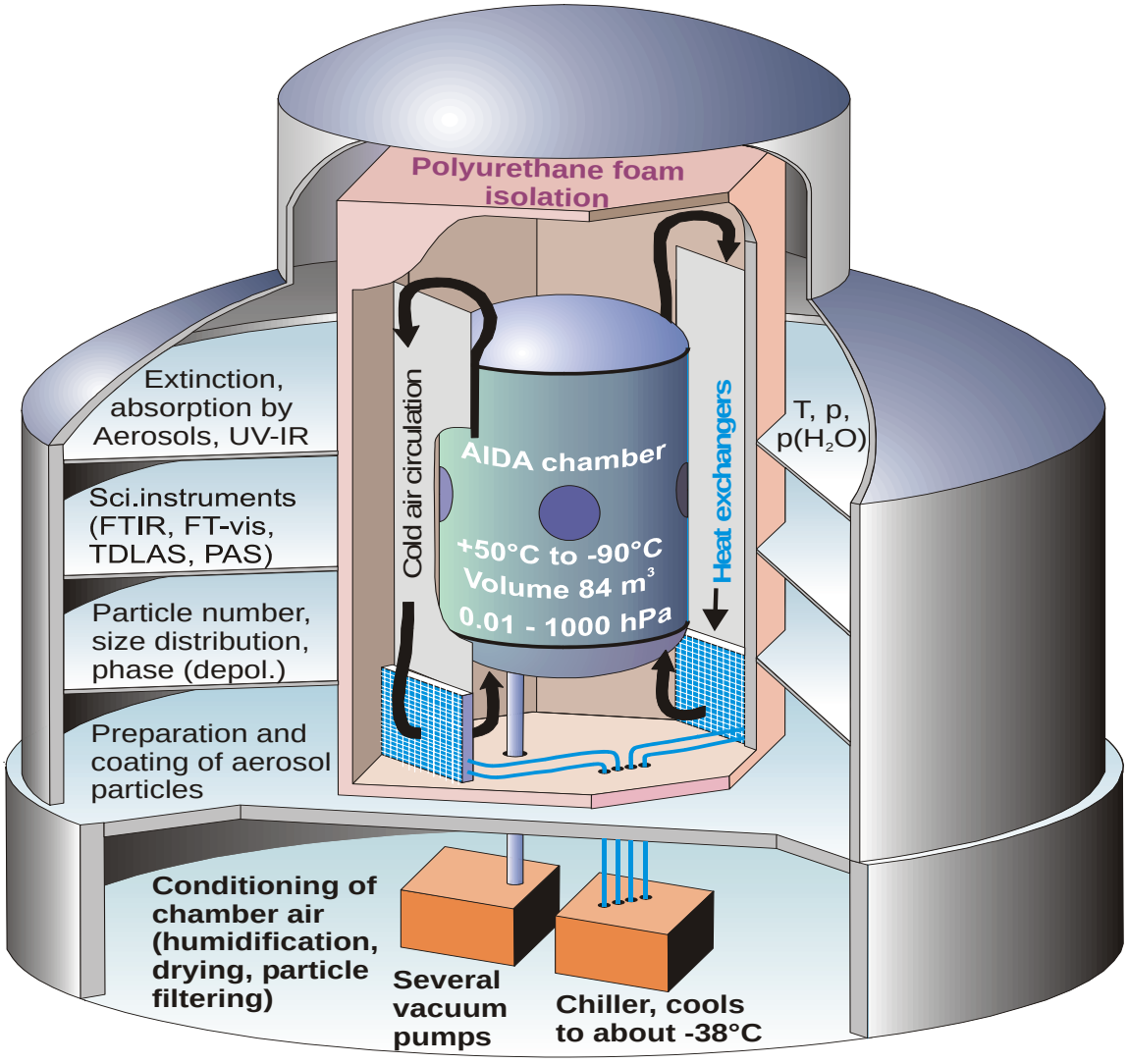

Figure 2.1 a: Exploded view of the circular AIDA laboratory building. The cylindrical aluminium chamber is mounted in a containment with carefully controlled uniform temperatures, as indicated, which is thermally isolated by 200 mm thick polyurethane foam walls. The containment is surrounded by three laboratory platforms. The vacuum pumps, the chiller and the conditioning system for the filling air are located in the basement below the ADIA laboratory building.

The temperature of the AIDA chamber and its uniformity are controlled by forcing dry air through two heat exchangers at a rate of 28,000 m^3 h^{-1} which circulates the cold air in the space between the chamber and the isolating containment. The walls of the latter consist of 200 mm thick polyurethane foam elements which are sandwiched between sheet metal. The chamber can be cooled to less than -35°C with a conventional chiller that is located in the basement below the AIDA laboratory building. For further cooling to a minimum temperature of about -90°C liquid nitrogen from a tank lorry is evaporated in two heat exchangers. The AIDA vessel can be evacuated to a final pressure of a few Pa with two vacuum pumps, hereafter denoted **principal pumps,** which are situated in the basement below the AIDA chamber. For most of the experiments the aluminium walls of the AIDA chamber were internally coated with a thin ice layer to establish near 100% relative humidity with respect to ice (RH_i, index *i* refers to ice) under static conditions. The ice layer was prepared in most cases by filling the chamber with humidified air at a higher temperature and cooling it slowly to the operating temperature, thereby depositing the excess water vapour directly on the walls. The relative humidity remains somewhat less than 100% RH_i though, because the static air temperature in the chamber is always slightly higher than the wall temperature due to several internal heat sources (e.g. the ventilator, heated optical mirrors, and several heated sampling tubes).

Relative humidities RH_i larger than 100% can be established by expansion cooling, i.e. by reducing the chamber pressure with the mechanical pumps. The cooling rate can thereby be varied from less than 0.1 K/min, as in a cirrus cloud, to more than 4 K/min, as in mountain lee waves, depending on the pumping speed. Since the dry adiabatic lapse rate $\gamma = -dT/dz = Mg/c_p$ in the atmosphere amounts to 9.75 K km^{-1}, these cooling rates correspond to updraft velocities between 0.15 m s^{-1} and 6.5 m s^{-1} in the troposphere (Möhler et al. 2003).

A schematic drawing of the AIDA chamber showing (in- and outside the thermostated containment) some of the relevant scientific instrumentation which was used in this work is presented in Figure 2.1b. Five fast thermocouples are fixed on a vertical wire which extends parallel to the chamber axis at a closest distance of about 1 m from the sidewalls of the chamber (the uppermost thermocouple is not included in the following considerations). The thermocouples which were carefully calibrated are used to continuously monitor the air temperature T_g at the lower, middle, and upper levels of the chamber as shown in Figure 2.2a. The gas temperature in the chamber is fairly uniform under static conditions, but fluctuates somewhat more (a few tenths of a degree) around its mean value during expansion cooling events, as shown in Figure 2.2b. The uniformity of the gas temperature is further improved by means of a ventilator, as shown schematically in Figure 2.1b, which is installed inside the chamber about 1 m above the bottom flange. The mean value of four

measured gas temperatures (i.e. excluding the uppermost thermocouple reading), hereafter referred to as $\overline{T_g}$, was used in our calculations.

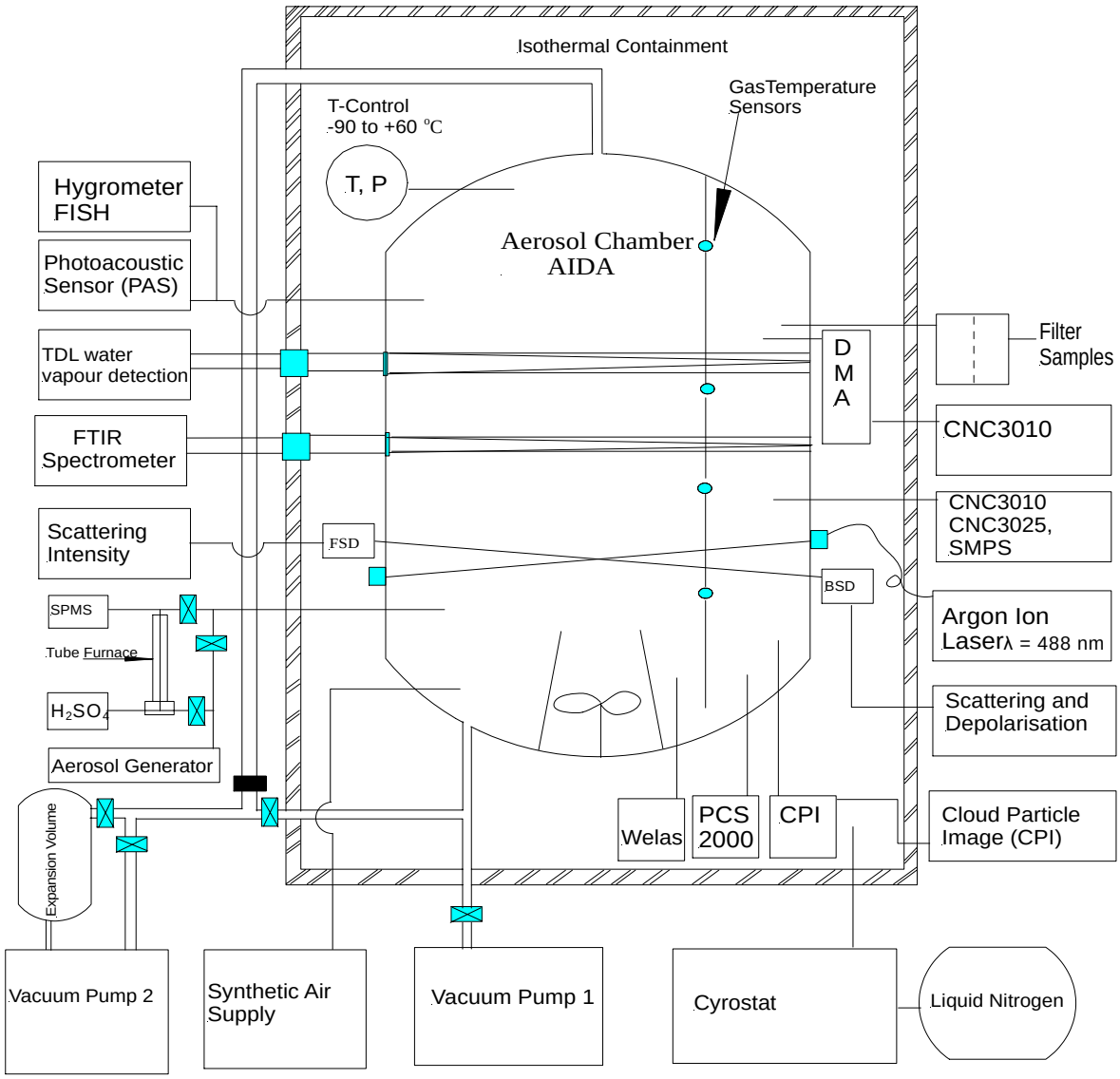

Figure 2.1 b: Schematic view of the AIDA experimental facility showing the technical components and the scientific instruments that were used for the experiments reported in this work. The expansion volume of 4 m^3 (lower left, above vacuum pump 2) is referred to as the NAUA vessel in Figure 2.2.

Before the measurements begin, the internally ice-coated chamber is evacuated and flushed several times with pure synthetic air to remove aerosols and other impurities from previous experiments (note that the ice coating is partially removed by these treatments; this limits the number of experiments which can be carried out with a single ice coating of the chamber walls). Then it is

filled to ambient pressure with particle-free synthetic air from a gas bottle bundle with remotely controlled valves that is located outside the AIDA laboratory building. Filling the chamber with synthetic air increases T_g considerably above the wall temperature, T_w. After turning off the synthetic air supply it takes more than 15 minutes until the air temperature T_g equilibrates with the temperature T_w of the chamber walls. T_w remains approximately constant throughout an experiment due to the large heat capacity of the thick aluminium walls and the active temperature control of the cold air which circulates in the space between the aluminium vessel and the isolating polyurethane foam walls. Before starting the pumps all instruments that are needed for that particular experiment are turned on. The obtained data are automatically stored for later analysis.

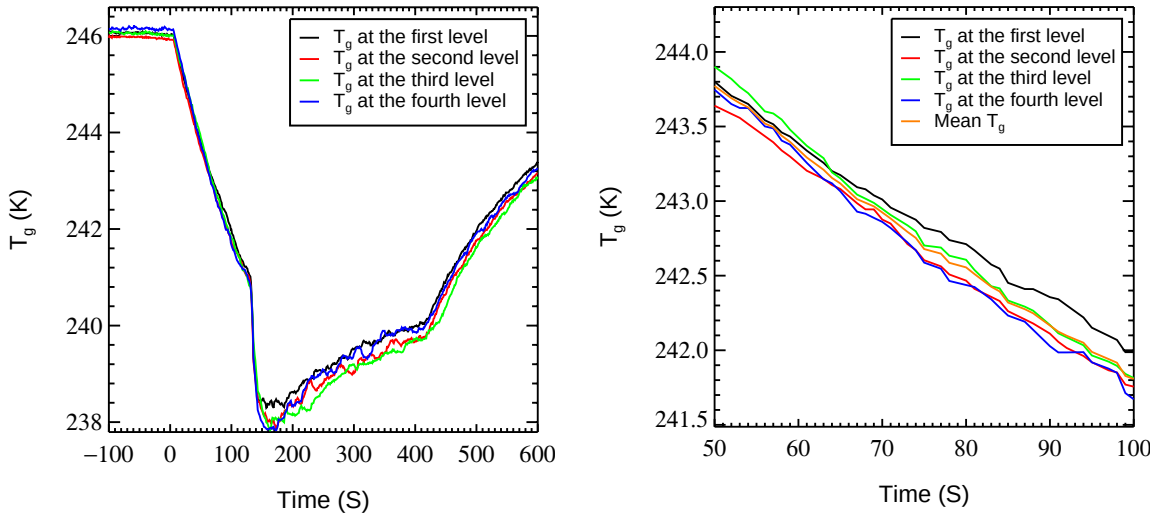

Figure 2.2: (a) An example showing the measured gas temperatures at the four vertical levels in the chamber during activation number 74 INO2. The steep temperature drop after t ~ 130 s results from a shock expansion into the pre-evacuated NAUA vessel, volume $V_{NAUA} = 4\ m^3$, see lower left of Figure 2.1b.
(b) As shown in (a) but on an expanded time scale and including the mean gas temperature for comparison.

When the principal pumps are turned on the air pressure starts to decrease continuously, inducing a reduction of the gas temperature while the temperature of the ice-covered chamber walls remains constant. This creates supersaturation of the air inside the chamber with respect to the ice phase. The cooling rate and the build-up rate of ice supersaturation depend on the speed of the principal pumps. The cooling process is comparable to adiabatic expansion cooling which happens when an air parcel is lifted in the free atmosphere. However, different from the free atmosphere, the presence of the isothermal chamber walls gives rise to a heat flux from the walls into the chamber air

which causes the cooling rate to diminish until after several minutes of pumping it levels off at a more or less constant ΔT below the wall temperature. Examples for two different pumping speeds are presented in Figure 2.3.

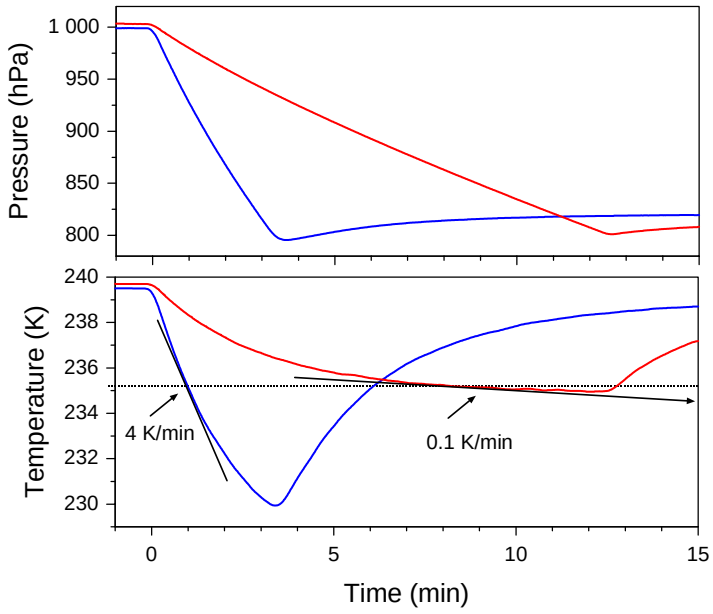

Figure 2.3: Pressure profiles for two different pumping speeds (upper panel) and associated temperature profiles (lower panel), recorded in this case with slow temperature sensors. Note that after about 13 min pumping at low speed T_g already starts to approach a steady-state ca. -5° below T_g(t=0), i.e. before the pump was started.

An extremely fast reduction of the gas pressure by about 5% within a few seconds and thereby of the mean gas temperature (cf. Figure 2.2a) can be realised by opening the connecting valve between the AIDA chamber and the pre-evacuated so-called NAUA chamber which has a volume of 4 m^3. In this case the rate of the pressure change and of the associated temperature reduction depends on the inner diameter of the connecting tube between the two chambers and the pressure difference between them. This nearly adiabatic expansion mode which uses the NAUA chamber as an evacuated buffer volume will be referred to later on as a **secondary expansion**.

2.2 Instrumentation for Chemical Analysis

2.2.1 Elemental Analysis

The mineral dust samples were analyzed chemically using an X-ray fluorescence spectrometer (SRS 303AS from BRUKER-AXS) at Institut für Materialforschung I, Forschungszentrum Karlsruhe. Amounts of 50 mg mineral dust were taken from each sample and annealed for about one hour at

1000°C. Eight elements Al, Fe, Mg, Na, Ca, Si, P, and Ti were measured two times by this technique. The averaged results are expressed as weight-% of their most stable oxides.

2.2.2 Ion Analysis

Ion chromatography is the only technique that can be used to analyse anions in aqueous solution at the ppb level. We used this technique to determine water-soluble ionic coatings on the particle surfaces of dust samples. The following inorganic ions were analyzed by Ion Chromatography (Dionex DX 500 IC): Na^+, NH_4^+, K^+, Mg^{2+}, $NO_2^-, NO_3^-, PO_4^{3-}, SO_4^{2-}$. The instrument consists of an eluent reservoir organizer, a gradient pump GP40 to move the eluent, a chromatography module LC20, a detector CD20 which measures the separated ions, and a recording system. The chromatography module contains the injection device and the analytical columns. A dual-channel system includes a second pump and the second detector. The pump delivers the eluent into the analytical columns and the connection tubes with a constant flow rate. The detector is sensitive to components which have different properties than the eluent (here: different conductivities). The detected signals are proportional to the concentration of the respective ions. The signal intensities, which appear as peaks in the ion chromatogram, are recorded and integrated to determine ion concentrations.

Before analysing the soluble ion contents of the mineral dust samples, the IC system was calibrated using standard solutions containing known concentrations of the anions Cl^-, NO_3^-, SO_4^{2-}, and of the cations $Na^+, NH_4^+, K^+, Mg^{2+}, Ca^{2+}$. Constant volumes of the standard solutions were injected into the analytical columns. Calibration curves were obtained by plotting the peak areas of each ionic species versus their concentrations in the injected standard solutions. Ideally the calibration curves should be straight lines, which were found to be the case within the scatter of the measurements. For our analyses, about 40 mg of each desert dust sample were extracted two times with 6 ml deionised water to dissolve ions from the particle surfaces as follows: The particle suspensions were treated 10 minutes in an ultrasonic bath, and the solutions were separated from the leached particles by filtering the suspensions through 0.2 µm membrane filters (Ø 25 mm). The obtained filtrates were analysed by injecting 2 ml into the IC to start the analysis process, which took about 25 minutes per injection. This procedure was repeated three times for each filtrate.

2.3 Instrumentation for Water Vapour Measurements

Water vapour mixing ratios in the ppmv (parts per million by volume) range occur at the low temperatures which prevail in the upper troposphere and lowermost stratosphere. Typical vertical profiles of water vapour mixing ratios in equilibrium with liquid or supercooled liquid water (blue line), or with ice (red line), are shown schematically in Figure 2.4. These profiles were calculated from the equilibrium vapour pressures p(T) over liquid / supercooled liquid water (Pruppacher and Klett, 1997) or ice (Marti and Mauersberger, 1993) which are, however, not very well know at very low temperatures where direct measurements of the vapour pressure in equilibrium with supercooled liquid water are not available (Murphy and Koop, 2005). Figure 2.4 is based on the assumption that the tropospheric temperature profile can be represented by the US Standard Atmosphere which assumes a constant adiabatic lapse rate of $\gamma = -(dT/dz) = 6.5$ K km^{-1} throughout the troposphere. True temperature and RH profiles differ considerably from this standard profile (see e.g. Figure 3 in Miloshevich et al., 2006), depending on latitude and season. While the true water vapour mixing ratios outside of a cloud may be less than the vapour pressure in equilibrium with liquid or super cooled liquid water at each altitude and temperature, it cannot exceed the liquid water saturation line significantly due to the formation of a liquid water cloud. The ice saturation line, however, can be exceeded in the absence of ice nuclei. Water vapour mixing ratios in the same range must also be accurately measured in the AIDA chamber, which can be done with several different ex-situ and in-situ instruments. These will be briefly discussed in the next section.

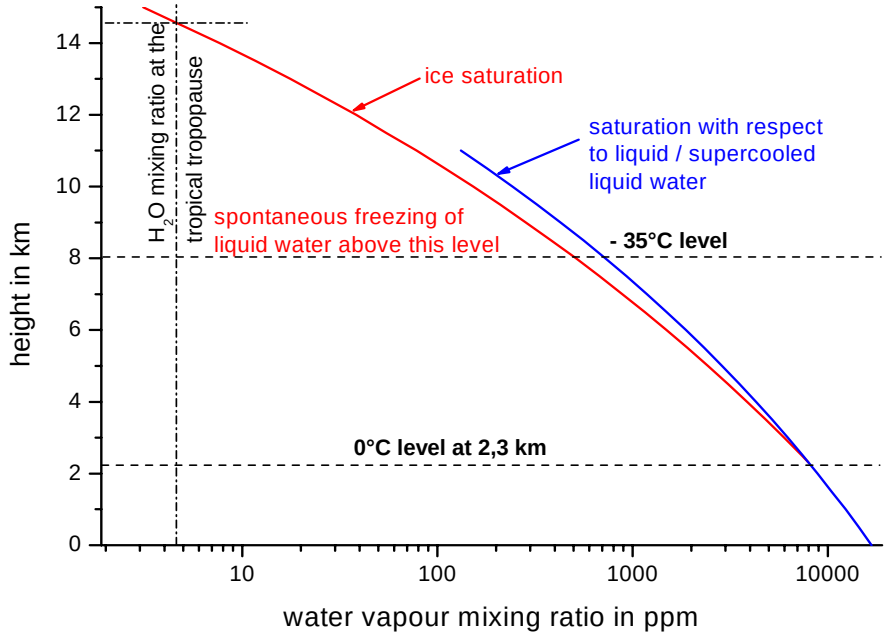

Figure 2.4: Vertical profile of tropospheric water vapour mixing ratios corresponding to 100% RH with respect to liquid water (blue line) or ice (red line), calculation based on the temperature profile of the US Standard Atmosphere (D.R. Lide, 1998).

2.3.1 The Fast In-situ Hygrometer FISH

The Fast In-situ Hygrometer FISH measures OH photofragment fluorescence at 308 nm, which arises from the photodissociation of water vapour molecules by a Lyman-α VUV photolysis lamp, λ_{photon} = 101.6 nm. The fluorescence intensity is proportional to water vapour mixing ratios in the range between several 100 ppmv and about 0.1 ppmv. The instrument, which was operated as an ex-situ detector during the AIDA experiments, was developed by Forschungszentrum Jülich, Institut für Chemie und Dynamik der Geosphäre (ICG), Stratosphäre (ICG-I), for balloon-borne and aircraft-borne water vapour measurements in the upper troposphere and in the stratosphere (Zöger et. al 1999). We used the FISH instrument to measure the total water content (i.e. interstitial water vapour plus water vapour from ice crystals which evaporate in the heated sampling line) with a time resolution of 1 second and an accuracy of about 6% after calibration. Air including aerosol particles and small ice crystals is sampled from the AIDA chamber at a flow rate of 5 l/min through a stainless steel tube of 10 mm inner diameter which is heated to ~ 300 K. The water vapour mixing ratio measured by the FISH instrument can also be used to calculate the interstitial vapour pressure up to the moment of ice nucleation, provided that the water content of the unfrozen seed aerosol can be neglected (Möhler et al. 2004). The detection limit of the FISH instrument is about 0.02 Pa at a chamber pressure of 1000 hPa (Mangold et al. 2005, Wagner et al. 2003).

2.3.2 The Frost Point Hygrometer MBW 373

The frost point hygrometer MBW 373 (see http://www.label.com.pl/en/rek_373.html) is a commercial high precision instrument which measures directly the frost point temperature of the sampled air. The hygrometer, which we also use as a reference instrument to calibrate other water vapour sensors, was connected in parallel with the FISH instrument to the same heated sampling line to measure total water content in the AIDA chamber. Measurements are based on the optical detection of condensation and evaporation of water vapour on a chilled mirror surface. This particular hygrometer can measure the frost point temperature below -80°C with an accuracy of ± 0.1°C, while the accuracy of water vapour concentrations at this temperature is about 5% and about 10% at -90°C. Below about -20°C the instrument unambiguously measures the frost point. However, in the temperature range between 0°C and about –20°C either ice or super cooled water droplets may condense on the chilled mirror. This gives rise to ambiguities in that temperature range because the vapour pressure in equilibrium with ice is significantly lower than the vapour pressure in equilibrium with supercooled liquid water at the same temperature (or altitude in the atmosphere, cf. Figure 2.4). A similar ambiguity may exist at very low temperatures (well below 200 K) where metastable cubic ice may nucleate on the chilled mirror surface which has a larger vapour pressure than hexagonal ice (Murray et al., 2005; Murphy and

Koop, 2005). Soluble deposits (e.g. ammonium sulphate aerosol particles) on the chilled mirror must be regularly removed by cleaning to eliminate further ambiguities due to the formation of solution droplets.

2.3.3 The Photoacoustic Spectroscopy (PAS) Water Vapour Sensor

Optical Absorption Spectrometry with tuneable diode lasers (TDLs) can be used in various ways to measure very low water vapour concentrations in the AIDA chamber and elsewhere. Ex-situ Photoacoustic Spectroscopy (PAS) of water vapour, a sensor developed in cooperation with Szeged University, Hungary, is based on the absorption of modulated laser light by a water vapour absorption line of an overtone transition near 1.36 nm in a photoacoustic cell made of stainless steel (Szakáll et al. 2001). The cell contains two acoustic resonators of 40 mm length and 4 mm diameter with identical microphones (Knowles, EK 3209) which are sampled by a differential amplifier to suppress acoustic noise: environmental noise affects both microphones simultaneously, while the beam of the TDL passes only through one of the resonators and produces a photoacoustic signal which is sampled by one microphone only. The PAS cell is placed between acoustic filters. The sensor can be operated with a continuous flow rate of up to 1 l/min. It is connected to the same sampling line as the FISH and the frost point hygrometer, i.e. it also measures total water. The detection limit of the PAS sensor is a function of the total pressure, as shown in Figure 2.5.

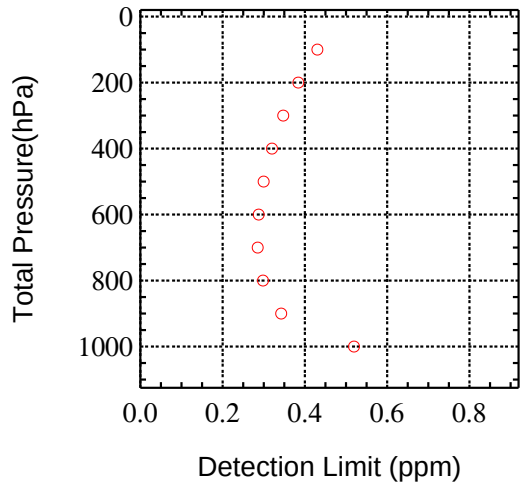

Figure 2.5: Detection limits in terms of water vapour mixing ratios for the PAS system plotted as function of the total pressure, optimised in this case for 700 hPa.

Another fully automatic PAS water vapour sensor was recently developed by the University of Szeged (Szakáll et al., 2004) for the CARIBIC payload. In December 2004 the PAS system has successfully operated on a first flight from Frankfurt to Buenos Aires, Santiago de Chile and back to

Frankfurt. The CARIBIC payload is a container which is regularly deployed on a Lufthansa Airbus A340-600 to automatically measure water vapour, ozone, aerosols and numerous other trace constituents at cruise altitude. For further details see http://www.caribic-atmospheric.com/.

2.3.4 In-Situ Tuneable Diode Laser Absorption Spectroscopy (TDLAS)

Interstitial water vapour in the AIDA chamber (i.e. excluding water in condensed phases like ice particles and liquid solution droplet aerosols) is measured in-situ by Tuneable Diode Laser Absorption Spectroscopy (TDLAS). The system was developed in cooperation with Physikalisch-Chemisches Institut (PCI), Heidelberg University (see Ebert et al., 2005). The Distributed Feedback (DFB) laser is tuneable in the range 1370 ± 2.5 nm. Several water vapour absorption lines with different line strengths can be selected in this wavelength interval, depending on the desired dynamic range. The software of the TDLAS system takes account of the pressure and temperature dependence of the line shapes and line strengths and yields water vapour concentrations with a time resolution of 1 second. The diode laser is located outside the cold AIDA containment at room temperature. The laser light is fibre-coupled to a White-type multipass cell between mirrors that are fixed on opposite flanges inside the AIDA chamber and provide 84 m optical path length. A resolution in water vapour mixing ratio of down to 15 ppb (parts per billion) has been demonstrated (Mangold et al. 2005, Giesemann et al. 2004, Ebert et al., 2005)

The ice saturation ratio is defined according to the following formula (Pruppacher and Klett 1997, Young, 1993)

$$S_{ice} = \frac{e_w}{e_{sat,i}} \tag{2.1}$$

where e_w is the interstitial water vapour partial pressure determined by TDLAS, while $e_{sat,i}$ is the saturation vapour pressure over ice that is calculated for the mean gas temperature according to the following equation which is related with the simplified Clausius-Clapeyron equation:

$$\log e_{sat,i} = 12.537 - \left(\frac{2663.5}{T} \right) \tag{2.2}$$

This equation yields $e_{w,ice}$ in Pa (Marti and Mauersberger, 1993). *T* is the temperature in K. Recently a slight modification of this equation has been recommended by Murphy and Koop (2005).

2.4 Detecting the Onset of Ice Particle Formation

In contrast to the formation of liquid water clouds which condense on soluble particulate matter according to Köhler theory when liquid water saturation is exceeded by just a few tenths of a %, ice saturation must be *significantly* exceeded until ice particles nucleate on any kind of particulate matter, e.g. by up to about 65% in the case of homogeneous freezing of liquid sulphuric acid aerosol particles below 200 K (Möhler et al., 2003; Koop et al., 2000). The ice saturation ratio at which ice nucleation occurs will be termed the critical saturation ratio with respect to ice S_{crit}. It strongly depends on the nature of the seed aerosol particles which act as ice nuclei.

The time at which ice crystal formation takes place in AIDA is detected optically during expansion cooling experiments. This is possible by measuring the intensity of forward scattered light which is extremely sensitive to particle size, and the depolarisation of laser light back-scattered by particles in the centre of the AIDA chamber. For this purpose, an Argon Ion laser beam of wavelength 488 nm is horizontally directed through the chamber *via* an optical fibre. The aperture of the detection optics at 4° and 176° scattering angles overlaps the laser beam inside the chamber at a distance of 2 m from the walls. The overlap defines a sensitive volume of ~ 1.8 cm^3, as shown schematically in Figure 2.6a.

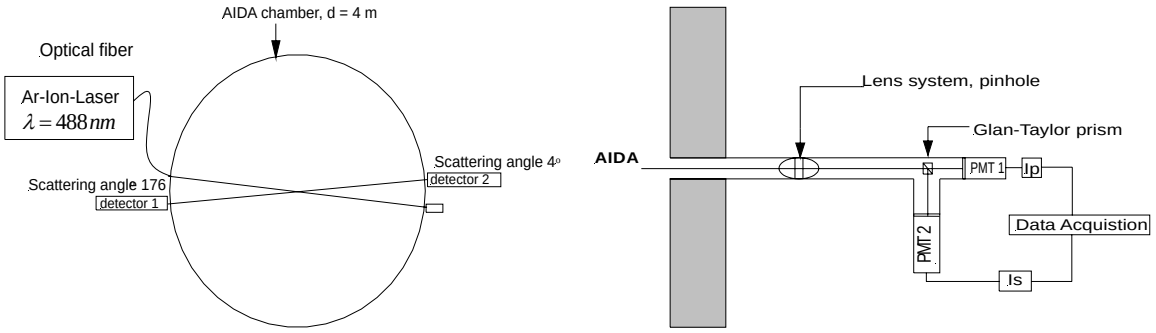

(a) (b)

Figure 2.6: (a) Schematic cross-section through the AIDA chamber showing the Argon Ion laser and the forward-backward scattering arrangement. (b) Measurement of the intensity and depolarisation of laser light forward and back-scattered from the overlap region of the laser beam with the optical field-of-view of the detector. After Möhler et al. 2000.

The back-scattered light intensity is split into the parallel $I_{\parallel}$ and the perpendicular $I_{\perp}$ components by a Glan-Taylor prism and then detected by two independent photomultipliers, PMT1 and PMT2 in the photon counting mode, using integration time steps of 1 second, as shown schematically in Figure 2.6b. A second optical detector is mounted in the forward direction at a scattering angle of 4° measuring total scattering intensity with a single photomultiplier as shown in

figure 2.6a, because depolarisation is negligible at this scattering angle, independent of particle shape. The depolarisation ratio is defined according to the following equation.

$$R_{depol} = I_{\perp} / I_{\parallel} \quad (2.3)$$

Mie theory predicts that no depolarisation occurs for light which is back-scattered by perfectly spherical particles, e.g. solution droplet aerosols, while light back-scattered by aspherical particles is partially depolarised. The degree of depolarisation due to ice crystals depends strongly on the habit and size of the ice crystals. R_{depol} increases suddenly when spherical particles (= droplets) become non-spherical (= ice crystals). The time at which ice nucleation occurs can thereby be determined with a time resolution of a few seconds (Schäfers et al., 2001; Büttner, 2004).

2.5 Method of Coated Aerosol Production and Cloud Seeding

Mineral dust aerosol particles which had been coated with sulphate by chemical reactions in the atmosphere were observed by Levin et al. (1996) and Noble and Prather (1996). A system was designed at the AIDA laboratory to simulate this atmospheric ageing process by condensing soluble material onto various insoluble cores such as soot or mineral dust aerosol particles to generate particles of mixed composition, namely aerosol particles coated with sulphuric acid. The coating system consists of two components: (a) the first is an aerosol generator followed by a heated H_2SO_4 reservoir and a temperature gradient tube where the H_2SO_4 vapour condenses on the aerosol particles without forming new particles; (b) the second is an instrument for particle characterisation, i.e. a scanning mobility particle sizer (SMPS) or Differential Mobility Analyser (DMA) which measures the number size distributions of the coated aerosol particles before they are sent to the AIDA chamber, as shown in Figure 2.7.

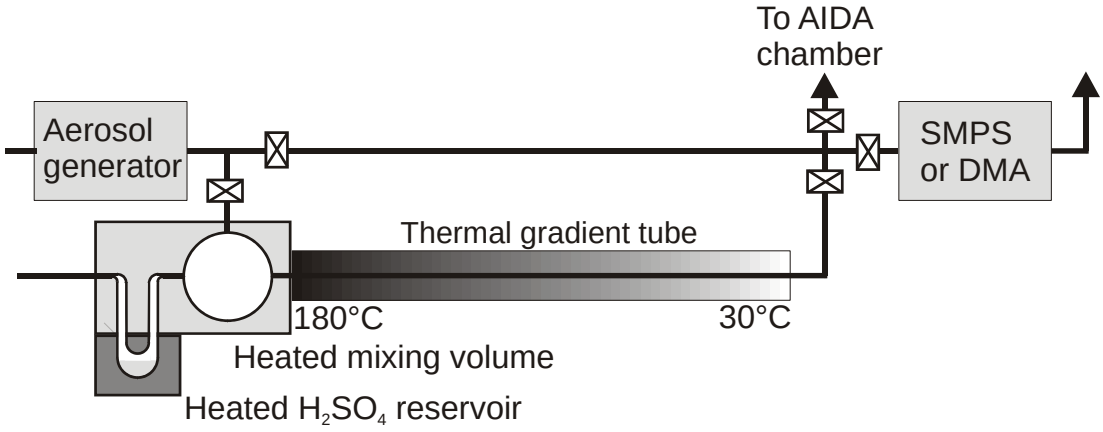

Figure 2.7: Schematic diagram showing the production of aerosol particles coated with sulphuric acid. The coated particles can be used for cloud seeding in the AIDA chamber.

The H_2SO_4 vapour from the heated sulphuric acid reservoir is swept into a heated volume where it mixes with the aerosol particles from the aerosol generator. The mixed materials enter a horizontal tube furnace (1.5 m long, 1.5 cm ID) that is surrounded by a series of tight-fitting aluminium block furnaces each of 15 cm length, with heating cartridges and thermocouples. The temperature of each block furnace can be regulated independently via temperature controllers. This technique allows us to control the temperature profile along the aerosol flow tube. A linear temperature profile from 180 ^{o}C at the beginning to 30 ^{o}C near the end of the tube was chosen. This ensures that the H_2SO_4 vapour is cooled at a controlled rate, thereby condensing on the seed aerosol particles without forming new sulphuric acid particles by homogeneous nucleation. The sulphuric acid coated aerosol particles are sent to an SMPS or DMA to measure their size distribution. The fully characterised internally mixed aerosol can then be used for cloud seeding experiments in the AIDA chamber.

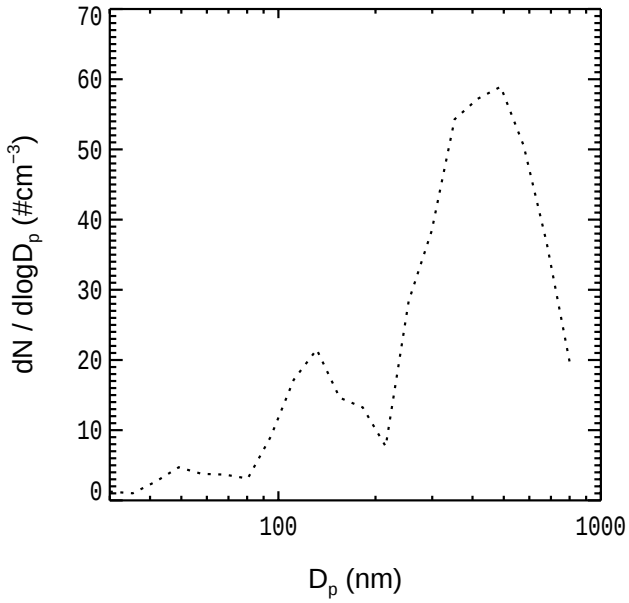

Figure 2.8: Mineral dust size distribution of pristine ATD based on DMA measurements during the second ice nucleation campaign. Three modes are found: (1) very small, (2) small, and (3) large. The first and the second modes are ignored in our studies

Figure 2.8 shows the calculated size distribution of pristine ATD based on DMA measurements. Three modes can be distinguished: (1) very small (from 30 to 80 nm), (2) small (from 80 to 210 nm), and (3) large (from 210 to 800 nm) particles. Only the largest mode will be taken as input to the AIDA process model. The geometric count median diameter and the geometric standard deviation of this mode were calculated to be 442 nm and 1.5, respectively.

2.6 Instruments Detecting Ice Particle Concentration

2.6.1 Fourier Transform InfraRed (FTIR) Spectroscopy

The time of ice nucleation, the mean size (or the size distribution) of the ice particles that nucleate in the AIDA chamber during adiabatic expansion experiments, and the ice water content can be detected by different methods. Depolarisation measurements of back-scattered laser radiation have already been described in the previous section. Fourier Transform Infra Red (FTIR) extinction spectra, measured in-situ with a White-type multiple reflection cell, horizontal optical path of 254.3 m, yield additional information on the time when ice nucleation occurs, on mean particle size, and on the ice water content. FTIR spectra were typically recorded in the wave number range 800 - 6000 cm^{-1} with a resolution of 4 cm^{-1} at time intervals between 40 and 10 seconds (Wagner et al. 2005 a & b, Möhler et al. 2003, Saathoff et al. 2003).

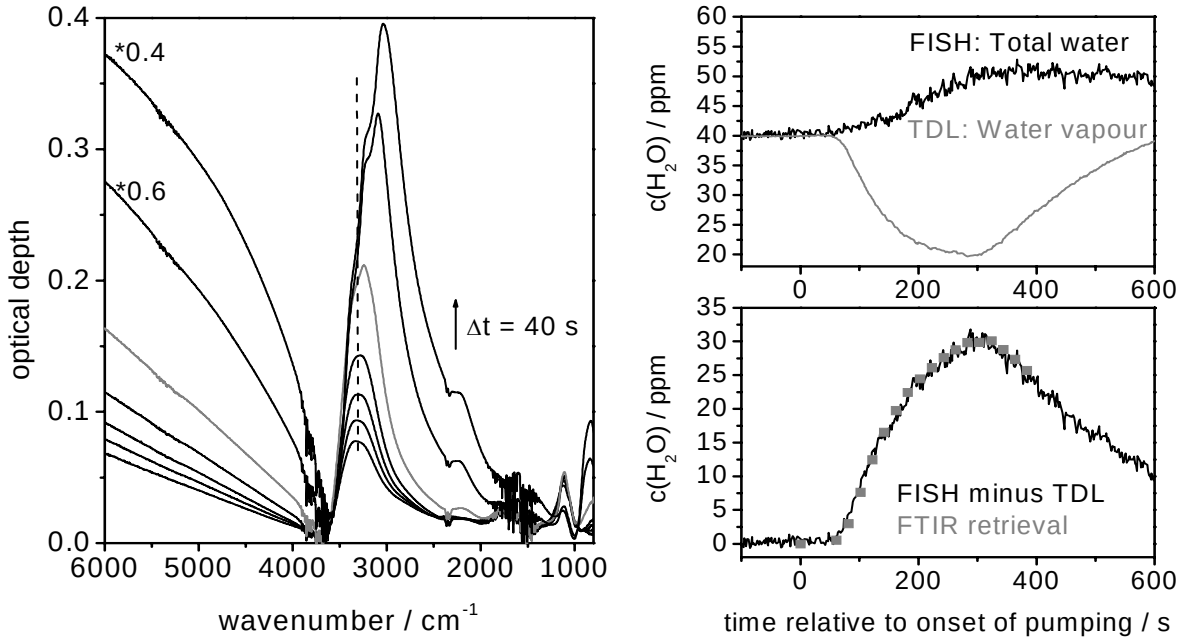

Figure 2.9: Left panel: FTIR spectra of sulphuric acid aerosol, recorded at time intervals of 40 s, during an expansion cooling experiment at stratospheric conditions. The increase in the OH stretching region is initially due to uptake of water vapour by the liquid droplet aerosol. Freezing at 204 K is evidenced by a sudden change of the band contour and a red shift of the OH band of water ice. Right upper panel: interstitial and total water vapour measured by TDLAS and by the FISH instrument. Right lower panel: comparison of condensed phase water by difference (FISH minus TDLAS, noisy line) and retrieved by Mie theory from the FTIR spectra (grey squares). After Wagner et al. (2005b).

The extinction spectra were analysed using the Lambert Beer equation which states that the optical density due to particles is proportional to the particle number density, to their size-averaged extinction cross section, and to the optical path length. Using the known optical constants of water ice, the FTIR spectra could be fitted by Mie theory. This theory, which yields the extinction cross section as function of size and refractive index, is strictly valid only for spherical particles, but may be applied to very small ice particles as a reasonable approximation. The fits yielded the mean particle size, the width of the size distribution, and (more accurately) the ice water content. FTIR spectra recorded during a homogeneous freezing experiment with sulphuric acid aerosol particles which froze at 204 K are shown in Figure 2.9. Also shown are measurements of interstitial and total water as well as a comparison of the ice water content, (a) obtained from the difference of both, and (b) retrieved from the FTIR spectra.

2.6.2 Optical Particle Counters (OPCs)

The number concentrations and size distributions of ice particles that are formed in the AIDA chamber during expansion cooling experiments are not only retrieved from in-situ Fourier Transform Infra Red (FTIR) extinction spectra, but are also measured directly by the optical particle counters (OPCs) that are referred to as PCS-2000 and Welas and developed by Palas manufacturers. These OPCs are directly located in the cold space below the AIDA chamber. They sample air at a flow rate of 5 l/min through vertical stainless steel tubes with an inner diameter of 10 mm from AIDA chamber. The most important difference between both instruments is the fact that the detection volume of PSC-2000 is at an elevated temperature because the instrument has to be protected against the cold in a thermostated box, while the detection volume of Welas remains at the temperature of the AIDA containment during the measurements. Evaporation of small ice crystals must therefore be considered in the case of ice particle sizing with the PCS-2000 instrument, while it is completely negligible for measurements with Welas. More details will be given in the following section.

2.6.2.1 PCS-2000

Ice particles which are formed during adiabatic cooling experiments in the AIDA chamber are detected with an optical particle counter, PCS-2000, as a function of particle diameters between 0.25 and 19 µm. Shown in Figure 2.12e is the total number of particles larger than 0.25 µm, which also includes some of the larger mineral dust particles before and after the simulated ice cloud event. It is interesting to note that C_n after 500 s, i.e. the number of mineral dust particles seen by PCS-2000 after the ice cloud has evaporated, is substantially less than before the ice cloud was formed. This indicates

that ice nucleates first on the largest dust particles, which are therefore preferentially lost by sedimentation of larger ice crystals.

The size range from 0.25 to 19 µm of PCS-2000 is sub-divided into 128 size bins. Particle number concentrations are obtained by using a volume correction of the counted scattering events as single particles pass through the illuminated detection volume. The intensities of the scattering events are used to assign the detected particles to one of the 128 size bins. It should be noted that the particle counter was designed to size-classify spherical particles. Therefore the ice particle size distributions must be regarded as crude approximations, while their total number concentration should be approximately correct.

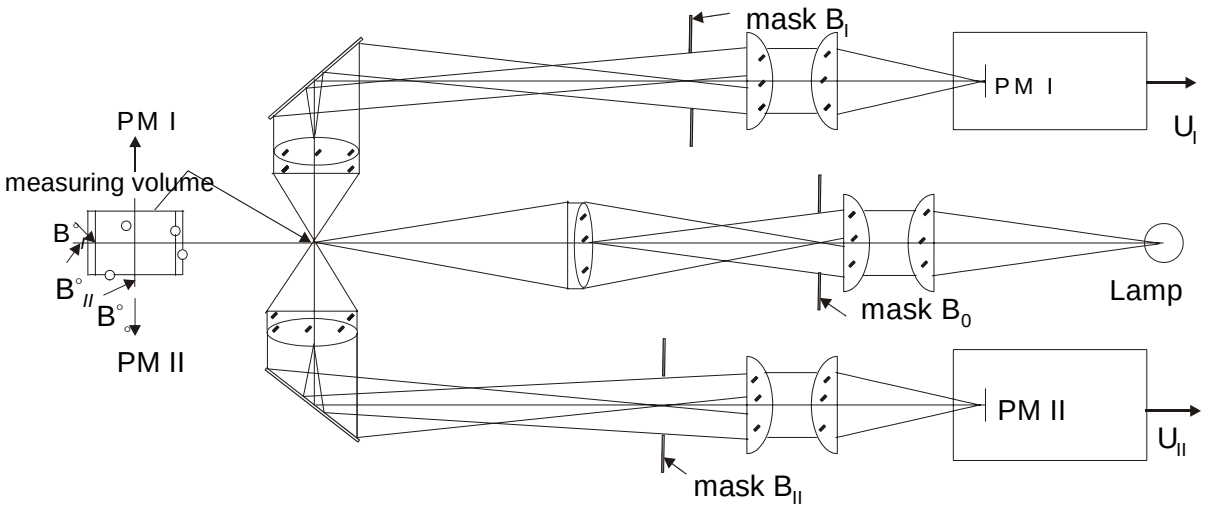

Figure 2.10: Schematic representation of PCS-2000 which illustrates its optical systems and different detection methods of particles that pass through its measuring volume. Particles pass through the detection volume perpendicular to the two optical axes. After PCS-2000 operating manual.

PCS-2000 that is used during the ice nucleation campaigns consists of three optical systems which are shown schematically in Figure 2.10: light from a Xenon high pressure arc lamp is focussed by a lens system into the measuring volume. The rectangular cross section of the beam is delimited by mask B_o in such a way that an area of 90 x 90 μm^2 is uniformly illuminated. The other two systems are photomultipliers that are independent of one another and detect light scattered in opposite directions at scattering angles of about 90 $\pm$ 12° by particles passing through a measuring volume with the same amplification (details are discussed in Section 2.9.1 where the exact ranges of scattering angles are listed in Table 2.1). The areas seen by each of the photomultipliers (90 $\times$ 90 μm^2 for PM1, and 130 $\times$ 90 μm^2 for PM2) are also bordered by different rectangular apertures B_I and B_{II}, as shown

schematically to the left of Figure 2.10, yielding detection volumes of 90 × 90 × 90 μm^3 and 90 × 90 × 130 μm^3, respectively.

By comparing the pulsed signals from PM1 and PM2 it is possible to distinguish between (spherical) particles that passed entirely through the inner measurement volume and particles that were at least partially outside the inner measurement volume in the following manner: both systems detect the same signal when a (spherical) particle passes entirely through the inner measuring volume of PM1 which is also part of the larger measuring volume of PM2 (Note that the signals of both photomultipliers may differ even if a particle passes entirely through the inner measuring volume if the scatterer is a non-spherical ice particle!). PM2 detects a signal, but PM1 does not if a particle passes only through that part of the larger measuring volume which does not overlap with the inner measurement volume of PM1. Both photomultipliers measure a signal, but the signal seen by PM2 is higher than that of PM1 if the particle passes along the border of the inner measuring volume that is perpendicular to the optical axis of the illumination system.

Both systems may also measure different signals if a particle passes through the outer border of both detection volumes which are parallel to the optical axis of the illumination system as a result of asymmetrical illumination in the border zone. This gives rise to the so-called borderzone error. It is eliminated by setting the discrimination amplitude of the software for the scattering signal relative difference of both photomultipliers, $\left(U_{PM_{II}} - U_{PM_I}\right) / U_{PM_{II}}$, to 33% in the case of irregular particles and 10% in the case of spherical particles. The choice must be made *before* the measurements begin. The measurement value is always taken from PM1 while PM2 only serves as a reference channel for the borderzone correction (Umhauer, 1981).

2.6.2.2 Welas

A new version of the optical particle counter PCS-2000, hereafter **Welas**, which was also developed by Palas manufacturers, has been used more recently to size-classify ice particles which are formed on seed aerosols during expansion cooling experiments in the AIDA chamber. The new instrument which classifies particles in 4096 size bins can be operated at a flow rate of about 5 liter per minute. It was mounted below the AIDA chamber where it samples air through a vertical tube of 10 mm inner diameter. The advantage of Welas is the fact that the particles remain at AIDA temperature throughout the sampling and detection procedures. This is important in the case of small ice crystals which evaporate rapidly when the air temperature is increased, as will be discussed in more detail later.

The principle of detecting particles by Welas is not fundamentally different from that of PCS-2000. Welas has two optical systems instead of the three systems of PCS-2000. A high pressure Xenon

arc lamp illuminates a T-shaped mask B_{T0}, which is imaged by a lens system into the measuring volume. The other system incorporates a photomultiplier that detects light which is scattered at approximately 90 $\pm 12°$ by particles which pass perpendicular to both optical axes throught a measuring volume. The field seen by the photomultiplier is also bordered by a T-shaped mask B_{TI}. The areas of both T-aperatures are equal. The arrangment of the two T-aperatures projects a measurement volume in the shape of two stacked cubes of different sizes, as shown in Figure 2.11. The measuring volume has a hight of 280 µm that is defined as the length from the upper base of the big cube to the lower base of the small cube and a square base of 280 × 280 µm^2 that is equal to the base area of the small cube. Thereby it is possible to measure particle size and number practically without border-zone-error.

Pulse shape analysis is used to discriminate between (a) particles P1 that move *only* through the detection volume with 280 × 280 µm^2 base area, (b) particles P2 that move through the upper large cube but not through the lower smaller cube, and (c) other particles P3 which move through the upper cube and along the border of the lower smaller cube. All particles P1 are counted, all particle counts P2 are rejected, while intermediate cases P3 are used for a correction.

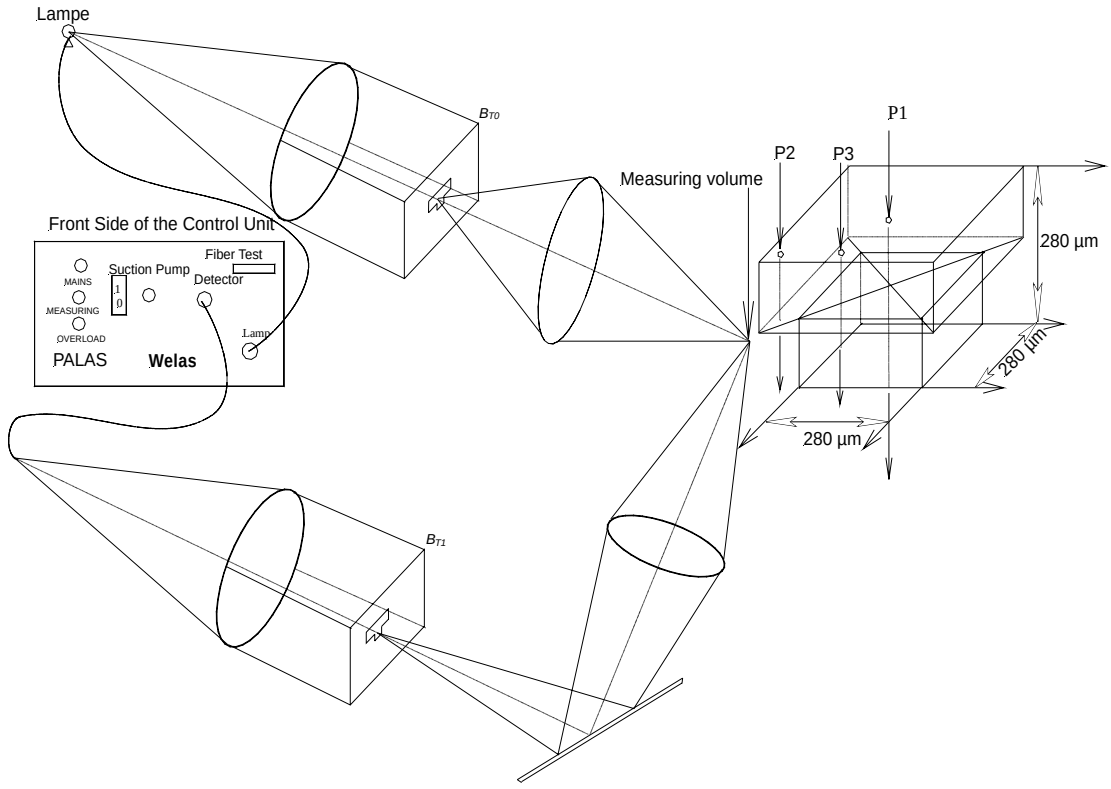

Figure 2.11: Schematic representation of Welas which illustrates the novel design of its optical systems and of the measuring volume that has the shape of two stacked cubes of different sizes. Three particle trajectories are shown to illustrate the discrimination principle (after Welas operating manual).

2.7 Cloud Particle Image (CPI)

High resolution images of particles were recorded by a Cloud Particle Imager (CPI). The instrument, which was contributed by the University of Manchester, was developed by SPEC Inc. (Stratton Park Engineering Company Inc., see http://www.specinc.com/cpi_operation.htm). It was installed below the AIDA chamber next to the PCS-2000 and Welas instruments, as shown schematically in Figure 2.1b. The CPI optics are shown in Figure 2.12: two continuous-wave (CW) diode laser beams are shaped into ribbons 2.4 mm wide and 0.5 mm thick. Their intersection defines the rectangular detection volume of 2.4×2.4×0.5 mm^3 which is inclined 45° with respect to the airflow. Particles are sampled from the AIDA chamber through a vertical connecting tube of 1.8 cm ID at a rate of 50 l per minute. The optical axis of the imaging system is orientated perpendicular to the rectangular detection volume, i.e. at 45° to the sampling flow. When a particle passes through the intersection of the two laser beams, the 25 ns imaging laser is pulsed and an image of the particle is cast on the CCD of the digital camera. The particle image is recorded with a resloution of 1024×1024 pixels, the pixel size is 2.3×2.3 μm^2.

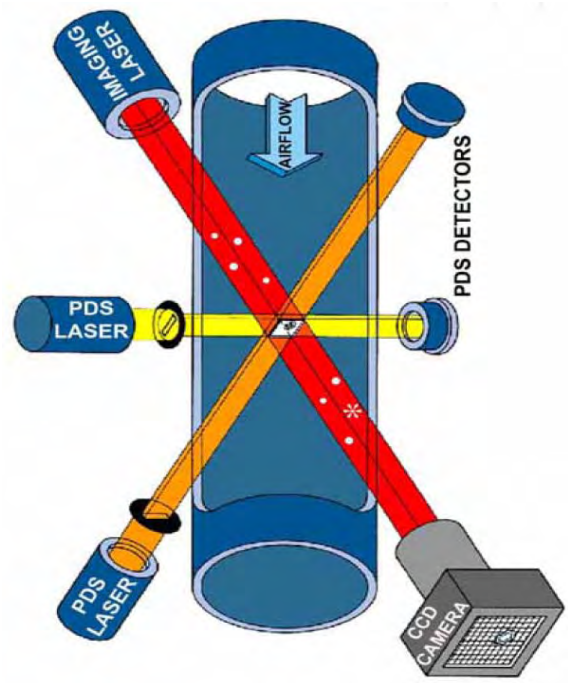

Figure 2.12:
Schematic representation of the CPI (as arranged under the AIDA cloud chamber): When a particle penetrates the detection volume which is defined by two ribbon-shaped overlapping cw diode laser beams, the pulsed imaging laser is triggered, and an image of the particle is recorded by the CCD camera.

2.8 Description of a Typical Ice Nucleation Experiment

In this section we will describe a typical ice nucleation experiment that involves measurements with those instruments which have been described so far. For the purpose of illustration we have chosen experiment N° 74 IN02 which was carried out with uncoated Arizona test dust as seed aerosol at an air temperature of –27°C. The number concentration of the seed aerosol was 88 #/cm^3. Data recording begins at least 100 seconds before an expansion is started, as shown in Figure 2.13. The physical state

variables of the chamber (the total pressure, the wall temperature, the slightly higher mean gas temperature, the back-scattered intensities $I_{\parallel}$ and $I_{\perp}$ and the corresponding depolarisation ratio, the partial pressure of water vapour, and the corresponding saturation ratio[1] S_{ice}) remain constant until the principal pump is started. This moment is defined as time t = 0 on the experimental time scale. Thereafter the total pressure, the air temperature, and the partial pressure of water vapour start to decrease. Note that the decay rates of interstitial (measured by TDLAS) and total water vapour (measured by FISH, PAS and MBW 373) are the same within their uncertainty limits as long as no ice particles are formed, and so is the rate of increase of the ice saturation ratio S_{ice}. Although S_{ice} = 1.00 is rapidly exceeded after about 55 seconds no ice particles are formed, as evidenced by the depolarisation ratio which remains very low and constant.

Approximately 2 minutes after the principal vacuum pumps were switched on, ice started to nucleate at S_{crit} ~ 1.2 on the seed aerosol, as indicated by the optical particle count of PCS-2000, Figure 2.13e, and the sharp rise of the depolarisation, Figure 2.13d. Then the connecting valve to the pre-evacuated NAUA chamber was suddenly opened. The sharp nearly step-wise 5% pressure drop is associated with a sharp temperature drop by more than 2 K which made sure that essentially *all* seed particles were converted into ice crystals.

This is confirmed by the maximum ice particle number density, $C_{n,ice}$, which is approximately equal to the seed particle number density at the time of freezing, C_n, cf. Figure 2.13e. After the NAUA expansion event the total pressure continues to decrease at the rate prescribed by the principal pumps. It should be noted that the interstitial water vapour decreases sharply after ice nucleation has occurred, cf. Figure 2.13b, while total water continues to decrease at a somewhat reduced rate because the loss of interstitial water vapour due to ice particle growth is partially compensated by an enhanced ice evaporation rate from the chamber walls. The ice water content can be derived from the difference between total and interstitial water. Figure 2.13c shows that S_{ice} (which can only be accurately derived from the TDLAS measurements) returns to S_{ice} ~ 1.0 after ice particles have been formed. This indicates that thermodynamic equilibrium between ice particles and interstitial water vapour is rapidly established.

The experiment is terminated by turning the principal pumps off after 400 seconds. This causes the air temperature to relax back to the conditions which prevailed before the experiment was started. Shortly afterwards all ice particles have evaporated, as evidenced by the depolarisation ratio, Figure 2.13d.

[1] Note that the ice saturation ratio is significantly less than unity under static conditions although the chamber walls had been coated with an ice layer. This is due to the relatively large difference between the mean wall temperature and the mean air temperature in the chamber which was higher due to internal heat sources.

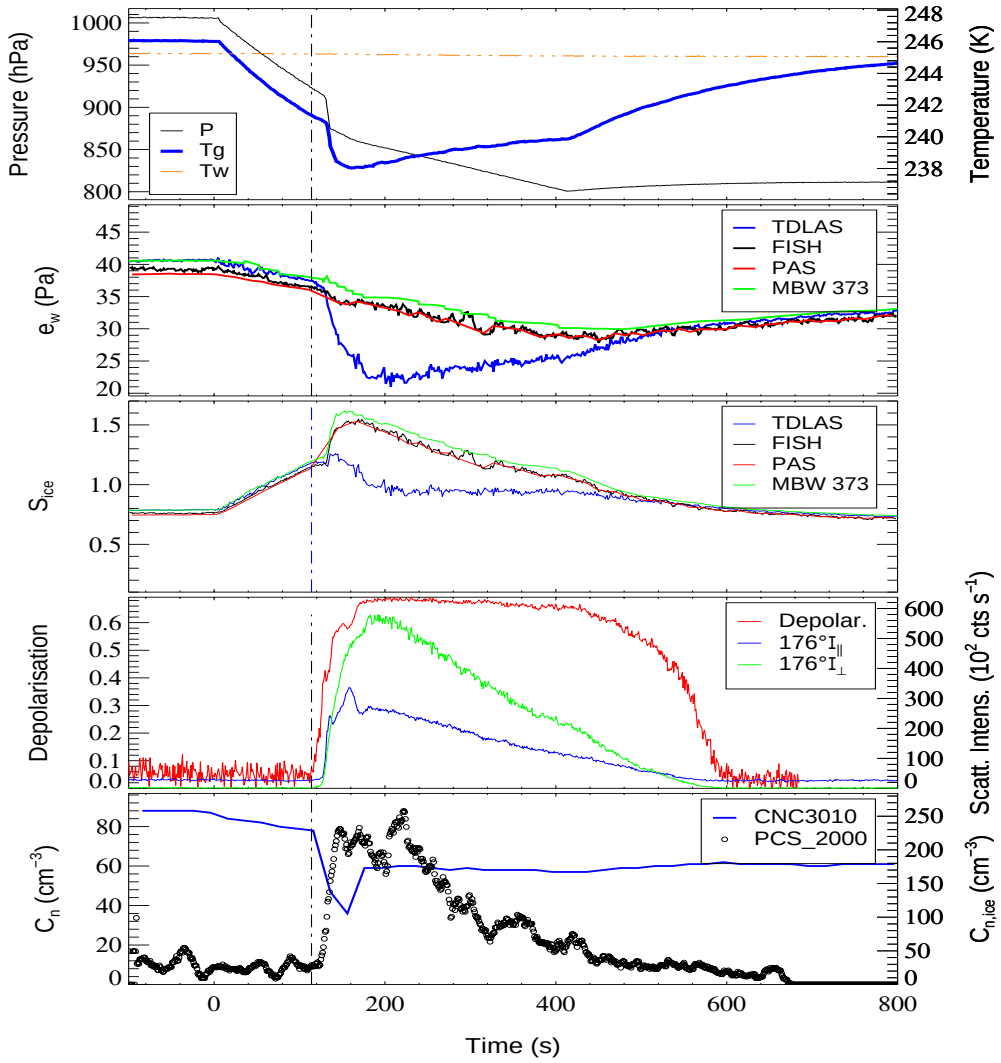

Figure 2.13: The measured state variables of the air in the AIDA chamber during activation experiment N° 74 INO2, from top to bottom:

(a) Total pressure, mean air temperature and mean wall temperature. The vertical line marks the moment when ice nucleation was first observed.

(b) Partial pressure of interstitial water vapour as measured by TDLAS, and of total water content measured simultaneously by FISH, PAS and MBW 373.

(c) The saturation ratio S_{ice} with respect to the ice phase, calculated from the mean gas temperature (Figure 2.12b) and the partial pressures shown in Figure 2.12 b.

(d) Back-scattered intensities $I_{\parallel}$ and $I_{\perp}$ and the corresponding depolarisation ratio for a scattering angle of 176°.

(e) The ice particle concentration that is measured by PCS-2000 (black circles) and the seed particle concentration that is measured by CNC 3010 (blue line). Note that the reduction in C_n is larger than expected by dilution, in particular while large ice particles are present between 120 and 400 s. This is due to incomplete sampling of ice crystals by the CNC 3010 and to sedimentation of large ice crystals in the ADIA chamber.

Chapter 3 Calibration of Optical Particle Counters (OPCs): Experimental Procedure and Modelling

3.1 Experimental Setup for the OPC Calibrations and Used Materials

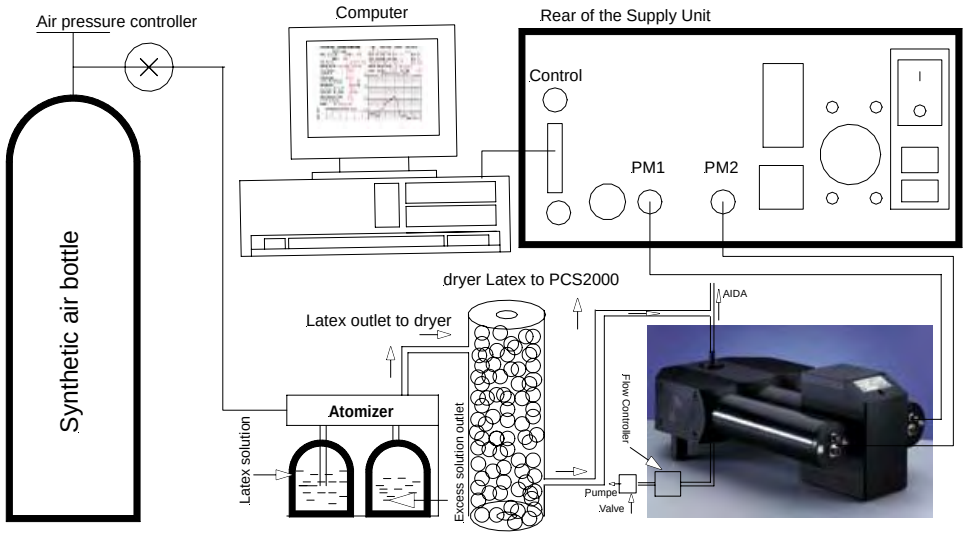

Figure 3.1: Systematic representation of PCS-2000 Calibration setup

The setup and procedures used to calibrate the OPCs differed somewhat. In order to calibrate the PCS-2000 Optical Particle Counter before using it to size classify ice particles at the AIDA chamber a constant output atomizer was used to generate a continuous stream of Latex particles of either 1.59 ± 0.05 µm, 0.805 µm, or 0.506 µm diameter. These test aerosols were dried and fed to the PCS-2000 as shown in Figure 3.1. Latex suspensions for the atomizer were prepared by diluting 1 ml of Postnove sulphate latex solutions with 999 ml pure water. The particle suspensions were homogenised using an ultrasonic bath (Bandelin Sonorex RK 510 H). The atomiser operates with 5 bar synthetic air at a flow rate of 8.4 liter per minute and produces a fine spray of water droplets which contain on average less than one latex particle per droplet to avoid the formation of dimers and multimers. Excess solution drains back into an empty bottle through the bottom of the atomizer. Before the latex particles can be used to calibrate the PCS-2000, the spray is firstly sent to a TOPAS dryer manufactured by Merck, where the liquid water is completely evaporated, leaving behind an aerosol consisting of dry monomer latex particles.

Monodisperse test dust of type Monosphere 1000 nm that has a scattered light equivalent diameter of 0.850 µm was used to calibrate the Welas. A flexible tube at the aerosol inlet of the instrument was connected to the supplied container of Monosphere. The particles were suspended in the air of the supplied container by shaking and knocking on it before they are sent to the instrument.

The monosphere peak must be detected at channel N° 40 when the instrument is properly calibrated for the size range 0.25 - 17.5 µm.

3.2 Calibration Results

3.2.1 PCS-2000

Before and after every campaign the calibration of the PCS-2000 must be checked with latex particles of 0.506 µm, 0.805 µm, and 1.59 µm diameter. Monomer latex aerosol particles of these sizes must appear at Channels N° 31, 43, and 57, respectively, i.e. the distribution of the latex number concentration must peak at one and only one of these channels, as appropriate.

The calibration channels were adjusted during the calibration process using a measuring duration of 300 seconds with an integration time step of 1 second and a gas flow rate of 5 liter per minute. The narrow latex size distribution must peak at the prescribed calibration channel number. If the peak of the calibration curve is shifted from the correct channel, the channel number deviation must be multiplied with the approximate voltage increment per channel (ca. 4 mV), and the high voltages for both photomultipliers must be changed manually by turning the potentiometers of PM1 and PM2 to the right or to the left according to this value. This process is repeated more than once until the narrow latex size distribution peaks at the correct channel.

The results of a typical calibration of PCS-2000 are shown in Figure 3.2: the blue, the green and the cyan curves represent the measured latex size distributions versus the channel numbers of PCS-2000. It is seen that after the calibration procedure the size distributions of the latex aerosols with nominal diameters of 0.506 µm, 0.805 µm or 1.59 µm have only one narrow peak at the correct channel numbers of 31, 43, and 57, respectively.

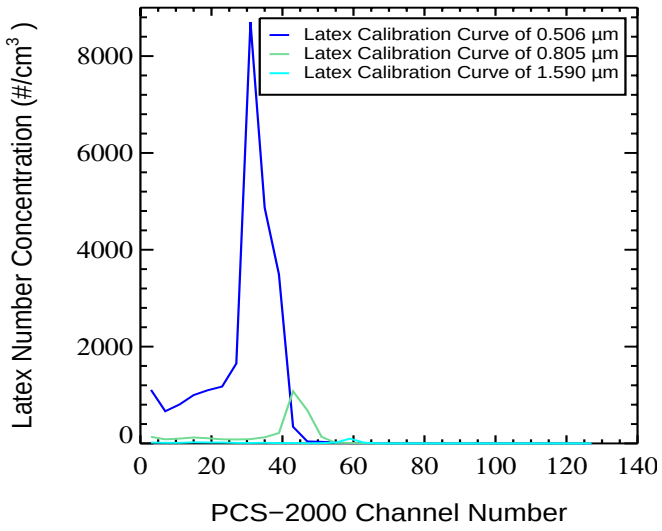

Figure 3.2: Size distributions for latex aerosol particles of 0.506 µm, 0.805 µm, and 1.59 µm diameter versus channel number after a successful calibration of PCS-2000.

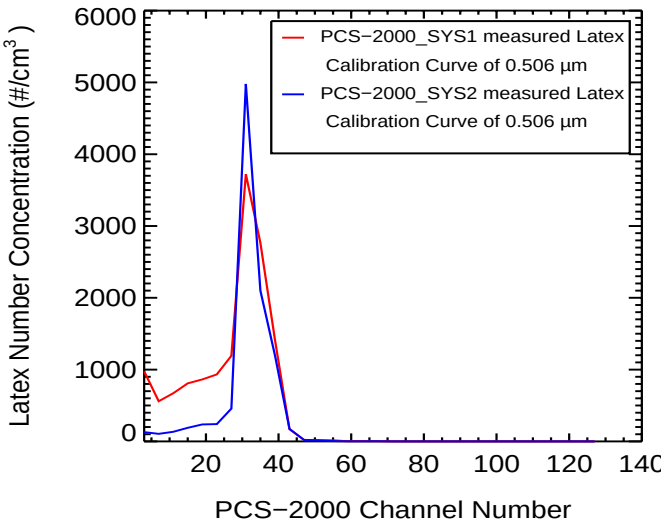

(a)

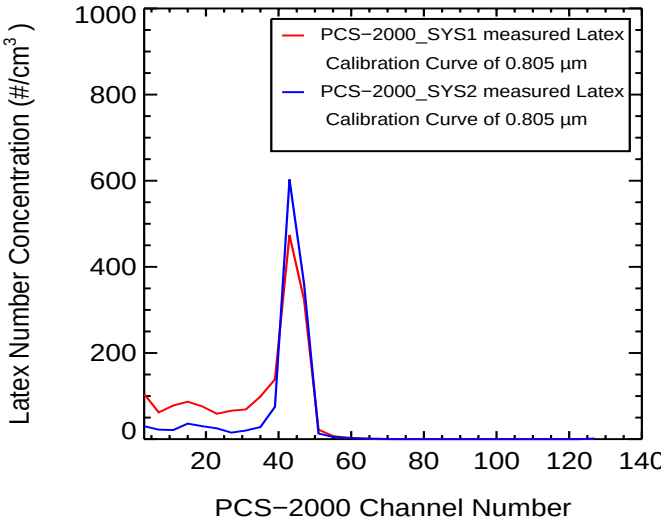

(b)

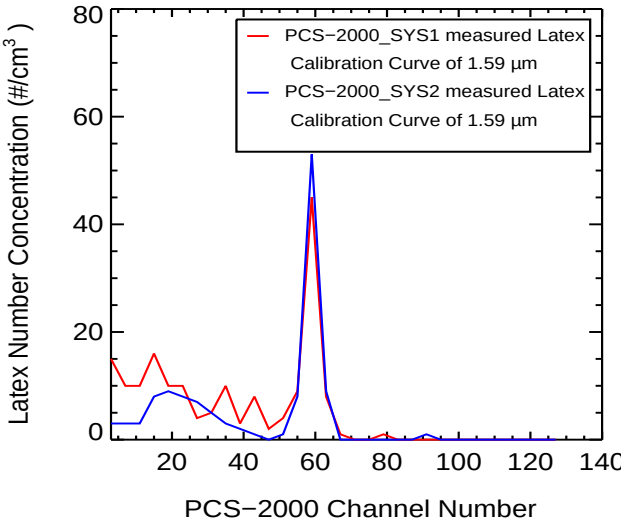

(c)

Figure 3.3: Latex calibration results for both optical channels of the PCS-2000 system, plotted versus the channel numbers,

(a) Latex 0.506 µm (b) Latex 0.805 µm (c) Latex 1.590 µm

The calibration curves for latex aerosol particles of 0.506 µm, 0.805 µm and 1.59 µm diameters are analysed and plotted versus the channel numbers for both optical systems of PCS-2000, hereafter PCS-2000_sys1 and PCS-2000_sys2 as shown in Figure 3.3 a, b, and c. It was found that both optical systems of PCS-2000 measured only one peak of a significant latex number concentration at the proper calibration channel for all three sizes of latex aerosol particles, as shown in Figure 2.14. This indicates that PCS-2000_sys1 and PCS-2000_sys2 are properly calibrated.

3.2.2 Welas

According to the description of the calibration process and information given in section 3.2, the monosphere peak must occur at channel N° 40 when Welas is properly calibrated for the 0.25 - 17.5 µm range. The approximate voltage increment per channel number amounts to 5 mV instead of 4 mV as in the case of the PCS-2000. Therefore, if the peak of the calibration curve is shifted from the correct channel, the channel number deviation must be multiplied by 5 mV, and the control voltage setting of the photomultiplier increased or decreased by this value, as in the case of PCS-2000. This process must be repeated more than once until the measured size distribution peaks at the nominal channel number of the calibration aerosol particles. Figure 3.4 shows that the size distribution of the monospheres used in this calibration appears at channel N° 40, as required.

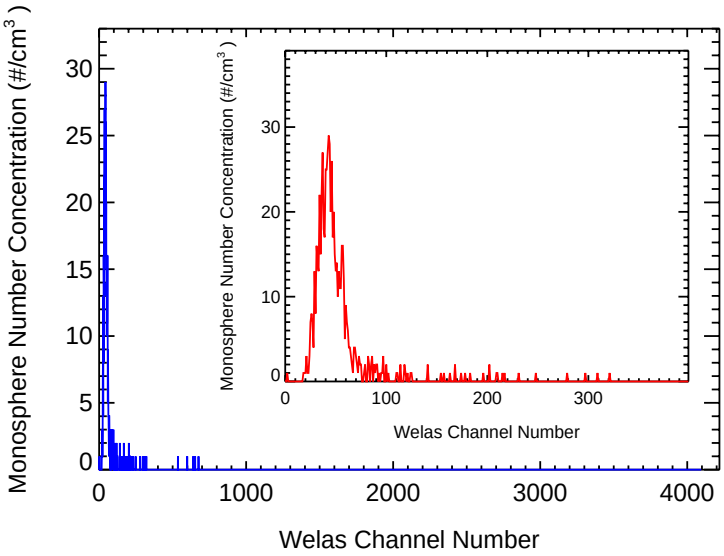

Figure 3.4: Measured monosphere size distribution after successful calibration of Welas, particle number concentration versus channel number.

3.3 Modelling of Calibration Curves by Mie Theory

According to the previous section only very few channels of the OPCs (three in the case of PSC-2000, only one in the case of Welas) are directly calibrated with latex particles of known diameters. The

main aim of this section is to calculate relative scattering intensities for all other particle sizes that can be detected by these OPCs. The results are then put on an absolute scale using the OPC calibrations, chapter 3, section 3.3.2. The obtained calibration curves will be compared with the standard calibrations provided by the instrument manufacturer.

Mie theory was used to calculate the light intensity scattered by spherical latex particles of a given diameter in the measuring range of the OPC instruments, i.e. from 0.25 to 19 µm for PCS-2000 and from 0.250 to 17.5 µm for Welas, since the scattered light can be explained in terms of the particle size, chapter 3, section 3.3.2. The light scattering angles corresponding to the measuring volume of the OPC under consideration are an input to a Mie subroutine that was written in IDL code (IDL = Interactive Data Language is a software developed and distributed by Research Systems, Inc., Boulder CO 80301, USA. The programming language IDL can be used to analyse and visualise large and complex experimental data sets, Busch et al., 2002). The scattered light intensity is calculated as a function of the optical geometries of the OPC instruments, namely the optical distance from the measuring volume to the lens center as well as the lens radius. Also the corresponding solid angles are calculated in section 3.3.1

The IDL code was written in general form to apply for all OPC instruments that have optical geometries similar to those of PCS-2000 and Welas as shown in chapter 3 sections 3.3.1 Figure 3.5.

3.3.1 Input Data to Mie Theory

The aim of this section is to calculate the light scattering angles at the measuring volume of the OPCs as an input to the Mie subroutine code including the corresponding solid angles.

Scattering Angle

This problem can be explained and solved in the following manner: The particles that pass through a measuring volume that is illuminated by a lamp can be considered as being located at the origin of a rectangular cartesian coordinate system (x, y, and z). The direction of propagation of the incident light defines the forward direction of the x-axis while the gas flows through the measuring volume of the OPC in the backward direction of the z-axis. The light is scattered in the forward and the backward directions of the y-axis forming a light cone that has its origin in the measuring volume and a circular base at both lenses. The height of the cone is equal to the normal distance from the (x, z) plane which is spanned by the particle beam (z-direction) and the optical axis (x-axis) of the illuminating light beam, while the radius of its base is equal to the lens radius as shown in Figure 3.5a and Figure 3.5b. The angle S^0 of the cone head encloses all scattering angles. An IDL code was written in general

form to calculate the scattering angle at the measuring volume as a function of the trigonometric functions of a right triangle OO`A. It has a value of S^0 is 90°∀0.5° and varies from X_0^o to X_1^o. The range of scattering angles was divided into small angle increments that were increased from the minimum value of X_0^o to the maximum value of X_1^o with an increment of inc^o that is equal to the cone angle S^0 of the OPC divided by a real number, hereafter denoted $\boldsymbol{n_{sca}}$. The value chosen in Table 2.1 was n_{sca} = 24. The calculated results of S^0, X_0^o, X_1^o and inc^o using $\boldsymbol{n_{sca}}$ = 24 for both optical particle counters are shown in table 3.1.

Table 3.1: The measurement geometries of the OPCs and their calculated values of S^0, X_0^o, X_1^o, and inc^o.

Meas. and calc. parameters / Instruments	Optical distance in mm	Lens radius in mm	Calculated cone angle (S^0)	Range of scattering angles		Increment inc^o
				X_0^o	X_1^o	
PCS-2000	15	3.25	24.4502°	77.7749°	102.225°	1.01876°
Welas-1100	20	4	22.6198°	78.6901°	101.310°	0.942494°

Solid Angle

In the x-direction, the lens of each OPC is divided into a number n_{sca} of narrow segments which correspond to the increments in the scattering angle. The areas of the segments are calculated as the difference between the areas of the lens sectors and the areas of the isosceles triangles that fit in the sectors, two sides being equal to the lens radius and one side coinciding with the chord which belongs to the sector, as shown in Figure 3.5.

In order to calculate the areas of the segments, the area of the isosceles triangles in the (x,z) plane is calculated as follows: the height of each triangle is perpendicular to its base in the (y, z) plane and can be calculated as a function of the optical distance of OPC and the tangent of the absolute value of scattering angle (90^o - ($X_0^o + i \times inc^o$)) in the (x, y) plane where i is varied from 0 to (n_{sca} -1). The base length of each triangle is calculated according to the theorem of Pythagoras as a function of the lens radius and the high of the isosceles triangle. The area of each sector is calculated secondly as of

$$\frac{\text{central angle of sectors } S}{360} \times \pi \times (\text{lens radius})^2,$$

where the central angle of each sector is equal to twice the value of the angle between the lens radius and the height of the triangle using cosine triangle function. Finally, the area of each segment is calculated as the difference between the area of the sector and the area of the isosceles triangle. This

result is shown in the left panel of Figure 3.6 where the y-axis represents the segment area in mm^2 while the x-axis represents the scattering angle in degrees. The red and blue curves represent the segment areas of PCS-2000 and Welas, respectively.

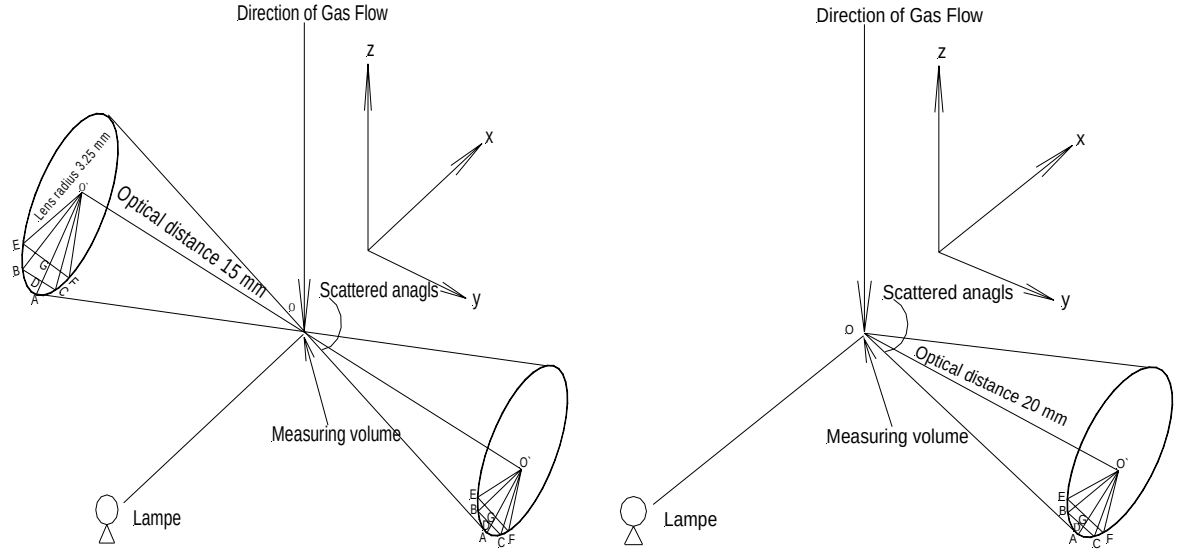

(a) PSC-2000 (b) Welas

Figure 3.5: Schematic representation of the flow of particles through the measuring volume of the OPCs. The method of calculating the light scattering angles as input to the Mie subroutine and its solid angle is illustrated.

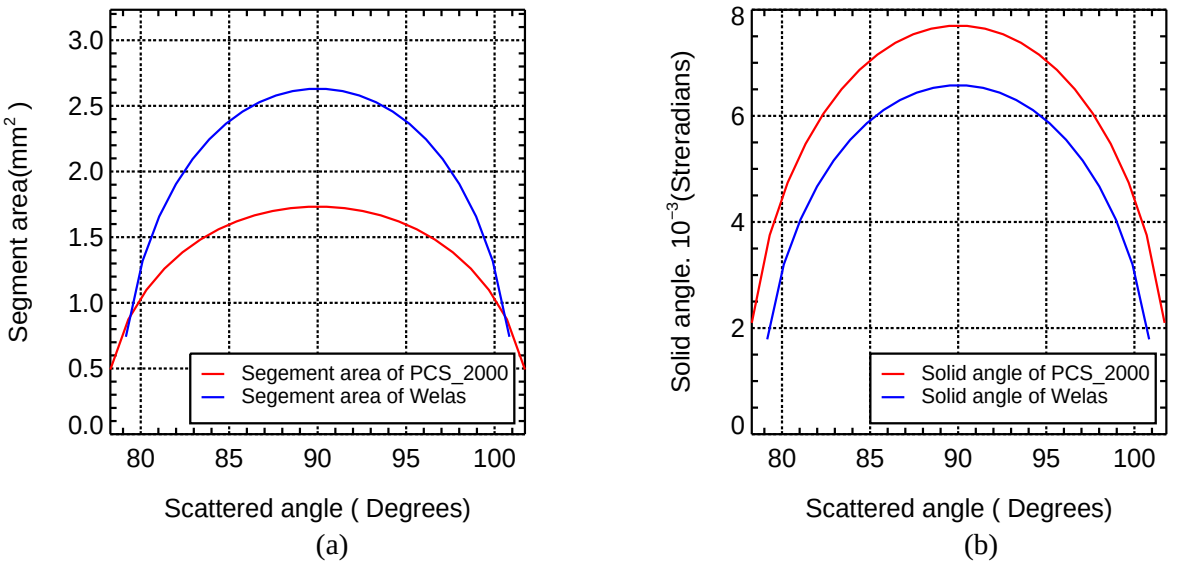

Figure 3.6: (a) Calculated lens segment areas in mm^2 versus the light scattering angles at the measuring volume of the OPCs; red and blue curves represent PCS-2000 and Welas-1100, respectively. (b) Calculated solid angles versus the light scattering angles at the measuring volume of the OPCs; red and blue curves represent PCS-2000 and Welas, respectively.

The distance between the center of every segment and the head of the cone in the plane (x, y) is calculated using the theorem of Pythagoras as a function of the optical distance and the mean value of the heights of sequential triangles. The solid angle that is spanned by every segment is equal to the segment area divided by the square of the distance between the segment and the head of the cone. This result is shown on the right panel of Figure 3.6 where the red and the blue curves represent the calculated solid angles of PCS-2000 and Welas versus the scattering angle.

3.3.2 Mie Calculation of the Scattered Intensity

The aim of this section is to calculate the scattered light intensities that are detected by the optical particle counters as function of the diameter of a spherical scatterer. For this purpose the range of particle diameters that are detected by the instruments is divided into small sub-ranges of 0.05 μm and 20 values per decade. The latex particles have a refractive index of 1.59 (note that the imaginary part of the complex refractive index is zero because latex is non-absorbing in the wavelength range of concern).

Spherical scatterers can be classified using a dimensionless size parameter *X*,

$$X = \frac{2\pi r}{\lambda} \tag{3.1}$$

where *r* is the particle radius and λ is the wavelength of the incident light in the surrounding medium (Bohren and Huffman 1997; Mishchenko et al. 2002). The size parameter, the refractive index of latex, and the cosines of the scattering angles that were discussed in chapter 3 section 3.3.1 are input data to a Mie subroutine that was written in IDL code by G. Thomas (2004). The subroutine is based on analytical derivatives of the Mie scattering amplitudes with respect to the particle size parameter and the complex refractive index (Grainger et al., 2004). The subroutine's output data are the extinction efficiency Q_{ext}, the scattering efficiency Q_{sca} (which is identical with Q_{ext} for non-absorbing latex particles), and the phase function that is an array of the same dimension as the scattering angles and agrees with data by van de Hulst but differs by a factor of 4π from phase functions given by other authors because they use a different normalisation condition (Bohren and Huffman 1997). In addition, the amplitudes of the scattered light polarized perpendicular and parallel to the plane of observation are also obtained.

The scattering cross section C_{sca} of a spherical particle is defined (Bohren and Huffman, 1997; Mishchenko et al., 2002) as the particle's cross-sectional area πr^2 times the scattering efficiency Q_{sca} that can be obtained from Mie theory:

$$C_{sca} = Q_{sca} \pi r^2 \tag{3.2}$$

The differential scattering cross section $dC_{sca}/d\Omega$ (where dΩ denotes the differential of the solid angle that is associated with a given scattering angle) is related with the scattering cross section C_{sca} via the phase function Ph:

$$\frac{dC_{sca}}{d\Omega} = C_{sca} Ph \tag{3.3}$$

Finally the *detected* scattered intensity $I_{sca,a}$ is summed over all solid angle increments ΔΩ corresponding to the lens area, as well as over all wavelength increments Δλ that are emitted by the lamp of the OPC and can be detected by its photomultiplier according to the following equation,

$$I_{sca,a} = \sum_{\lambda} \sum_{lens\ area} \frac{dC_{sca}}{d\Omega} \Phi_{\lambda} \Delta\lambda \Delta\Omega \tag{3.4}$$

The term Φ_λ denotes the overall efficiency factor of the optical system. It includes contributions by the intensity distribution I_λ of the Xenon high pressure lamp, the wavelength-dependent sensitivity $\varphi_{pho}(\lambda)$ of the photomultiplier, the wavelength-dependent reflectivity $R_{mirror}(\lambda)$ of the focussing mirror, the wavelength-dependent light attenuation $A(\lambda)$ by the lense material which also depends on the lense thickness l_{lens}, and by wavelength-dependent reflective losses at the surfaces of the antireflection-coated lenses, f_{lens}. These factors are tabulated in the PCS-2000 operating manual.

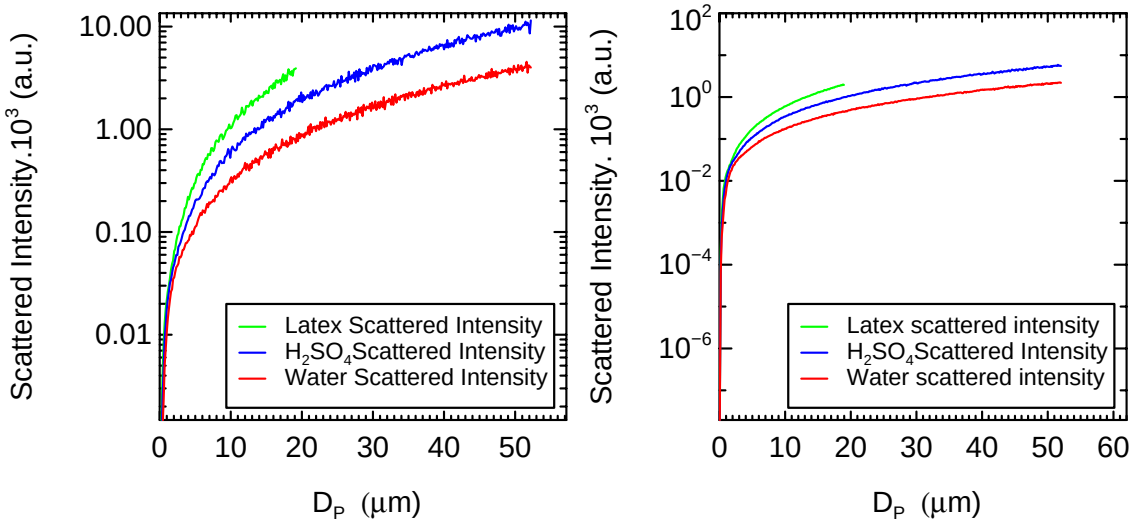

Figure 3.7: (a) Calculated scattered intensities I_{sca} of different aerosol particles in arbitrary units versus particle diameter, for PCS-2000.

(b) As in (a) but for Welas.

These instrument-corrected Mie calculations of the *detected* scattered I_{sca} have been carried out not only for latex particles but also for sulphuric acid and water droplet aerosols which differ from latex particles by their refractive indices, 1.44 and 1.33, respectively. The results for PCS-2000 and

Welas are plotted in arbitrary units (a.u.) versus particles diameters D_p on the left and right panels of Figure 3.7, respectively.

3.3.3 Obtained Calibration Curves

The OPCs used in this work could not be calibrated with liquid aerosol particles which differ from the latex particles by their refractive indices. Therefore, the calibration curves in terms of particle diameters D_p as function of channel number must be known as a function of the particles refractive index. We proceed as follows: (a) the *detected* scattered intensities are calculated as function of particle diameters D_P in the measuring range of the OPCs using Mie theory, as explained previously in section 3.3.2 (results shown in Figure 3.7). (b) the intensities scattered by latex particles with known diameters (those which were used for the calibrations), hereafter denoted $I_{calib.,}$ are attributed to the corresponding channel numbers (N^os 31, 42, 57 for PCS-2000; N^o 40 for WELAS) and voltages. (c) knowing that log(intensity) detected by PCS-2000 scales linearly with channel number (log(intensity) detected by WELAS scales linearly with log(channel number), see operating manuals provided by manufacturer), one can easily attribute *detected* scattered intensities (in Volt) to all other channel numbers of both OPCs by linear extrapolation of log/lin and log/log plots, respectively. The procedure is illustrated in Figure 3.8: panels a, b are cut outs from Figure 3.7 focussing on the size range of the latex particles used for calibration, while panels c and d show the functions $I_{scal.,ch}$ fitted through the calibration points.

We know from the Mie calculations the detected scattered intensities (in arbitrary units) for latex, H_2SO_4, and water droplets as a function of particle diameter, Figure 3.7, which can be converted to Volt using the latex calibrations. Furthermore we know Figure from 3.8c, d the relation between the detected scattered intensities (in Volt) and the channel numbers. By combining these informations we can construct the calibration curves in terms of particle diameters D_p versus channel number for these materials. The results are shown in Figure 3.9. It is not surprising that the green latex curves nearly coincide with the standard calibration data from the operating manuals of PCS-2000 and Welas since the properties of the lamp and of all other optical components used in our calculations were taken from the operating manuals. Slight deviations give an impression of the reproducibility of the calibrations, which may be regarded as a lower limit of the uncertainty, see section 3.4.

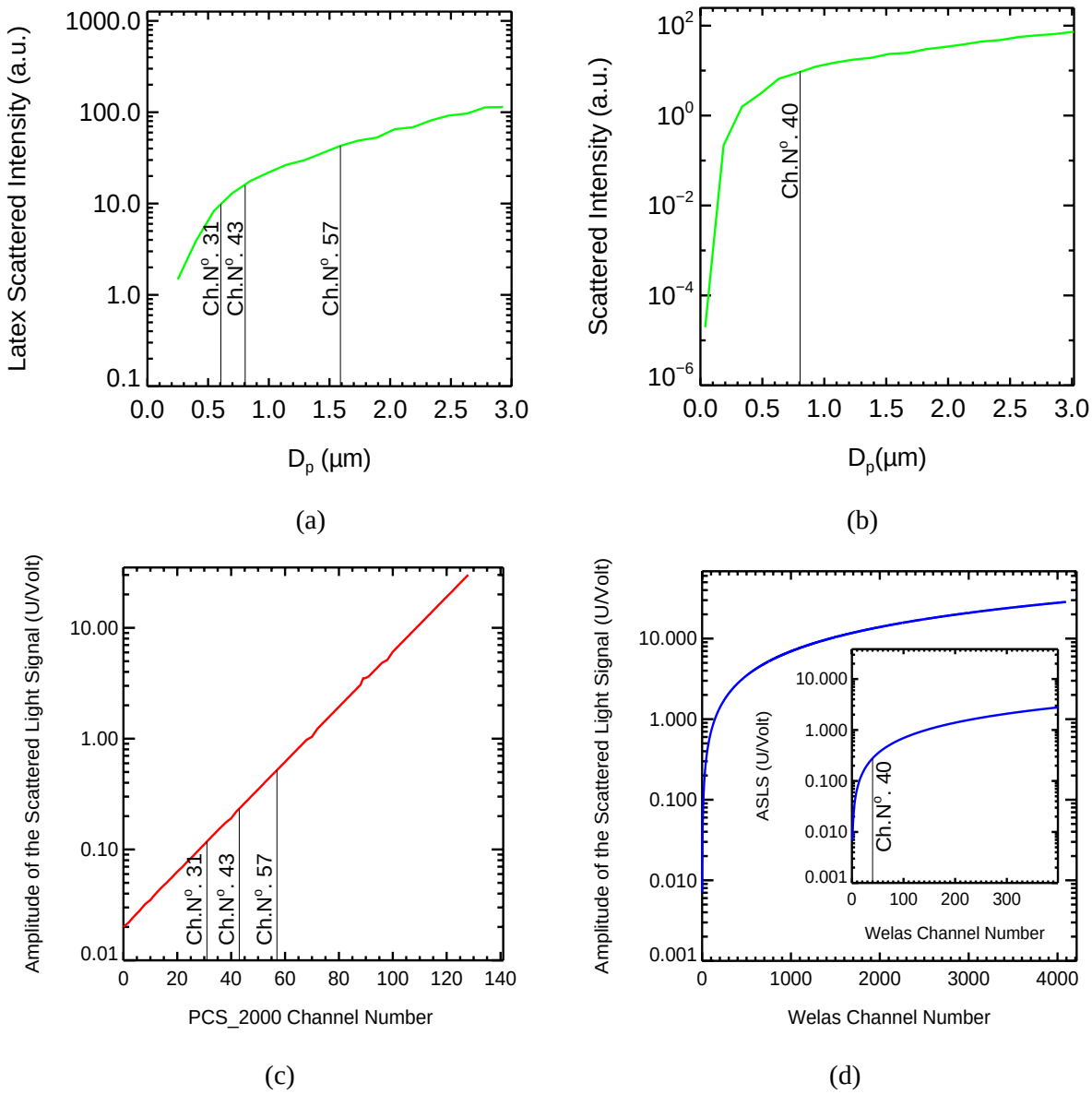

Figure 3.8:

(a) The calculated *detected scattered* intensity for PCS-2000 (in arbitrary units) as function of latex particle diameter D_P. Note that only the diameter range 0.25 µm to 3.2 µm is shown. The vertical lines show at which channel numbers latex particles of D_P = 0.506 µm, 0.805 µm and 1.59 µm are detected by the properly calibrated PCS-2000.

(b) As in Figure 2.19a, but for Welas. The vertical line shows at which channel number latex particles of D_P = 0.850 µm are detected by the properly calibrated Welas.

(c) Linear correlation between log (scattering signal) and PCS-2000 channel number (the scattering signal is measured in Volt).

(d) Same as in Figure 2.19c but for Welas. Note, however, that the correlation between the scattering signal and the Welas channel number differs from PCS-2000 since it has been changed by the manufacturer to be linear when plotted on a log-log scale.

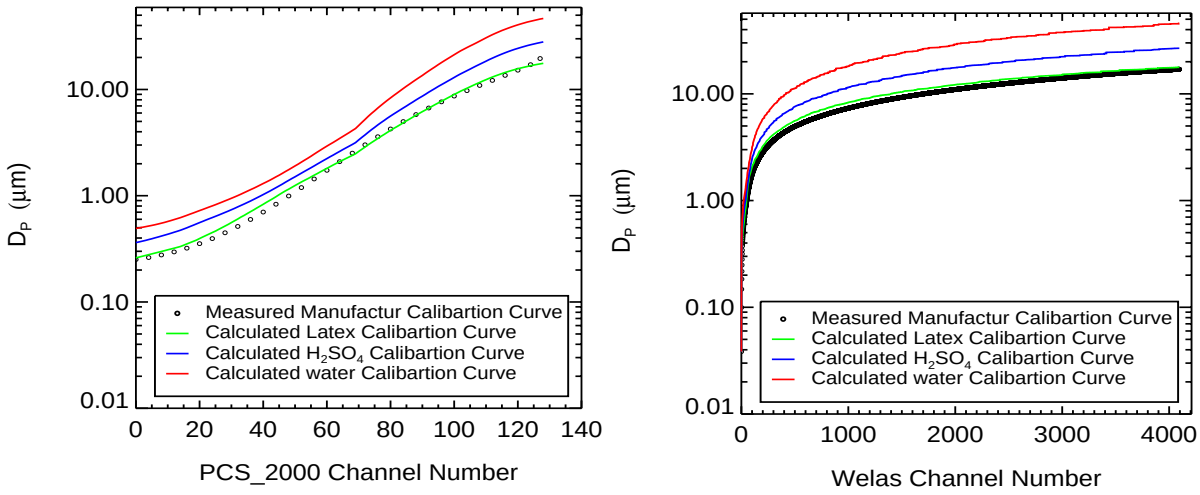

Figure 3.9: Comparison of the standard calibration curves of the OPCs with calculated calibration curves for latex particles, for H_2SO_4 droplets, and for water droplets

Left panel: PCS-2000 Right panel: Welas

3.4 Uncertainty Estimation

The deviation of the measured latex calibration curve, section 3.3.3, from the standard calibration curve that was provided by the manufacturer Palas gives an impression of the calibration uncertainty. It was found that the relative deviation at all channel numbers of PCS-2000 lies in the range of $\pm 12\%$ as shown in Figure 3.10 left panel. The deviations of the Welas instrument calibration vary between extremes of -3.5% and +20% for small particles with channel numbers < 200. However, as can be seen in Figure 3.10 right panel, the average deviation at channel numbers larger than about 200 is close to +9%, with a systematic drift from slightly larger to slightly smaller deviations from channel number 200 to channel number 4000.

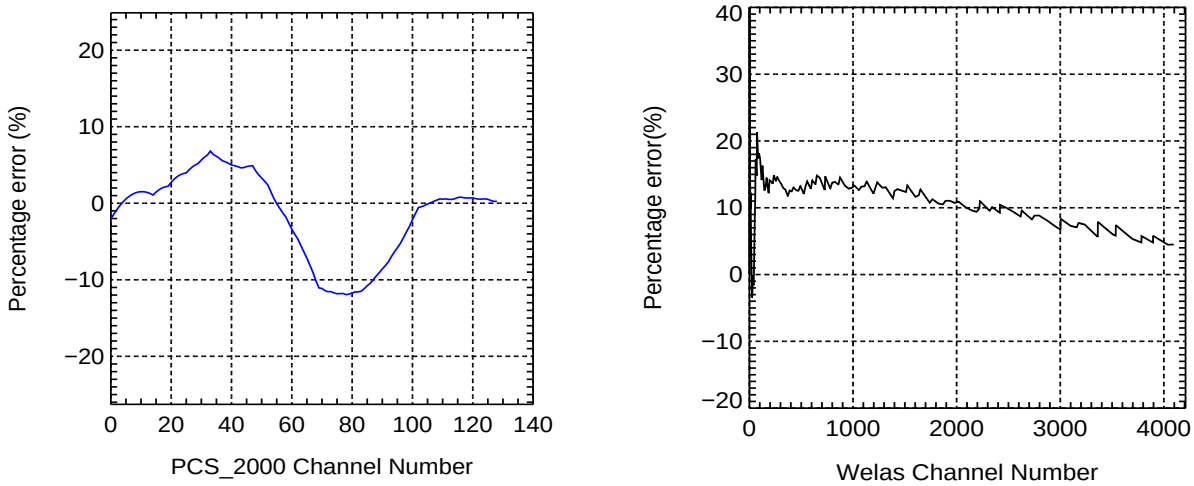

Figure 3.10: Percentage deviation of calibrations with latex particles from "true" particle diameters according to the manufacturer's calibration, as function of channel number:

Left panel: PCS-2000 Right panel: Welas

Chapter 4 Physical Problem of PCS-2000 Setup and Solution Methods

4.1 Sampling Geometry of PCS-2000 under the AIDA Chamber

The optical particle counter PCS-2000 (see photograph in Figure 3.1) was located in a box below the AIDA chamber, as shown schematically in Figure 2.1b of chapter 2. The box was thermostated near room temperature to protect the lamp and the electronics of the instrument from the low temperatures in the AIDA containment. Details of the setup are shown in Figure 4.1. The connecting stainless steel tube between the AIDA chamber and the measurement volume of PCS-2000 is 775 mm long, has an internal diameter (ID) of 10 mm and a wall thickness of 1 mm. Downstream of the measurement volume, the tube has the same ID. At a distance of 75 mm from the measurement volume a thermocouple measures the gas temperature approximately at the center of the tube, as shown schematically in Figure 4.1.

PCS-2000 samples 5 liter per minute from the AIDA chamber through the connecting tube. While travelling through the connecting tube, the ice crystals are not at a constant temperature, but are exposed to progressively higher temperatures as they approach the measuring volume of the optical particle counter. This causes either complete evaporation, or at least a reduction of ice particle diameters before the particles are sized in the measuring volume of the OPC. A model has been developed to correct for this effect. The following section outlines the temperature profile which was taken into account.

The connecting tube between the AIDA chamber and PCS-2000 can be divided into three sections according to its surface temperature as follows: the first section inside the AIDA chamber is 405 mm long and has approximately the same temperature as the gas, **hereafter denoted** $\overline{T_g}$. The second section between the chamber flange and the isothermal box of PCS-2000 is 145 mm long and has approximately the same temperature as the chamber wall and the ADIA containment, **hereafter** T_w. The temperature in the tube inside the isothermal box (**hereafter** T_{up}) is measured with a thermocouple. This section of the tube is 300 mm long. The gas temperature in the tube is also measured downstream of the PCS-2000 detection volume at a distance of 850 mm from the tube entrance with another thermocouple, **hereafter** T_{down}. The gas pressure downstream of PCS-2000, **hereafter** P_{out}, is measured in front of the flow controller which is shown in Figure 4.2 (tube lengths not to scale), at a distance of 10 m from the tube entrance where it has dropped 10 hPa below its value in the AIDA chamber. Latex aerosol could be introduced to PCS-2000 during the calibration processes via a pipeline that was connected directly with the sampling tube at the upper part of the third section, while the lower end of the sampling tube was connected with a vacuum pump via a flow controller and

a valve. The flow controller is set to a sampling rate of 5 litres per minute. The temperatures $\overline{T_g}$, T_w, T_{up} and T_{down} are measured once per second.

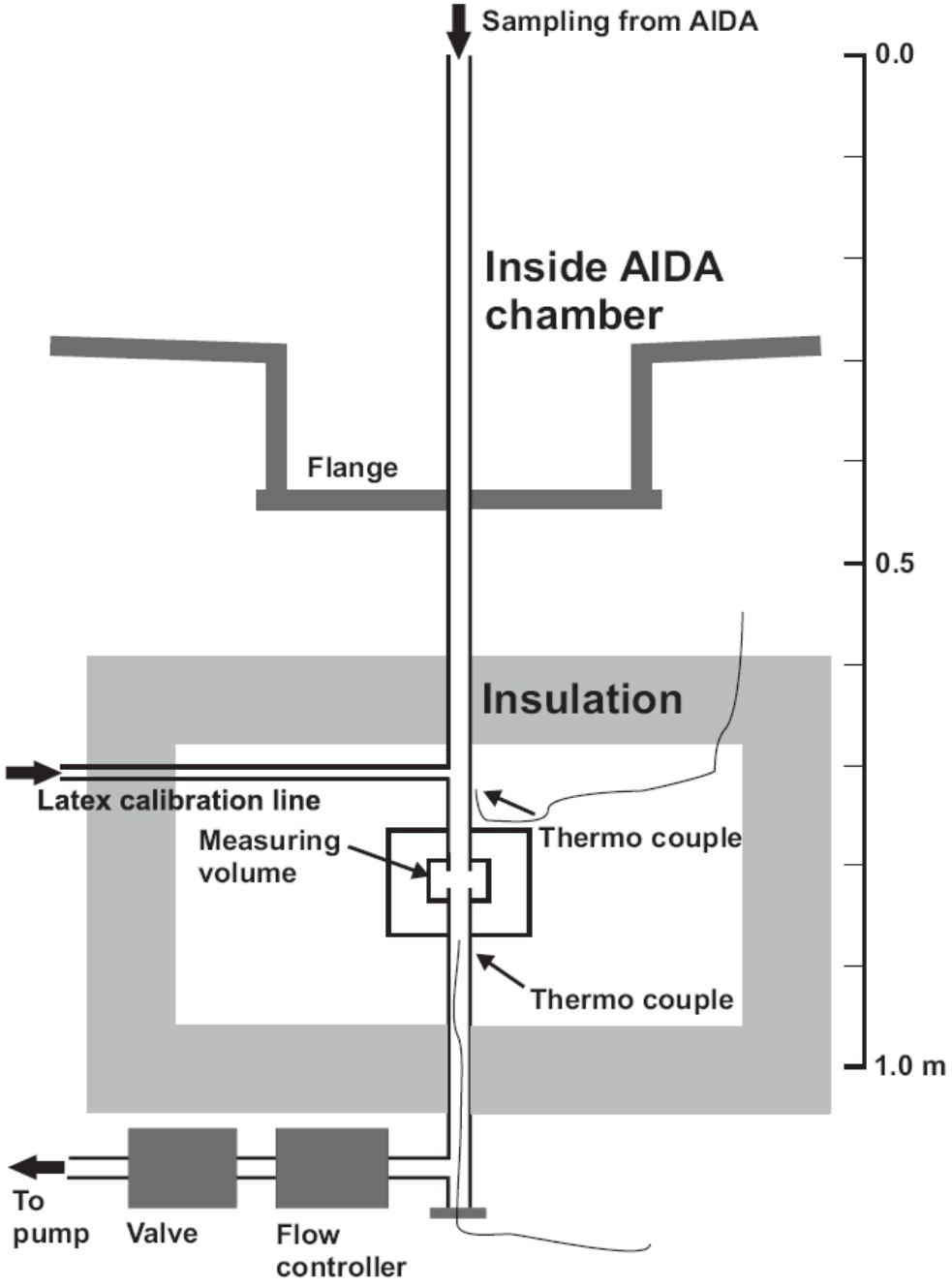

Figure 4.1: Schematic view showing the sampling geometry of PCS-2000 below the AIDA chamber. Note that the temperature along the sampling tube varies from $\overline{T_g}$ in the AIDA chamber to T_w and then to the temperature of the PCS-2000 instrument inside the box. The tube temperature T_{up} and the gas temperature T_{down} inside the tube at a short distance below the detection volume are measured with thermocouples.

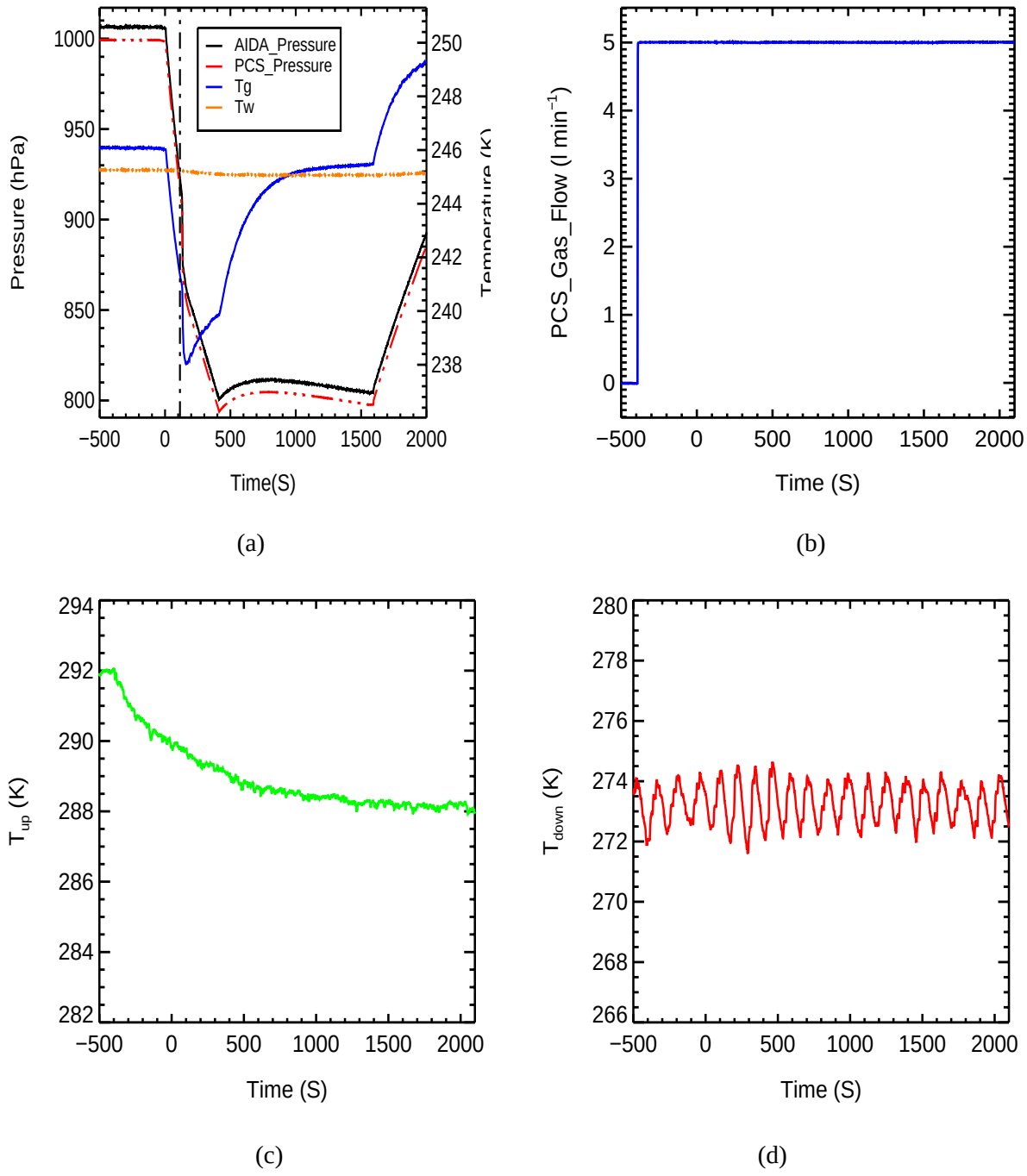

Figure 4.2: (a) The gas pressure in the chamber, the mean gas temperature T_g at the upper end of the connecting tube, the chamber wall temperature T_w and the outlet gas pressure at a distance of 10 m from the tube entrance are shown for activation N^o 74 IN02.

(b) the gas flow rate in the tube.

(c) the temperature T_{up}.

(d) the outlet gas temperature T_{down}.

4.2 The Problem of Measuring Correct Ice Particle Sizes Using the Sampling Geometry of PCS-2000 shown in Figure 4.1

Considering Figures 4.1 and 4.2 which show the connection between the AIDA chamber and the measurement volume of PCS-2000 as well as the measured temperatures along the connecting tube, the following problem must be taken into account:

The gas which has a known mean temperature in the chamber, enters the 850 mm long, 10 mm ID tube. At first it flows through a 405 mm long isothermal section where the tube temperature is approximately equal to the gas temperature. Then it flows through a 145 mm long section where the tube temperature is approximately equal to the chamber wall temperature. In this section the gas temperature is slightly higher than the tube temperature before the adiabatic expansion begins while it is slightly lower than the tube temperature during the adiabatic expansion. After that the gas flows through a warmer 300 mm long tube section.

The direction of heat transfer between the gas and the tube wall depends on which part is hotter than the other. From Figure 4.2, one sees that the tube temperature in the last section is higher than the gas temperature when it enters that section. So the heat will be added to the gas and the gas temperature will increase.

According to the rising temperature of the gas, the ice particles will start to evaporate before they reach the measuring volume of the PCS-2000, and the ice particle radius will decrease. So, the aim of the next section is firstly to calculate the distribution of the gas temperature along the tube axis in section 4.21 and secondly to calculate the variation of the ice particle radius due to this effect in section 4.2.2.

4.2.1 The True Gas Temperature in the Sampling Tube of PCS-2000

The heat flow inside the cirular tube which connects the AIDA chamber with the PCS-2000 instrument occurs under steady-state conditions. The gas flow causes laminar forced convection due to the pump of PCS-2000. In a region sufficiently far away from the inlet the velocity and temperature profiles are fully developed. We consider two models to study the heat transfer between the tube wall and the gas.

In the first model, the heat transfer to the gas starts as soon as the gas enters the tube. Both the velocity and the thermal boundary layers begin to develop immediately and simultaneously. These regions are characterised by the hydrodynamic entrance length L_h and the thermal entrance length L_t which in this case are both measured from the tube inlet. This is shown in Figure A.1 in Appendix A.

In the second model, the heat transfer to the gas starts with a delay after an isothermal section. For such a case, the hydrodynamic entrance length L_h is measured from the point where the gas enters the tube, but L_t is measured from the location where the heat transfer starts, because the thermal boundary layer begins to develop in the heat transfer section. This is shown in Figure A.2 in Appendix A.

By comparing the above two models with our problem, it is obvious that one has to choose the second model to solve our heat flux problem for thermally developing, but hydrodynamically developed conditions. The reason for this choice can be seen in Figure A.2 Appendix A: the temperature difference between the gas temperature inside the tube and the tube walls is zero or negligible in the first 585 mm of the connecting tube, sufficiently long to develop a parabolic velocity profile. The solution of this problem in the case of laminar forced convection inside a circular tube with a uniform wall surface was given by Greatz and later quite independently by Nusselt (Özişik, 1985; Welty et al., 1984).

An IDL code was written, based on the mathemathical model which is explained in Appendix A, to calculate the distribution of the gas temperature in the connecting tube between the AIDA chamber and the PCS-2000 according to the following equation

$$\frac{T_w - \overline{T_g}}{T_w - T_{out}} = \exp\left(\frac{4 l h_m}{D_T u_m \rho C_p}\right) \tag{4.1}$$

where $\overline{T}_g$ is the gas inlet temperature, T_w the tube wall temperature, l is the tube length and T_{out} is the outlet temperature at a distance l from the entrance, h_m the heat transfer coefficient, D_T the tube diameter, u_m the mean gas velocity, ρ the gas density, and C_p the specific heat of the gas at constant pressure (Özişik, 1985; Welty et al., 1984).

The time spent by ice particles in the connecting tube between the ADIA chamber and PCS-2000 is only a fraction of a second, ~ 0.4 s, before they are optically detected in the measurement volume of the PCS-2000. This time is short in comparison with the time until the next measurement of state variables in the AIDA chamber occurs. The length of the connecting tube between AIDA and

PCS-2000 is divided vertically into increments of 1 mm. The following equation (4.2) was used to calculate the distribution of the gas temperature along the tube axis in time steps of one second. The gas temperature every 1 mm along the tube axis was calculated from the following equation,

$$T_{out}[i+1] = T_w + \left(T_w - \overline{T_g}[i]\right) e^{-\left(\frac{4l\,h_m}{D_T\,u_m\,\rho C_p}\right)} \tag{4.2}$$

where $T_{out}[i+1]$ is the exit gas temperature at the position of i+1 as a function of the inlet gas temperature at the position i while the parameters h_m, u_m and ρ are calculated as explained in Appendix A. Figure 4.3 shows the calculated profile of the gas temperature along the tube center line as a function of time for experiment N° 74 IN02, cf. Figure A.2 in Appendix A. In the three dimensional plot the x-axis represents the running time of the experiment, the y-axis represents the distance from the tube entrance in mm while the z-axis represents the gas temperature along the center line of the tube in K.

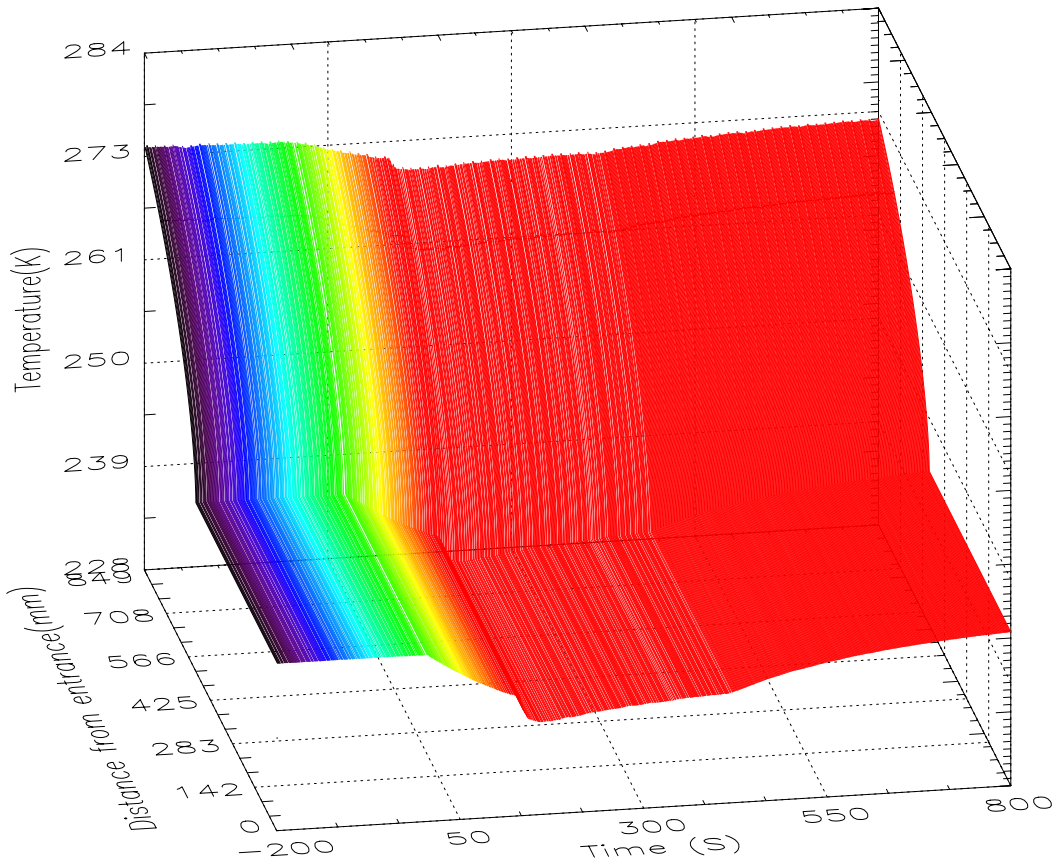

Figure 4.3: Profile of the gas temperature along the tube center in a three dimensional plot where the x, y and z axes represent the run time of the experiment, the distance from the tube entrance, and the gas temperature, respectively. Activation N° 74 IN02.

The time dependence of the gas temperature at 0 mm (tube entrance) during the running time of the experiment is of course the same as the mean gas temperature versus time, which is shown in Figure 2.13 in section 2.7 chapter 2. The temperature along the tube center line stays constant until, downstream of the hydrostatic length, it increases slowly with the beginnig of the heat transfer section (cf. Figure A.2 in Appendix A), and much more strongly with the beginning of the third thermal section.

The accuracy of this calculation was examined by plotting in Figure 4.4 the difference between the calculated gas temperature at 850 mm from the tuber entrance and it is value measured by the thermocouple at the same position. Figure 4.4 shows that the model underestimates the gas temperature at this position by a few degrees. It should, however, be noted that the position of the thermocouple is not exactly at the tube center, and therefore does not measure precisely the calculated gas temperature which applies to the tube center. The oscillations of T_{down} in Figure 4.2d, which are also superimposed on $\Delta T = T_{down,meas} - T_{down,cal}$ in Figure 4.4, are caused by the heat source in the box which encloses the PCS-2000 instrument: it is switched on and off at regular intervals by the temperature controller. These oscillations are neglected in the model.

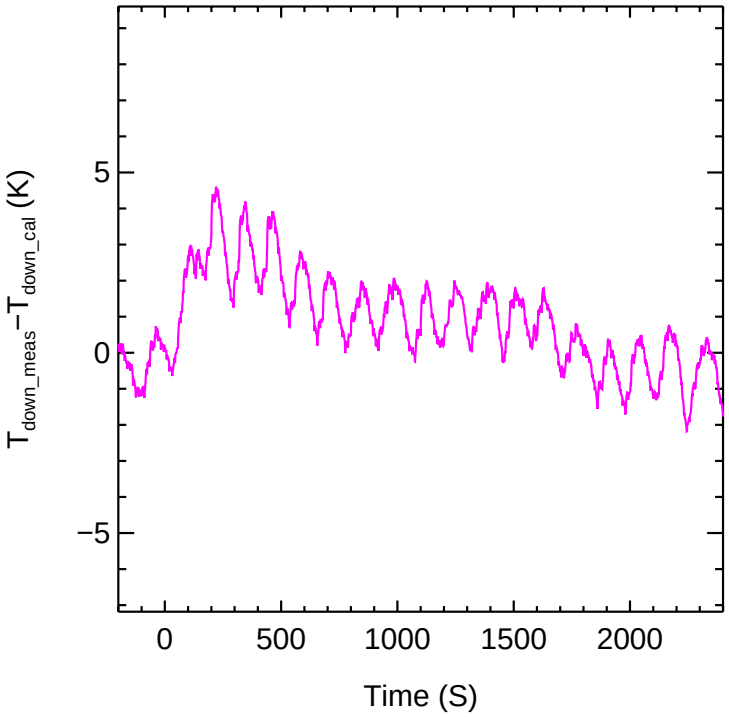

Figure 4.4: Difference $\Delta T = T_{down,meas} - T_{down,calc}$ between the measured outlet temperature and the calculated gas temperature at a distance of 850 mm from the sampling tube entrance. Activation N° 74 IN02. The temperature fluctuations are due to the heat source in the PSC-2000 box which is switched on and off by the temperature controller.

4.2.2 The Effect of Ice Crystal Evaporation in the Sampling Tube

The evaporation rate of ice particles (assumed to be spherical in the following considerations) depends upon their size and on the environmental parameters, in particular on the relative humidity of the air. The ice particles that are formed in the AIDA chamber are transported through different heated sections of the connecting tube under a forced convection as shown in Figure 4.1. The gas temperature at the tube inlet is equal to the mean gas temperature in the AIDA chamber. It remains constant along the hydrostatic length and increases slowly at the beginning of the heated section as shown in Figure 4.3 The gas becomes subsaturated with respect to ice with the beginning of the heated section as shown in Figure 4.6. The evaporation of ice crystals in the tube before they are detected in the PCS-2000 measuring volume was calculated as explained briefly in Appendix B.

The variation of the ice crystal radius is calculated along the tube axis according to the following equation

$$r_n^2 = r_0^2 + \frac{2n}{u_m}\sum_{i=0}^{n-1} C_i \qquad (4.3)$$

where r_n is the calculated particle radius at a step n, $r_\circ$ is the initial radius at the AIDA chamber, n is an array referring to the tube length in 1 mm, u_m is the particle fall velocity, C_i is the time dependent change of the particle mass, equal to the right-hand side of Equation B.1 in Appendix (but not to be confused with the capacity factor C in the same equation). It varies as function of the temperature at the center line of the sampling tube along which the ice particles are assumed to travel from the AIDA chamber to the detection volume of the OPC. The IDL code was written based on the explained model in Appendix B. All input physical parameters of the model were calculated as function of the calculated gas temperature along the tube axis. The supersaturation S_i (actually a sub-saturation) varies along the tube axis as follows: the partial pressure of water vapour along the tube axis can be considered approximately constant and equal to the vapour pressure in the AIDA chamber, while the *saturation* vapour pressure over ice (according to Marti and Mauersberger, 1993) is calculated as a function of the calculated gas temperature along the tube axis, equation 2.2 in section 2.3 of chapter 2. The obtained sub-saturation is shown in Figure 4.5. The sub-saturation is zero (i.e. the ice saturation ratio is unity) along the hydrostatic length and decreases with increasing mean gas temperature at the beginning of the heated section.

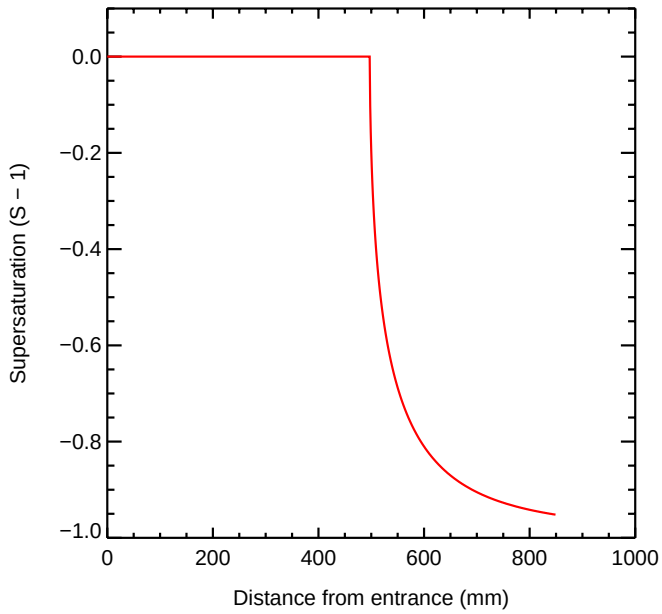

Figure 4.5: Variation of super saturation along the tube axis during experiment N° 74 IN02.

Equation 4.3 was applied for ice crystal radii between 0.5 µm and 12 µm at time equal to 250 s after the principal pump was started in experiment N° 74 IN02. The variations of ice crystal radii from 1 µm to 10 µm that were calculated according to equation 2.20 and are shown in Figure 4.6

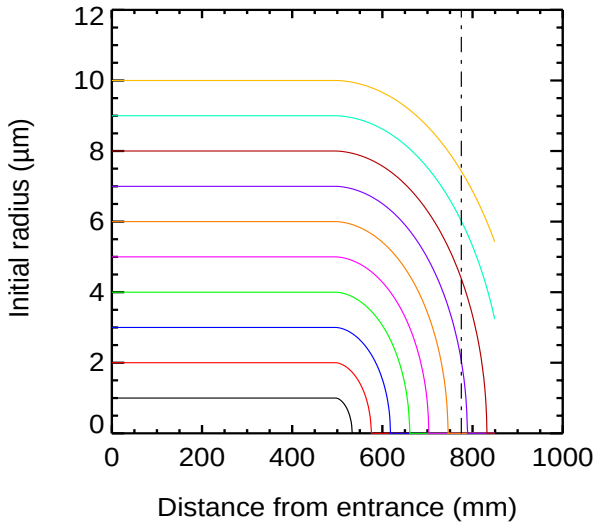

Figure 4.6: Variation of ice particle radii versus the tube length. The vertical dash-dotted line represents the position of the PCS-2000 measuring volume. Experiment N° 74 IN02.

Figure 4.6 shows clearly that ice particles evaporate completely or partially before their size can be measured in the detection volume of PCS-2000. The loss due to evaporation in terms of ice particle radius in % has been calculated at the measuring volume of PCS-2000 and is shown in Figure

4.7. It is defined as the difference between the calculated particle diameter at the measuring volume and the particle diameter in the AIDA chamber in %.

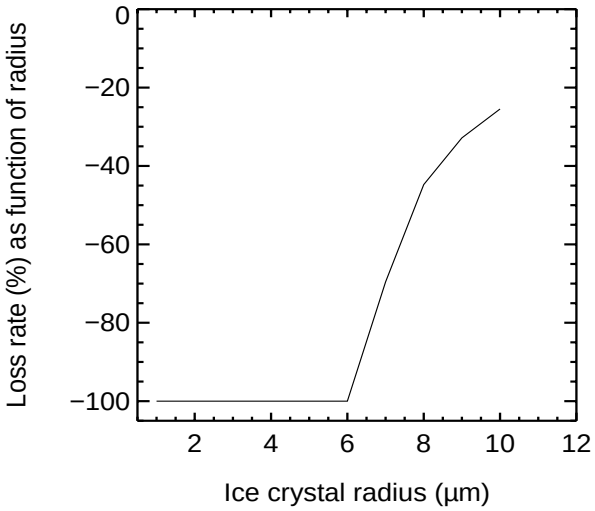

Figure 4.7: The evaporative loss of ice particle radius in % at the PCS-2000 measuring volume versus the initial ice crystal radius in the AIDA chamber, experiment N° 74 IN02. Note that ice particles < 6 μm evaporate completely. Information on their number and size distribution is irreversibly lost.

These results are taken into consideration when we analyse size distributions of ice crystals which were measured by PCS-2000. An IDL program was written to calculate the original sizes of the ice crystals in the AIDA chamber (i.e. before their partial evaporation in the sampling tube) from the sizes of partially evaporated ice crystals which were detected by PCS-2000. It is of course not possible to reconstruct the number of those ice crystals which have evaporated completely before reaching the detection volume of PCS-2000. This information is irreversibly lost. While this may introduce a large error in the reconstructed number distribution if many small ice crystals were present which evaporate completely, the error introduced in the reconstructed mass density is much less serve since the very small completely evaporating ice crystals make a small contribution to the mass density which is dominated by large ice crystals.

5. Experimental Results

This chapter is sub-divided into six sections. Experimental results and analytical procedures are reported that relate, either indirectly or directly, with the ability of different types of mineral dust particles to act as ice nuclei in the atmosphere. In view of the wide temperature range that can be covered by cloud simulation experiments in the AIDA chamber, ice nucleation may occur *via* different heterogeneous nucleation modes, as pointed out in section 1.3.2 chapter 1. A common goal of all experiments was to determine, as accurately as possible, the critical saturation ratio S_{ise} at which ice nucleation occurs. The contents of the six sections of this chapter can be summarised as follows:

- The first section is devoted to the geographic locations where desert dust samples were collected, to the sampling techniques, and to the identification of the source regions of the different samples.
- The second section reports the elemental composition of the mineral dust particles as well as the ionic composition of their water-soluble coatings.
- In the third section, an attempt is made to relate the maximum fraction of particles that are converted to ice particles in the AIDA chamber experiments with particle morphologies. For this purpose, different samples of desert dust particles were extracted from the chamber and deposited on filters. SEM images of the deposited particles were used to classify the mineral dust particles as either spherical or non-spherical with the help of special image analysis software.
- In the fourth section, the ice evaporation model developed in Chapter 4 was used to correct PSC-2000 ice particle size distributions for evaporative losses in the sampling line. These size distributions are validated by comparison with data derived from long-path FTIR extinction spectra in the ADIA chamber. The FTIR spectra had been analysed by Mie theory. Since this theory is only approximately valid for sufficiently small ice crystals, it yields only rough estimates of the count median diameters, while the obtained total ice water contents are much more accurate.
- The fifth section is devoted to the raw data analysis of all ice nucleation experiments in the AIDA chamber, which were carried out with the previously characterised mineral dust samples. An unbiased method is described whereby the critical ice saturation ratio for heterogeneous ice nucleation can be obtained from experimental raw data. This is done either by filtering measured depolarisation ratios from the laser backscatter experiment described in section 2.4, or by plotting relative humidity measurements versus the perpendicular component of the backscattered intensity. The errors of the obtained critical super-saturations

at freezing onset are assessed. The results of the raw data analysis are presented in comprehensive tables and in graphical form.

- The sixth and last section of chapter 5 is devoted to data interpretation. We present a formalism whereby heterogeneous nucleation rates can be determined from experimental data. The results are discussed in relation with their dependence on potentially relevant parameters.

5.1 Desert Dust Samples for AIDA experiments

5.1.1 Collection of Dust Samples

For this study I collected two samples of airborne mineral dust which had been carried by the winds from the Sahara desert to a sampling point which is located at 30.27°N, 31.11°E, at a place close to Benha university, about 50 km north of Cairo city and about 150 km from the Mediterranean coast of Egypt. This area is a part of the Middle East, North Africa, very close to the East Mediterranean basin which is bounded by three continents: Europe to the north, Africa with the Sahara to the south, and Asia to the east. The geographical situation influences the properties and distribution of atmospheric aerosols in this area.

These samples were collected during 24 hours by gravitational settling on a clean horizontal surface of 2 × 3 m^2 which was exposed ~ 20 m above ground level in an empty room with open windows, during two sand storm events on 18 Feb and 19 Mar 2003. Hereafter these samples are denoted “Cairo dust 1 (CD1)” and “Cairo dust 2 (CD2)”. The method of gravitational settling has been previously applied by De Tomasi et al. (2003) to collect and characterise Saharan dust, which was transported to a LIDAR site at Lecce, south-eastern Italy, in May 2001. It has the advantage that the relatively large mineral dust particles settle much more efficiently than small aerosol particles from local sources, which remain airborne. We collected approximately 18 g of CD1 and 13.5 g of CD2. The samples were stored in clean bottles for further analysis at **Forschungszentrum Karlsruhe, IMK-AAF**. Both samples were passed through sieve shakers (Retsch GmbH, Germany) to isolate particles with diameters less than 20 μm. The procedure yielded 12.5 g CD1 and 9.4 g CD2.

Another sample of Egyptian Sahara dust, hereafter denoted as “Sahara Dust (SD)” was collected from a hole of 1.5 m depth at a place, which lies in the desert 70 km northeast of Cairo city. The original desert dust sample (4 kg) was sifted at the **Geology Department, Al-Azhar University**, Egypt, yielding 250 g of mineral dust with particle diameters less than 150 μm. This sample was further refined at **Forschungszentrum Karlsruhe, IMK-AAF**, by passing it through sieve shakers, as described above. This produced 7.5 g SD with particle diameters less than 20 μm.

An Asian dust sample, particle diameters less than 20 μm, was kindly provided by the University of Mainz, Germany. It had been collected from the ground in the eastern part of the Takla Makan Desert, northwest China, east of the Dalimu Basin between Kuerle and Ruoquiang. This sample is hereafter denoted as "Asian Dust (AD)".

A significant number of AIDA experiments were carried out with so-called "Arizona Test Dust (ATD)". This standardised material is often used in laboratory experiments, serving as a surrogate for airborne mineral dust. Arizona Test Dust, which can be purchased from Powder technology, Inc. (Minnesota, USA), is made by milling desert sand. The size fraction, which was purchased for the AIDA experiments, consisted of particles with diameters less than 5 μm.

5.1.2 The Sources of African Airborne Mineral Dust Samples.

The chemical and mineralogical composition of airborne desert dust depends on the source region of the material and on possible interactions with pollutant gases during transport. It is therefore important to specify the original source regions of the airborne mineral dust particles CD1 and CD2, which had been transported to the sampling point near Cairo city. This information can be derived by combining trajectory model calculations with remotely sensed satellite data, as explained in sections 5.1.2.1 and 5.1.2.2 below. Similar techniques have recently been applied by Sodemann et al. (2006) to identify the source regions of dust events, which were archived in a glacier in the Swiss Alps, and could be dated to October and March 2000 from the depth of the dust layers.

5.1.2.1 Trajectory Model Calculations

We used the FLEXTRA trajectory model version 3.1 to calculate air mass back trajectories at the sampling point of CD1 and CD2. The model was developed by Andreas Stohl while he was at the University of Agricultural Sciences in Vienna. He published version 3 on the web in 1999 while he was a co-worker of Prof. Fabian at the Lehrstuhl für Bioklimatologie und Immissionsforschung, University of Munich. The model is able to calculate forward and backward air mass trajectories based on girdded meteorological data from the European Centre for Medium-Range Weather Forecasting (ECMWF). A comprehensive description of the FLEXTRA model can be found at the URL http://zardoz.nilu.no/~andreas/flextra/flextra3.html, which also lists a number of relevant publications. The FLEXTRA trajectory model needs four meteorological input fields: The horizontal wind components in the east and the north direction, the vertical wind velocity and temperature, in addition to the topography and the surface pressure. Back trajectories were calculated for air masses which

arrived above the sampling point north of Cairo at pressure levels of 1000, 900, 850, 700 and 500 hPa (corresponding to altitudes of ~100 m, ~1 km, ~1.5 km, ~3 km, and ~5.5 km), while the dust samples CD1 and CD2 were collected, as shown in Figures 5.1 and 5.4, respectively.

5.1.2.2 Satellite Observations

Satellite instruments for remote sensing are powerful tools to detect, on a global scale, the transport of dust clouds over sea and – in some cases, see below – over land, with high resolution in space and time. The Moderate Resolution Imaging Spectroradiometer (MODIS) Terra and Aqua satellites are operating for this purpose with resolutions of 0.25, 0.5, 1, and 2 km at nadir, see http://modis.gsfc.nasa.gov/index.php and also http://www.parstimes.com/spaceimages/mideast/. Daily satellite images (resolution of 500 m at nadir) which were taken during the dust storm events confirm the presence of dust-loaded air masses above the sampling point near Cairo. MODIS / Terra and Aqua satellite images are shown on the right panels of Figures 5.2 and 5.3 for CD1, and Figures 5.5 and 5.6 for CD2.

The Earth Probe Total Ozone Mapping Spectrometer (EP/TOMS), on the other hand, measured backscatter radiances by atmospheric aerosols. It can detect aerosols from the spectral contrast between the 340 and 380 nm channels in the near Ultra Violet (nUV) (Ginoux and Torres, 2003). This technique does not rely on the uniform and very low albedo of the sea surface and is therefore successful not only over the sea, but also over land, although it cannot fully detect aerosols in the lower 1–2 km above the surface, and is sensitive to cloud cover (N.J. Middleton and A.S. Goudie, 2001). The data product can be used to investigate the properties of aerosols and the radiative forcing by airborne Sahara dust, and to initialize forecasting models of dust aerosols (Ginoux and Torres, 2003). EP/TOMS provides daily and global information on the distribution of nUV absorbing aerosol at 1200 UTC with a resolution of 1.25^{o} longitude by 1^{o} latitude. We have interpolated the EP/TOMS satellite raw data for the dust storm events to produce colour-coded aerosol index (AI) maps. These are shown on the left panels of Figures 5.2 and 5.3 for CD1, and of Figures 5.5 and 5.6 for CD2. We have omitted AI values <1 because they are not reliable.

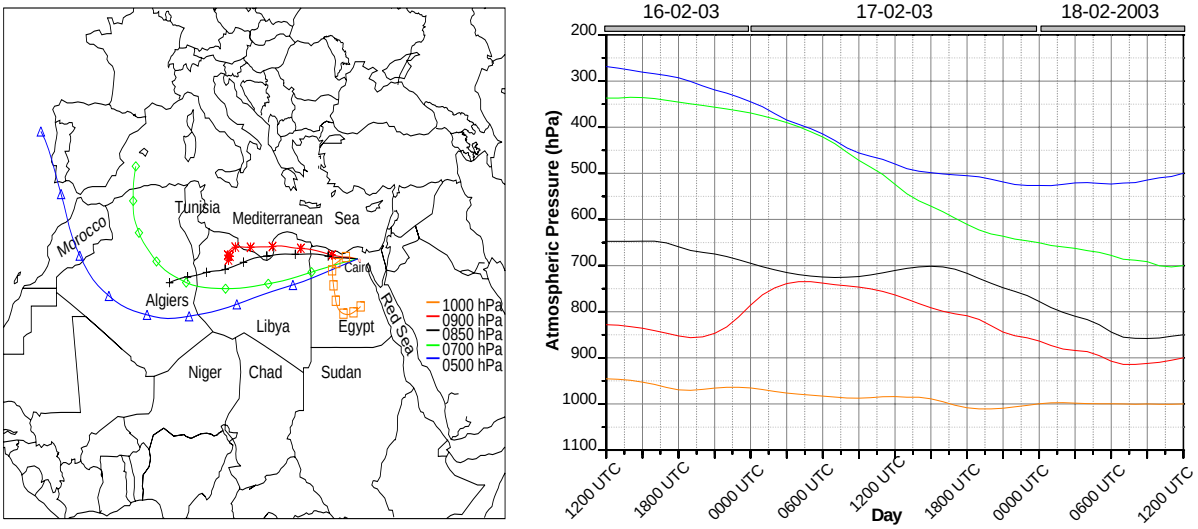

(a) (b)

Figure 5.1: (a) 48 h back-trajectories ending at the sampling point before 18 Feb 2003, for 1000, 900, 850, 700, and 500 hPa, calculated with the FLEXTRA trajectory model, based on ECMWF data.

(b) Pressure profiles along the same back-trajectories ending at the sampling point at the 1000, 900, 850, 700, and 500 hPa pressure levels.

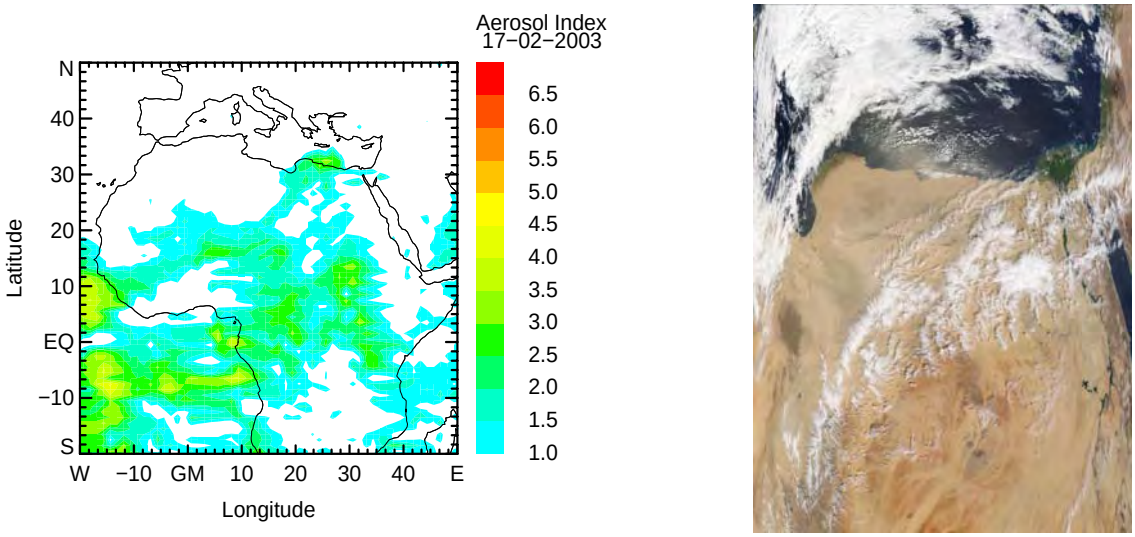

Figure 5.2: Left panel, EP/TOMS aerosol index at 1200 UTC, 17 Feb 2003. Right panel, MODIS/Terra Satellite image at 09:10 UTC.

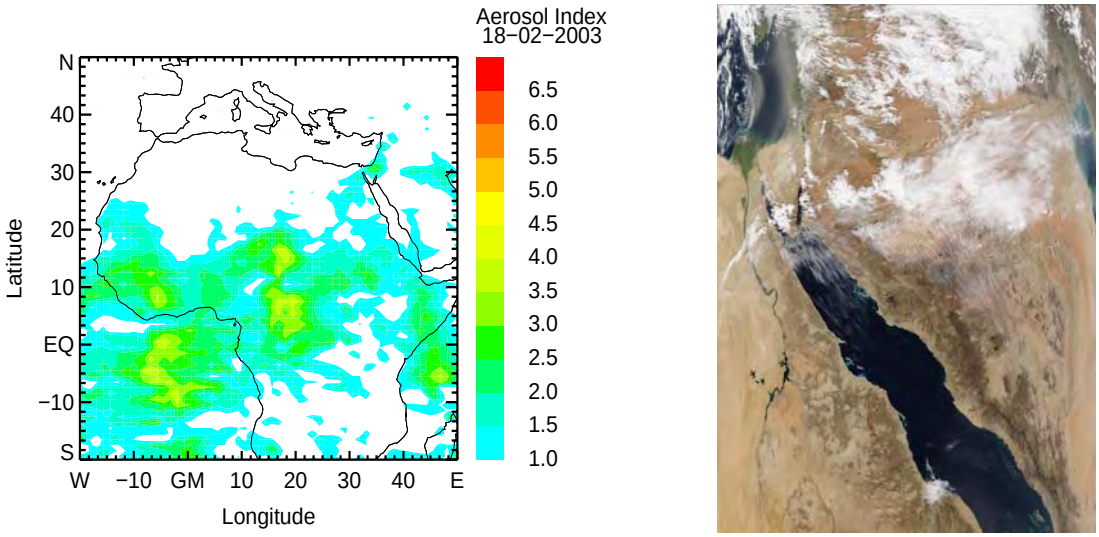

Figure 5.3: As in Figure 3.2 but on 18 Feb 2003. MODIS/Terra satellite image at 08:15 UTC.

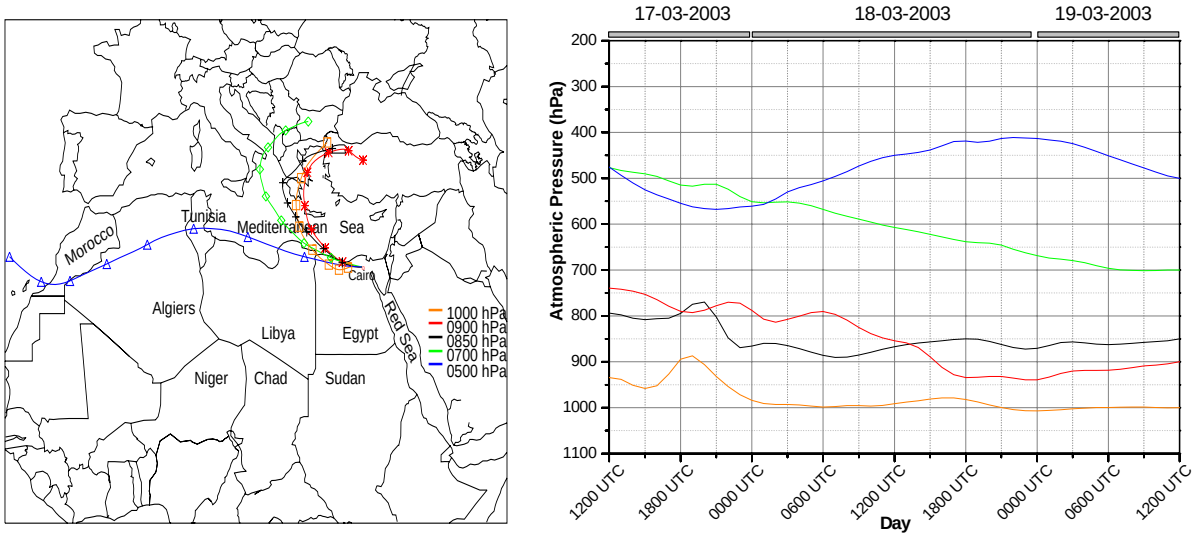

Figure 5.4: Back-trajectories as in Figure 5.1a and b, but ending near Cairo on 19 Mar 2003.

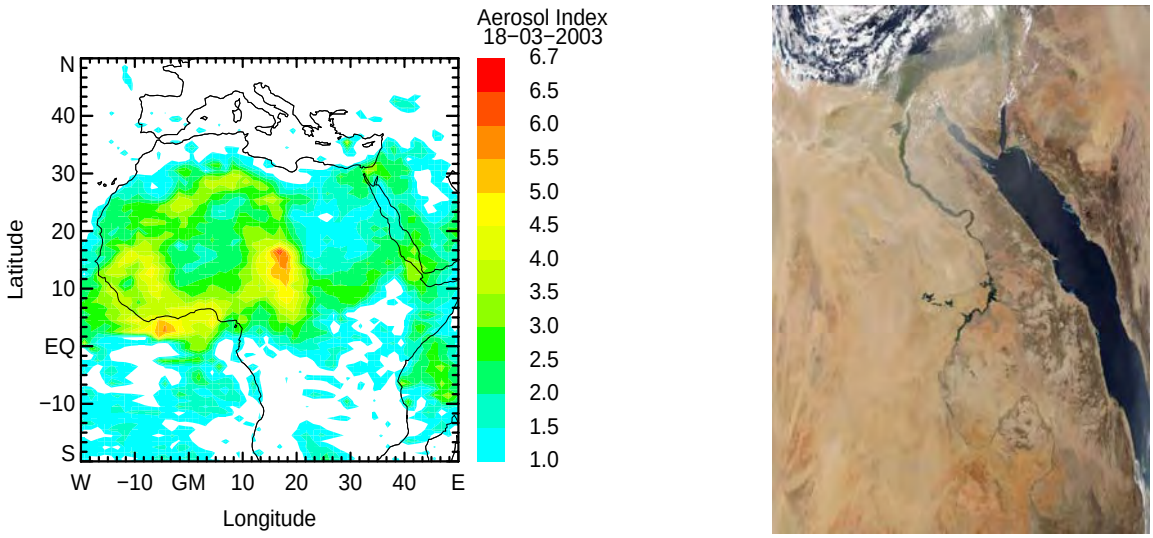

Figure 5.5: As in Figure 5.2 but on 18 Mar 2003, MODIS/Terra satellite image, 18-03-2003 08:40:00 UTC, 0.5 km resolution

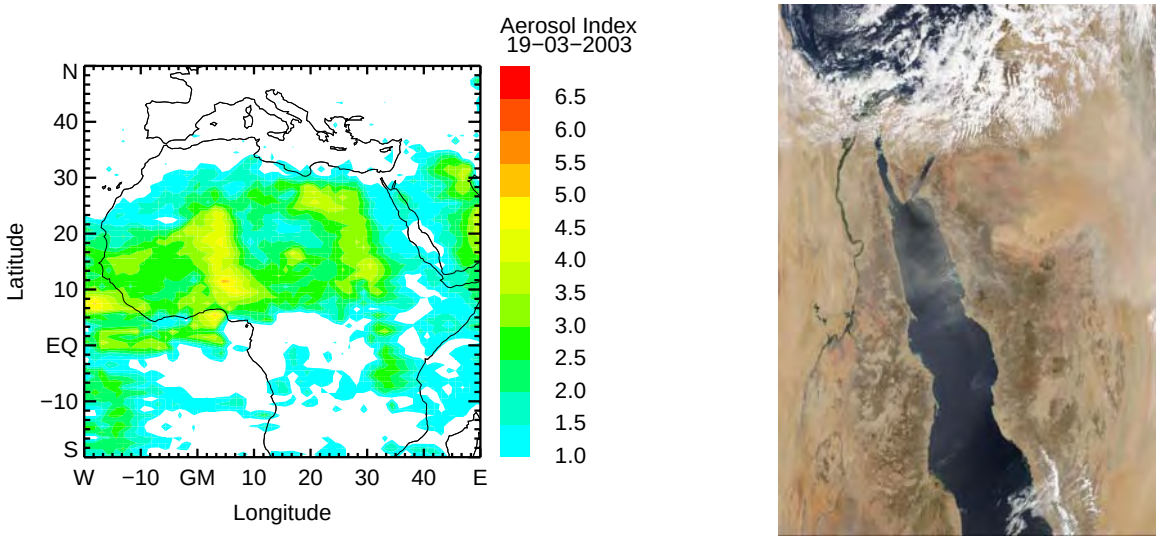

Figure 5.6: As in Figure 5.3 but on 19 Mar 2003, MODIS/Aqua satellite image, 19-03-2003 10:50:00 UTC, 0.5 km resolution

5.1.2.3 Transport of Mineral Dust to the Sampling Point

48 hour air mass back trajectories arriving at the sampling point on 18 Feb 2003 and on 19 Mar 2003 were calculated as shown in Figure 5.1 and 5.4. They clearly indicate that the Sahara dust samples CD1 and CD2 originated from different source regions. The air mass arriving close to the surface at the sampling point of CD1 had permanently travelled within the boundary layer for the past two days. It started from Central Egypt on 16 Feb 2003, first moving from east to west, turning northward above the western desert of Egypt, then changing direction and moving from west to east on 18 Feb 2003 to the sampling point, as shown in Figure 5.1a. The passage of dust-loaded air masses across the sampling area is qualitatively confirmed by the EP/TOMS AI data, as it can be seen on the left panels of Figures 5.2 and 5.3. We conclude from these considerations that the mineral dust sampled as CD1 on 18 Feb 2003 originated most likely from the west desert of Egypt, and may have already been contaminated by particulate matter when moving from Central Egypt to the desert.

It is interesting to note that the air mass which moved permanently within the boundary layer followed a completely different trajectory than the air masses reaching the sampling point at higher altitudes. Those air masses which arrived at the sampling point on the 900 hPa and 850 hPa levels had permanently moved from west to east, originating two days before above the Mediterranean coast of Libya and above east Algeria, respectively. The free upper air mass trajectories ending north of Cairo at 700 and 500 hPa are also eastbound, but travelled much longer distances from above the Mediterranean and Atlantic coast of Spain across central Algeria, south west Libya and west Egypt.

Important additional information can be obtained by combining the horizontal components of the back-trajectories, Figure 5.1a, with their vertical components, which are shown in Figure 5.1b. The trajectories arriving above the sampling point at altitudes corresponding to 500 and 700 hPa are permanently down-sloping from 260 hPa (~10 km altitude, i.e. close to the tropopause) and 330 hPa (~8,5 km altitude), respectively. These free tropospheric air masses, which are certainly free of desert dust because they never contacted the surface of the desert, are associated with anticyclonic conditions in the middle and upper troposphere. In contrast, the air mass arriving at 900 hPa above the sampling point near Cairo, originated from northwest Libya two days earlier. The horizontal wind velocity was very low while the air mass circulated above the area at about 850 hPa. In the evening of 16 Feb, the same air mass suddenly started to rise very rapidly to 730 hPa. This situation is representative of a zone of low pressure which leads to instability in the atmosphere, creating a region of strong vertical motion and therefore a zone in which desert dust can be lifted from the surface layer to about 730 hPa (ca 2.7 km altitude) in the case considered here. This occurred roughly 30 h before the air subsided from 730 hPa along the Mediterranean coast of Egypt to about 900 hPa at the sampling point north of Cairo city. The source region of the up-lifted desert dust can thus be safely identified as the Mediterranean coast of north east Libya (Figure 5.1b). The resulting dust cloud is also seen in the EP/TOMS AI data of 17 Feb at noontime, left panel of Figure 5.2: it appears as a large circular spot over the Mediterranean coast of Libya and Egypt, covering partially the Mediterranean Sea, and extending eastward to the Nile Delta. The MODIS/Terra satellite image, which was taken during the dust storm event on 17 Feb 2003 at 0910 UTC (Figure 5.2, right panel), reveals a yellow dust cloud above the Mediterranean coast of Libya and Egypt, confirming the EP/TOMS AI data over the sea surface. It cannot be excluded that the dust cloud associated with the red back-trajectory in Figure 5.1 also made a contribution to the mineral dust sampled as CD1 on 18 Feb 2003 north of Cairo city.

The large circular spot of AI values larger than unity that covered the Mediterranean coast of Libya and Egypt and partially the Mediterranean Sea on 17 Feb. 2003 has totally disappeared on 18 Feb. 2003. Figure 5.3 implies that the dust cloud has moved further to the east and then to the north along the coastline of Israel. This interpretation agrees well with the MODIS/Terra satellite image, right panel of Figure 5.3, which was taken during the dust storm event on 18 Feb 2003 at 0815 UTC. - In conclusion, the best we can say about the origin of the desert dust sample CD1 is that it originated from areas south and west of the sampling point, with contributions from central Egypt, the western desert of Egypt, and possibly the north western desert of Libya.

The dust sample CD2 which was collected on 19 Mar 2003 at the same sampling point north of Cairo City was found to be associated with a completely different air mass history. The calculated 48 h back trajectories of air masses which arrived at noontime above the sampling point at pressure levels of 1000, 900, 850, 700 and 500 hPa (corresponding to altitudes of ~100 m, ~1 km, ~1.5 km, ~3

km, and ~5.5 km) while sample CD2 was collected, are shown in Figure 5.4. All trajectories on Figure 5.4a (with the exception of a free tropospheric air mass back-trajectory arriving above the sampling point at 500 hPa) started 48 h earlier in Rumania and in the utmost western part of Turkey, following a circular path across the Balkans and Greece, then cross the Mediterranean sea, and finally passing over land very close to the coastline of north-western Egypt. We note that very similar 24 h back-trajectories, passing practically over our sampling point north of Cairo city, and ending at a sampling point on a mountain near Jerusalem on 13 and 14 Feb 2004, respectively, have recently been calculated with the NOAA HYSPLIT trajectory model by Laskin et al. (2005).

The vertical components of the air mass back-trajectories are shown in Figure 5.4b. The back-trajectory ending at the sampling point at 500 hPa rises on 18 Mar 2003, indicating a cyclone in the free troposphere. The cyclone can also be seen in the cloud pattern on the MODIS/Terra satellite image that was taken on 18 Mar 2003 at 08:40:00 UTC, right panel of Figure 5.5. This cyclone, which is located above the east Mediterranean basin, gives rise to a wind system that is reflected by the red, black, and green back-trajectories in Figure 5.4a. Soil dust is taken up by the lowermost air masses as they descend over the desert due to an anticyclone which is located over the coast of Libya and Egypt, about half a day before the same air masses pass over the sampling point. The EP/TOMS aerosol index data on 18 Mar 2003 confirm that the air over the entire Sahara is heavily loaded with dust up to the Mediterranean coast of Egypt. The lack of AI data over the Nile Delta and the Mediterranean coast of Egypt on 19 Mar 2003, left panel of Fig. 5.6, is due to a cumulus cloud system which interferes with the measurements of the EP/TOMS instrument. In conclusion, the combined evidence from the MODIS satellite images, the EP/TOMS AI data, and the back trajectory calculations all support a narrow sector W-NW of the sampling point as the source region of the CD2 sample which was collected on 19 Mar 2003, about 50 km north of Cairo city.

5.2 Elemental and Water-Soluble Ionic Composition of the Dust Samples

5.2.1 Elemental Composition

Aerosols are known to be composed of various externally and/or internally mixed chemical compounds: refractory material like mineral dust, soluble salts, and organics. Because the samples studied in this work consisted predominantly of refractory minerals, they were analysed for their elemental composition using an X-ray fluorescence spectrometer (SRS 303AS from BRUKER-AXS) at the Institute für Materialforschung I, Forschungszentrum Karlsruhe, as mentioned before. The elemental composition of the different dust samples, expressed in weight-% of their oxides, are shown as a bar diagram in Figure 5.7. It is not surprising that all mineral dusts contained as the highest percentage silicon dioxide, with minor contributions of other crustal elements.

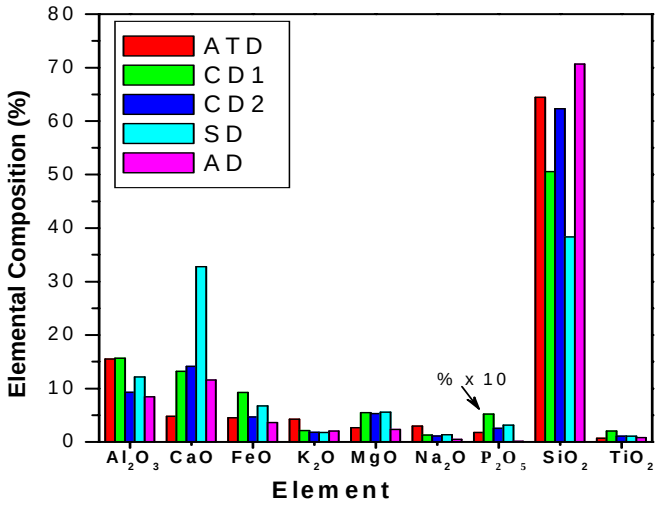

Figure 5.7: Elemental composition of all dust samples studied in this work

Note that the Saharan dust samples, in particular the real desert dust sample SD, contain significantly more calcium than, e.g., Arizona test dust. Calcium in the form of calcite ($CaCO_3$) makes mineral dust particles alkaline, thereby increasing their ability to react with inorganic and organic acids in the atmosphere to form highly soluble calcium nitrate $Ca(NO_3)_2$ and weakly soluble coatings of calcium sulphate (gypsum, $CaSO_4$). These heterogeneous chemical reactions lead to soluble particle coatings which have indeed been observed in aged dust particles collected by aircraft (Levin et al., 1996) and on a mountain site, in Israel (Laskin et al., 2005). Phosphorus oxide, which can (but need not) be an indicator of biogenic material, contributes the smallest percentage to all dust samples.

5.2.2 Soluble Ions

As mentioned before in section 2.2.2 of chapter 2, ion chromatography was used to analyse the composition of the water soluble inorganic ionic fraction of the dust samples. Because the sampling

method by gravitational settling is highly selective for mineral dust particles, the soluble ionic fraction of samples CD1 and CD2 is most likely due to surface coatings of the dust grains. The ion contents in weight-% are shown as bar diagrams in Figure 5.8. It should be noted that the ion chromatographic analyses of individual aqueous extracts was highly reproducible. However, larger differences were found between different aqueous extracts of the same dust samples. Therefore, only qualitative conclusions can be drawn from these results.

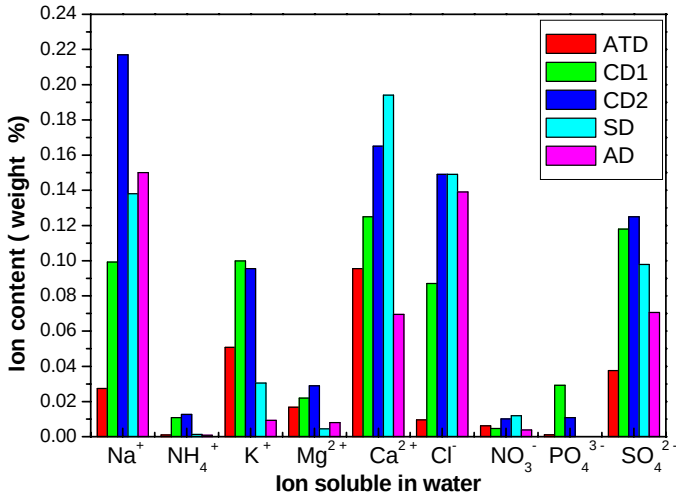

Figure 5.8: Ionic composition of aqueous extracts of the mineral dust samples

Note that the contents of Na^+ and Cl^- ions are largest in the water soluble extract of CD2. As was shown above, this dust sample was lifted near the coastline of western Egypt into an air mass which had previously crossed the Mediterranean. The presence of NaCl, which was also observed in Saharan dust samples collected by gravitational settling in Italy (De Tomasi et al., 2003) after crossing the Mediterranean in the opposite direction, is attributed to mixing between mineral dust and sea salt aerosol. CD1, on the other hand, shows a relatively high fraction of PO_4^{3-}, probably due to the continental origin of the corresponding air mass which had passed over phosphate mines in central Egypt. The presence of relatively large amounts of sulphate SO_4^{2-} in the airborne samples CD1 and CD2 may be due to heterogeneous reactions with SO_2 from local pollution, particularly in air masses which had passed over a sugar factory that is located in south Egypt and is still using mazoot (a heavy fuel oil) and the residue of sugar cane as burning fuels (EEAA, 2001). Both airborne mineral dust particles contain conspicuous amounts of ammonium NH_4^+ and potassium K^+ which we attribute to local biomass burning activities in the Nile Delta. The water soluble ion contents of all dust samples studied in this work are as follows:

ATD, 0.25 wt. %; CD1, 0.60 wt. %; CD2, 0.81 wt. %;
SD, 0.63 wt. %; AD, 0.45 wt. %.

These numbers support our assumption that the airborne Sahara dust samples CD1 and CD2 had accumulated soluble coatings during their transport by interaction with air pollutants. The lowest weight-fraction of soluble ions is associated with Arizona Test Dust, which has not been exposed to atmospheric pollutants.

The thickness of the soluble coating (neglecting possible organic coatings) was estimated from the soluble mass fraction (minus the soluble mass fraction of uncoated Arizona Test Dust) under the following assumptions: a) the particles are spherical, b) the refractory particles and the soluble coating have approximately the same density. It can be shown that the ratio (layer thickness)/ (particle radius) = $\Delta R/R \sim \Delta M/3M$, where M and R are the mass and the radius of the refractory core, while ΔM and ΔR are the mass and thickness of the coating. This yields a coating thickness for mineral dust particles with radius R = 2 µm of less than 6 nm.

It is interesting to note that Laskin et al. (2005) report complete *in situ* processing of calcite-bearing dust particles by HNO_3, following interaction between mineral dust (and sea salt) particles with polluted air "either in Egypt or in the Israeli coastal area". The authors present 24 h back-trajectories, calculated with the NOAA HYSPLIT trajectory model, which are amazingly similar to our own back-trajectories for CD2. Their trajectories originate over the Mediterranean, close to the east coast of Libya, and pass practically over our sampling site north of Cairo city, before ending at a sampling point on a mountain site near Jerusalem on 14 Feb 2004.

5.3 Microscopic Investigations

A very large number of cloud simulation experiments have been carried out in the AIDA chamber of IMK-AAF over the past years. In many experiments, mineral dust samples from various sources were used as seed aerosols to induce heterogeneous ice nucleation. It is also well known that the heterogeneous ice nucleating ability depends on the surface properties of the seed particles. Real samples of mineral dust are composed of a very large number of particles which differ individually by their morphologies, porosities, degrees of agglomeration, and so on. These properties may be used as proxies for their surface properties. One may also expect differences between the morphologies of mineral dust particles collected in the field and commercially available samples, like Arizona Test Dust (ATD), which may explain their different ice nucleating abilities. In this chapter we report an attempt to relate particle morphology with ice nucleating ability, using imaging software to distinguish between particles of different roundness.

The morphologies of mineral dust particles which were used as ice nuclei in the AIDA chamber were investigated by Scanning Electron Microscopy (SEM). For this purpose, mineral dust

was collected on Nuclepore polycarbonate membrane filters with a diameter of 47 mm and pore sizes of 0.2 µm. The airborne mineral dust was collected directly from the AIDA chamber at different flow rates and sampling times, depending on the particle number concentration in the chamber and the desired dust concentration on the filter. The collected samples were stored in desiccators for later use. Segments of 15 mm^2 were cut from the filter halfway between the centre and the filter edge for SEM imaging. The SEM images were made at magnifications of ×2,500 times or ×10,000, and analysed using Imatec image software version 2.3. For this purpose, the image had to be loaded into the display window of the software for automatic counting. The important issue is referred to as "segmentation", whereby the object is distinguished from the background, and its exact contour is determined. The segmented images are saved for later analysis. The dimensions of the objects are obtained by using the scale bar at the bottom of the image, as shown in the left panel of Figure 5.9. Various informations regarding the particle dimensions and their concentrations are obtained automatically and saved in a separate file for later representation. We have used the software to distinguish between non-spherical and spherical particles. As an example, a blow-up of a particle cluster, framed in red on the left panel, is shown on the right-hand side of Figure 5.9.

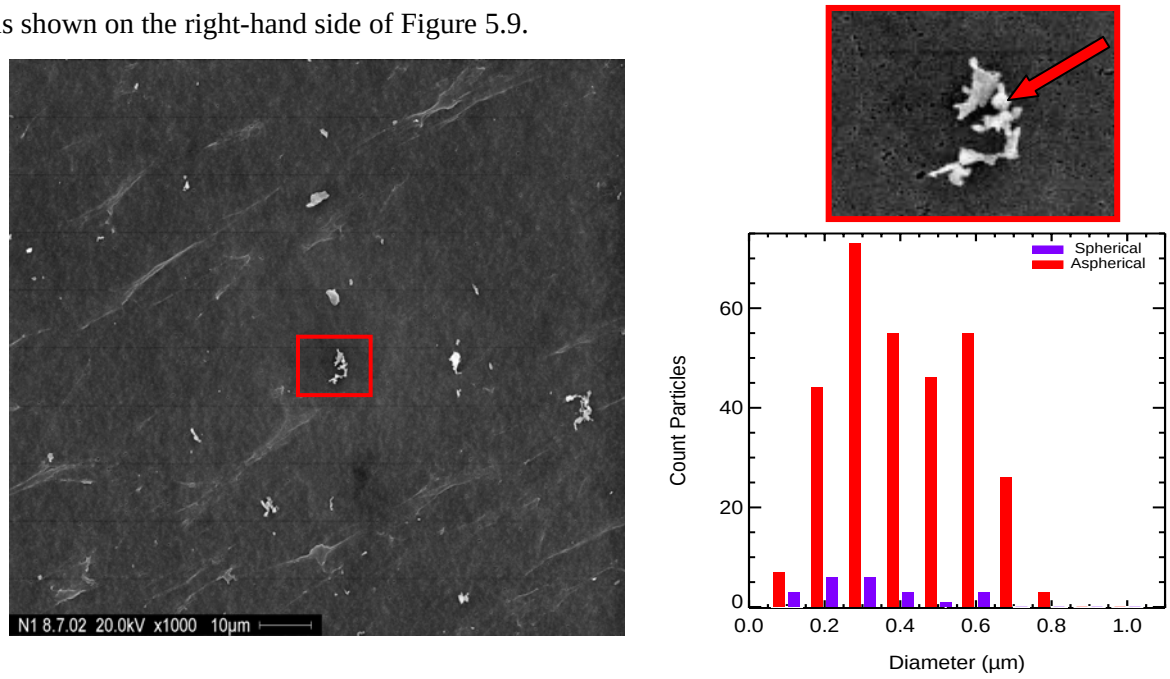

Figure 5.9: Left and upper right: SEM Image of ATD sample N° IN03-83 taken at a magnification of ×1,000. The scale bar (10 µm) is included. The lower right panel shows size distributions of non-spherical and spherical particles on the filter. See text for details.

An obviously spherical particle is marked by a red arrow. The software classifies each individual particle as either spherical or non-spherical. The result of the classification is shown as a bar diagram in Figure 5.9. The distribution of particle sizes, shown here on a linear size scale, agrees reasonably well with the distribution shown as Figure 2.8 in section 2.5 chapter 2 when the different

scales are taken into account. The bar diagram confirms the subjective impression that only a very small fraction of all particles (actually their projections) are spherical.

The percentages of spherical and non-spherical particles were determined for all experiments. The results are listed in Table 5.1 for ATD, Table 5.2 for SD and Table 5.3 for AD. The fraction of spherical particles is always significantly less than 10 %. To find out if the ice nucleating efficiency is related with particle shape, groups of experiments which were carried out at approximately constant cooling rates are colour-coded in the tables. Also listed are the maximum frozen fractions which are calculated in section 5.7 of this chapter. It was found that the maximum frozen fraction in each group increases when the fraction of spherical particles in the dust sample increases for all dust samples investigated. This is a surprising result, because it contrasts with the usual assumption that non-spherical particles with a rough surface are more efficient ice nuclei than spherical particles with a smooth surface.

Table 5.1: Classification of ATD in fractions of spherical / non-spherical particles (% of total particle number), their total areas, maximum frozen fractions, and cooling rates (in K min^{-1}). Total projected areas are given in μm^2

Ex_No	Temp.	Spherical	Non-spherical	Total area of spherical	Total area of non-spherical	Maximum frozen fraction	Cooling rate K/min
IN02_83	261.5	6.6	93.40	1.30	23.70	0.50	-2.18
IN02_84	261.9	8.51	91.49	0.70	8.80	0.97	-2.00
IN02_147	223.3	3.05	96.95	3.60	108.5	0.88	-1.55
IN02_148	223.4	5.19	94.81	1.70	22.90	0.89	-1.53
IN02_149	223.5	7.32	92.68	2.19	24.68	0.87	-1.33
IN02_150	225.5	9.33	90.67	2.03	8.64	1.00	-1.33
IN03_1	225.7	5.40	94.60	0.40	7.45	0.97	-1.58
IN03_2	225.7	2.86	97.14	0.26	6.24	0.76	-1.42
IN03_4	211.1	3.43	96.57	0.42	22.19	0.80	-1.90
IN03_5	210.8	3.84	96.16	0.10	1.87	0.80	-1.87

Table 5.2: As in Table 5.1 but for SD

Ex_No	Temp.	Spherical	Non-spherical	Total area of spherical	Total area of non-spherical	Maximum frozen fraction	Cooling rate K/min
IN03_11	210.0	3.21	96.79	0.96	23.40	0.60	-1.53
IN03_16	196.9	6.66	93.34	0.57	9.58	1.00	-1.34
IN03_17	197.0	5.88	94.12	0.29	14.00	0.90	-1.40
IN04_4	275.1	7.14	92.86	0.37	10.83	0.35	-2.58
IN04_6	253.4	9.37	90.62	0.59	6.20	0.50	-2.04
IN04_11	209.1	5.00	95.00	0.18	6.44	0.40	-1.96
IN04_35	238.6	7.14	92.85	0.37	10.62	0.45	-1.84
IN04_40	223.9	2.32	97.68	1.43	11.91	0.30	-1.80

Table 5.3: As in Table 5.1 but for AD

Ex_No	Temp.	Spherical	Non-spherical	Total area of spherical	Total area of non-spherical	Maximum frozen fraction	Cooling rate K/min
IN04_15	272	4.88	95.12	0.37	9.99	0.37	-1.98
IN04_17	269.2	6.46	93.54	0.37	12.45	0.47	- 2.22
IN04_26	222.1	3.49	96.51	0.54	3.67	0.13	- 1.86

5.4 Correction of Ice Particle Size Distributions for Evaporative Losses

5.4.1 Application of the Evaporation Model

We have shown in Chapter 4 that the evaporation of ice particles in the sampling line of the PCS-2000 optical particle counter is very sensitive to the gas temperature which differs from experiment to experiment. All input data for our evaporation model (temperatures, pressures, as well as particle size distributions = PSDs) were entered as averages over time intervals of 20 s. This allows us to compare our modelling results with retrievals from FTIR extinction spectra. Our model was evaluated over a wide range of gas temperatures. The evaporation-corrected count median diameters (CMDs) were either compared with Mie retrievals from in-situ measurements of FTIR extinction spectra, or with Welas measurements which are unaffected by ice particle evaporation, or with the AIDA microphysical model that was developed by H. Bunz. Input parameters of the Bunz-model are T_{wall} (assumed to be constant during each experiment), the initial relative humidity, the pressure p(t), and the gas temperature T_g(t). Furthermore, the number concentration of the mineral dust particles must be provided, as well as the freezing threshold saturation ratio for heterogeneous ice nucleation. A parameterisation of the freezing threshold saturation ratio over ice, S_{cr}, by Kärcher and Lohmann (2003) was implemented. It was proposed for the cirrus cloud regime and should not be used above 235 K.

Using evaporation-corrected ice particle spectra of PSC-2000 for the AIDA campaigns IN02 and IN03, and ice particle spectra obtained with the Welas OPC for the other AIDA campaigns, we have also calculated ice water contents using the following equation which assumes spherical ice particles,

$$IWC = \int_0^\infty \frac{4}{3}\pi \rho_{ice} r^3 n(r)\,dr \qquad (5.1)$$

where ρ_{ice} is the density of ice, taken as 0.9 g cm^{-3}, $n(r)dr$ is ice number concentration in each size bin, and r is the evaporation-corrected ice particle diameter. The same equation was used to calculate the ice water contents based on Mie-fit retrievals from FTIR extinction spectra. Selected results of our calculations are presented, and compared with other data where possible, in the following sub-sections:

● Model Calculation at Temperature of 262 K: IN02_87

The uncorrected and evaporation-corrected size distributions of super-cooled cloud droplets that condensed on ATD at 262 K (IN02_87) are compared in Figure 5.10, left and right panels. The corrected size distributions are shifted to larger diameters in the AIDA chamber. Water droplets with

diameters smaller than a temperature dependent threshold evaporate completely and are therefore not detected by PCS-2000. Their size distribution is irreversibly lost and cannot be reconstructed by the model. The narrow width of the size distribution, Figure 5.10, implies that no ice was formed in this experiment. Unfortunately, no FTIR spectra are available to support this conclusion. However, measurements with a cloud particle imager (cf. section 5.6.1) showed that a small number of ice crystals were formed in this experiment, although in a large excess of super cooled water droplets.

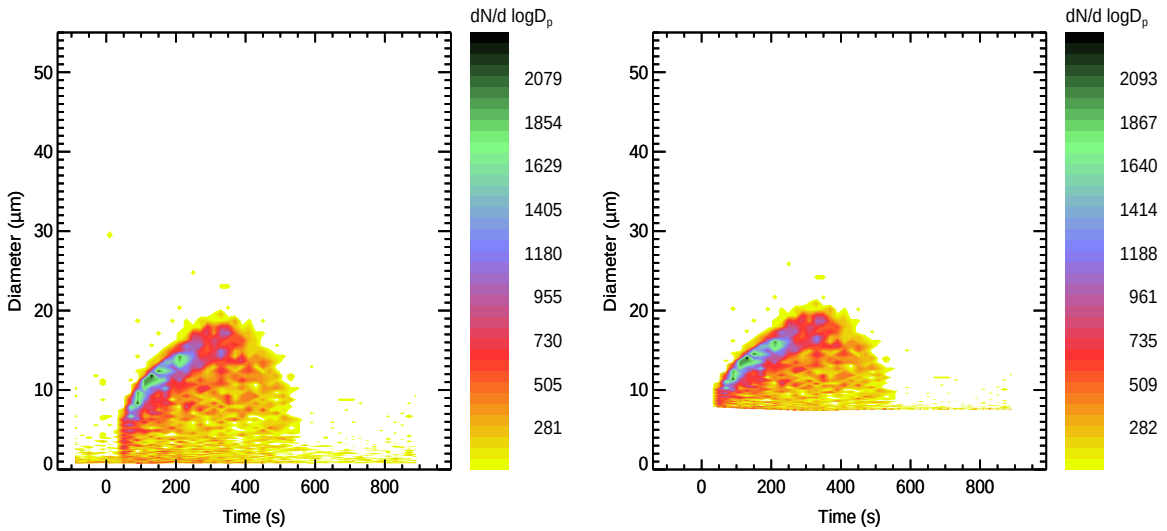

Figure 5.10: Cloud droplet condensation on ATD at 263 K, IN02_87. Left panel: size distribution (20 s time averages) as measured with PCS2000; same spectrum, but corrected with evaporation model (the thermodynamic properties of super-cooled water were taken into account). Note that some large ATD particles are also detected by PCS2000

● Model Calculation at Temperature of 223 K: IN02_147

The uncorrected / corrected size distributions of ice particles that nucleated on the same dust aerosol, but at 223 K (IN02_147) are compared in Figure 5.11. The count median diameters (CMDs) of the corrected size distributions agree reasonably well with the FTIR retrievals, but both are larger than the CMDs calculated with the Bunz-model. Surprisingly, the ice water contents (IWCs) are rather insensitive to evaporation. The uncorrected and corrected IWCs are ca. 30% larger than the FTIR-retrieved IWCs.

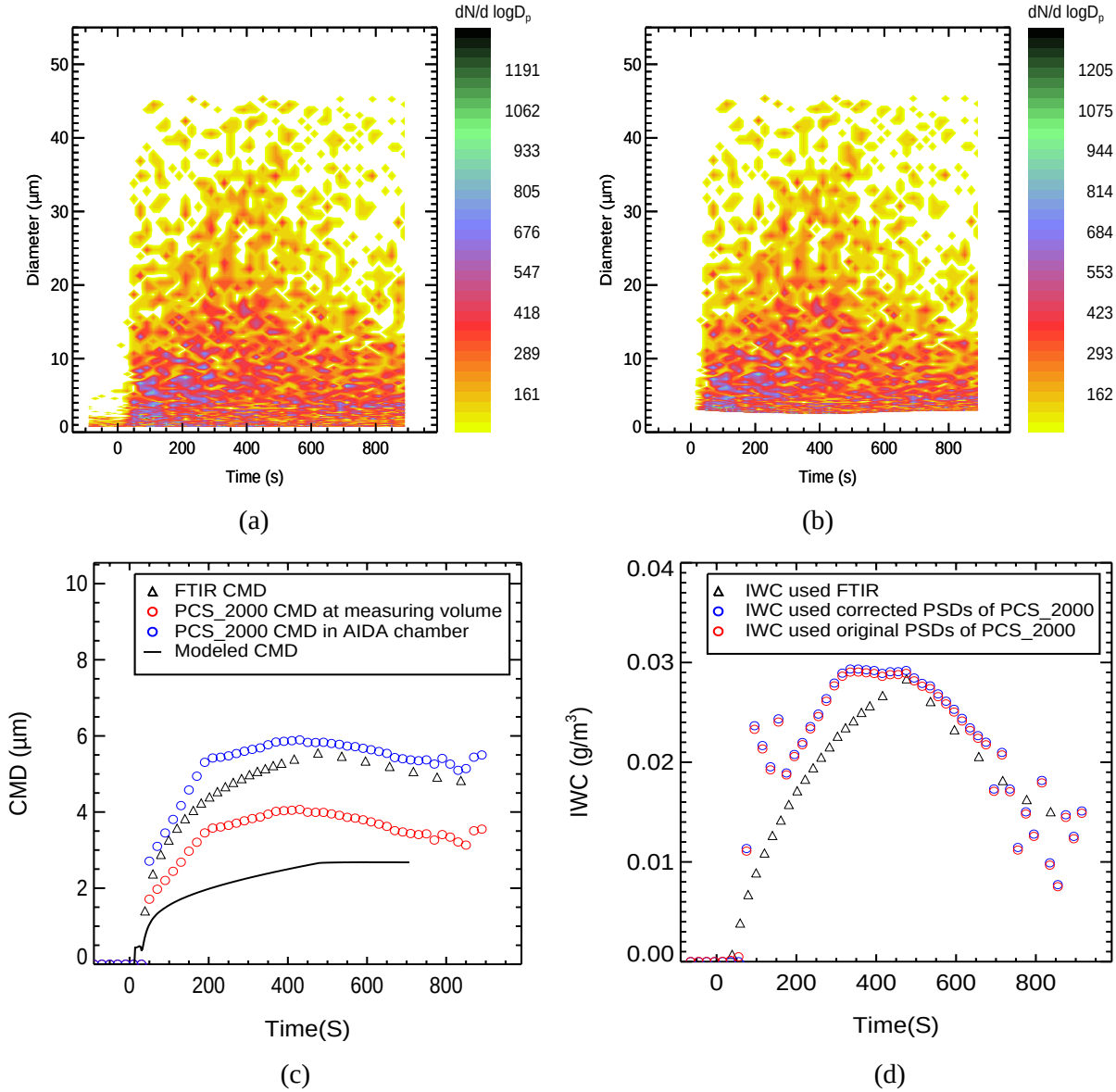

Figure 5.11: (a) and (b) as in Figure 5.10 but for ice nucleation on ATD at 223 K, IN02_147
(c) comparison of uncorrected/corrected count median diameters with FTIR retrievals and with the Bunz model.
(d) uncorrected /corrected IWC, comparison with FTIR retrievals

● Model Calculation at Temperature of 223 K: IN03_2

Uncorrected / corrected size distributions of ice particles that nucleated at 223 K in another AIDA experiment (IN02_147) are compared in Figure 5.12. The corrected CMDs agree well with Welas data and reasonably well with the FTIR retrievals, while the uncorrected CMDs are too small. The corrected IWC agrees very well both with the Welas data and the FTIR retrievals.

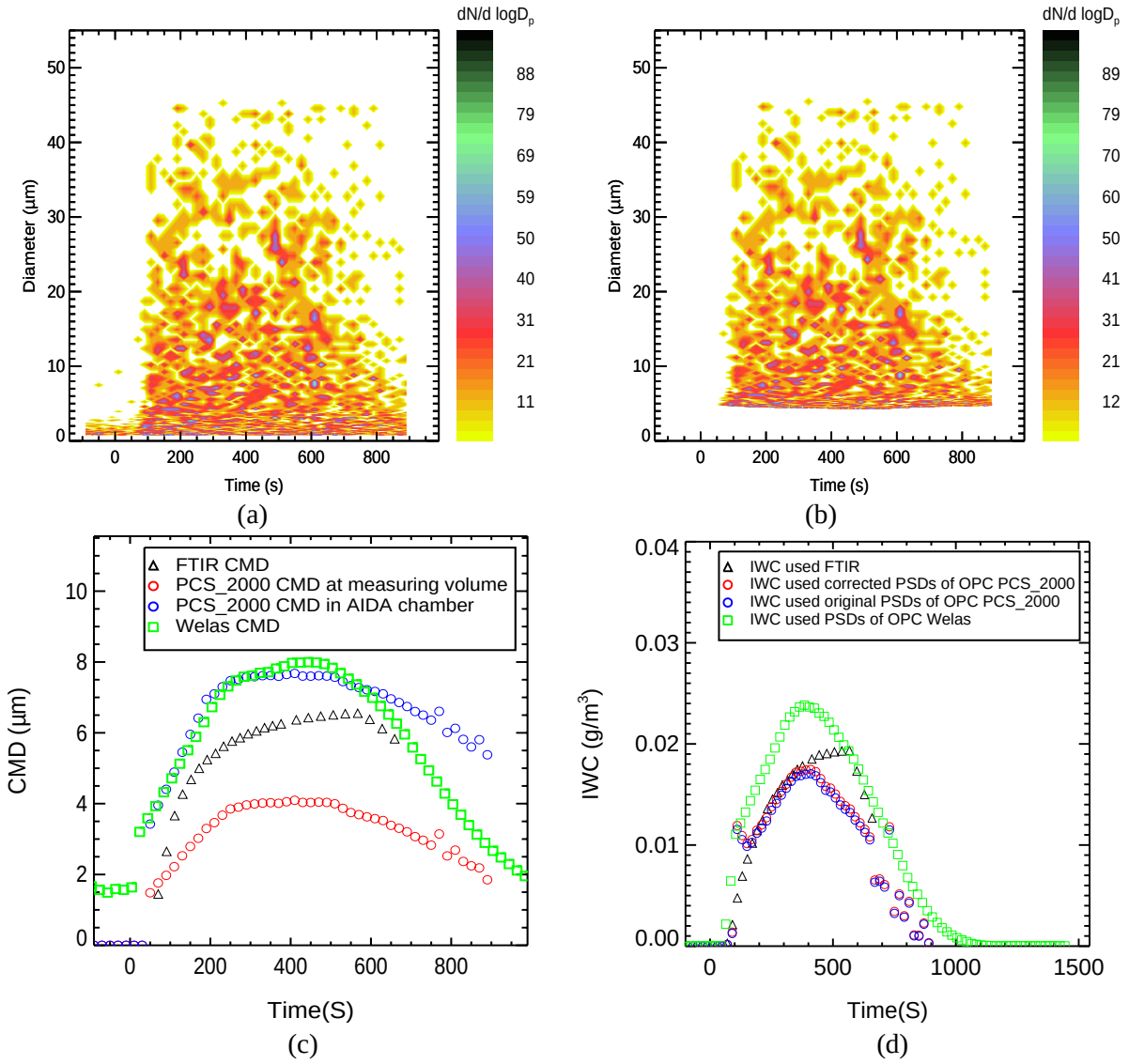

Figure 5.12: (a) and (b) as in Figure 5.11 but for ATD at 223 K, IN03_2.

(c) comparison of uncorrected/corrected count median diameters with FTIR retrievals and with Welas results

(d) uncorrected/corrected IWC, comparison with FTIR retrievals and with Welas results

● Model Calculation at Temperature of 210 K: IN03_7

Uncorrected / corrected size distributions of ice particles that nucleated at 210 K in experiment N° IN03_7 are compared in Figure 5.13. The corrected CMDs agree well with Welas CMDs, while the FTIR retrievals agree better with the uncorrected CMDs. The corrected IWC agrees very well both with the Welas data and the FTIR retrievals, while the uncorrected IWC is slightly too large. Large dust particles which are seen by PSC2000, but do not evaporate, are responsible for this artefact.

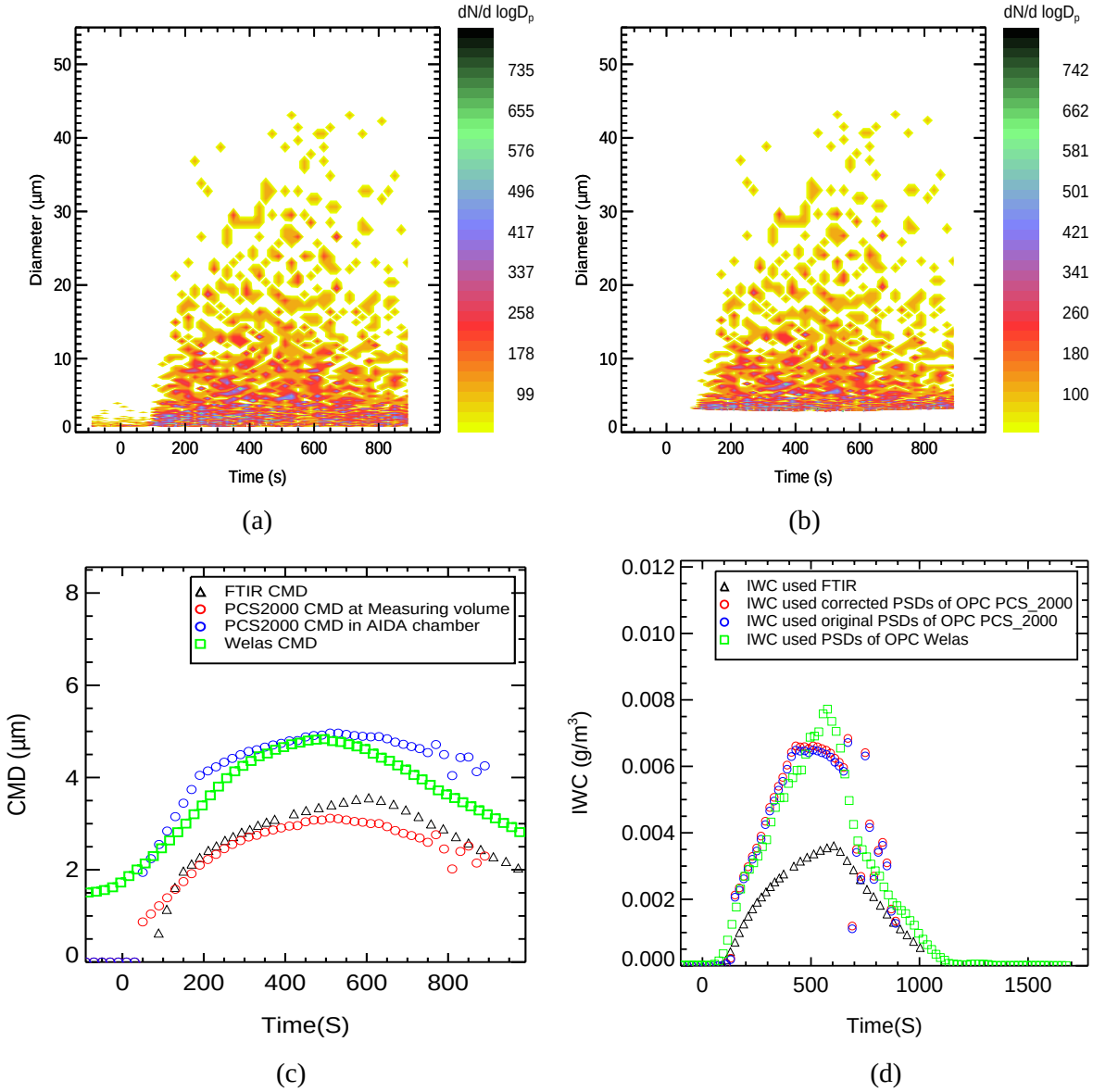

Figure 5.13: (a) - (d) as in Figure 5.12 but for ATD at 210 K, IN03_7

Summary and conclusion:

It is rewarding that the model-based correction of the PSC-2000 data (CMD as well as IWC) improves the agreement with the Welas data. The lesser agreement of the OPC-based CMD with FTIR-retrieved CMD is expected, because both methods assume that the ice crystals are spherical, while this is certainly not the case. The errors introduced by this assumption should be different for different methods. The agreement between the OPC-based and FTIR-retrieved IWC is surprisingly good in two out of three experiments. - A method for estimating maximum ice water yields (IWYs) that can be formed when a rising air parcel exceeds the nucleation threshold will be presented in the next section. We will also discuss the reason for the principal difference between this upper limit and the ice water contents which have been observed in AIDA experiments with ice-coated chamber walls.

5.4.2 Measured Ice Water Content in Artificial Cirrus Clouds

The method presented in section 5.4.1 was applied to determine maximum ice (and liquid water) contents for all AIDA experiments which resulted in ice nucleation on mineral dust as seed aerosol.

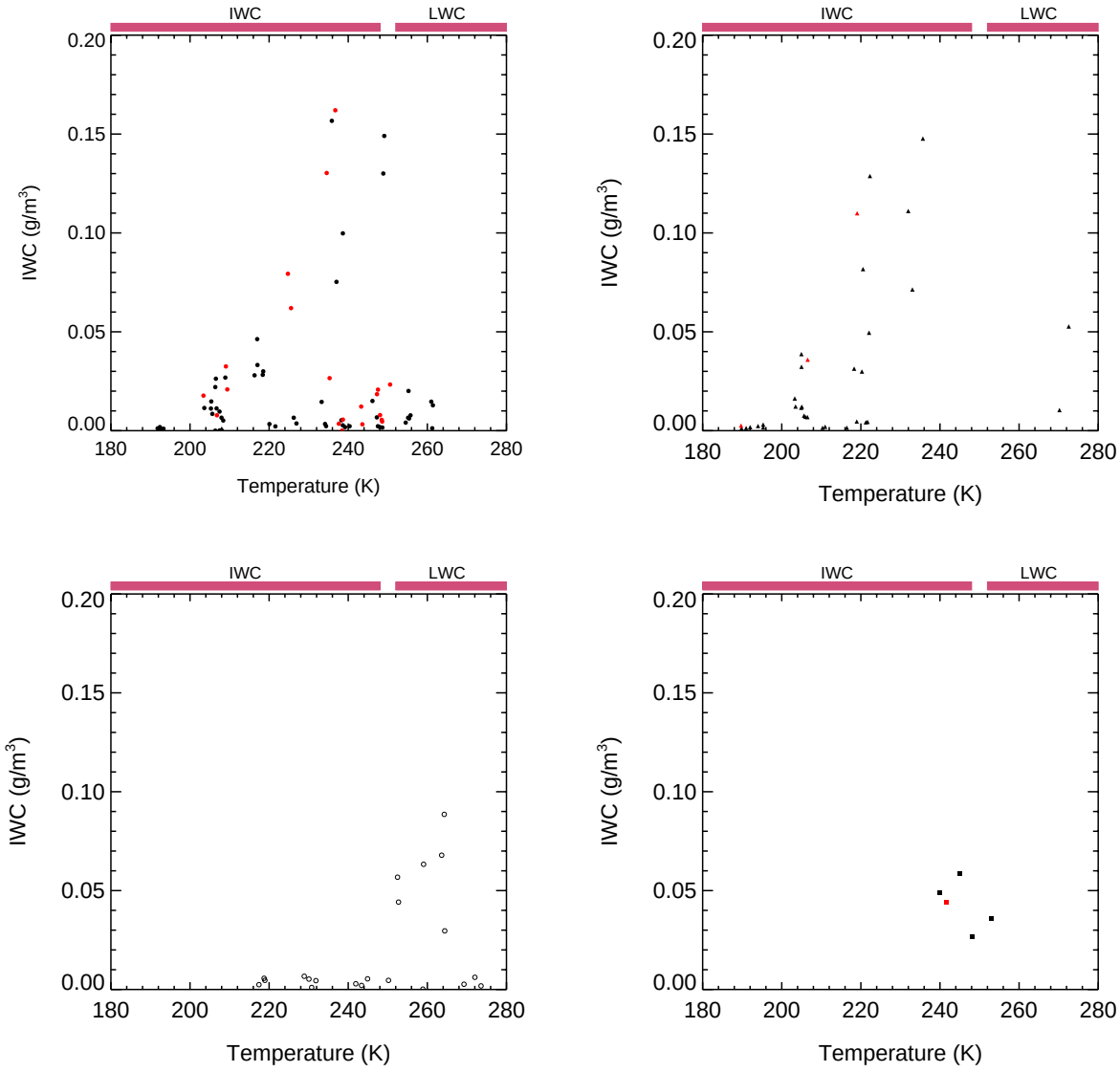

Figure 5.14: Ice water and liquid water contents, respectively, in g m^{-3} for uncoated ATD (●), SD (▲), AD (○), and CD1 (■) and it's mixed with CD2 (■), and for sulphuric acid-coated ATD (●) and SD (▲), as function of gas temperature. The temperature range where liquid or mixed clouds were formed is marked by the red bar "LWC".

Figure 5.14 (left panels) summarises maximum ice water contents in which were determined in AIDA experiments with uncoated ATD, SD, AD, CD1, and with sulphuric acid-coated ATD and SD. The maximum IWCs are plotted as function of the corresponding gas temperature. All data for IN02 and IN03 are based on particle size distributions measured with the optical particle counter PCS-2000 and

are corrected for particle evaporation in the warm sampling line. The data from the ice nucleation campaigns IN04, IN05, IN07 and IN08 are based on measurements with the optical particle counter Welas because the PSC-2000 optical particle counter was not used in these experiments. In that case, no correction was needed for particle evaporation.

As expected because of the exponential temperature dependence of the vapour pressure in equilibrium with either ice or liquid water, the lowest ice water contents, $\leq$ 0.01 g m^{-3}, were determined at temperatures below 210 K. The highest IWC of ca. 0.16 g m^{-3} was observed for ice that nucleated on sulphuric acid-coated ATD at about 235 K. Beyond this general observation, no clear correlation could be found between type of dust, uncoated or coated, and temperature. The most that can be said is that the observed maximum IWCs are in general agreement with upper tropospheric measurements during the INCA aircraft campaign (Gayet et al., 2006; Monier et al., 2006). The reported IWCs were measured in the upper troposphere. Further details will be given in chapter 6. We postpone the presentation of these data and their detailed discussion to chapter 6 where it will be shown that (under thermodynamic equilibrium conditions) the IWC in the atmosphere should be independent of the freezing mechanism (homogeneous freezing of solution droplets, or heterogeneous freezing mechanisms including deposition freezing on various types of mineral dust). The number and the activity of the ice nuclei may, however, affect the number and size of the formed ice crystals, thereby inducing non-equilibrium and sedimentation effects (Monier et al., 2006).

5.4.2.1 Ice Water Yields in AIDA Experiments

To better understand the following more detailed presentation of IWC measurements in ADIA chamber experiments it seems appropriate to discuss briefly how and why the ice water *yield* is limited in the atmosphere, and why this limitation does not apply to AIDA experiments with ice-coated chamber walls. The subject will be resumed and expanded in chapter 6:

The *maximum possible* ice water yield[1] (IWY) in a humid air parcel which expands and cools in the atmosphere can be calculated *exactly*, provided that the mixing ratio of H_2O (= water vapour + ice) is constant (i.e. entrainment does not occur). The calculation yields the true IWY if the air parcel contains a sufficiently large number of active ice nuclei to establish thermodynamic equilibrium between water vapour and ice particles at all times. We use the following nomenclature: Initial state of a cooling air parcel:

[1] A distinction should be made between (maximum) IWC and IWY, because the latter is well defined as the amount of water vapour which can be converted to ice, while the former may be smaller as well as larger as IWY, if ice particles are lost from the considered air parcel by sedimentation, or are added from above.

Air temperature	T_0	[K]
Air pressure	p_0	[Pa]
Water vapour partial pressure	e_0	[Pa]

State of the air at some time *t* when the maximum ice water yield is observed:

Temperature	T_t	[K]
Air pressure	p_t	[Pa]

Let us first assume that no ice is formed while the air expands and the temperature decreases from T_0 to T_t *although* the ice saturation ratio exceeds unity (this may happen when no active ice nuclei are present, or when the relative humidity with respect to ice remains below the threshold relative humidity of the ice nuclei). Under these conditions the mixing ratio of water vapour remains constant during the expansion, and the partial pressure *e* varies with the total pressure:

$$e_t = e_0 \times \frac{p_t}{p_0} \tag{5.2}$$

However, *if* ice nucleation has occurred on extremely efficient ice nuclei, and *if* thermodynamic equilibrium between the ice phase and the vapour phase is established, *then* the partial pressure e_t of the interstitial water vapour must be $e_{ice}(T_t)$, and can be calculated using the expression of Marti and Mauersberger (1993), or the more accurate expression of Murphy and Koop (2005). The difference (e_t - $e_{ice,t}$) is the ice water yield, i.e. the amount of water vapour which has been converted to ice crystals under the given conditions (T_t, p_t). It should be noted that we *do not* stipulate that the temperature change is strictly adiabatic, i.e. we allow diabatic cooling or heating (but no entrainment!). This includes AIDA experiments with uncoated chamber walls. We only need to know the temperature T_t which may or may not be the result of adiabatic cooling.

These considerations define an *upper limit* of the IWY because thermodynamic equilibrium between the ice phase and the vapour phase may *not* be perfectly established due to kinetic limitations, particularly for fast cooling rates, low temperatures, and small number concentrations of active ice nuclei (Gayet et al., 2006; Monier et al., 2006). The maximum ice water yield at equilibrium can be calculated by combining equation (5.2) with the ideal gas law:

$$IWY_{equil} = \frac{m_{ice,max}}{V} = \frac{M_{H_2O}}{R} \frac{e_0 \frac{p_t}{p_0} - e_{ice}(T_t)}{T_t} \tag{5.3}$$

Units:			
	mass	m	[kg]
	Volume	V	[m^3]
	H_2O vapour pressure	*e*	[Pa]
	Temperature	T	[K]
	Molar mass	M	[kg mol^{-1}]
	Universal gas constant	R	8.314 J K^{-1} mol^{-1}

We now consider the special case of ice nucleation in AIDA experiments *with ice-coated chamber walls*. In that case, which does not occur in the real atmosphere, the IWY (once ice particles have been formed) can *exceed* the upper limit given by equation (5.3) since T_{gas} (and therefore the temperature of the airborne ice crystals) drops below T_{wall}. Apart from reducing the effective cooling rate below the adiabatic cooling rate owing to the temperature gradient, a gradient of water vapour is established between the ice film on the walls and the airborne ice particles inside the chamber, i.e.

$$e_{wall} = e_{ice}(T_{wall}) > e_{ice}(T_{gas}) \tag{5.4}$$

The difference in vapour pressure gives rise to diffusion of water vapour from walls into the chamber. Consequently, there is additional ice particle growth at the expense of the ice film, and the IWY_{equil} given by equation (5.3) can be exceeded. The additional growth (and therefore the additional IWY) is kinetically controlled by the diffusion rate of water vapour through the laminary boundary layer separating the ice film from the well-mixed chamber air. The average thickness of the boundary layer, which also controls the exchange of heat between the walls and the chamber air, could be shown in separate AIDA experiments to be in the order of 1 – 2 cm.

Diffusion of water vapour from the ice-coated AIDA walls into the chamber is implemented in the Bunz-model. The excess IWY can also be determined experimentally by measuring the mixing ratio of "total" water, i.e. the sum of interstitial water vapour and ice water which evaporates in the heated sampling line of the chilled mirror hygrometer MBW and/or the FISH instrument, and comparing it with the IWY according to equation (5.3). Examples are presented in Figures 5.15a, and 5.15b. Figures 5.15a and b refer to experiment N° IN02_147 with pristine Arizona Test Dust (cf. Table 5.5a in section 5.6.1). This run exhibited an extremely low threshold relative humidity of ~103% with respect to ice. It was reached 25 s after pump start, cf. Figure 5.15b where the same data as in the left panel of Figure 5.15a are shown, but choosing the experimental time instead of the gas temperature as the independent variable. It can be nicely seen that the interstitial water vapour (blue noisy signal of the TDL hygrometer) practically coincides with the equilibrium vapour pressure of ice at the air temperature. This shows that a sufficiently large number of ice crystals were formed to minimise the kinetically controlled super-saturation of the artificial ice cloud in the chamber (see upper panels in Figure 5.11 for confirmation). The black dashed line in Figure 5.15b reveals that total water always *exceeded* the red line, which represents the dilution of total water for a wall-less system, equation (5.2). The exceedance is due to the additional input of water vapour which evaporates from the ice-covered walls of the AIDA chamber. The noisy orange line in Figure 5.15a (right panel) represents the difference between total water and interstitial water, dashed black and dashed blue lines in Figure 5.15a (left panel) and Figure 5.15b, and therefore the measured ice water content. It is in excellent agreement with the IWC retrieved from FTIR spectra (green squares), and also in good agreement with the blue circles which were calculated from the measured size distribution of the ice crystals. The

black solid line in Figure 5.15a (right panel) is the calculated maximum IWY for a hypothetical "wall-less" chamber. It is exceeded by the measured IWC shortly after freezing onset owing to the contribution of the ice coated AIDA walls.

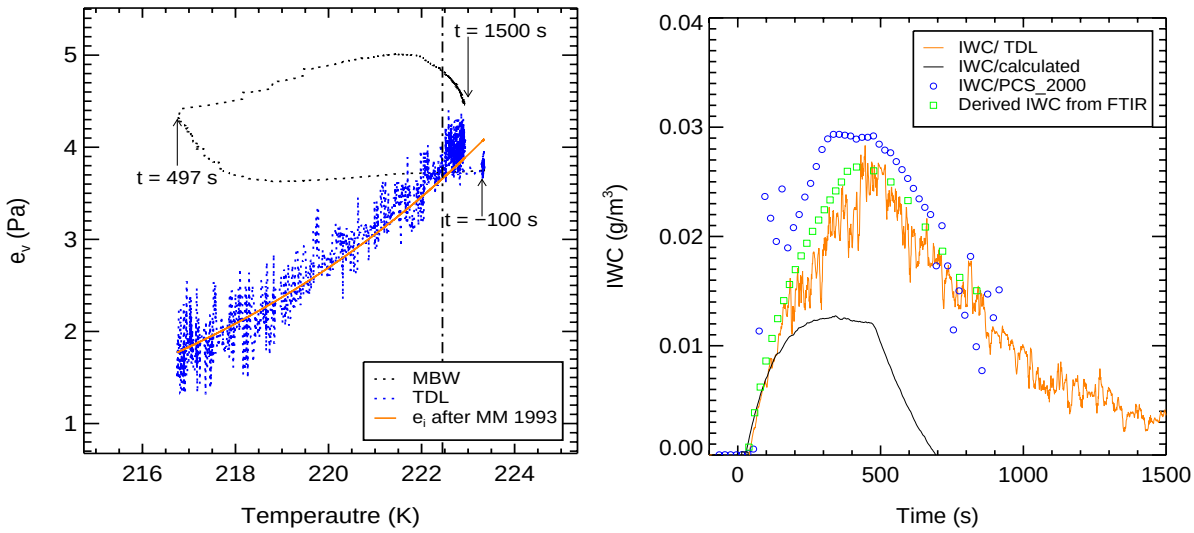

Figure 5.15a: Ice water content (IWC) and theoretical ice water yield (IWY) neglecting ice on the chamber walls, for an experiment with ATD at 223 K, IN02_147. Left panel: interstitial water vapour measured with TDL (dashed blue line), total water measured with the frost point hygrometer (MBW, black dashed line), and calculated water vapour $e_i(T)$ in equilibrium with ice (in orange, after Marti and Mauersberger, 1993). Important experimental times are marked with arrows. Right panel: IWC = difference between MBW and TDL data (noisy orange line), from FTIR retrieval (green squares), and from PCS-2000 data (blue circles); the solid black line shows the *calculated* IWY based on equation (5.3).

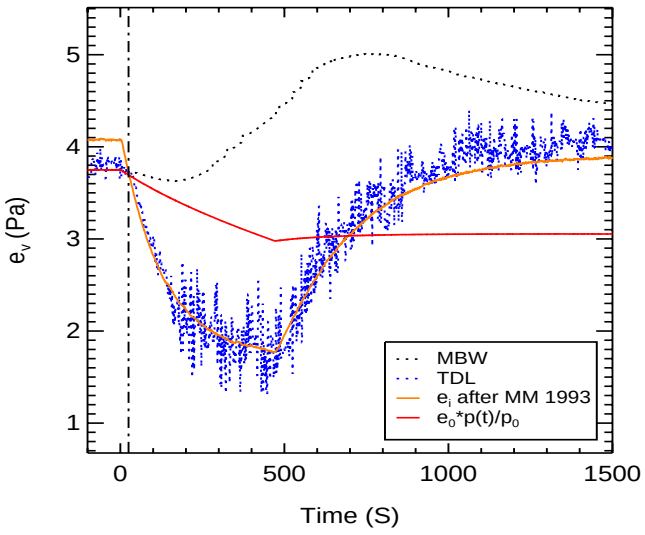

Figure 5.15b:
Same data as shown on the left panel of Figure 5.15a, but plotted as function of experimental time (defined as 0.0 s at pump start). The dilution according to equation (5.2) is included as a red line. The dash-dotted vertical line marks the nucleation threshold. The orange line shows the vapour pressure in equilibrium with the ice phase, calculated from the profile of the gas temperature according to Marti and Mauersberger (1993).

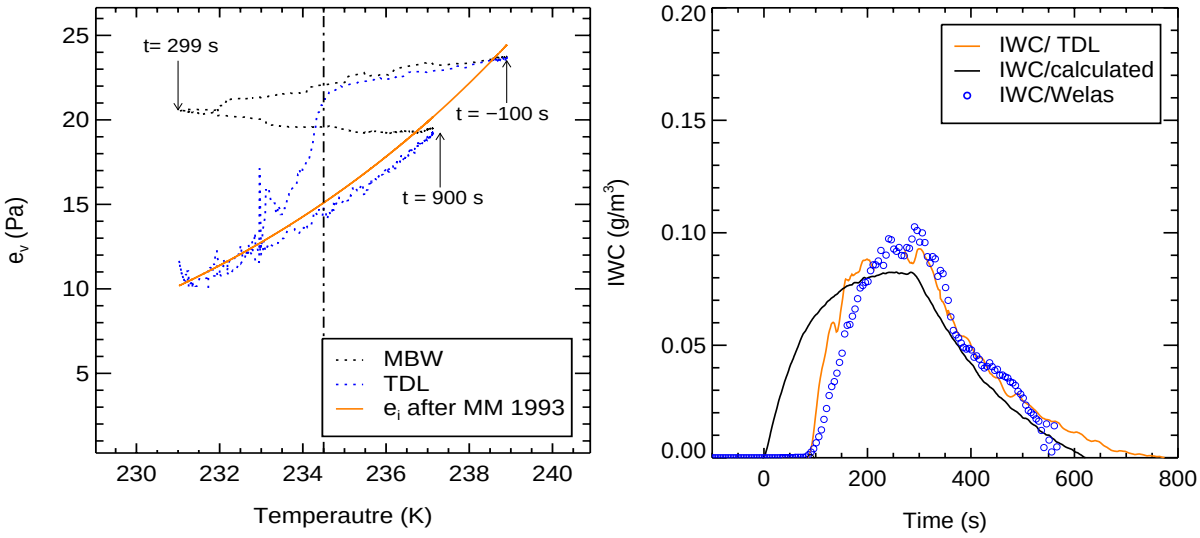

Figure 5.16a: Same as Figure 5.15a, but for experiment N° IN04_36 with Sahara dust as seed aerosol (cf. Table 5.5a). The nucleation threshold in terms of relative humidity with respect to ice is 141%, which is exceeded about 90 s after pump start.

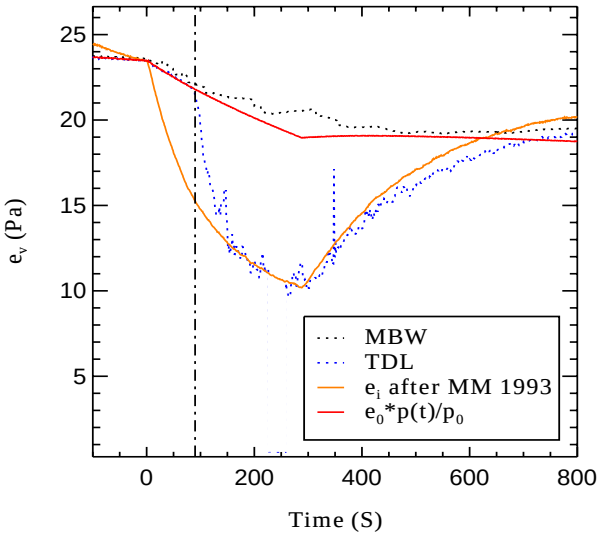

Figure 5.16b:
Same data as shown on the left panel of Figure 5.16a, but plotted as function of experimental time (defined as 0.0 s at pump start). The dilution according to equation (5.2) is included as a red line. The dash-dotted vertical line marks the nucleation threshold. The orange line shows the vapour pressure in equilibrium with the ice phase, calculated from the profile of the gas temperature according to Marti and Mauersberger (1993).

An example of measured and calculated ice water content after the exceedance of a fairly high nucleation threshold of 141% will now be presented. The left panel in Figure 5.15a reveals that the data of the frost point hygrometer MBW and of the TDL system agree within experimental accuracy up to the ice nucleation threshold temperature, which is marked by the dash-dotted vertical line. Thereafter the interstitial water vapour pressure drops suddenly and approaches the equilibrium vapour pressure over ice asymptotically within about one minute, while the total water content which is measured with the frost point hygrometer MBW continues smoothly. The ice water content, orange line in Figure 5.16a (right panel) is deduced from the difference between the BMW and TDL data. It agrees well with the ice water content calculated from the ice particle size distributions which were

measured with the Welas instrument, but lags behind the maximum possible IWY for a hypothetical "wall-less" chamber (black line). However, when ice nucleates ~90 s after pump start, the theoretical IWY is quickly approached *and then exceeded*. The exceedance is again due to the contribution of the ice-coated chamber walls. Note that the exceedance of the maximum IWY for a hypothetical "wall-less" chamber is about twice as large in *absolute* units (though less in relative units, due to kinetic limitations) than in experiment N° IN02_147 (cf. Figure 5.15), which can be understood on the basis of model calculations. Figure 5.16b shows nice agreement between calculated dilution effect (red line) and the measurements of interstitial (TDLAS) and total water (MBW) *before* ice nucleation at t = 90 s. After this time, the interstitial water vapour drops to the equilibrium vapour pressure (orange line), while total water starts to exceed the red line due to the wall effect, as previously explained.

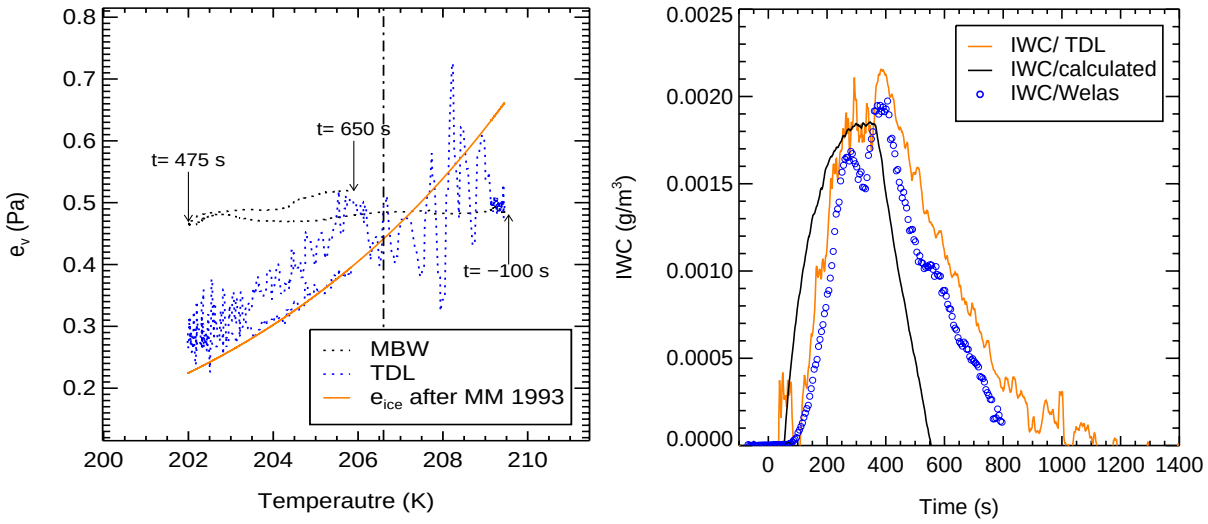

Figure 5.17a: Same as Figure 5.15a, but for experiment N° IN04_11 with Sahara dust as seed particles (cf. Table 5.5a). The nucleation threshold in terms of relative humidity with respect to ice is 141%, which is exceeded about 90 s after pump start.

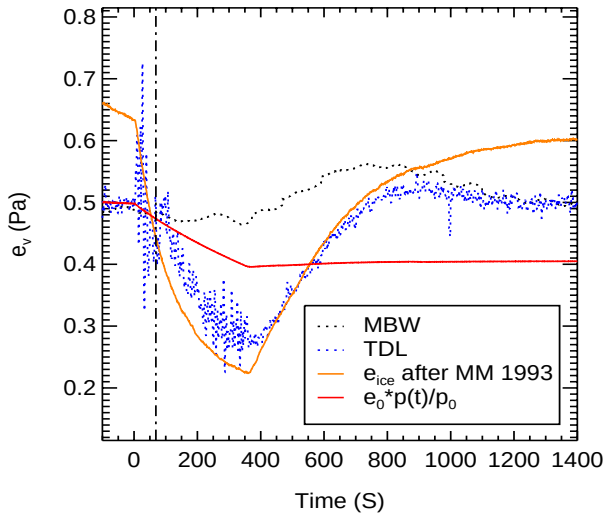

Figure 5.17b:
Same data as shown on the left panel of Figure 5.17a, but plotted as function of experimental time (defined as 0.0 s at pump start). The dilution according to equation (5.2) is included as a red line. The dash-dotted vertical line marks the nucleation threshold. The orange line shows the vapour pressure in equilibrium with the ice phase, calculated from the profile of the gas temperature according to Marti and Mauersberger (1993).

A final example of an AIDA experiment where ice nucleation occurred at a very low temperature of about 206.6 K, i.e. not far from the PSC regime, is presented in Figures 5.17a and b. Although accurate measurements of interstitial water vapour (with the TDLAS system) and of the total water content (with the BMW instrument) are technically very demanding, the results can be understood along the lines which have been explained in the previous examples. However, there are also clear indications of non-equilibrium effects which arise from the limited rate of ice particle growth at these low temperatures.

Summary and conclusion:

We have presented a detailed analysis of three artificial cirrus cloud experiments in AIDA which were carried out with ice-coated chamber walls. The results show that the maximum possible ice water yield (IWY) in naturally forming cirrus, which is obtained by inserting the *observed* cooling rate of an air parcel with a constant total water mixing ratio[2] in equation (5.3), may be significantly exceeded in chamber experiments with identical cooling rates. The reason is that the assumption of a constant total water mixing ratio does not hold in AIDA experiments with ice-coated walls: the ice film provides an additional source of water vapour which is not present in naturally forming cirrus. This must be kept in mind when comparing IWCs measured in natural cirrus (e.g. during the INCA campaign, Gayet et al., 2006) with IWCs of artificial cirrus which were formed in AIDA expansion experiments. Non-equilibrium effects relating to the INCA campaign data have been discussed by Monier et al. (2006).

[2] Note that equation (5.3) depends on the *observed* cooling rate, i.e. it may differ from the adiabatic cooling rate. Diabatic effects (which occur in AIDA experiments when heat flows from the isothermal chamber walls into the cooling gas) are thereby included!

5.5 AIDA Experiments

In recent years, a series of comprehensive laboratory investigations of water cloud and ice cloud seeding processes have been carried out under simulated atmospheric conditions by the team of IMK-AAF. Experiments were carried out in the cloud simulation chamber ADIA which is described in detail in chapter 2, section 2.1 and 2.7. A large number of experiments were done with re-suspended desert dust to study its impact on cloud formation. The samples, which had been collected in Egypt and elsewhere, were used as seed aerosols in experiments covering a wide range of temperatures and super-saturations with respect to ice, thereby simulating different atmospheric cloud regimes. The goal of the investigation was to determine the ice nucleating efficiencies of different desert dust samples (including a commercially available dust sample serving as reference material) in terms of their threshold relative humidities with respect to ice, RH_i, which must be exceeded to induce heterogeneous ice nucleation. Pristine mineral dust aerosols as well as particles coated with sulphuric acid (to simulate ageing during transport in polluted air) were used. For details of the coating procedure see chapter 2 Section 2.5, where the determination of the size distributions with a DMA or an SMPS is also briefly described.

Laboratory experiments at the AIDA chamber have been (and are still being) carried out to simulate two fundamentally different modes of ice nucleation: the first refers to the spontaneous freezing of cloud droplets and haze particles of deliquesced and completely soluble (e.g. ammonium sulphate) particles. This mode of ice nucleation is called homogenous freezing because it involves the formation of ice nuclei in the liquid phase. The second mode involves the surface of solids as nucleation catalyst, and is therefore called heterogeneous freezing. Heterogeneous ice nucleation may occur as deposition freezing on dry particles, or as immersion or condensation freezing at the solid-liquid interface. The latter mode may occur when the aerosol particles are partially soluble. If deliquescence of the soluble coating or cloud droplet activation of an insoluble particle occurs first, the solid inclusion may induce freezing of the aqueous layer on active surface sites above the homogeneous freezing temperature. Both modes are defined and described in more detail in chapter 1, sections 1.3.1 and 1.3.2. This thesis focuses only on the heterogeneous ice nucleation modes of either pristine or sulphuric acid coated mineral dust samples.

The impact of mineral dust on the nucleation of cirrus ice crystals has been studied by numerous investigators. However, little is known about the role of mineral dust as heterogeneous ice nuclei under the conditions of relatively warm mixed clouds on the one hand, and very cold polar stratospheric clouds on the other. This is the reason why experiments were carried out by the AIDA team to simulate heterogeneous ice nucleation on pristine and coated mineral dust aerosols (ATD, SD, CD1, CD2 and AD) over the full range of tropospheric and stratospheric temperatures. For

experiments carried out under cirrus conditions, a comparison is made with a new parameterization of heterogeneous nucleation rates which is based on the widely accepted homogenous freezing rate parameterization for aqueous solution droplets (Koop et al., 2000).

5.5.1 Determination of Accurate Freezing Thresholds (Experimental Time or Relative Humidity)

The ice activation parameters which are determined in these experiments are the gas temperature and the partial pressure of water vapour (or the water vapour mixing ratio and the total pressure, depending on instrumentation) at the time of freezing onset. These parameters yield the threshold relative humidity RH_i, a result which can then be compared with other laboratory studies. The exact time when freezing occurs, a very critical parameter in our studies (see Appendix C), can be determined by in-situ and ex-situ techniques. The optical in-situ techniques used in the AIDA studies were (a) FTIR spectroscopy, whereby the first appearance of the ice phase can be determined from the superposition of a sharp band at about 3000 cm^{-1} on the broader OH band of liquid water near 3250 cm^{-1}, and (b) the detection of depolarised laser light which is back-scattered by ice crystals when they pass through the scattering volume at the centre of the chamber. Both methods, which were simultaneously available in some cases, yield the in-situ freezing time. The appearance time of ice crystals in the AIDA chamber was also determined with one or both of the optical particle counters, PCS-2000 and Welas, and will be called the ex-situ freezing time. It requires that the ice particles grow fast enough, e.g. by the Bergeron-Findeisen process in the mixed cloud regime, to be discriminated against the background signals of the OPCs from large dust particles. Occasionally, a cloud particle imager (CPI) was also available. The instrument can distinguish between spherical droplets and non-spherical ice crystals which may coexist for the duration of an experiment in the mixed cloud regime above -35°C when the relative humidity with respect to water exceeds 100%.

The ex-situ freezing time is defined as the experimental time when the number of particles exceeding the detection threshold of one of the Optical Particles Counter (OPCs) suddenly increases, as shown in Figure 2.13 panel e, cf. section 2.8 in chapter 2. The determination of the in-situ freezing time by means of FTIR extinction spectroscopy depends on the detection threshold for the characteristic narrow band of ice at about 3000 cm^{-1}, as shown on the left panel in Figure 2.9, cf. section 2.6.1 in chapter 2. The time resolution of this technique is furthermore limited by the scan rate of the FTIR spectrometer, which ranged between 40 and 10 s. The sensitivity of the other in-situ technique, which measures the intensity and depolarisation of laser light that is back-scattered by ice crystals, depends strongly on the habit and size of the crystals, as has recently been confirmed by numerical calculations (S. Büttner, 2004). A typical application of the depolarisation method is shown in Figure 2.13 panel d, cf. section 2.8 in chapter 2. The in-situ freezing time based on this technique is

considered very accurate under most conditions. The ex-situ freezing time, based on the count rate of an OPC, is often less accurate for the following reasons: (a) the OPCs suffer from a significant background count rate by mineral dust particles which exceed the detection size threshold. Therefore, detection of the nucleation threshold time requires that the ice particles exceed a critical size to unambiguously exceed the background count rate, (b) ice particles partially evaporate in the warm sampling line of PCS-2000, as discussed in chapter 4 section 4.2.2.

For these reasons, the question which of the freezing onset times determined by the available techniques should be preferred had to be decided on a case-by-case basis. It turns out that the laser depolarisation technique was preferred in most instances. The other methods had to be used when the laser was not working properly, or not at all. Examples for the time resolution of the depolarisation method are presented in Figure 5.18a and b in section 5.5.1.1. We find that the depolarisation ratio remains noisy and changes slowly at the nucleation threshold in Figure 5.18a which refers to experiment 22 IN03 with uncoated ATD, while it becomes less noisy and changes sharply at the freezing threshold in Figure 5.18b, which refers to experiment 3 IN03 with the same type of mineral dust[1]. This makes it sometimes difficult to determine correctly the freezing onset time by looking at the data. It is very important to avoid ambiguities and to get accurate values of the time of freezing onset at which the ice activity parameters must be determined. For this purpose, two different numerical methods are presented in the following sections which help to verify the estimated values of the freezing threshold times.

5.5.1.1 Noise Reduction Based on Numerical Data Filtering

This method applies the CONVOL function (software supplied by IDL) as a numerical filter for 9-point data smoothing to reduce excessive noise of the time-resolved depolarisation data. The filtered data are superimposed as white lines on the noisy raw data in Figure 5.18a and b, third and fourth panels from top. The estimated freezing onset times are clearly less uncertain when based on the smoothed data. As a result, the estimated freezing times (the vertical blue lines in Figure 5.18a and b, third and fourth panels from top) are significantly shifted to the right from their initial estimates which are based on the count rate of the optical particle counter PSC-2000. The drawback of deriving exact nucleation onset times based on this ex-situ technique has been discussed above. Also, the uncertainties δt of the freezing time is significantly reduced.

[1] Note that the depolarisation ratio is expected to *increase* at nucleation threshold, in contrast to Figure 5.15a. However, the increase of the backscattered intensity $I_{\parallel}$ is a clear indication that ice particles have indeed started to grow when the depolarisation signal changes. The initial decrease of the depolarisation ratio is an artefact which is caused by the narrow size distribution of the formed ice crystals: their coherent growth causes the phase function to oscillate at the detection angle of 176°. The geometry differs from similar experiments with the laser technique where the angle is (nearly) exactly 180°.

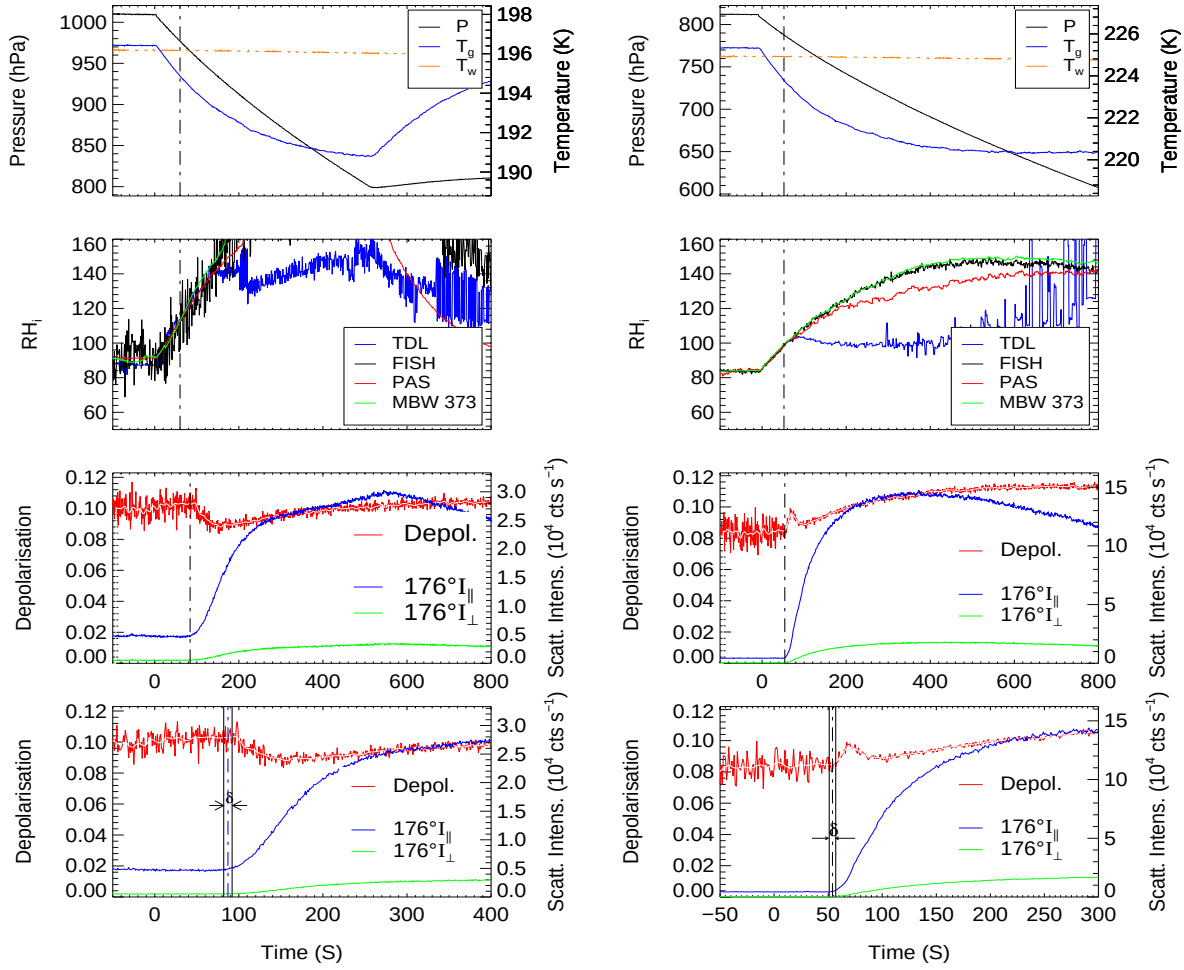

Figure 5.18: Determination of freezing onset times in (a) experiment 22 IN03, (b) experiment 3 IN03, which were carried out with uncoated ATD. The focus is on the depolarisation ratios, third panels from top. The fourth panels show the same data on an expanded time scale.

5.5.1.2 Plotting Calculated Values of the Relative Humidity with Respect to Ice versus Scattered Light Intensity

The component $I_\parallel$ of the laser light back-scattered by particles was used to estimate the time at which freezing occurs since $I_\parallel$ is also very sensitive on the size of the scatterers. This method has the advantage that $I_\parallel$ is less noisy than the depolarisation signal, but unfortunately, this method cannot be used for coated dust particles which may grow by deliquescence before ice is formed, and in the mixed cloud regime where super-cooled liquid droplets may form. The relative humidities which were redundantly determined with different water vapour detectors (TDL, MBW 373, Fish and PAS) during the same experiment are observed to change as soon as the pumps are started. Being functions of the experimental time, they can be used as horizontal axes in plots of the total intensity that was simultaneously measured at a scattering angle of 176°. Such plots are shown in Figure 5.19a and b for

the same experiments as discussed above: 22 IN03 and 3 IN03, respectively. The scattered intensity is approximately constant, i.e. does not depend on the relative humidity before freezing occurs. However, when the critical relative humidity with respect to ice, RH_i, is exceeded the scattered intensity starts to increase more or less suddenly. The method yields directly ranges of threshold relative humidities RH_i and their estimated uncertainties δRH_i, which can be converted into freezing onset times and their errors δt, for direct comparison with the noise reduction method described in section 5.5.1.1.

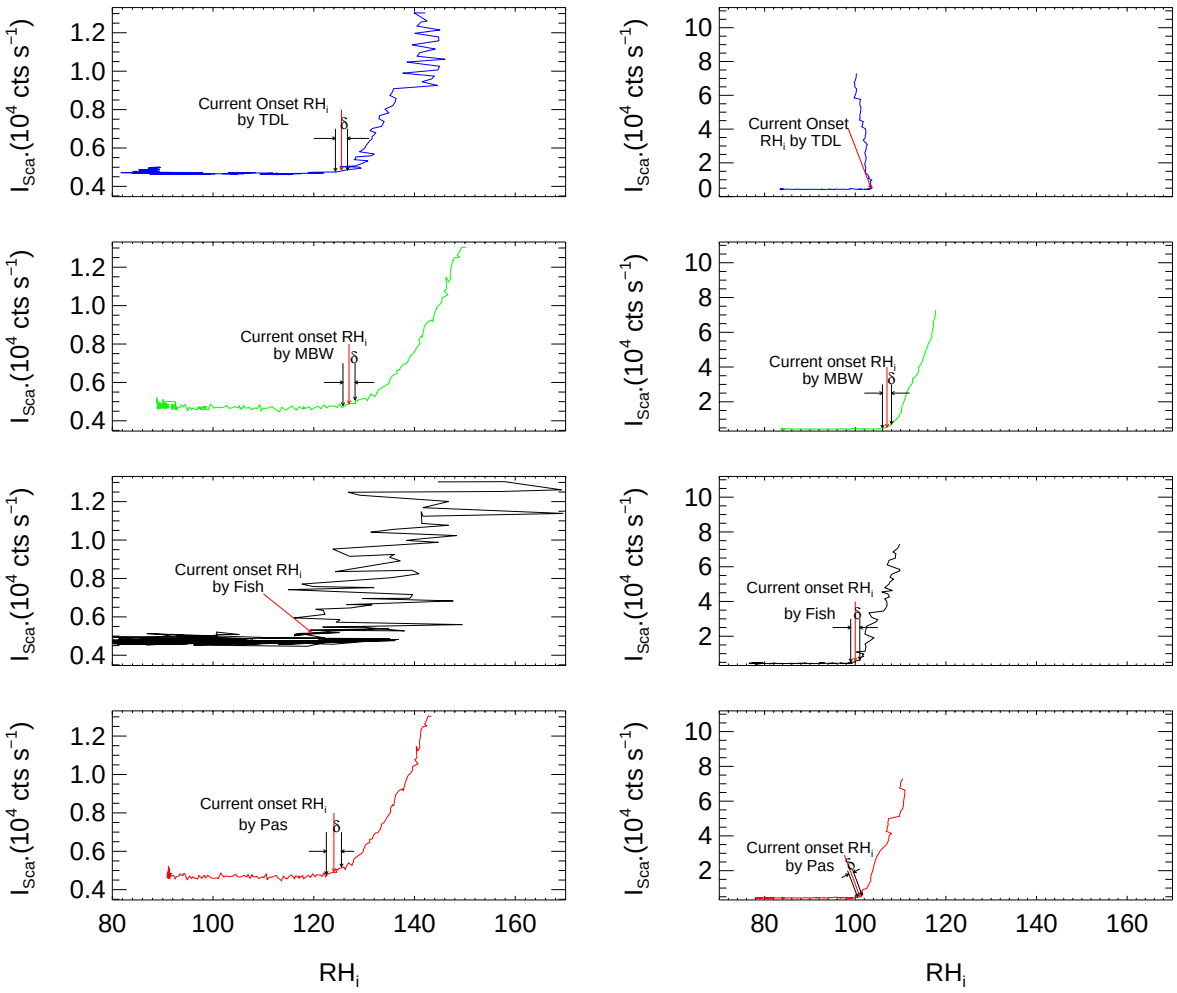

Figure 5.19: Intensity of scattered laser light at a scattering angle of 176°, plotted versus humidities relative to ice, as obtained with different water vapour detectors (TDL, MBW, FISH, and PAS). Red vertical lines mark the determined onset relative humidities HR_i. Also shown are the estimated statistical errors δ of the threshold relative humidities HR_i. Note that the estimated errors δ *do not* include systematic errors of the different water vapour detectors and the uncertainty in T_{gas}, cf. discussion of error propagation in Appendix D;

(a) data from experiment 22 IN03, cf. Table 5.4a

(b) data from experiment 3 IN03, cf. Table 5.4a

This helped us to determine the "best" freezing onset times / threshold relative humidities with respect to ice, and to estimate the associated errors. This strategy was followed to calculate all freezing relative humidities at the freezing thresholds. Examples which are based on the data shown in Figures 5.18 and 5.19 are presented in Table 5.4a and b.

Table 5.4a: Freezing onset times based on different methods, data from experiment 22 IN03

Method	Freezing threshold time	Freezing threshold ($RH_i \pm \delta(RH_i)$)
Depolarisation onset time	87 ± 5 s	(125.3 ± 1.2%)
$I_{\parallel}$ vs. *RH* from TDL	(85 ± 3 s)	125.5 ± 1%
$I_{\parallel}$ vs. *RH* from MBW	(88 ± 3 s)	127.2 ± 1%
$I_{\parallel}$ vs. *RH* from FISH	Data not included because of excessive noise	
$I_{\parallel}$ vs. *RH* from PAS	(89 ± 3 s)	124.5 ± 1.2%
Final choice	85 ± 3 s	125.5 ± 1%

Table 5.4b: Freezing onset times based on different methods, data from experiment 3 IN03

Method	Freezing threshold time	Freezing threshold ($RH_i \pm \delta(RH_i)$)
Depolarisation onset time	54 ± 5 s	(100.3 ± 1.2%)
$I_{\parallel}$ vs. *RH* from TDL	(72 s)	103.5%
$I_{\parallel}$ vs. *RH* from MBW	(87 ± 2 s)	107.0 ± 1%
$I_{\parallel}$ vs. *RH* from FISH	(58 ± 3 s)	100.1 ± 1%
$I_{\parallel}$ vs. *RH* from PAS	(62 ± 3 s)	101.2 ± 0.5%
Final choice	58 ± 3 s	101.0 ± 1%

5.5.1.3 Error Propagation: The Error of the Threshold Relative Humidities RH_i

The errors in the relative humidities RH_i with respect to ice at the freezing thresholds are functions of the errors in all measured physical quantities from which RH_i is calculated: the partial pressure of water vapour, the gas temperature, and the total pressure in the AIDA chamber, each of which has a mean value and an associated error, see equation 2.1 Chapter 2 section 2.2.4. Furthermore, the values of these physical quantities depend on the estimated time of freezing onset which is associated with an uncertainty δt, as explained in the previous sections. The fractional error in the ice relative humidity at freezing threshold can be calculated from the contributing random errors according to the law of error propagation after Gauss (Taylor, 1982). As is shown in Appendix C, it can be calculated numerically from the following equation,

$$\frac{\delta RH_i}{RH_i} = \sqrt{\left(\frac{e_v\left(t_f+\delta t\right)-e_v\left(t_f-\delta t\right)}{2e_v\big|_f}\right)^2 + \left(\frac{\Delta H}{RT^2\big|_{t_f}}\left(0.3+\frac{T\left(t_f+\delta t\right)-T\left(t_f-\delta t\right)}{2}\right)\right)^2} \quad (5.5)$$

where e_v is the *measured* partial pressure of water vapour which depends on the water vapour sensor and is a function of the freezing time t and its error δt. The error of the mean gas temperature is composed of the uncertainty δT = 0.3 K of the temperature sensors, and it is also a function of the time of freezing which is uncertain by δt. ΔH is the enthalpy of sublimation of ice (e.g. from the equation of Marti and Mauersberger, 1993), which is needed to relate the uncertainty of the relative humidity over ice with the uncertainty δT via the Clausius-Clapeyron equation.

5.6 Heterogeneous Ice Nucleation

Threshold relative humidities for heterogeneous ice nucleation on different types of airborne mineral dust (Arizona Test Dust = ATD, Saharan Dust = SD, Asian Dust = AD, Cairo Dust collected at site 1 = CD1, and Cairo Dust collected at site 2 = CD2) were measured in the AIDA chamber, as previously described. Mineral dust from the Sahara and from other deserts has been observed in the atmosphere over a wide range of altitudes, from the ground to the upper troposphere, as was discussed in chapter 1. The role of heterogeneous ice nucleation by mineral dust in cirrus has been studied in the field, using research aircraft and remote sensing techniques, as well as in laboratory experiments, but relatively little is still known about the role of mineral dust in mixed clouds and in the temperature regime of polar stratospheric clouds. This is the reason why the cloud seeding experiments with different mineral dust samples in the AIDA chamber were extended over a very wide range of gas temperatures.

5.6.1 Heterogeneous Ice Nucleation on Arizona Test Dust (ATD)

Threshold relative humidities RH_i for heterogeneous ice nucleation on pristine (i.e. uncoated) as well as sulphuric acid coated Arizona Test Dust aerosols were determined as function of the gas temperature in AIDA chamber experiments covering the range 265 to 190 K. The obtained critical relative humidities RH_i(T) for ice nucleation (and in some instances cloud droplet activation in the mixed cloud regime) on uncoated ATD particles are plotted versus the corresponding gas temperatures T_{nuc} in Figure 5.20. The vertical error bars, which were calculated using equation 5.5, illustrate the random errors due to the combined uncertainties of all contributing experimental parameters. It should be noted that the largest contribution to the fractional error $\delta RH_i/RH_i$ arises from the uncertainty δT = ±0.3 K of the mean gas temperature in the AIDA chamber. This estimated error is the same for all

measurements. We have omitted horizontal error bars for the uncertainties δT_{nuc} of the gas temperature T_{nuc} at freezing threshold, which are in the order of ±0.5 K or less. The sloping black line denotes liquid water saturation. The green line, which is based on the parameterisation of Koop et al. (2000), see chapter 6 for further details, represents the threshold relative humidity for homogeneous freezing of aqueous solution droplets with diameters of 0.5 µm. This is an important process at temperatures colder than about 235 K where solution droplets freeze homogeneously *before* cloud droplet activation occurs at the water saturation line. The Koop mechanism is believed to be instrumental in the formation of cirrus clouds in the absence of solid or partially solid ice nuclei. Above ~237 K, ice formation by homogeneous freezing of cloud droplets is not feasible (Benz et al., 2005). The existence of mixed clouds (i.e. clouds consisting of both supercooled water drops and ice crystals) well above this temperature limit is therefore generally attributed to heterogeneous ice nucleation by immersion freezing or condensation freezing, which would imply that water saturation is reached before ice nucleation occurs. Deposition nucleation may also occur in this regime.

The measured threshold relative humidities for ATD, Figure 5.20, do not evenly cover the studied temperature range from 265 to 190 K. This motivated us to group the complete data set into several clusters, each cluster being composed of data which cover a range of ±1.5 K around the mean cluster temperature $\overline{T_{nuc}}$. Weighted means of the critical ice relative humidities RH_i ($\overline{T_{nuc}}$) were calculated for the clusters and plotted versus the corresponding weighted mean gas temperatures. The obtained cluster averages are shown in Figure 5.20. The error bars of the cluster averages were calculated using the law of error propagation after Gauss (Taylor, 1982). The detailed data sets for ice nucleation on pristine and coated ATD aerosol particles are listed in Tables 5.5a and b, respectively.

- **Mixed Cloud Condition**

The mixed cloud regime is marked by a red bar on top of Figure 5.20a and b. It is generally assumed that, when ice occurs in this regime, it is due either to immersion or to condensation freezing, i.e. occurs by heterogeneous ice nucleation in the aqueous phase. This implies for insoluble particles that water saturation must be exceeded before either of these heterogeneous mechanisms can take effect. However, the AIDA results in Figure 5.20a and b seem to indicate that heterogeneous ice nucleation on *uncoated, i.e. insoluble* ATD occurred well *below* the water saturation line. This would imply that deposition freezing is operative: the data seem to indicate that deposition freezing occurred very close to ice saturation above 260 K. The threshold relative humidities RH_i in the mixed cloud regime seem to scatter around a line which is shifted ca. 10% below the water saturation line. Formal extrapolation to higher temperatures would imply that ice nucleation on ATD above 265 K occurs below ice saturation, i.e. under sub-saturated conditions. However, this is thermodynamically impossible, and

merely shows that the relatively large vertical error bars are realistic, and must be taken into account before drawing far-reaching conclusions.

To distinguish ice crystals from supercooled droplets in the mixed cloud regime, measurements with the Cloud Particle Imager (CPI) were consulted. The CPI yields number concentrations of spherical particles (droplets) and non-spherical particles (ice crystals) as function of experiment time. Connolly et al. (2004) had classified the particle images into seven classes: the first class "sph" represents spherical particles, i.e. supercooled cloud droplets. The other classes "col, plt, ros, bud, sir and bir" represent different crystal habits: columnar ice crystals, plate crystals, rosettes, budding rosettes, small irregular crystals < 200 µm, and large irregular crystals > 200 µm, respectively. For our purposes it is appropriate to distinguish only between spherical particles = super-cooled cloud droplets on the one hand, and ice crystals (i.e. the sum of all non-spherical habits) on the other. The obtained number concentrations of ice crystals and cloud droplets were plotted versus the experiment time at different gas temperatures where mixed clouds can be formed. The results are presented in Figures 5.22 – 5.25, in the order of decreasing temperatures.

We found that ice particle initiation occurs in three temperature regimes:

(1) The first regime above 260 K is represented by experiments No. 103 and 87. These are marked in blue in Table 5.5a. The CPI data in Figure 5.22 show that a very small fraction of ice particles appeared almost simultaneously with a much larger number of cloud droplets. The ice fraction in experiment No. 103 was larger than in experiment No. 87 which represents the lower temperature of 261 K. We speculate that these ice particles are due to condensation freezing on a very active sub-set of dust particles. However, this is only possible if water saturation was exceeded, which implies that the corresponding error bars in Figure 5.20a are too small, and should overlap the water saturation line. Note that the ratio of supercooled droplets and ice crystals does not change significantly as function of time. The predominance of supercooled cloud droplets in this regime was confirmed by FTIR spectroscopy.

(2) The second regime from 260 to 250 K is marked red in Table 5.5a. It is represented by experiments No. 86 to 83. As shown in Figure 5.23, droplets and ice crystals appeared almost simultaneously, and the initial number of supercooled droplets still exceeded the number of ice particles. However, the ice crystal number continued to increase, while the number of super-cooled droplets decreased. We therefore conclude that immersion freezing is important in this temperature range, which implies that ice nucleation did *not* occur below water saturation was exceeded. It is likely that the disappearance rate of the super-cooled droplets was further enhanced by the Bergeron-Findeisen process.

(3) In the coldest part of the mixed-cloud regime below 250 K, marked green in Table 5.5a, CPI data shown in Figures 5.24 and 5.25, the ice crystals exceeded the number of particles classified as "spherical" by the CPI at all times, which implies that deposition freezing did indeed occur before water saturation was reached and a few super-cooled droplets were formed on the remaining dust particles at a late time. Note that the time resolution of the CPI for nucleation threshold measurements is rather poor because both ice crystals and supercooled droplets must first grow to significant sizes to be detected and classified according to their habits. Therefore it is likely that the depolarization-based low RH_i thresholds in Figure 5.20a and b, significantly below the water saturation line, are real. - The predominance of ice particles in this regime was confirmed by FTIR spectroscopy.

Figures 5.21a and b show similar data for ATD which was coated with sulphuric acid before being introduced in the AIDA chamber. The experimental results with coated particles lead to the conclusion that the differences between the freezing relative humidities RH_i of uncoated and coated ATD are not significant in the mixed cloud regime.

- **Cirrus Cloud Condition**

The cirrus cloud regime, which is marked by a red bar at the top of Figure 5.20a and b, spans temperatures between the homogeneous freezing threshold of pure water clouds at about 235 and the polar stratospheric regime which extends below 200 K. It is generally assumed that cirrus ice is most frequently formed by homogeneous freezing of solution droplets, a process which is only controlled by the water activity and the temperature (Koop et al., 2000). However, AIDA chamber experiments show that heterogeneous ice nucleation by the deposition mode on uncoated ATD in the cirrus cloud regime already occurs at threshold relative humidities RH_i between 105 and 110%, while homogeneous freezing of aqueous solution droplets would require relative humidities between 145 and nearly 160% with respect to ice in the same regime. Although the range between 225 and 235 K is not covered by ATD data, the transition from very low threshold relative humidities RH_i in the cirrus regime to threshold relative humidities RH_i of ca. 125% at the lower bound of the mixed cloud temperature regime seems to be fairly abrupt.

In contrast to the mixed cloud regime, Figures 5.21a and b show threshold relative humidities for sulphuric acid coated ATD particles in the cirrus regime which are higher than those of uncoated ATD, closer to but still significantly below the freezing threshold of aqueous solution droplets. This implies that the observed threshold relative humidities of sulphuric acid coated ATD are due to the following mechanism: (a) dilution of the sulphuric acid coating as the relative humidity increases, (b) immersion freezing of the dilute sulphuric acid coating below its *homogeneous* freezing threshold.

● Polar Stratospheric Cloud (PSC) Conditions

Figure 5.20a shows a cluster of results from three ice nucleation experiments with pristine (uncoated) ATD at 193 K, which are combined into one data point in Figure 5.20b. 193 K is at the upper bound of the temperature range which is marked as the "PSC" regime by the red bar on top of Figure 5.20. We find that the threshold relative humidity RH_i increases systematically from ca. 105 % and 108 % T at 223 and 208 K in the cirrus regime to ca. 125 % at 193 K at the upper bound of the PSC regime. Note that the temperature trend is significant, as indicated by the reduced error bars of the clustered data in Figure 5.20b. However, these threshold relative humidities are altogether much lower than the homogeneous freezing thresholds for 0.5 μm solution droplets according to Koop et al. (2000), green lines in the figures, which increase somewhat less in the same temperature range from 220 K to 193 K. These results underpin the unusually high ice nucleating ability of Arizona Test Dust which is often used as a surrogate for real desert dust in laboratory experiments. – In the colder PSC regime, no AIDA chamber experiments are available with sulphuric acid coated ATD particles.

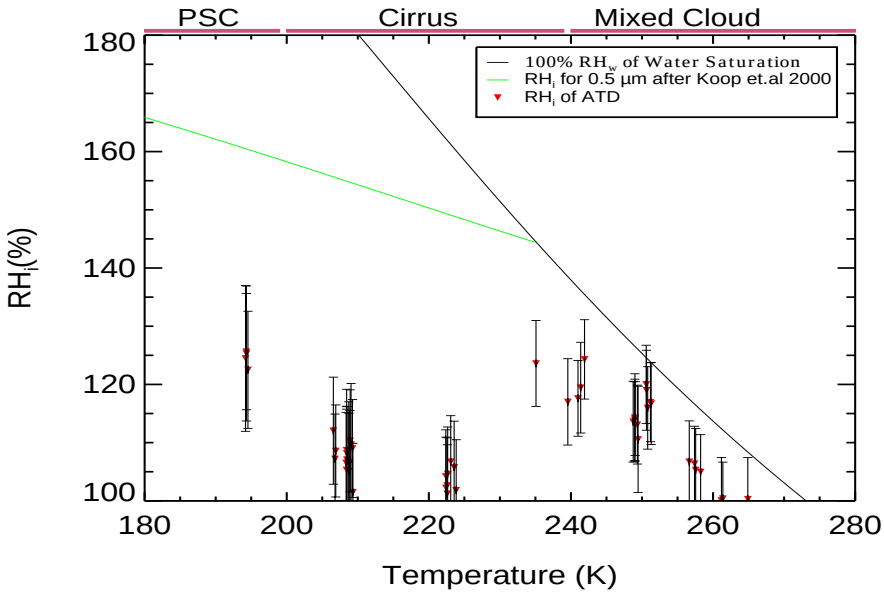

Figure 5.20a: Plot showing all threshold relative humidities RH_i (T) for heterogeneous ice nucleation on pristine Arizona Test Dust (ATD) which were measured in AIDA chamber experiments. The data (▼) include error bars $\pm\delta RH_i$ which are based on equation 5.2. The green line (—) denotes the freezing threshold for aqueous solution droplets of 0.5 µm diameter, following the work of Koop et al. (2000). The black line (—) represents liquid water saturation. The red horizontal bars at the top indicate temperature regimes where mixed, cirrus, and polar stratospheric clouds are predominantly observed.

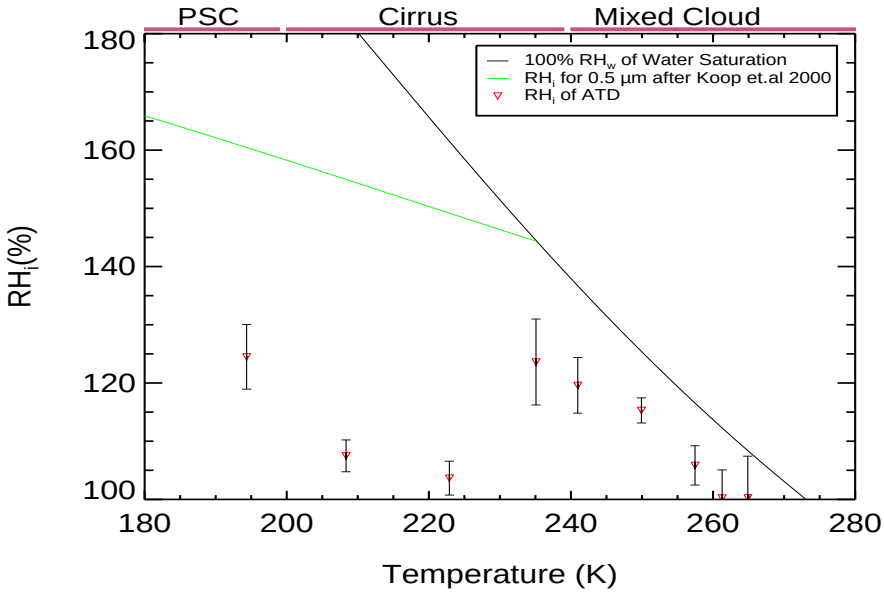

Figure 5.20b: Threshold relative humidities for ice nucleation on uncoated Arizona Test Dust, based on the complete data set which was shown in Figure 5.20a, but representing weighted mean nucleation thresholds for groups of data clustering around mean threshold temperatures $\overline{T_{nuc}}$. See text for details.

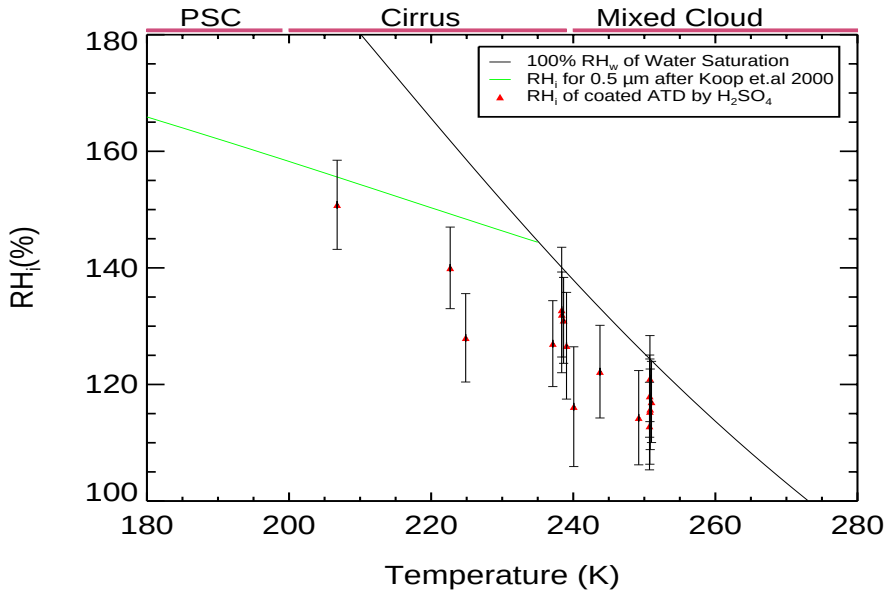

Figure 5.21a: Same as Figure 5.20a, but for sulphuric acid coated ATD.

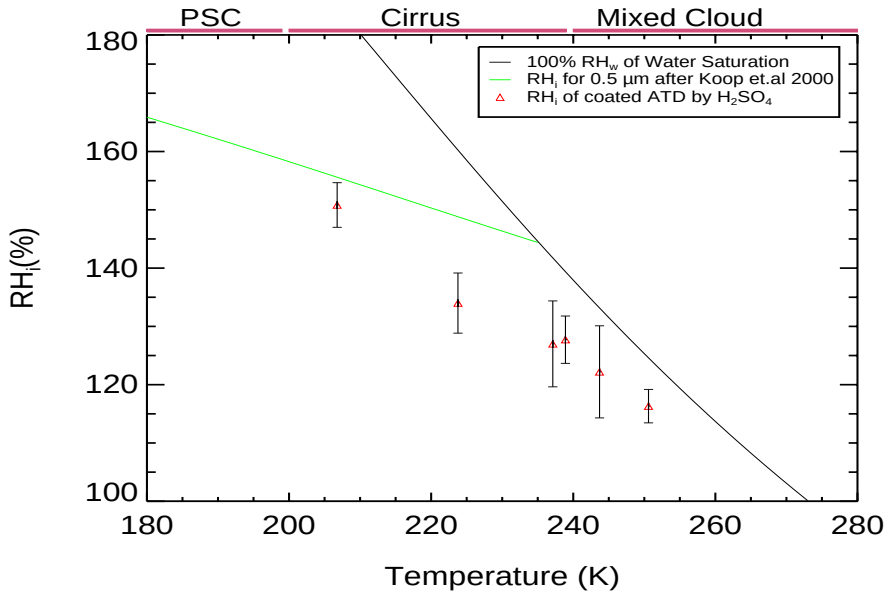

Figure 5.21b: Same as Figure 5.20b, but for sulphuric acid coated ATD.

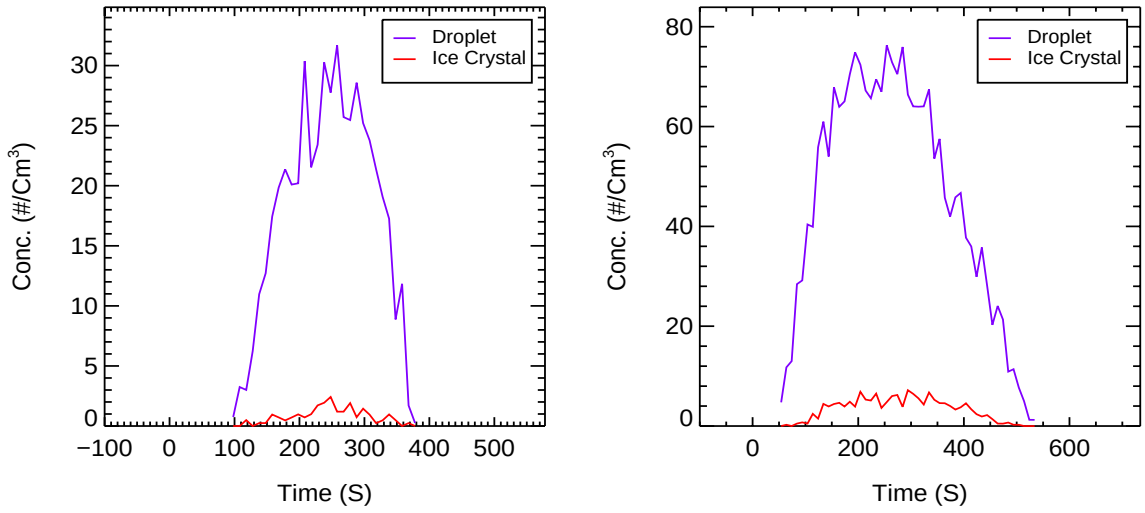

Figure 5.22: CPI data for ATD experiments IN02_103 and IN02_87 at 265 and 261 K, respectively. Super-cooled droplets are shown in blue, ice crystals in red.

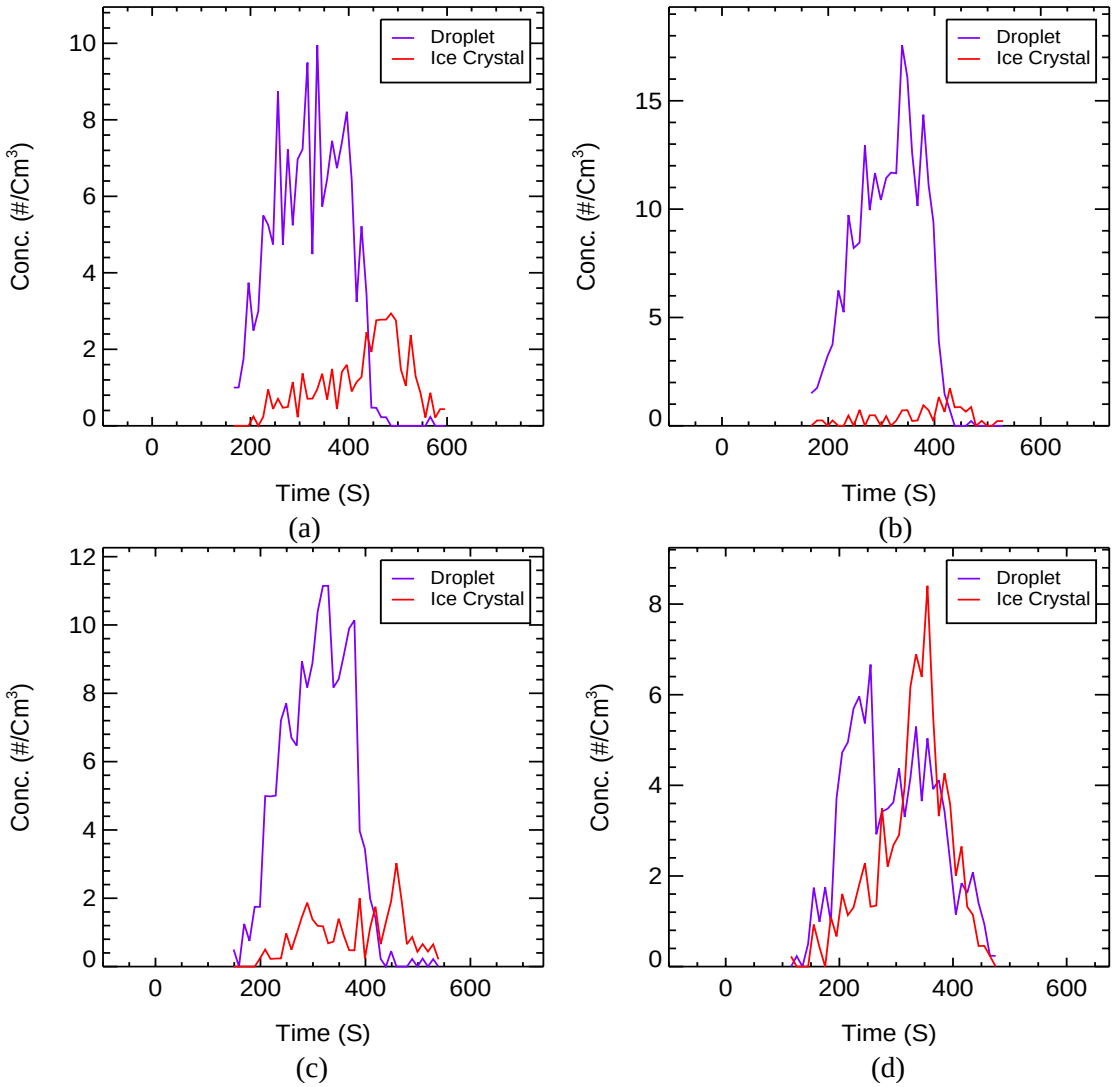

Figure 5.23: Same as Figure (5.22), but for the following experiment numbers:

(a) IN02 N° 86 at 258 K (b) IN02 N° 85 at 257.5 K

(c) IN02 N° 84 at 257.5 K (d) IN02 N° 83 at 256.5 K

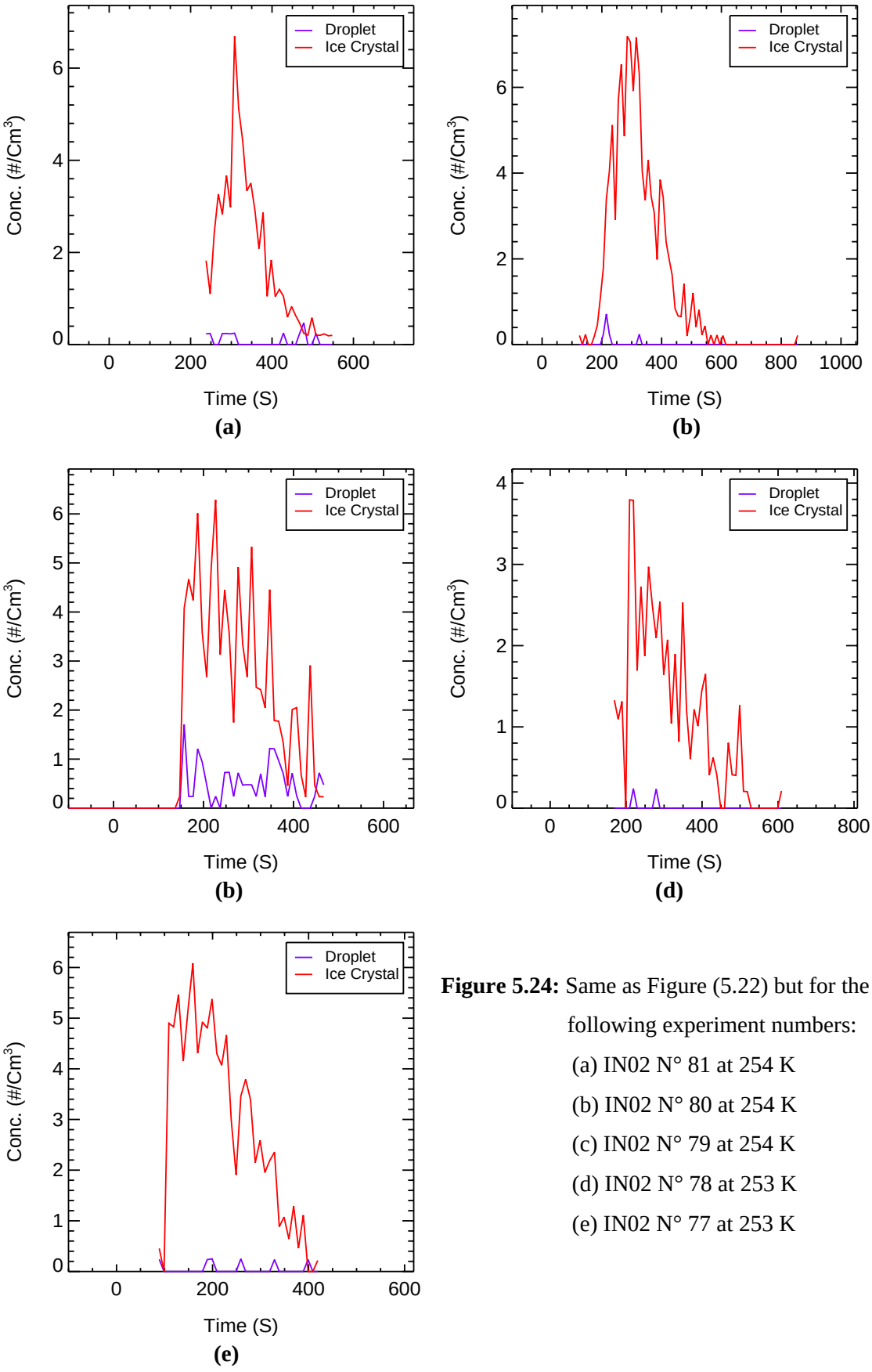

Figure 5.24: Same as Figure (5.22) but for the following experiment numbers:

(a) IN02 N° 81 at 254 K

(b) IN02 N° 80 at 254 K

(c) IN02 N° 79 at 254 K

(d) IN02 N° 78 at 253 K

(e) IN02 N° 77 at 253 K

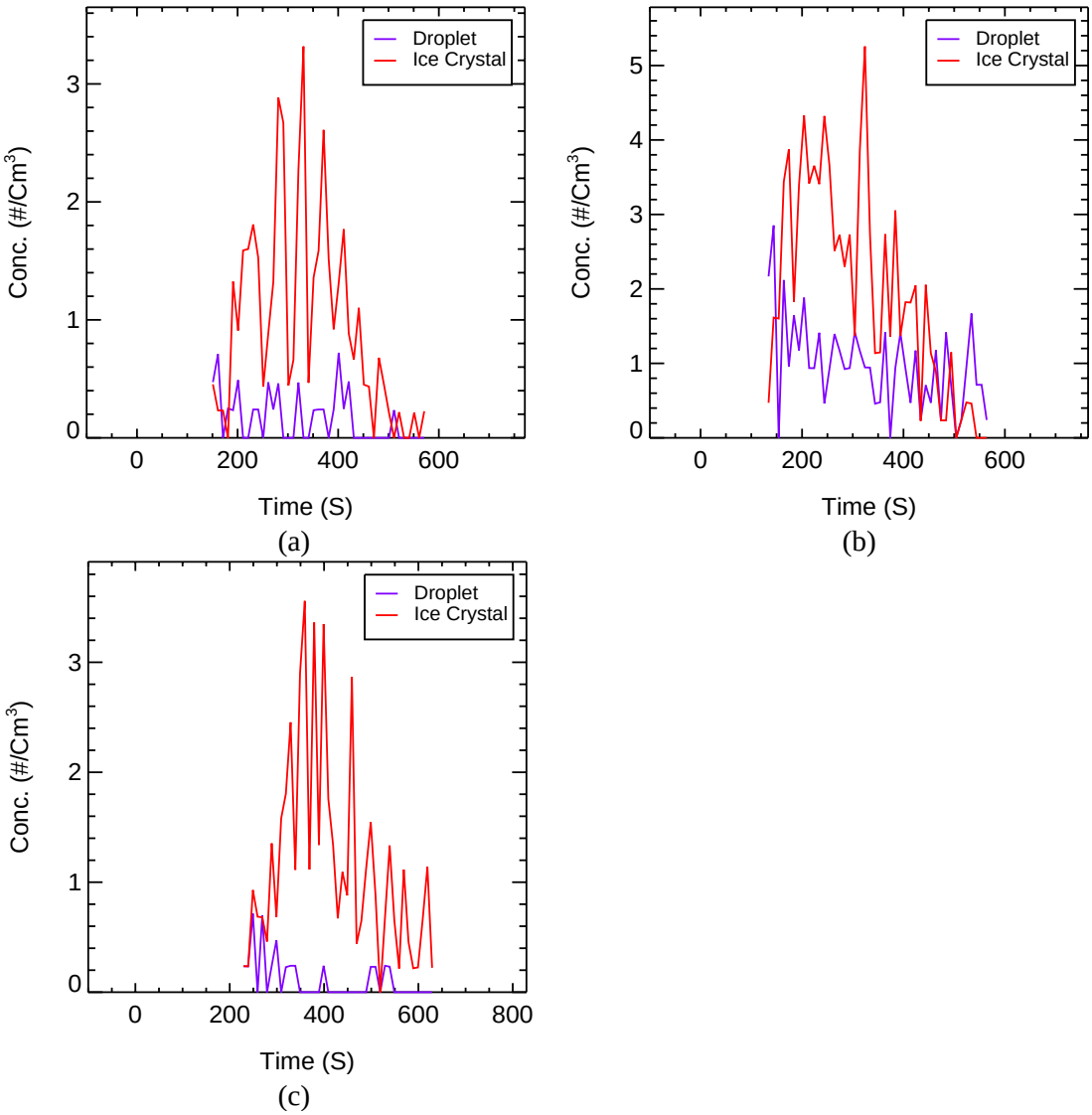

Figure 5.25: Same as Figure (5.22) but for the following experiment numbers:

(a) IN02 N° 75 at 246 K (b) IN02 N° 74 at 246 K

(c) IN02 N° 73 at 246 K

Table 5.5a: Ice nucleation parameters for AIDA experiments with uncoated ATD: p_0, p_{nuc} = pressure (in hPa) at pump start and at nucleation threshold; T_0, T_{nuc} = gas temperature at pump start and at nucleation threshold; t_{nuc} = time at nucleation threshold (in seconds) relative to $t = 0$ at pump start, index *d* or *w* indicates that freezing time is based on depolarization or Welas data, respectively; RH_i = threshold relative humidity (%) with respect to ice, the letters T, M, F, P indicate that RH_i is based on TDL, MBW, FISH, or PAS data; *dp/dt* = rate of pressure change (hPa min^{-1}) at nucleation threshold; *dT/dt* = rate of temperature change (K min^{-1}) at the nucleation threshold. Cluster averages are overlined (see text for definition of clusters). See text for the colour code.

Exp.-N°	p_O	T_O	$t_{nuc} \pm \delta t$	p_{nuc}	T_{nuc}	$\overline{T_{nuc}}$	$RH_i \pm \delta RH_i$	$\overline{RH_i}$	*dp/dt*	*dT/dt*
IN02_103	1009.9	268.9	75±5 d	945.4	264.9	264.9	100.3±7.1 M	100.3±7.1	-48.7	-2.5
IN02_ 87	1004.3	262.6	31±5 d	980.3	261.2	261.2	100.1±7.3 M	100.1±4.8	-48.7	-2.8
IN02_86	1005.1	262.3	104±5 d	935.3	258.3		104.9±6.3 M		-36.6	-1.5
IN02_85	1004.3	262.1	123±10 d	925.0	257.6	257.4	105.3±7.1 M	105.8±3.4	-33.9	-1.1
IN02_84	1004.4	261.9	120±5 d	926.4	257.4		106.4±6.4 M		-35.6	-1.0
IN02_83	1005.3	261.5	111±5 d	921.4	256.6		106.7±7.0 T		-39.9	-1.7
IN08_23	1022.0	253.8	80±5 w	966.3	250.3		120.3±7.9 T		-34.0	-1.5
IN08_24	1022.1	253.8	80 ±5 w	963.9	250.6		119.4± 7.9 T		-35.0	-1.6
IN02_77	1007.9	253.8	82±5 d	932.4	249.4		110.5±7.9 M		-49.0	-2.5
IN02_79	1007.4	254.0	135±5 d	922.9	249.3	249.0	113.1±6.7 M	114.9±2.4	-81.9	-3.8
IN02_80	1007.6	254.0	190±5 d	907.3	249.0		114.1±7.9 M		-25.8	-0.8
IN02_81	1008.0	254.0	220±5 d	902.9	248.9		113.9±7.9 F		-23.6	-0.6
IN02_78	1007.5	253.9	155±5 d	910.8	248.7		113.5±7.9 M		-31.7	-1.1
IN02_74	1005.4	246.0	114±5 d	923.6	241.3		119.5±7.7 M		-83.8	-3.0
IN02_75	1006.5	246.2	125±5 d	927.9	241.9	241.4	124.3±6.8 T	121.9±3.6	-31.8	-1.3
IN02_73	1005.6	246.0	192±5 d	907.6	240.9		117.6±8.3 T		-26.8	-0.7
IN08_3	1010.4	242.6	95±5 w	950.4	239.5	239.5	117.3± 8.3 T	117.3±8.3	-32.7	-1.6
IN03_1	1006.3	225.7	42±5 d	970.8	223.8		101.8±8.6 M		-47.9	-2.8
IN03_2	1006.3	225.7	78±5 d	966.4	223.6		105.7±7.9 M		-25.7	-1.4
IN03_3	806.9	225.7	87±5 d	775.7	223.1		101.2±7.9 P		-19.4	-1.1
IN02_149	1003.5	223.5	31±5 d	988.4	222.6	222.8	104.6±8.0 P	102.9±2.9	-28.7	-1.8
IN02_148	1003.6	223.4	28±5 d	988.0	222.6		101.2±8.3 M		-35.4	-2.1
IN02_147	1004.1	223.3	25±5 d	989.2	222.6		102.7±8.1 P		-35.9	-2.0
IN02_151	799.7	223.3	25±5 d	785.8	222.4		102.2±8.7 P		-37.7	-2.7
IN02_150	1003.7	223.5	39±5 d	984.2	222.4		104.2±7.9 M		-29.8	-1.8
IN03_4	991.1	211.1	49±10 d	951.6	209.1		109.6±10.4F		-44.1	-2.3
IN05_30	992.8	210.5	80±10 w	961.5	208.9		110.3±8.7 M		-22.2	-1.1
IN05_29	992.9	210.2	65±10 w	966.6	208.9		106.6±8.8 M		-23.1	-1.1
IN03_6	1004.2	210.6	78±15 d	967.5	208.7		105.2±9.9 M		-26.4	-1.2
IN03_5	1004.8	210.8	50±10 d	965.8	208.7		106.4±10.6 T		-44.7	-2.3
IN03_7	1004.1	210.5	84±10 d	964.6	208.5		107.1±9.0 M		-25.0	-1.2
IN05_31	989.0	211.1	150±10	933.7	208.5	208.2	108.2±8.0 M	107.8±2.6	-17.9	-0.6
IN05_28	992.4	209.8	40±10w	964.7	208.4		105.3±10.4 M		-36.4	-2.1
IN05_33	991.0	210.5	265±10w	899.5	206.9		108.6±7.9 M		-15.2	-0.3
IN05_34	990.0	210.5	280±10w	894.6	206.8		107.2±7.7 M		-15.2	-0.3
IN07_1	1008.3	210.3	40±5 w	987.1	209.2		109.0± 10.1 T		-30.9	-1.6
IN07_2	1004.6	210.3	40±5 w	982.7	209.3		101.4± 10.1T		-31.2	-1.6
IN03_24	1011.3	196.6	125±20 d	965.1	194.5		122.5±10.0 T		-19.3	-0.7
IN03_22	1008.8	196.4	84±20 d	964.7	194.3	194.3	125.3±11.5 T	124.4±5.5	-29.4	-1.3
IN03_23	1009.9	196.5	105±15 d	961.8	194.3		125.6±9.9 M		-25.6	-1.0
IN03_21	1013.1	196.4	73±20 d	968.5	194.2		124.5±12.5 M		-36.2	-1.6

Table 5.5 b: As in Table 5.5a but for ATD with sulphuric acid coating

IN02_132	1001.6	254.8	111±5 D	932.8	250.8		115.7±6.9 T		-33.4	-1.3
IN08_26	1018.9	254.0	75 ± 5 d	961.9	250.7		121.2± 7.3T		-33.9	-1.7
IN08_27	1018.9	254.1	80±5 d	966.4	251.01		117.3± 6.9 T		-35.2	-1.8
IN02_133	1002.3	255.1	131±10d	923.6	250.7		112.9±7.5 T		-33.4	-1.2
IN02_128	1007.1	253.5	74±15 d	959.1	250.8	250.6	115.3±9.0 T	116.4± 2.8	-36.8	-1.7
IN08_25	1015.7	253.7	75±5 d	962.3	250.7		118± 7.0 T		-34.8	-1.7
IN02_129	826.3	253.3	142±15d	762.1	249.2		114.3±7.9 T		-24.8	-1.1
IN08_22	1017.2	243.7	60±5 d	1016.7	243.7	243.7	122.2±7.9 T	122.2±7.9	-46.2	-2.6
IN02_137	1006.1	245.6	116±15d	909.5	240.1		116.2±10.2 T		-43.3	-2.2
IN05_64	1001.1	242.4	75±10 w	940.7	239.0		126.6± 9.1 T		-45.2	-2.3
IN08_10	1012.2	242.5	117±5 d	942.8	238.6	238.8	131.2± 7.3 T	127.7±4.03	-31.6	-1.5
IN05_65	1002.1	242.4	60±10 w	932.4	238.3		132.7± 10.7T		-31.4	-1.6
IN08_9	1012.1	242.3	120±5 d	941.3	238.3		132.1± 7.2 T		-31.4	-1.6
IN08_8	1014.1	241.0	115±5 d	942.7	237.1	237.1	127.0±7.3 T	127.0±7.3	-31.2	-1.4
IN08_17	1000.0	229.4	150±5 d	912.0	224.8		128.2± 7.5 T		-30.3	-1.3
IN08_18	1001.0	228.2	190±5 d	890.6	222.6	227.7	140.3±6.9 T	134.25±5.01	-29.2	-0.9
IN07_13	1010.9	210.5	200±5 w	920.5	206.7	206.7	150.8± 7.6 T	150.8± 7.6	-34.8	-1.7

5.6.2 Heterogeneous Ice Nucleation on Sahara Dust (SD)

Threshold relative humidities RH_i for heterogeneous ice nucleation on pristine (i.e. uncoated) as well as sulphuric acid coated Saharan Dust aerosols were determined as function of the gas temperature in AIDA chamber experiments covering the range 273 to 193 K. The obtained critical relative humidities RH_i(T) for uncoated SD particles are plotted versus the corresponding gas temperatures T_{nuc} at the freezing threshold in Figure 5.26a. All other details (calculation of error bars, significance of the black and green lines) are analogous to Figure 5.20a, as explained in section 5.6.1. Figure 5.26b is analogous to Figure 5.20b: the SD data were pooled in groups clustering around mean gas temperatures $\overline{T_{nuc}}$ and mean relative humidities RH_i ($\overline{T_{nuc}}$) at their nucleation thresholds, in the same way as outlined for the ATD data. The cluster averages for SD (see section 5.6.1 for the derivation of error bars) are plotted in Figure 5.26b. The detailed data sets for ice nucleation on pristine and coated SD aerosol particles are listed in Tables 5.6a and b, respectively.

- **Mixed Cloud Conditions**

The threshold relative humidities RH_i for ice and/or cloud droplet nucleation on uncoated SD in the mixed cloud regime (cf. red bar on top of Figure 5.26a and b) are systematically higher than those for ATD: the RH_i´s of SD fall only a few % short of the water saturation line. This includes four data points which were measured at about 235 K, i.e. roughly 5 K *below* the mixed cloud regime. At this temperature, RH_i falls only a few % below the threshold for homogeneous freezing of aqueous

solution droplets (green line, Koop et al., 2000), in contrast to the remainder of the cirrus regime, see below. Since most of the error bars in the mixed cloud regime overlap with the water saturation line, we speculate that supercooled cloud droplets condense on SD, probably accompanied by condensation freezing. To support these speculations, CPI data for experiments with SD were analysed, as previously explained for ATD. CPI data for SD are shown in Figures 5.28 to 5.30. In all cases, small fractions of ice particles were detected in a large excess of supercooled cloud droplets. The corresponding nucleation thresholds in Figures 5.26a and b overlap with the water saturation line within their uncertainty ranges. This supports the conclusion that ice nucleation on SD above 250 K is due to condensation freezing on a small fraction of very active dust particles. Figures 5.28 to 5.30 imply furthermore that immersion freezing on SD is not important, in clear contrast to ATD.

It is interesting to note that ice was formed at all temperatures in the mixed cloud regime, even very close to the triple point of water. This implies that a small fraction of the SD particles (see below) are efficient ice nuclei for the condensation freezing mode. However, it seems that ice nucleation at the highest temperatures occurred well *above* the water saturation line, although this conclusion is ambiguous in view of the large error bars. In conclusion, although SD is not as efficient as ATD with respect to ice nucleation in the mixed cloud regime, it may still nucleate ice crystals via the condensation mode. This implies that SD may be an important source of ice crystals when water saturation is exceeded in convective cloud systems with high updraft velocities.

- **Cirrus Cloud Conditions**

Figure 5.26a and b shows that the threshold relative humidity RH_i for ice nucleating on uncoated SD drops dramatically from 137% at 235 K to 109% at 223 K. Unfortunately there are no measurements between these temperatures to better assess the slope of RH_i in the transition region. Below 223 K the measured RH_i´s scatter within their error ranges around 110%, indicating that ice is formed by the deposition freezing mechanism under cirrus cloud conditions. The RH_i´s are slightly higher than the corresponding threshold relative humidities for ice nucleation on ATD, but the difference may not be significant as it is still within the combined error limits.

Only three measurements of ice nucleation on sulphuric acid coated SD are available at cirrus and PSC temperatures. The results are shown in Figure 5.27. Ice was found to nucleate significantly *below* the threshold relative humidity for homogeneous freezing of solution droplets (Koop et al., 2000, green line in Figure 5.27), but the sulphuric acid coating raises the nucleation threshold above that of uncoated SD, at least in the cirrus regime. Below 210 K the nucleation threshold of coated ATD was found to be significantly higher than that of coated SD, cf. Figures 5.21a&b and 5.27.

However, this observation should not be overemphasized because it is based on a single measurement with coated ATD at 207 K.

- **Polar Stratospheric Cloud Conditions**

SD nucleates ice well below the homogeneous nucleation threshold of aqueous solution droplets, green line in Figure 5.26, at approximately 120% relative humidity with respect to ice at temperatures between 193 and 195 K. This is less than the threshold of 125% for ATD. The relatively small difference is, however, not significant in view of the large scatter between individual measurements. Coating with sulphuric acid does not seem to affect the threshold relative humidity for ice nucleation on SD at PSC conditions.

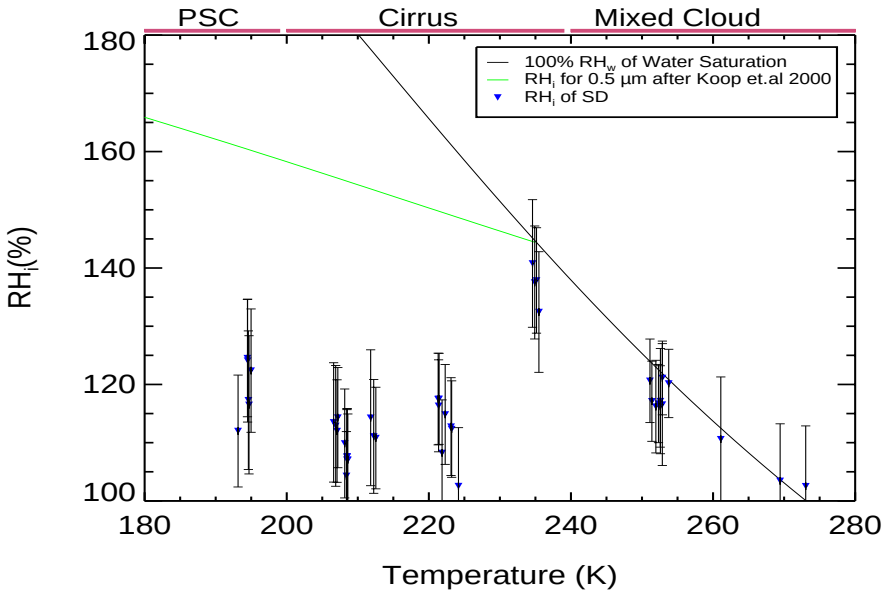

Figure 5.26a: Same as Figure 5.20a, but for ice nucleation on Sahara Dust (SD)

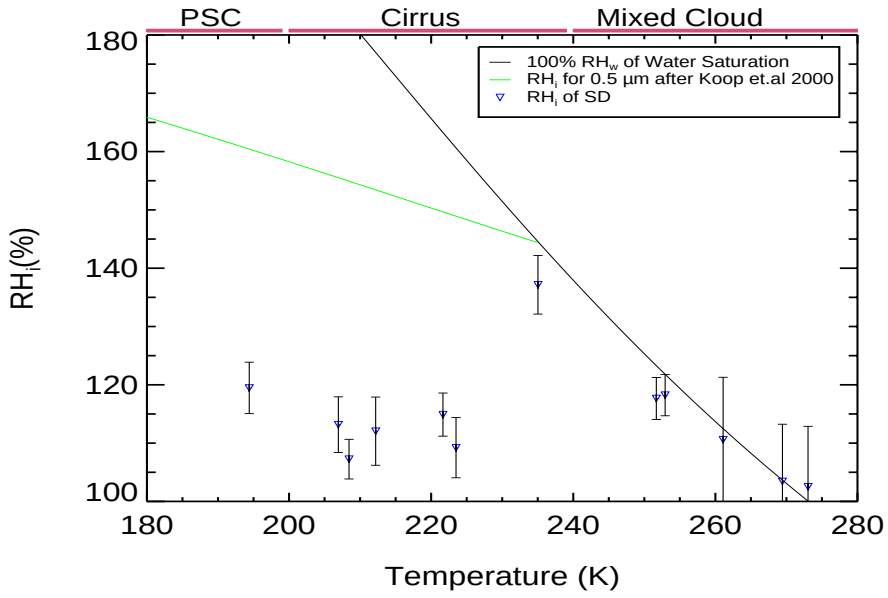

Figure 5.26b: Same as Figure 5.20b, but showing cluster-averaged nucleation thresholds for Saharan Dust (SD).

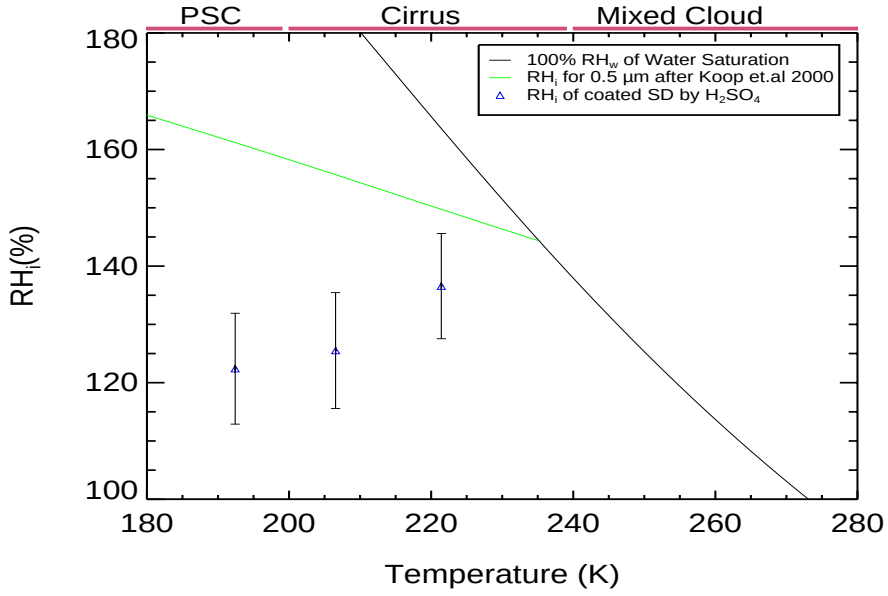

Figure 5.27: Same as Figure 5.21a, but for sulphuric acid coated Saharan Dust (SD).

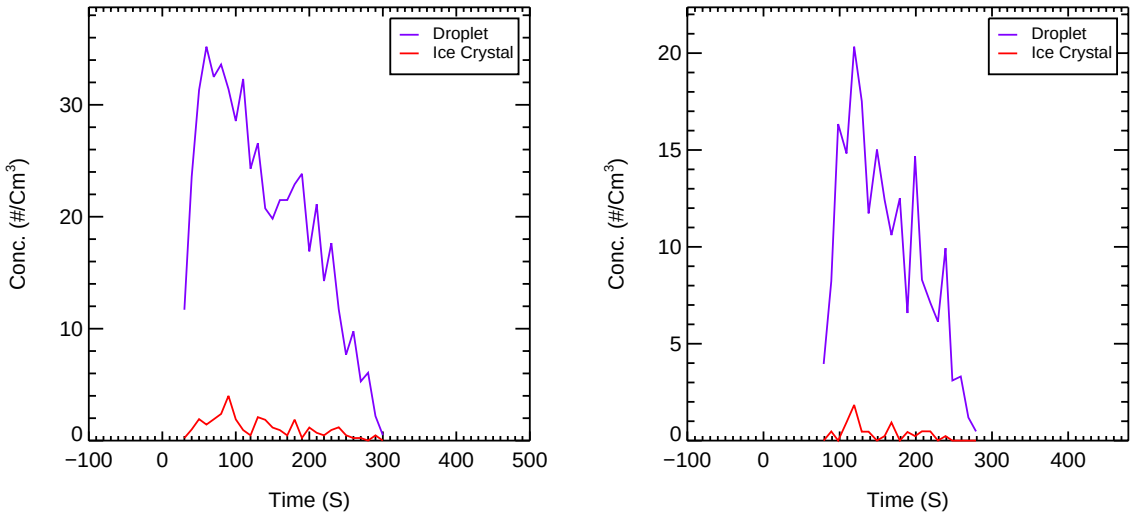

Figure 5.28: CPI data for SD, number concentrations classified by particle habit. Data are shown for the following experiments:
(a) IN04 N° 4 at 273 K (b) IN04 N° 5 at 269K

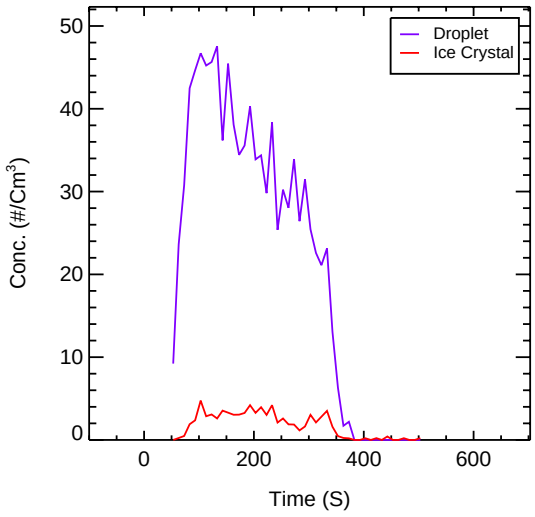

Figure 5.29: Same as Figure 5.28, but for SD experiment IN05 N° 50 at 261 K

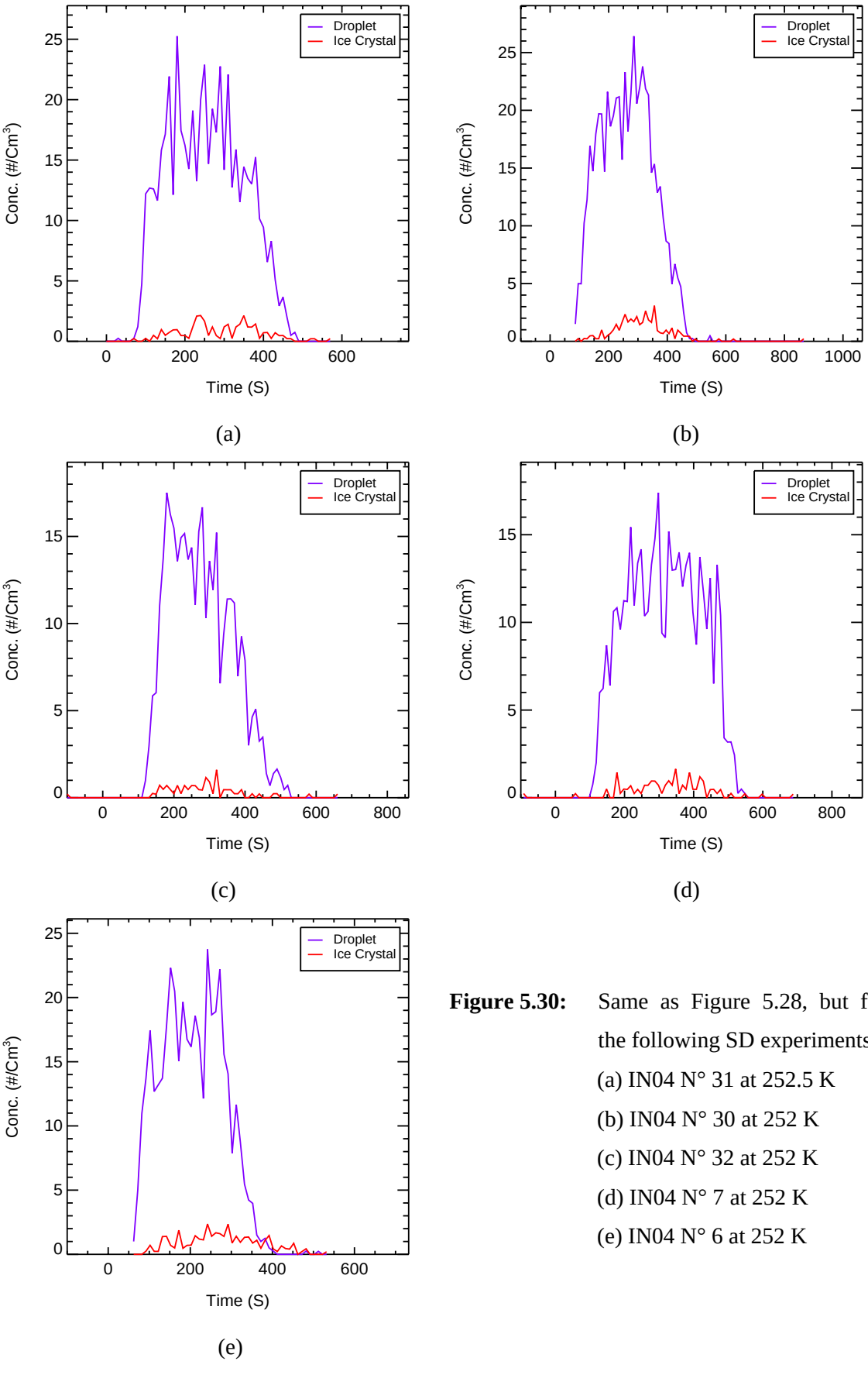

Figure 5.30: Same as Figure 5.28, but for the following SD experiments:
(a) IN04 N° 31 at 252.5 K
(b) IN04 N° 30 at 252 K
(c) IN04 N° 32 at 252 K
(d) IN04 N° 7 at 252 K
(e) IN04 N° 6 at 252 K

Table 5.6a: Same as Table 5.5a, but showing ice nucleation parameters for AIDA experiments with uncoated Saharan Dust (SD)

Exp.-N°	p_o	T_o	$t_{nuc} \pm \delta\, t$	p_{nuc}	T_{nuc}	$\overline{T_{nuc}}$	$RH_i \pm \delta\, RH_i$	$\overline{RH_i}$	*dp/dt*	*dT/dt*
IN04_4	996.1	275.1	25± 10 w	957.3	273.0	273.0	102.5±7.2 T	102.5±7.2	-82.7	-4.9
IN04_5	982.4	274.7	60± 5 w	899.7	269.4	269.4	103.4±7.2 M	103.4±7.2	-76.8	-4.2
IN05_50	1010.1	263.2	30± 10 w	971.1	261.0	261.0	106.3±7.5 M	106.3±7.5	-76.1	-4.5
IN04_33	996.3	254.3	38± 10 w	961.1	252.8		121.1±7.8 P		-37.6	-2.1
IN04_31	991.8	254.3	35± 5 w	960.7	252.5		116.2±7.8 T		-51.6	-2.8
IN04_30	994.2	254.0	32± 5 w	963.8	252.3		116.7±7.8 F		-49.4	-3.1
IN04_32	991.9	254.6	70± 10 w	944.1	251.9	251.6	116.1±7.8 M	118.6±7.8	-35.2	-1.7
IN04_7	1006.4	253.8	69± 10 w	963.2	251.3		117.1±7.7 T		-38.1	-1.7
IN04_6	994.2	253.4	40± 5 w	953.8	251.1		120.6±7.8 T		-56.7	-3.5
IN04_37	986.6	238.4	90± 5 w	930.4	235.4		132.4±8.5 T		-33.2	-1.6
IN04_35	990.8	238.6	78± 10 w	925.7	235.1	235.0	137.8±8.5 M	136.9±8.5	-42.0	-2.1
IN04_36	989.3	238.5	90± 10 w	918.5	234.5		140.7±8.5 T		-44.1	-1.9
IN05_5	992.3	224.8	20± 10 w	976.6	224.1		102.5±9.1 F		-44.3	-2.5
IN05_6	995.7	225.2	90± 10 w	957.3	223.1	223.3	112.7±9.2 F	109.2±9.1	-25.3	-1.2
IN05_7	990.5	225.1	80± 10 w	957.6	223.2		112.3±9.2 M		-23.5	-1.2
IN04_40	987.5	223.9	37± 10 w	958.2	222.3		114.8±9.2 M		-44.6	-2.6
IN05_4	997.4	225.0	90± 10 w	937.5	221.8		108.2±9.2 M		-36.1	-1.6
IN04_41	985.9	223.5	65± 10 w	945.9	221.4	221.6	117.5±9.3 T	114.8±9.3	-33.2	-1.6
IN04_43	994.8	223.7	73± 10 w	951.2	221.3		116.3±9.3 T		-33.2	-1.6
IN04_42	989.7	223.5	71± 5 w	947.0	221.3		117.4±9.3 T		-32.8	-1.7
IN04_44	987.0	213.1	16± 10 w	977.0	212.5		110.7±9.9 F		-37.9	-1.9
IN04_45	997.0	213.5	39± 10 w	973.7	212.2	212.2	111.1±9.9 M	112± 9.9	-32.0	-1.9
IN04_46	994.2	213.4	52± 5 w	962.7	211.8		114.2±9.9 T		-35.0	-1.7
IN03_14	999.0	210.3	89± 10 w	965.6	208.6		107.1±10.2 F		-21.2	-0.9
IN03_12	999.3	210.1	66± 10 w	968.0	208.5		107.7±10.2 M		-26.8	-1.3
IN03_13	999.7	210.2	76± 10 w	963.9	208.4	208.4	107.5±10.2 M		-25.0	-1.2
IN03_11	999.7	210.0	47± 5 w	968.9	208.4		107.1±10.2 M	107.3±10.2	-37.5	-1.9
IN03_15	809.8	209.9	127± 5 w	783.3	208.4		104.3±10.2 M		-15.0	-0.7
IN03_10	999.9	209.8	41± 10 w	967.4	208.1		109.8±10.2 F		-45.6	-2.5
IN05_10	1000.7	209.1	100±10 w	960.7	207.1		114.3±10.3 M		-21.1	-0.9
IN05_11	1001.2	208.9	100± 5 w	962.4	207.0	206.8	111.9±10.3 F	115.1±10.3	-21.3	-0.9
IN04_12	1005.1	209.0	60± 10 w	961.1	206.8		112.8±10.3 M		-42.4	-2.0
IN04_11	1006.2	209.1	69± 5 w	956.6	206.6		113.4±10.3 T		-42.5	-1.9
IN03_18	1005.8	197.1	108±10 w	959.2	194.9		122.3±11.4 T		-24.4	-0.9
IN03_17	1008.2	197.0	86± 5 w	958.0	194.6		116.4±11.4 F		-33.5	-1.4
IN03_16	1006.4	196.9	86± 5 w	956.5	194.6	194.5	117.2±11.4 M	119.4±11.4	-33.1	-1.3
IN03_19	1005.7	196.8	117±10 w	954.7	194.4		124.0±11.4 M		-22.2	-0.9
IN03_20	1006.1	196.6	130±10 w	958.6	194.4		124.5±11.4 M		-19.0	-0.7
IN05_15	1006.4	193.8	40± 10 w	991.0	193.1		112.0±11.6 M		-24.4	-1.1

Table 5.6b: Same as Table 5.5b, but showing ice nucleation parameters for AIDA experiments with sulphuric acid coated Saharan Dust (SD)

IN05_8	978.7	224.9	100 ± 10 W	913.7	221.4	221.4	136.5±10.2 T	136.5±10.2	-32.8	-1.5
IN05_12	1004.3	209.1	80 ± 10 w	952.6	206.5	206.9	125.5± 9.5 T	117.3± 9.7	-33.0	-1.7
IN05_13	757.0	208.8	100 ± 10 w	734.3	207.3		109.2 ± 9.8 T		-14.7	-0.83
IN05_16	1002.8	194.1	80 ± 10 w	966.6	192.4	192.4	122.4±10.5 T	122.4±10.5	-25.3	-1.09

5.6.3 Heterogeneous Ice Nucleation on Asian Dust (AD)

The threshold relative humidities RH_i for ice nucleation on pristine Asian mineral dust, which were determined in AIDA chamber experiments, are plotted in Figure 5.31a and b as a function of the gas temperature at freezing onset. The further data treatment (calculation of error bars, clustering of data to yield group-averaged nucleation thresholds which are shown in Figure 5.31b) was done in full analogy to the procedures described in sections 5.6.1 and 5.6.2. The detailed data sets for ice nucleation on Asian mineral dust are listed in Table 5.7. Note that the impact of coatings on the ice nucleating efficiency of Asian dust was not studied.

- **Mixed Cloud Condition**

Comparison of Figure 5.31a and b with the corresponding Figure 5.26a and b shows that the threshold relative humidities RH_i for supercooled droplet condensation or ice nucleation on Asian dust in the mixed cloud regime do not differ significantly from the RH_i´s of Sahara Dust (SD) in the same temperature range. Although the nucleation thresholds are systematically shifted below the water saturation line by about 5%, the large error bars support the hypothesis that ice nucleation may have occurred by condensation or immersion freezing, i.e. *after* cloud droplet activation had taken place at 100% r.h. with respect to super-cooled liquid water.

The relative importance of supercooled cloud droplet condensation and ice nucleation was assessed on the basis of CPI data, as previously explained for ATD and SD. The results are shown in Figures 5.32, 5.33, and 5.34. They confirm that ice particles were formed in the mixed cloud experiments in all cases studied. We can draw the following conclusions: At the warmest temperatures of 267 K and 262 K, cf. Figure 5.32, only a very small fraction of ice crystals were formed in an excess of super-cooled cloud droplets. The results at 257 K and 253 K are similar, although in the latter case the ice particle number density continued to increase, probably by immersion freezing of water droplets, which evaporated before the ice number concentrations reached its maximum. At the lowest temperatures between 243 K and 240 K, which are close to the homogeneous freezing threshold of pure water droplets, Figure 5.34, the following observations are made: liquid droplets are only in excess for the first few seconds, while afterwards ice crystals become the dominant phase, probably by immersion freezing. Note, however, that the statistics of the CPI are poor in these experiments. Therefore, the data should not be over-interpreted.

- **Cirrus Cloud Condition**

The first notable result in this regime is that the nucleation threshold RH_i at about 221 K is on average less than 110%. This is very close to the nucleation threshold for ATD, and slightly below that of SD at similar temperatures. However, while no RH_i data are available for ATD and SD in the transition region between 225 and 235 K, an average nucleation threshold of 119% RH_i was observed for AD between 232 and 233.4 K. The RH_i´s in this very narrow range show an unusually wide spread from 107% to 129%, which implies that the transition between high critical RH_i´s at 235 K (cf. Figure 5.26) and very low critical RH_i´s at 225 K (cf. Figures 5.20 and 5.26) is rather steep for uncoated mineral dust.

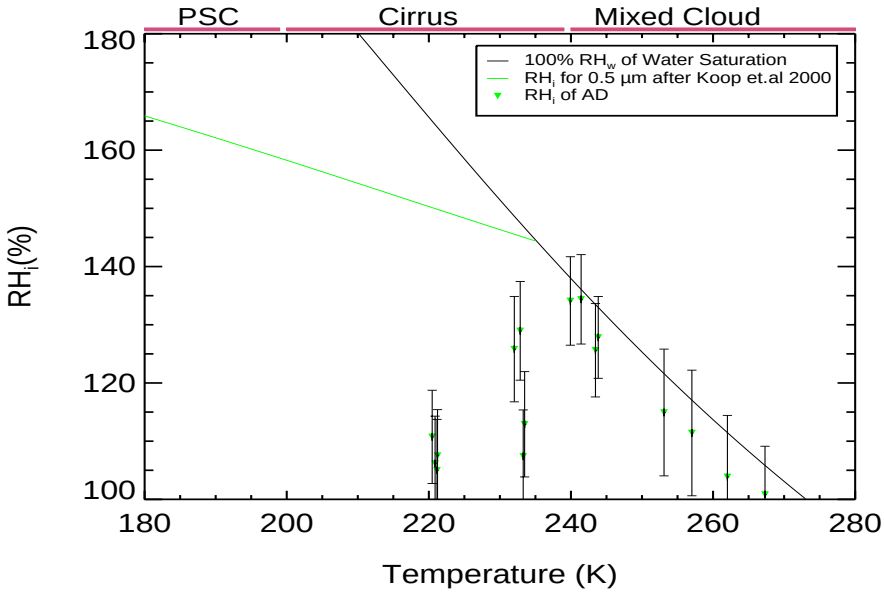

Figure 5.31a: Same as Figure 5.20a, but for ice nucleation on Asian Dust (AD)

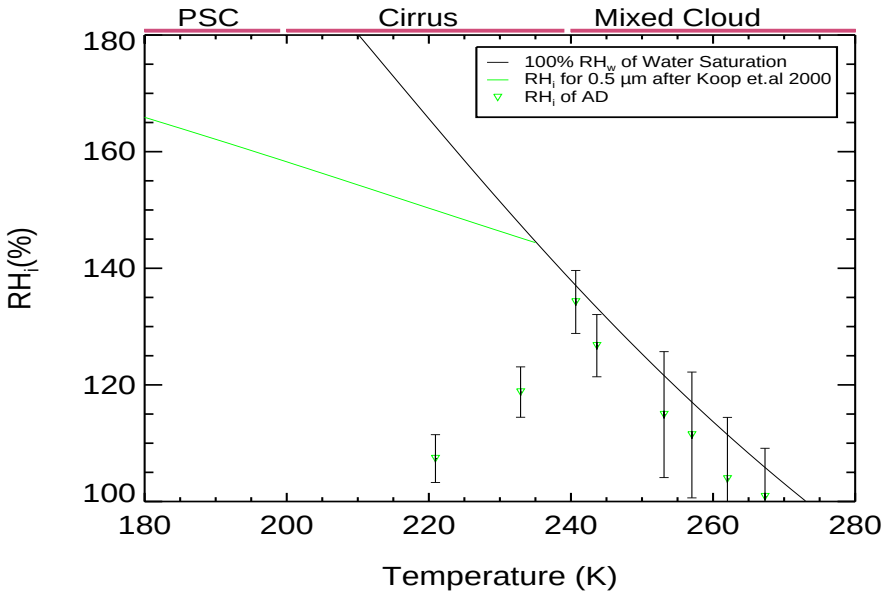

Figure 5.31b: Same as Figure 3.20b, but for ice nucleation on Asian Dust (AD).

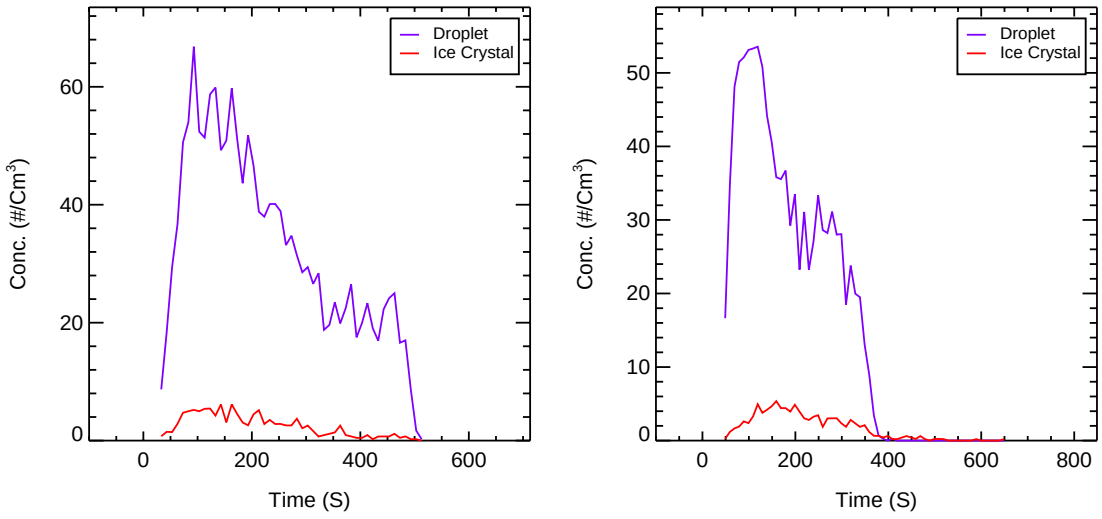

(a) (b)

Figure 5.32: CPI data for AD, number concentrations classified by particle habit. Data are shown for the following experiments:

(a) IN05 N° 45 at 267 K (b) IN05 N° 48 at 262K

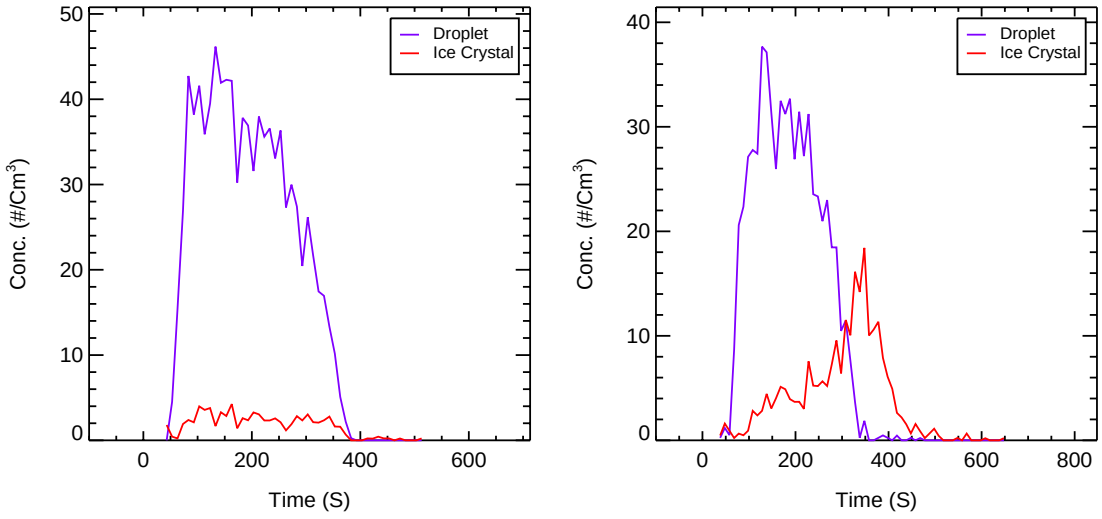

(a) (b)

Figure 5.33: Same as Figure 5.32, but for the following AD experiments:

(a) IN05 N° 55 at 257 K (b) IN05 N° 51 at 253K

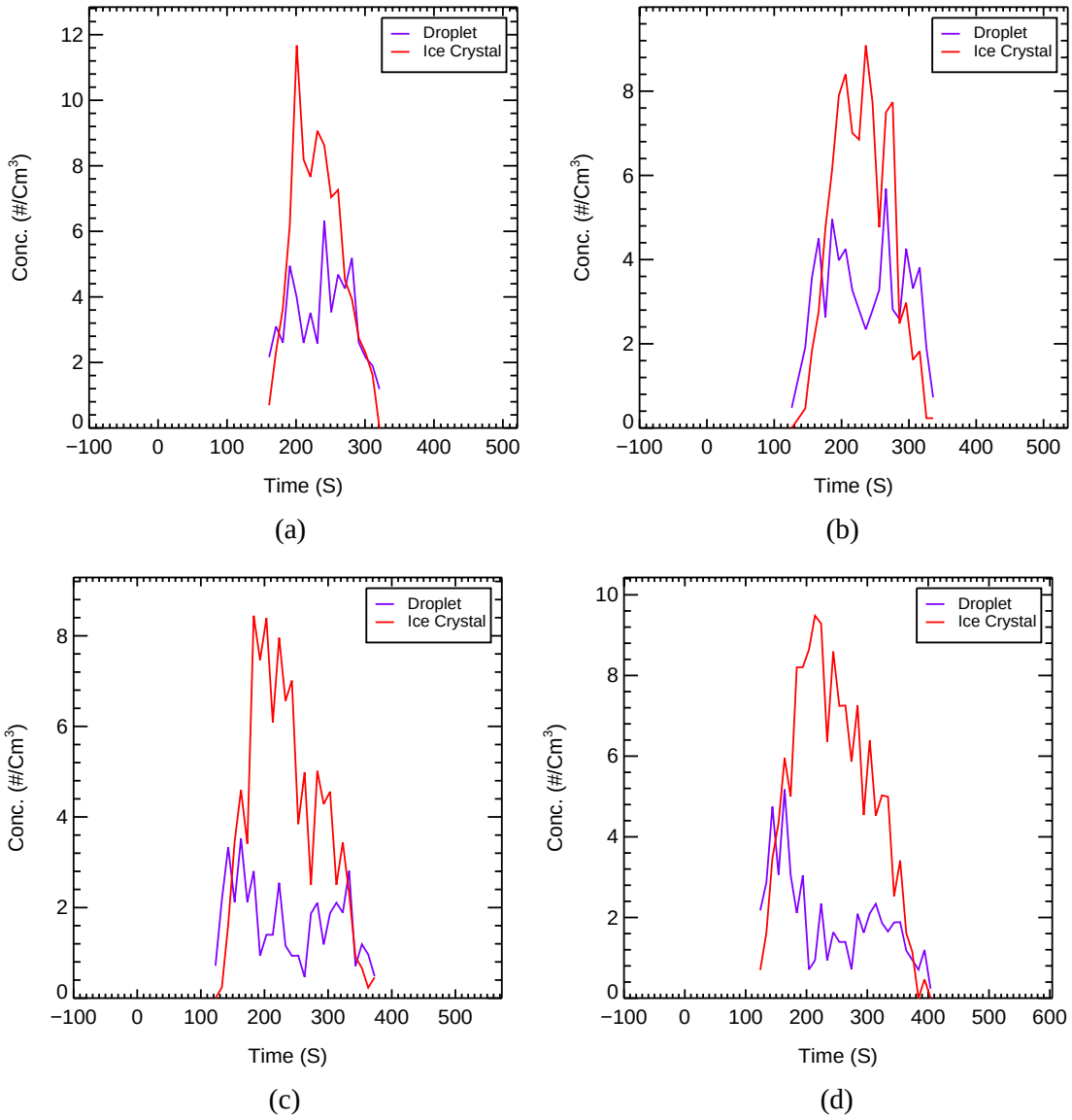

Figure 5.34: Same as Figure 5.32, but for the following AD experiments:

(a) IN04 N° 18at 243 K (b) IN04 N° 19 at 243K

(c) IN04 N° 20 at 241 K (d) IN04 N° 21 at 240 K

Table: 5.7: Same as Table 5.5a but showing ice nucleation parameters for AIDA experiments with Asian dust (AD)

Exp.-N°	p_o	T_o	$t_{nuc} \pm \delta\, t$	p_{nuc}	T_{nuc}	$\overline{T_{nuc}}$	$RH_i. \pm \delta\, RH_i.$	$\overline{RH_i}$	*dp/dt*	*dT/dt*
IN05_45	996.8	267.6	10 ±10w	990.3	267.3	267.3	100.8±8.3 M	100.8±8.3	-38.2	-1.9
IN05_48	1014.2	263.2	20± 10w	990.3	262.0	262.0	103.9±10.6 M	103.9±10.6	-79.9	-4.4
IN05_55	1010.3	259.0	30±10w	973.5	257.0	257.0	111.4 ±10.7 M	111.4±10.7	-74.5	-4.4
IN04_51	1015.0	255.3	35±10w	975.1	253.1	253.1	114.9 ±10.8 M	114.9±10.8	-74.4	-4.4
IN04_18	1007.1	253.5	145±5d	829.7	243.8		127.8± 7.0 M		-58.5	-2.1
IN04_19	1018.3	252.6	103±5d	856.7	243.4	243.6	125.6± 8.0 M	126.7±5.3	-64.2	-2.4
IN04_20	1009.3	250.4	99±5d	853.7	241.4		134.3 ±7.6 F		-57.9	-2.1
IN04_21	1004.9	248.3	93±5d	858.4	239.9	240.6	134.0 ±7.5 F	134.2±5.4	-60.0	-2.2
IN04_23	1000.1	237.4	90±10d	929.1	233.4		112.9 ±9.0 T		-43.9	-2.0
IN04_25	1003.0	237.5	143±10d	918.7	233.2	232.9	107.4 ±7.9 T	118.7±4.3	-28.7	-1.1
IN04_22	1004.6	238.0	126±10d	905.8	232.8		128.9 ±8.4 M		-43.3	-1.7
IN04_24	996.3	237.1	111±10d	896.6	232.0		125.8 ±9.0 M		-49.5	-1.9
IN04_26	1001.5	222.1	21±3d	984.0	221.2		107.5 ±7.8 M		-49.1	-2.7
IN04_27	1002.8	222.2	25±5d	981.4	221.1	220.9	105.0 ±8.7 M	107.7±4.7	-49.8	-2.7
IN04_29	990.3	221.9	47±5d	962.2	220.4		110.7 ±8.0 M		-34.1	-1.7

5.6.4 Heterogeneous Ice Nucleation on Mineral Dust Collected Close to Cairo (CD1 & CD2)

AIDA chamber experiments were also carried out with desert dust which was collected by gravitational settling at a sampling point located at 30.4°N, 31.2°E, close to Benha university, about 50 km north of Cairo city and about 150 km from the Mediterranean coast of Egypt. The material was representative of two sandstorms on 18th February (CD1) and 19th March 2003 (DC2). Note that it had been exposed to polluted air on its way to the sampling point, as evidenced by back-trajectory calculations in combination with satellite images, as described in section 5.1.2. The elemental composition of the material as well as the ionic composition of the water soluble fraction is reported in section 5.2. The soluble ions (which amounted to ~0.5 wt-% only) are mainly due to surface coatings, but may also include other environmental aerosols, which were scavenged by coagulation with mineral dust particles during transport. Only limited amounts of both samples were available. It appeared reasonable to study these materials in the mixed cloud regime only, since it is most likely playing a role in natural cloud seeding events in this area.

The results of this study are presented in Figures 5.35a and b. Shown are threshold relative humidities RH_i in the temperature range 242 – 253 K. Note that two measurements with CD1 which nucleated supercooled cloud droplets and/or ice at the upper bound of this temperature range reproduced a threshold relative humidity of 116% with respect to ice, both with error bars overlapping the water saturation line, while two measurements with CD1 at 243 and 245 K nucleated ice at 104%

and 115% relative humidity, significantly *below* water saturation. Their cluster averages are shown in Figure 5.35b. Only one measurement could be done with CD2. The sample had to be mixed with some CD1 to obtain the amount needed for an appropriate filling of the AIDA chamber: it nucleated ice only slightly above ice saturation at 245 K. i.e. far below water saturation. We want to emphasize that the polluted mineral dust particles which were collected by gravitational settling during two dust storms near Cairo city are by far the most efficient ice nuclei in this temperature range. They even exceed the efficiency of Arizona Test Dust (ATD), cf. Figure 5.20a and b, which is often assumed to be representative of desert dust in many laboratories worldwide.

To make sure that ice was indeed formed in these experiments, and to assess the nucleation mechanism, we analysed CPI data which were, however, only available for experiments IN05_58 and IN05_59 at 252 K. Figure 5.36 confirms that a small fraction of ice particles was indeed formed in an excess of liquid droplets, probably by condensation or immersion freezing. Note that we found similar results for SD and AD in the same temperature range. No CPI data were available for experiment IN08_46 at 245 K which was unique because it exhibited the lowest threshold $RH_i \approx 105\%$ of all experiments with CD1. In this case, ice particles could be unambiguously identified in the FTIR spectra, Figure 5.37, which were recorded at time intervals of 10 s. They feature two sharp Christiansen bands at 3500 and 950 cm^{-1} (Arnott et. al., 1995), which are specific for ice crystals. The spectra also reveal that no super-cooled cloud droplets were formed in this experiment. We conclude that ice formation in experiment IN08_46 was due to deposition freezing. The detailed data sets for ice nucleation on Cairo dust are listed in Table 5.8.

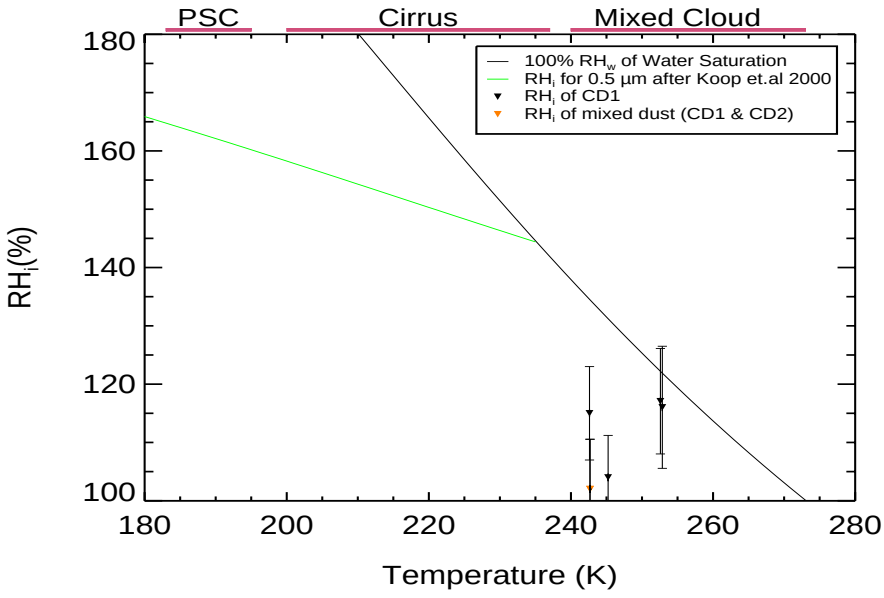

Figure 5.35a: Same as Figure 5.17a, but for ice nucleation on airborne desert dust which was collected near Cairo city: CD1 (▼) and CD2 (▼).

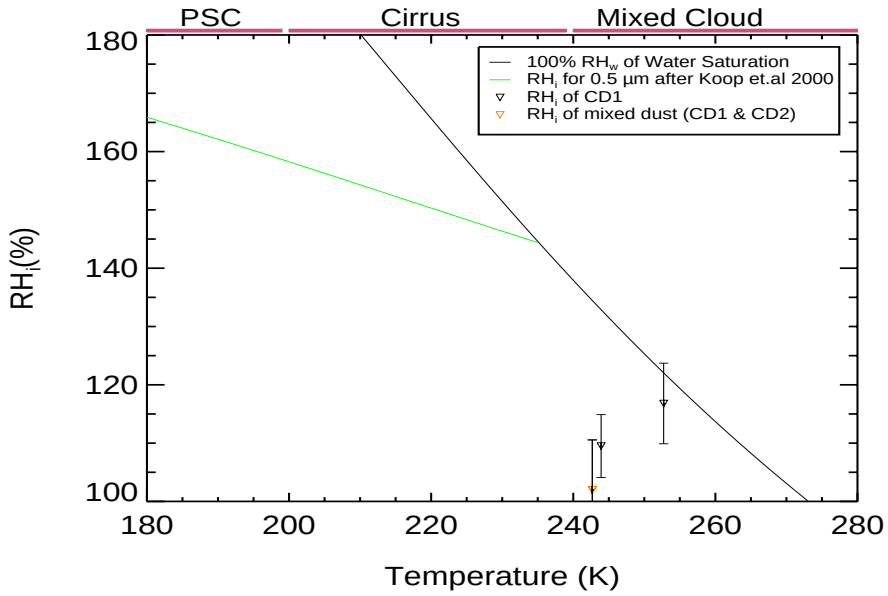

Figure 5.35b: Same as Figure 5.17b, but for ice nucleation on airborne desert dust which was collected near Cairo city: CD1 (▽) and CD2 (▽).

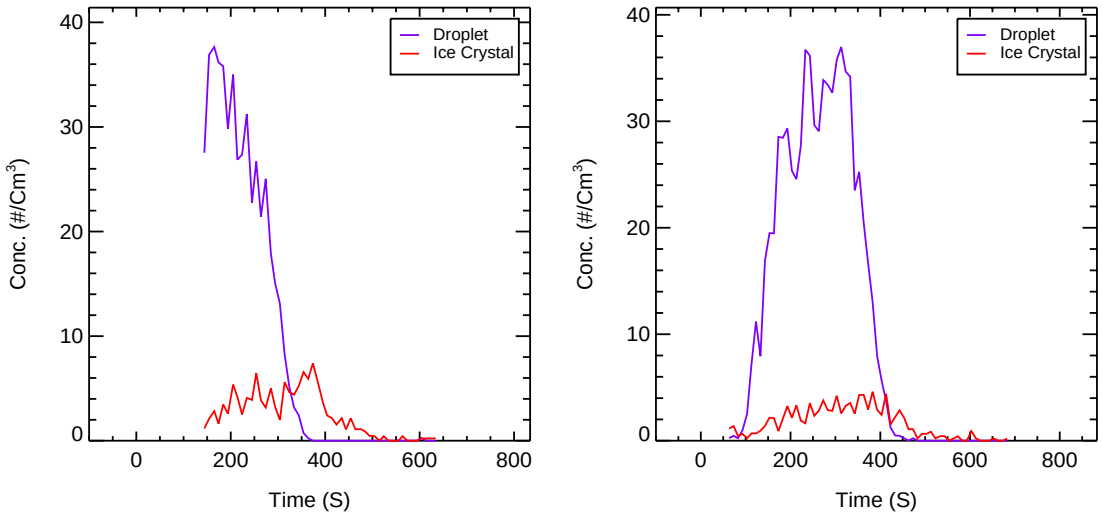

Figure 5.36: CPI data for CD1, number concentrations classified by particle habit. Data are shown for the following experiments:

(a) IN05 N° 58 at 252 K (b) IN05 N° 59 at 252K

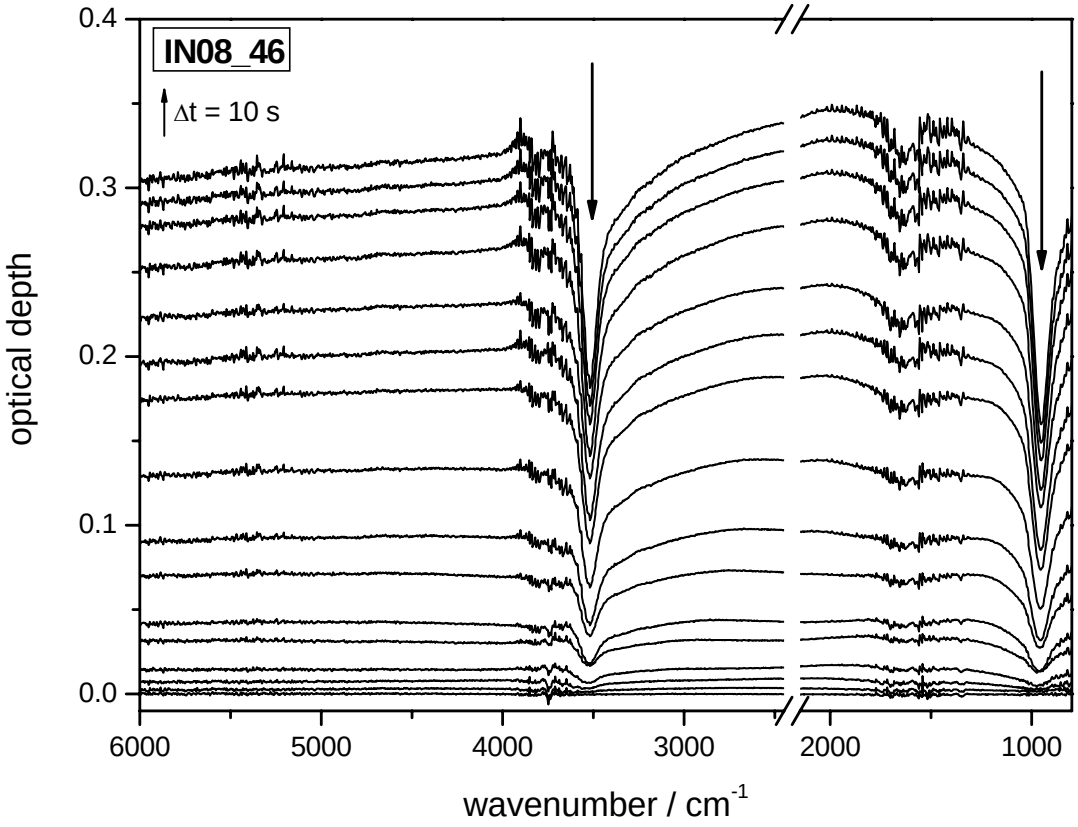

Figure 5.37: FTIR extinction spectra of CD1 experiment IN08_46 at 245 K, recorded at time intervals of 10 s, during an expansion cooling experiment at mixed cloud conditions. Two sharp bands, the so-called Christiansen bands of ice, evolve at 3500 and 950 cm^{-1}.

Table: 5.8: Same as Table 5.5a but showing ice nucleation parameters for AIDA experiments with Cairo dust samples. m indicates that a mixture of CD1 and CD2 was used.

Exp.-N°	p_o	T_o	$t_{nuc} \pm \delta t$	p_{nuc}	T_{nuc}	$\overline{T_{nuc}}$	$RH_i \pm \delta RH_i$	$\overline{RH_i}$	*dp/dt*	*dT/dt*
IN05_58	1008.6	255.5	40±10w	963.1	252.8	252.6	118.0± 10.4 T	116.8±7.1	-67.4	-4.0
IN05_59	1002.9	255.4	55±10w	954.8	252.5		115.6± 9.0 T		-49.1	-2.5
IN08_46	1002.9	248.3	90±5d	951.2	245.2	243.9	104.1± 7.2 T	109.6±5.3	-31.5	-1.7
IN08_47	1002.9	246.4	120±5d	936.1	242.6		115.2± 8.0 T		-29.9	-1.5
IN08_48 (m)	1002.8	245.1	70 ±5d	962.7	242.6	242.6	102.0± 8.6 T	102.0±8.6	-32.2	-1.9

5.7 Determination of Heterogeneous Nucleation Rates

In Chapter 5.2 we have presented comprehensive data sets of freezing *thresholds* for various types of insoluble mineral dust particles, including authentic Saharan dust samples which were characterised in Chapter 5.1. In this chapter we will show that nucleation rates for deposition freezing on mineral dust particles can be derived from the same simulation experiments in the AIDA chamber, in those favourable cases where reliable time-resolved size-segregated ice particle number densities are available from measurements with optical particle counters in the vicinity of the nucleation thresholds. We introduce the chapter by briefly reviewing the kinetics of homogeneous ice nucleation which has been applied by numerous authors (e.g. Duft and Leisner, 2004; Benz et al., 2005). On this basis, an analogous rate equation for deposition freezing will be derived and applied.

Background: Kinetics of homogeneous liquid droplet freezing:

The ice nucleation rate J of super-cooled water droplets (or solution droplets, see below) is defined as follows: Imagine a large number N of super-cooled droplets. To simplify matters, we assume that all droplets have the same volume V_0. The formation of an ice nucleus in super-cooled water, which causes immediate freezing of the entire droplet, is a stochastic process. The probability of critical ice germ formation is proportional to the volume of the liquid phase[1], and therefore the rate of change of the liquid particle number density N as well as the formation rate of ice particles due to droplet freezing is given by

$$-\left(\frac{dN}{dt}\right)_T = +\left(\frac{dn_{ice}}{dt}\right)_T = V_{total}(t)\,J(T) = N_t\,V_0\,J(T) \qquad (5.6)$$

Integration at constant temperature[2] (i.e. constant J) yields $N_t = N_0 \exp(-J\,V_0\,t)$. The dimension of the nucleation rate J is [# cm^{-3} s^{-1}]. Since – for the conditions chosen above - the number of frozen droplets is $n_{ice} = N_0 - N_t = N_0\,(1 - \exp(-J\,V_0\,t))$, we can introduce the freezing probability $P_{freez}(t) = (n_{ice}/N_0)_t = (1 - \exp(-J\,V_0\,t))$. P_{freez} is the fraction of the equally sized droplets which have frozen (at constant temperature!) after the time t has elapsed. This equation can be used to derive J(T) from measurements of the freezing statistics of a series of equally-sized droplets which are injected into an

[1] This is at least correct for droplets with diameters larger than about 8 µm, as has been shown by Duft and Leisner (2004). However, very recent theoretical evidence seems to indicate that for significantly smaller droplets, freezing might preferentially start in a sub-surface layer of about 1.5 nm thickness rather than in the bulk of the droplet (Vrbka and Jungwirth, 2006). Further experiments are needed to prove or disprove the transition from volume dominated to surface dominated ice nucleation in very small droplets.

[2] This is an important constraint, because the nucleation rate J of super-cooled water is an extremely steep function of the temperature. E.g., the nucleation rate J (T) of liquid water changes by ca. 3 orders of magnitude when T changes by 2 K (Benz et al., 2005). The reason for the strong temperature dependence can be understood on the basis of classical nucleation theory (Pruppacher and Klett, 1997). In the case of solution droplets, the saturation ratio is also important (Koop et al., 2000)

electromagnetic trap at a constant gas temperature (e.g. Duft and Leisner, 2004). Koop et al. (2000) have extended this formalism to include homogeneous freezing of more concentrated solution droplets which nucleate ice below the homogeneous freezing limit of pure water droplets (ca. -36°C): They assumed that, when the ice/solution coexistence line in the phase diagram as well as $J(T)$ for supercooled pure water droplets are known, the nucleation rate $J(T,a_w)$ of the solution droplets can be expressed as a unique function of the temperature *and* the water activity a_w of the solution, irrespective of the nature of the solute(s).

Kinetics of heterogeneous ice nucleation:

Lohmann and Kärcher (2003) have adopted the formalism of Koop et al. (2000) to parameterise rates of heterogeneous ice nucleation in a model of cirrus formation. Their approach is based on the assumption that heterogeneous ice nucleation is due to immersion freezing, which implies that the solid particles which act as heterogeneous ice nuclei are embedded in a liquid solution. They also make the unreasonable assumption (Zuberi et al., 2001) that the size of the immersed solid nuclei does not significantly affect the freezing rate.

Note that the parameterisation of Lohmann and Kärcher (2003) cannot be applied to heterogeneous ice nucleation on uncoated, i.e. totally insoluble particles below the homogeneous freezing threshold of pure water droplets (ca. -36°C), because immersion freezing requires that the insoluble particles are embedded in a liquid solution. In the remainder of this chapter we focus on insoluble mineral dust particles which act as *deposition freezing nuclei* at temperatures below the homogeneous freezing threshold temperature of pure water. At warmer temperatures, different modes of ice nucleation are feasible: (a) deposition freezing may occur significantly below the water saturation line if the insoluble particles have very active surfaces; (b) for less active insoluble particles, the relative humidity must increases above the water saturation line to activate the particles, i.e. form super-cooled cloud droplets with solid nuclei which cause immersion freezing.

Deposition freezing on a solid surface requires that a critical ice germ is formed on an active surface site. The number of active sites on an ensemble of particles consisting of the same material (e.g. mineral dust from the Sahara) is expected to scale with the surface area A_{total} of all particles. It is therefore reasonable to assume that the probability of critical germ formation per unit time per unit volume of air is also proportional to A_{total} which is the sum of the surface areas $A(D_p)$ of all active mineral dust particles contained in the considered volume. By analogy with equation (5.6) which applies to homogeneous nucleation in an ensemble of liquid droplets, we can define a surface-specific heterogeneous nucleation rate J [# cm^{-2} s^{-1}] for deposition freezing, which for a given type of mineral dust particles depends on the gas temperature and the saturation ratio S_{ice} with respect to ice:

$$-\left(\frac{dN}{dt}\right)_{T,S_{ice}} = +\left(\frac{dn_{ice}}{dt}\right)_{T,S_{ice}} = A_{total}(t)\,J(T,S_{ice}) \qquad (5.7)$$

The active surface area is simply the sum over the surface areas of all dust particles. The active surface area A_{total} decreases with time because frozen particles must be omitted from the summation. It is possible to determine the deposition nucleation rate by solving equation (5.7) for $J(T,S_{ice})$, provided that both the rate of ice particle formation $\left(dn_{ice}/dt\right)_t$ and the remaining active surface area $A_{total}(t)$ are available from time-resolved measurements shortly before and after the nucleation threshold has been crossed.

The rate of ice particle formation can be measured with an optical particle counter (either PCS-2000 or WELAS). This is illustrated in Figure 5.38 for experiment IN02_147 which was done with Arizona test dust at a temperature of 223.3 K at pump start: the black circles represent number concentrations of particles which were detected by the optical particle counter PCS-2000. By subtracting the OPC background count rate before ice nucleation onset from the count rates beyond the nucleation threshold, and by applying a correction for dilution by pumping, one obtains the ice particle number density $n_{ice}(t)$. The noise of the original ice particle number density trace was reduced by applying the CONVOL function (software supplied by IDL), which resulted in the red trace in Figure 5.28. This function is based on the Savitzky-Golay smoothing filter that is described in section 14.8 of "Numerical Recipes in FORTRAN: Second Edition", published by Cambridge University Press, 1993. The ice particle number density is zero before ice nucleation takes place, increases sharply afterwards, and levels off and oscillates around a mean value when the nucleation burst is over.

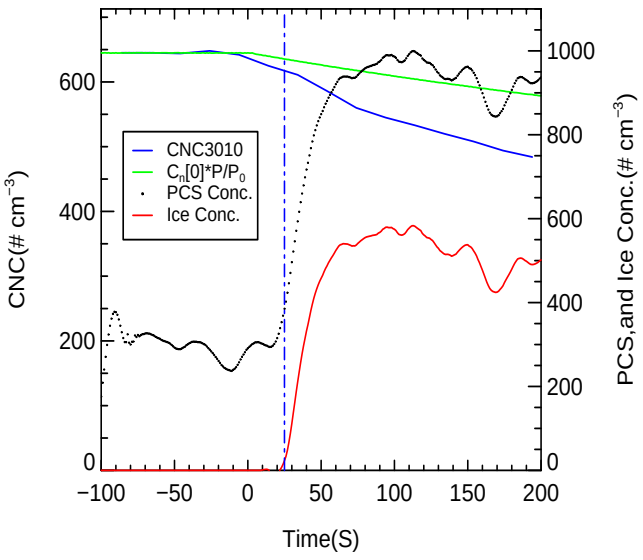

Figure 5.38: Experiment IN02_147 with Arizona test dust, 223.3 K at pump start. Black circles: CONVOL filtered count rate of the optical particle counter PCS-2000. Red trace: derived ice particle number density n_{ice}(t). The blue line represents the CNC count rate which decreases faster than expected from dilution (represented by the smooth green line) because large ice crystals are lost in the sampling line of the CNC.

The surface area of all mineral dust particles was derived as follows: Figure 5.39 (left panel) shows as a dashed black line the size distribution of Arizona test dust in the AIDA chamber, as measured with a DMA before the pump was started in experiment IN02_147. It was fitted with a log-normal distribution (magenta) to reconstruct the unknown part of the size distribution with mobility diameters D_p > 0.8 µm, which exceeded the sizing range of the DMA. The number distribution $dN/d\log D_p$ was converted to a surface area distribution, $dA/d\log D_p$, making the simplifying assumption that the dust particles are spherical (dotted black line in Figure 5.39, left panel). Again, the unknown contribution of large dust particles to the surface area distribution $dA/d\log D_p$ had to be reconstructed by fitting a log-normal distribution to the dotted line, which yielded the green line in Figure 5.39, left panel. Integration of the surface area distribution (including the reconstructed contribution of particles with mobility diameters D_p > 0.8 µm) yielded the surface area $A_{total}(t=0)$. It corresponds to the horizontal section of the dashed green line before ice nucleation onset on the right panel of Figure 5.39.

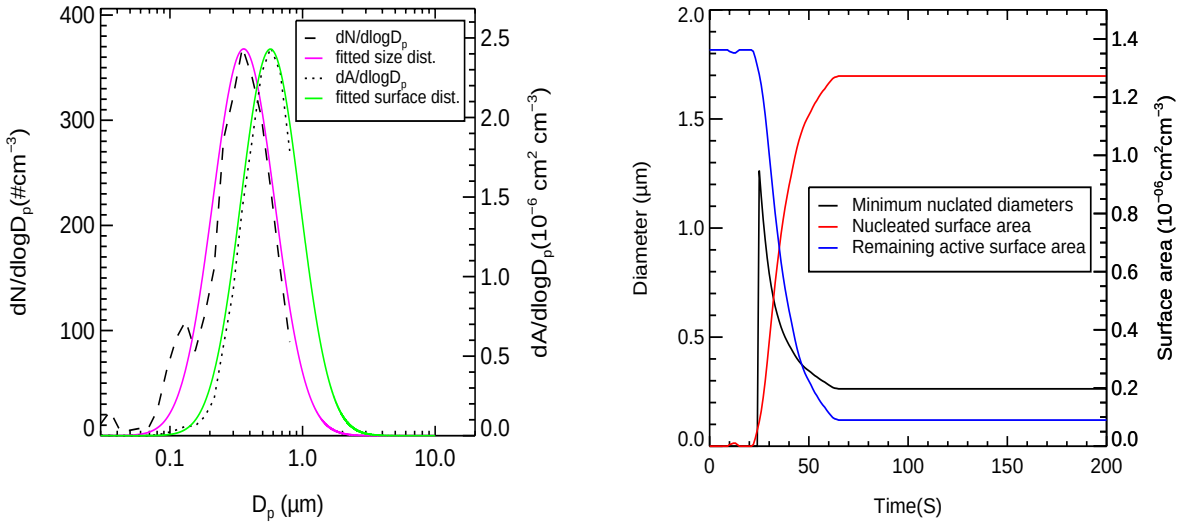

Figure 5.39: **Left panel,** number distribution (dashed black line) and surface area distribution (dotted black line) in experiment IN02_147. The fitted log-normal distributions are shown in magenta and green, respectively. **Right panel,** black line: minimum diameter of dust particles which have nucleated ice crystals; red line: surface area of those particles which have nucleated ice crystals; blue line: remaining active surface area.

Note that, once heterogeneous ice nucleation has started, the active surface area density $A_{total}(t)$ starts to decrease because frozen particles do not contribute to $A_{total}(t)$. Therefore $N(t) = N(t=0) - n_{ice}(t)$, disregarding a small trivial correction for dilution by pumping. However, since the deposition nucleation probability scales with the surface area, large particles are more likely to form ice than

smaller ones. We have therefore assumed that the dust particles are activated strictly in the order of decreasing surface areas[3]. As a consequence, the shapes of the number and surface area distributions (shown in magenta and in green in Figure 5.39, left panel) change. This is illustrated in Figure 5.40, where that fraction of the number distribution which has been converted to ice *t* seconds after ice nucleation onset, and therefore is no longer available for subsequent deposition freezing, is shown as magenta-coloured area. The corresponding part of the surface area distribution which has contributed to deposition freezing until time *t*, and therefore is no longer active at later times, is shown in green.

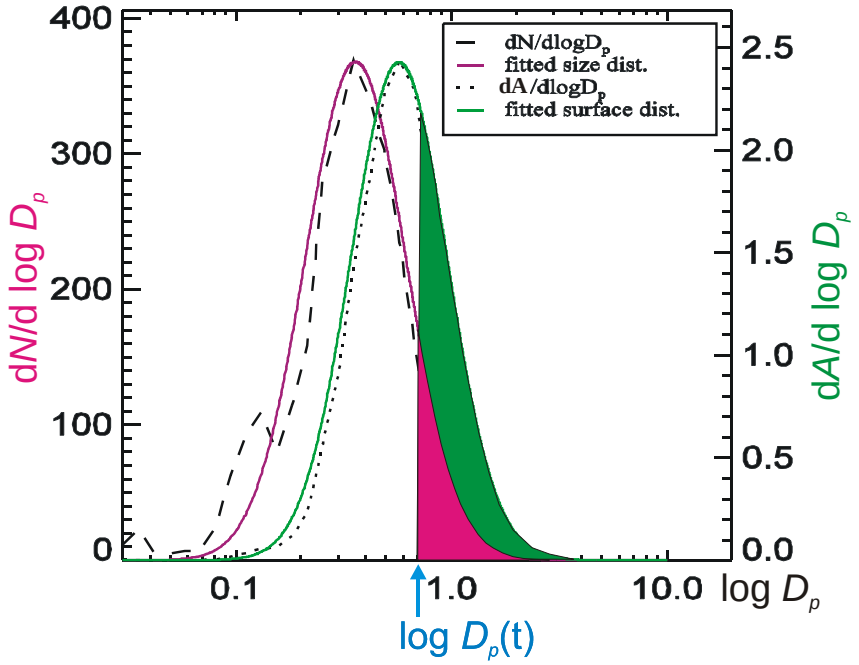

Figure 5.40: Illustration of the assumption that the mineral dust particles are activated in the order of decreasing surface area (see text for details). At time *t* after freezing onset the coloured areas of the size distribution / of the surface area distribution are no longer available for subsequent freezing, because they have already been converted to ice particles.

Since the number of ice particles $n_{ice}(t)$ is known from measurements with the OPC, red trace in Figure 5.38, the "minimum nucleated diameter" $D_p(t)$ (marked by the blue arrow in Figure 5.40) can be obtained by numerically solving the following implicit equation:

$$n_{ice}(t) = -\int_{D_p(t)}^{\infty} \frac{dN}{d\log D_p}\, d\log D_p \qquad (5.8)$$

However, the maximum number of ice particles $n_{ice,max}$ in Figure 5.38 *exceeded* the total number of dust particles N_{total} obtained by integrating the size distribution on the right-hand side of equation (5.8)

[3] This is a crude over-simplification, because there is always a probability ≠ 0 that smaller particles freeze while some larger particles still remain unfrozen.

from D_p = 0 to infinity. This physically unreasonable result is attributed to a calibration error of the DMA. It was eliminated by multiplying the right-hand side of equation (5.8) with a scale factor f_{scale} which yielded N_{total}(DMA) = N_{total}(CNC), green line in Figure 5.38. The "minimum nucleated diameter" $D_p(t)$ was then derived by solving the *corrected* implicit equation (5.8) for the measured ice particle numbers $n_{ice}(t)$, as illustrated by the sketch in Figure 5.40. The surface area distribution (see below) was of course multiplied with the same scale factor. Note that n_{ice}(t) equals the magenta-coloured area in Figure 5.40. Some results of this procedure, applied to experiment IN02_147, are shown in Figure 5.39, right panel: The black line shows how the "minimum nucleated diameter" D_p(t) evolves in time. As a consequence of the assumption that ice nucleation occurs strictly in the order of decreasing particle size, only dust particles with diameters larger than about 0.25 µm are converted to ice in this experiment. Also shown in red, right panel in Figure 5.39, is the already nucleated surface area:

$$A_{nucleated}(t) = -\int_{D_p(t)}^{\infty} \frac{dA}{d\log D_p}\, d\log D_p \qquad (5.9)$$

The blue line on the right panel of Figure 5.39 shows A_{total}(t=0) – $A_{nucleated}$(t). This is the remaining surface area which did not contribute to deposition freezing in this experiment. Note that ca. 95% of the available surface area is lost by deposition freezing. The frozen fraction n_{ice}(t)/N(t=0) which is shown in Figure 5.41 increased sharply at the freezing threshold to reach a maximum value of ca. 87% approximately 70 s after the vacuum pumps were switched on. Later on the frozen fraction starts to oscillate around this maximum value due to the poor counting statistics of the optical particle counter. We assume that the frozen fraction remains constant after reaching 87%, as indicated by the red horizontal line in the same Figure.

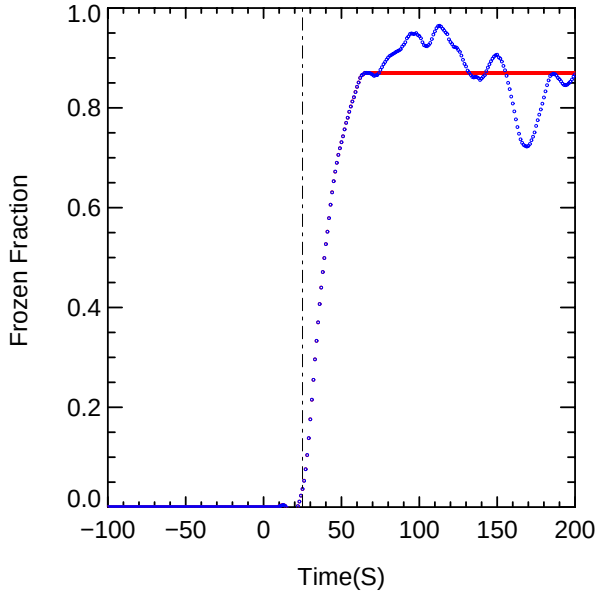

Figure 5.41: Fraction of mineral dust particles, which have contributed to ice formation by deposition freezing in experiment IN02_147

Now we have collected all the information which is needed to derive nucleation rates $J(T,S_{ice})$ from AIDA experiments. Our evaluation is based on equation (5.7), which can be rearranged as follows:

$$J(T,S_{ice}) = \left(\frac{dn_{ice}}{dt}\right)_{T,S_{ice}} \frac{1}{A_{total}(t)} = \left(\frac{dn_{ice}}{dt}\right)_{T,S_{ice}} \left(\sum_{D_{p(\min)}}^{D_p(t)} A(D_p)\right)^{-1} \qquad (5.10)$$

The IDL software provides an algorithm which calculates the time derivative $(dn_{ice}/dt)_{T,S}$ of the ice particle number density $n_{ice}(t)$ in Figure 5.38. We have shown above how the remaining active surface area $A_{total}(t)$, blue line on the right panel of Figure 5.39, can be derived from the corrected surface area distribution function, as illustrated in Figure 5.40. An IDL routine was written to derive nucleation rates $J(T,S_{ice})$ for each time step from the experimental data, applying, where necessary, corrections for dilution effects. The heterogeneous nucleation rate $J(T,S_{ice})$ for deposition freezing on Arizona test dust in experiment IN02_147 is shown in Figure 5.42. It increases sharply after freezing onset for about 20 seconds, then oscillates around a maximum value of about 1.4×10^7 # cm^{-2} s^{-1}. The abrupt collapse of the nucleation rate to $J = 0$ may be an artefact: it may result from the assumption that the fraction of activated dust particles remains *exactly* constant after reaching a maximum of 87%.

To better understand the time dependence of the nucleation rate $J(T,S_{ice})$ in Figure 5.42, we consult the time dependence of the saturation ratio S_{ice}, Figure 5.43, which is expected to strongly affect the nucleation rate by deposition freezing. We find that the ice formation threshold hardly exceeds RH_{ice} = 100%. The relative humidity with respect to ice, green noisy line, continues to increase for about 15 s, but hardly exceeds 104% RH_{ice}. At longer times, the relative humidity with respect to ice seems to decrease again until it reaches RH_{ice} ~100% about 70 seconds after pump start (this is not quite clear because of increasing noise on the TDL signal). This is in keeping with the observation in Figure 5.42 that the nucleation rate $J(T,S_{ice})$ drops to zero after 70 seconds.

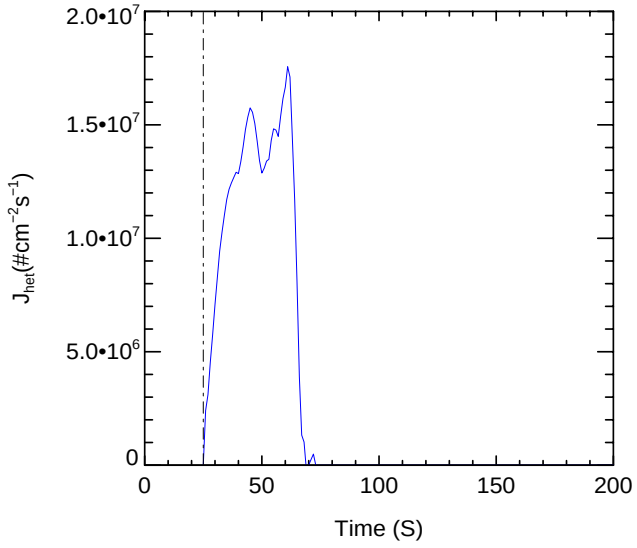

Figure 5.42: Time evolution of the heterogeneous nucleation rate by deposition freezing on Arizona test dust in experiment IN02_147.

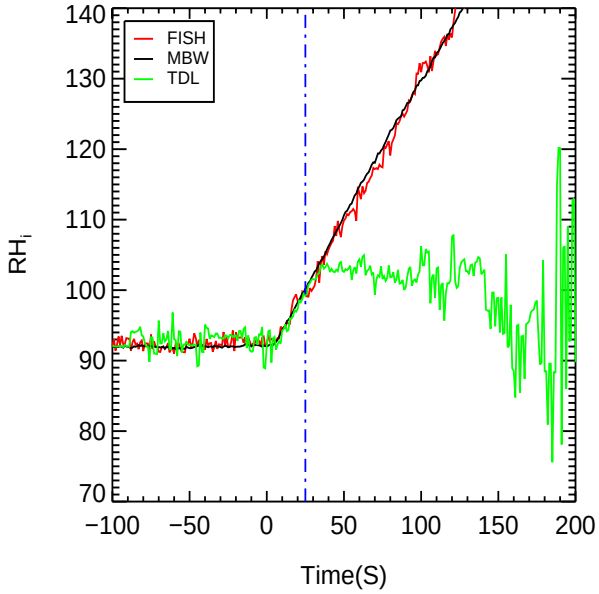

Figure 5.43: Relative humidities with respect to ice, using the Tunable Diode Laser system which measures water vapour in situ (TDL, green line), as well as ex situ measurements with the FISH and MBW hygrometers. The ex situ measurements include water vapour from ice crystals which evaporate in the heated sampling line. Experiment IN02_147 with Arizona test dust.

5.7.1 Temperature and Humidity Dependence of Nucleation Rates for Deposition Freezing

We have used the IDL-based methodology described above to determine heterogeneous nucleation rates for a wide range of temperatures and relative humidities RH_{ice} (= 100 × saturation ratios S_{ice}). Included are experiments with Arizona Test Dust (ATD), Saharan Dust (SD), and Asian Dust (AD). Only those data were selected for the evaluations were the formation of ice crystals was unambiguously due to deposition freezing. The results are presented as a pseudo-3D semi-logarithmic bar graph in Figure 5.44. The oval symbols (colour codes: red, cyan, and black for ATD, SD, and AD, respectively) represent the nucleation rates on the vertical log scale. The corresponding temperatures and relativities over ice are identified by the foot points of the red bars in the quasi-horizontal plane, which is spanned by the coordinates RH_{ice} and T. A more detailed discussion of these results will be presented in chapter 6, section 6.5.

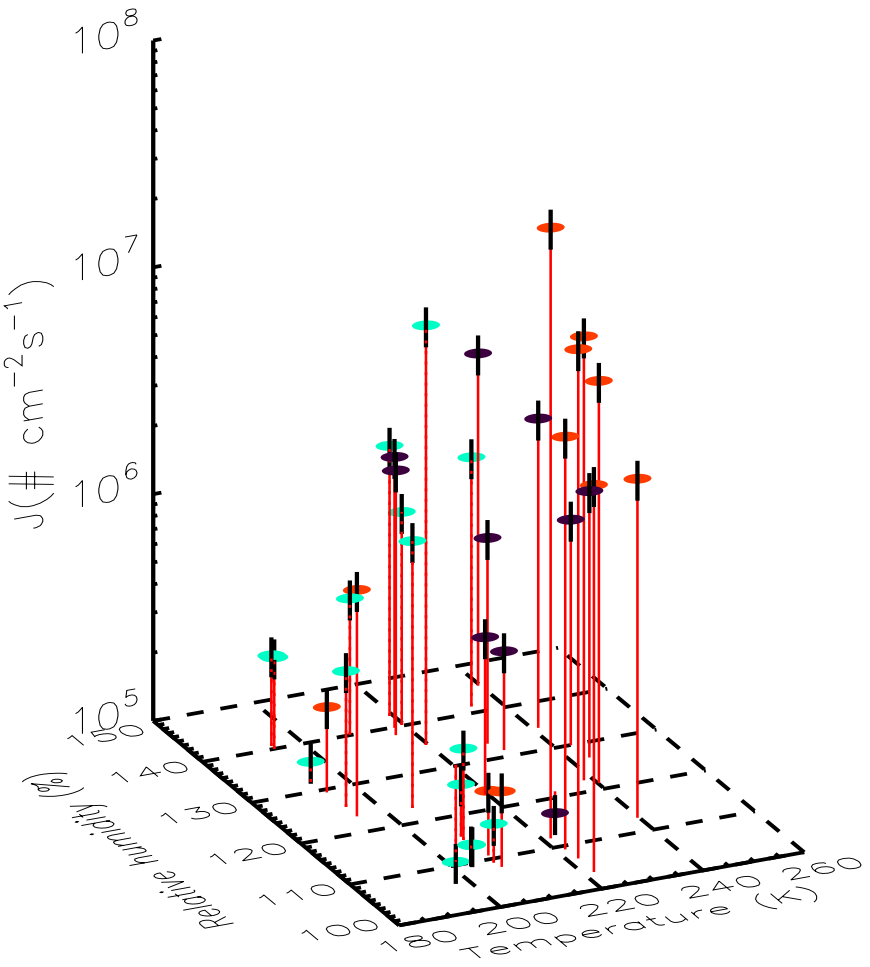

Figure 5.44: Pseudo-3D plot of the nucleation rates for deposition freezing on Arizona Test Dust (ATD, symbols in red), Saharan Dust (SD, symbols in cyan), and Asian Dust (AD, black symbols). The corresponding temperatures and relative humidities over ice are marked by the foot points of the red vertical bars. The estimate error ranges of the nucleation rates are shown in black.

6. Discussion and Conclusions

This chapter will be organised as follows:

- Section 6.1 is divided into three sub-sections: The first one is devoted to homogeneous ice nucleation probabilities in aqueous solution droplets, which – according to the work of Koop et al. (2000) - are functions of temperature T, droplet volume V, and water activity a_w only, regardless of chemical composition. The second sub-section summarises an analysis of FIRE-II campaign data which prompted Heymsfield and Miloshevich (1995) to propose a new T-dependence of threshold relative humidities RH_{ice} for cirrus formation. The last sub-section focuses on a comprehensive data set of RH_{ice} and T which were measured in the upper troposphere and lower stratosphere during the INCA project (**IN**terhemispheric differences in **C**irrus properties from **A**nthropogenic emissions; co-ordinated by DLR).
- Section 6.2 summarises results from microphysical investigations of dust samples in relation with their ice nucleating properties.
- Section 6.3 is divided into three sub-sections: The first one summarises threshold relative humidities RH_{ice} for different kinds of pristine and coated mineral dust samples from AIDA chamber experiments. These are compared in the second sub-section with other laboratory results, in particular with those of Bailey and Hallett (2002). A novel comparison between threshold relative humidities $RH_{ice}(T)$ from AIDA experiments and field observations is presented in the third sub-section.
- Section 6.4 presents a comparison between ice water contents of artificial cirrus in the AIDA chamber and natural cirrus.
- Section 6.5 concludes chapter 6 with a summary of nucleation rates for deposition freezing which have been derived from AIDA measurements with different types of mineral dust.

6.1 Parameterisations of Homogeneous Droplet Freezing Rates

6.1.1 Water Activity-based Homogeneous Freezing Rate Parameterisation

Koop et al. (2000) found convincing evidence from numerous measurements of concentration-dependent homogeneous freezing temperatures of small solution droplets, as well as from pressure dependent freezing point measurements of pure water droplets, that the homogeneous nucleation rate J in these systems is a unique function of the water activity only, i.e. *independent of the chemical nature*

of the solute. They hypothesized that the homogeneous freezing temperatures $T(a_w)$ of equally sized solution droplets, when plotted versus their water activities a_w, can be obtained from the melting points $T(a_w^i)$ of pure water ice in contact with aqueous solutions at the same temperature by displacing the melting point line on the a_w-scale by an amount

$$\Delta a_w = a_w - a_w^i \quad , \tag{6.1}$$

where a_w is the water activity of, or alternatively, the saturation ratio S_w(T) in equilibrium with a solution droplet which freezes at $T(a_w)$, and a_w^i is the water activity of a solution in equilibrium with pure water ice at the *same* temperature. Note that a_w^i(T) can be expressed as the difference between the chemical potentials μ_w^i(T) of pure ice and μ_w^0(T) of pure liquid water at the given temperature:

$$\ln(a_w^i) = \frac{\mu_w^i(T) - \mu_w^0(T)}{RT} = \frac{\Delta\mu_{i,w}(T)}{RT} \tag{6.2}$$

This difference vanishes at the melting point of pure water ice, 273.15 K, where the pure phases are at equilibrium. The authors present the following parameterisation for $\Delta\mu_{i,w}$, which is valid from the freezing point 273.15 K to 150 K:

$$\Delta\mu_{i,w}(T) = \mu_w^i(T) - \mu_w^0(T) = 210368 + 131.438\,T - 3.32373\times10^6\,T^{-1} - 41729.1\ln T \tag{6.3}$$

The shift Δa_w in equation (6.1) for solution droplets of a given volume V cm^3 which freeze after spending (on average) Δt seconds at the temperature T relates with the freezing probability P(T) *via* the nucleation rate $J(T)$ as follows:

$$P(T) = 1 - \exp(-J(T)V\Delta t) \tag{6.4}$$

The freezing probability P which can be experimentally observed with a given time resolution Δt defines the nucleation threshold. It depends on the sensitivity of the experimental method. E.g., Haag et al. (2003) assumed that a freezing probability of 0.63 can be detected with a time resolution Δt = 1 s when a sulphuric acid aerosol freezes homogeneously in a typical AIDA chamber experiment.

If the above hypothesis of Koop et al. (2000) is correct, the homogeneous nucleation rate J of aqueous solution droplets should also be a unique function of the water activity a_w, independent of their chemical composition. Koop et al. (2000) recommend the following parameterisation of the nucleation rate which fits numerous experimental results in the range $0.26 < \Delta a_w < 0.34$:

$$\log(J) = -906.7 + 8502\,\Delta a_w - 26924(\Delta a_w)^2 + 29180(\Delta a_w)^3 \tag{6.5}$$

We have used the above formalism to calculate critical ice saturation ratios S_{ice} for solution droplets (e.g. sulphuric acid droplets) of 0.5 μm diameter, assuming that a freezing probability P = 0.5 can be detected with a time resolution of 1 s in AIDA chamber experiments. This yields critical ice saturation

ratios $S_{ice,crit}(T)$ which correspond to a nucleation rate $J = 10^{10}$ cm^{-3} s^{-1}. The function $S_{ice,crit}(T)$ is included as a green line in Figure 6.1.

6.1.2 Critical Ice Saturation Ratios $S_{ice,crit}(T)$ Based on Field Observations before 1995

Five years before the work of Koop et al. (2000), which is entirely based on laboratory data, Heymsfield and Miloshevich (1995) had already parameterised critical relative humidities with respect to liquid water $RH_{crit}(T)$ which give rise to the formation of cirrus clouds under tropospheric conditions. The authors assumed that the appearance of cirrus ice was due to a rapid transition from solution droplets to ice crystals when a critical relative humidity RH_{crit}(T) was exceeded. Their parameterisation was based on a numerical analysis of microphysical field measurements in orographic wave clouds, and in cirrus clouds during the FIRE-II project (FIRE stands for **F**irst **I**nternational Cloud Climatology Project **R**egional **E**xperiment). The following equation describes an envelope of the observed peak relative humidities with respect to supercooled liquid water for ice formation, which were measured with a frost point hygrometer in updrafts. The envelope was assumed to represent the critical relative humidities addressed above:

$$RH_{crit,water}(T) = 188.92 + 2.81(\mathrm{T} - 273.15) + 0.013336(\mathrm{T} - 273.15)^2 \quad (6.6)$$

The authors have used the Goff-Gratch equation (Murphy and Koop, 2005) for the equilibrium vapour pressure of supercooled liquid water in their calculation of relative humidities. We have used the equilibrium vapour pressure of ice after Marti and Mauersberger (1993) to convert their parameterisation of critical relative humidities with respect to supercooled liquid water, equation (6.6), into critical relative humidities with respect to ice. The result is included as a red line in Figure 6.1.

6.1.3 Critical Ice Saturation Ratios $S_{ice,crit}(T)$ Based on Humidity Data from the INCA Project

Although large differences exist between natural cirrus and artificially generated ice clouds in the AIDA chamber, we have attempted to compare data sets from AIDA simulation experiments with measurements of relative humidities in- and outside cirrus clouds which were measured during the INCA project (**IN**terhemispheric difference in **C**irrus properties form **A**nthropogenic emissions)[1].

[1] We are indebted to Prof. Ulrich Schumann, director of IPA-DLR Oberpfaffenhofen, for allowing us to use the INCA data, and to Andreas Minikin for his help.

A frost point hygrometer and other instruments on the research aircraft FALCON of DLR had measured relative humidities over ice and other atmospheric parameters during two campaigns in March/April 2000 and September/October 2000, respectively. The first campaign was launched from the airport of Punta Arenas at 53°S in Chile and covered higher latitudes of the Southern Hemisphere. The second campaign, based in Prestwick, Scotland at 55°N, covered higher latitudes of the Northern Hemisphere. The flights during both campaigns summed up to a total of 130 flight hours. For our purposes we have selected the complete data set of 1 min time averaged relative humidities over ice, both inside and outside of cirrus clouds. These RH_i data are plotted as function of the air temperature in Figure 6.1, left panel. The sloping black line is the water saturation line. The green line denotes the homogeneous freezing threshold of solution droplets according to the work of Koop et al., see section 6.1.1 for details. The red line is based on the parameterisation of Heymsfield and Miloshevich (1995) and describes the envelope of peak relative humidities which had been measured in the updraft regions of wave clouds, see section 6.1.2 for details.

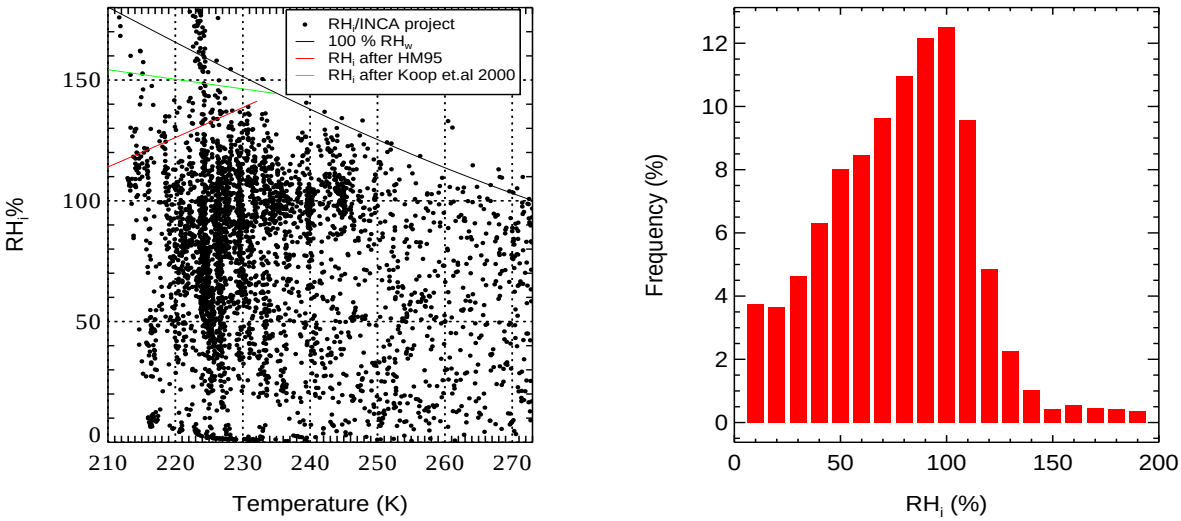

Figure 6.1: Left panel, scatter plot of relative humidities with respect to ice (RH_i, 1 minute time averages) which were measured during the INCA project 2000 inside and outside of cirrus clouds. The sloping black line marks 100% relative humidity with respect to super-cooled liquid water; the green line, which marks the homogeneous freezing threshold for solution droplets, is based on the work of Koop et al. (2000); the sloping red line is an envelope of measured peak relative humidities in the updraft regions of wave clouds (Heymsfield and Miloshevich, 1995), see text for details. The right panel is a frequency distribution of those relative humidity data which are shown on the left panel.

Also shown in Figure 6.1 (right panel) is a frequency distribution of the relative humidities over ice, binned into intervals of 10% RH_i, which is based on all 1 minute time averaged RH_i data from the INCA campaign (left panel in Figure 6.1). The peak is at 100% relative humidity, which represents equilibrium conditions between ice particles and the interstitial air within the cirrus clouds. Relative humidities in excess of 100% represent supersaturated air in updrafts. Their frequency of occurrence decreases rapidly to about 0.5% at 150% RH_i, remaining approximately constant afterwards. Only 2% of all data exceed 160% RH_i. This implies that the uppermost 2% of all data are outliers, invalid due to instrumental scatter. We have therefore marked the highest 2% of the RH_i data from the INCA campaign as *invalid* outliers. We will recur to this classification when comparing the INCA data set with the threshold relative humidities observed in AIDA chamber experiments in section 6.3.3.

6.2 The Impact of Particle Shape on Their Ice Nucleating Activity

It is very likely that the micro-morphology of dust particles, e.g. their surface roughness, has an influence on their ice nucleating activity. However, surface roughness is very difficult to investigate because it is not clearly defined, and varies from particle to particle. We have therefore chosen a much simpler shape parameter to represent large variations in surface roughness between different types of mineral dust particles. For this purpose, we have used Imatec software to analyse SEM images of dust particles which were collected on filters. This enabled us to determine percentages of spherical and non-spherical particles for different types of mineral dust. The results are listed in Tables 5.1 – 5.3, chapter 5 section 5.3. They seem to indicate that, for all types of mineral dust studied, larger percentages of spherical particles lead to more dust particles being converted to ice crystals in AIDA expansions under otherwise similar conditions. However, the effect is not dramatic, and is furthermore dependent on the ability of the Imatec software to distinguish spherical from non-spherical particles in clusters, cf. Figure 5.9.

6.3 Threshold Relative Humidities for Ice Nucleation

6.3.1 Heterogeneous Ice Nucleation Thresholds

Figure 6.2 summarises nucleation thresholds of all pristine dust samples which were investigated in AIDA chamber experiments and have been analysed in this work. Nucleation thresholds for sulphuric acid-coated ATD and SD samples are shown separately in Figure 6.3. Note that both figures show weighted means of nucleation thresholds. The means have been derived from clusters of measurements in narrow temperature intervals, and are plotted versus the mean cluster temperature in Figures 6.2 and 6.3. The complete data sets can be found in chapter 5.6. We also note that the

thresholds observed in the mixed cloud regime, which is marked at the top of the figures, include cloud droplet activation thresholds which did not – or not immediately – lead to the formation of ice crystals, particularly at the highest temperatures above 260 K where only very small amounts of ice crystals could be identified with a cloud particle imager (CPI) in a large excess of super-cooled liquid cloud droplets which did not freeze immediately.

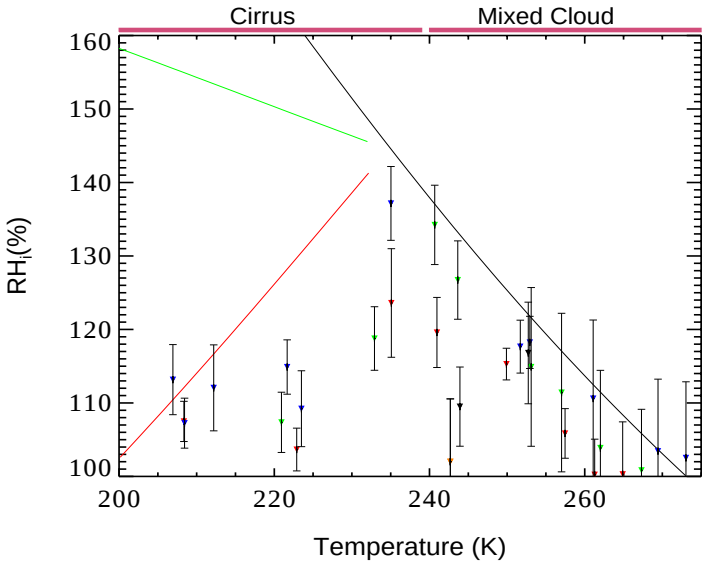

Figure 6.2: As in Figure 5.20b but for ATD (▼), SD (▼), AD (▼), and CD1 (▼) and its mixture with CD2 (▼). The green line (—) denotes the freezing threshold for aqueous solution droplets of 0.5 µm diameter, following the work of Koop et al. (2000). The black line (—) represents liquid water saturation. The red line (—) denotes the parameterisation of Heymsfield and Miloshevich (1995).

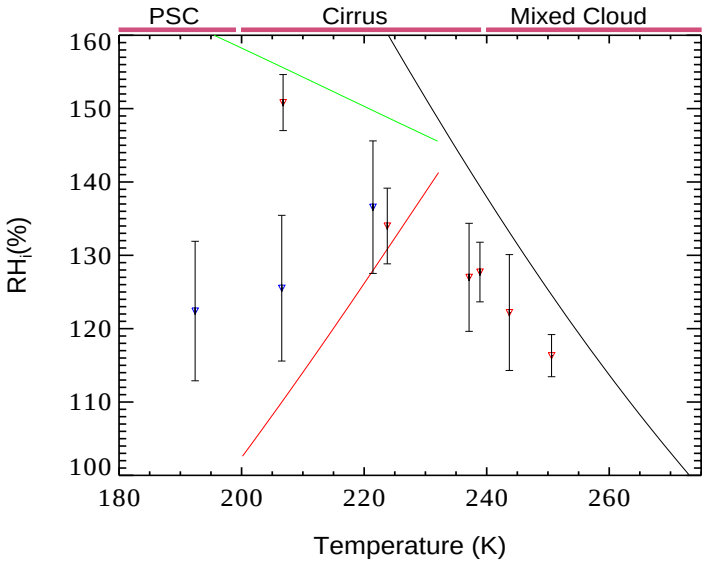

Figure 6.3: As in Figure 5.21b but for dust samples which had been coated with sulphuric acid: ATD (▽) and SD (▽). The other lines are the same as in Figure 6.2.

Mixed cloud Conditions:

The temperature range where mixed clouds can be formed is marked on top of Figures 6.2 and 6.3. In the temperature range 273 to about 250 K, liquid cloud droplets were observed to form on pristine mineral dusts before small amounts of ice crystals were detected with the cloud particle imager, or almost simultaneously. The cloud formation thresholds evolve parallel to, but somewhat below the water saturation line. However, since it is not possible to form cloud droplets below liquid water saturation, we must conclude that the relative humidity measurements are systematically too low, or that the particles behaved as if partially soluble. In other words, no deposition freezing seems to occur at these high temperatures, and the small percentages of ice particles which have been observed by the CPI are most likely due to condensation or immersion freezing, initiated by a few very active dust particles in the supercooled droplets. However, at temperatures below about 250 K, the CPI data indicate that significant numbers of ice crystals were already formed *before* supercooled droplets could condense on an excess of less active dust particles at the water saturation line. This implies a transition from condensation freezing which requires water saturation, to deposition freezing which occurs below the water saturation line. There is evidence that the transition temperature depends on the nature of the dust particles. E.g., the CPI data (Figure 5.24) indicate that more ice crystals than supercooled cloud droplets nucleate on ATD at temperatures as high as 254 K. This lends credibility to the low threshold relative humidities, red triangles in Figure 6.2, which imply that deposition freezing *does* occur at relatively warm temperatures on this exceptionally active material. In contrast, activation of SD and AD requires water saturation even at 240 K, which implies that immersion or condensation freezing are the predominant modes of ice nucleation on these materials throughout the mixed cloud regime. Notable exceptions in Figure 6.2 are the very low (and carefully cross-checked, see end of Section 5.2) ice nucleation thresholds of CD1 and of a mixture between CD1 and CD2, black and orange triangles in the temperature range 242 – 244 K, which must be due to deposition freezing.

The freezing thresholds of sulphuric acid-coated ATD in the mixed cloud regime, the only type of coated mineral dust studied in this regime, do not differ significantly from those of uncoated ATD within the combined error limits of the measurements.

Cirrus cloud conditions:

The cirrus cloud regime, with an upper bound at the homogeneous freezing threshold of pure water droplets, and a more arbitrarily chosen lower bound at 200 K, is marked at the top of Figures 6.2 and 6.3. Supercooled droplets of pure water cannot persist in this regime, and deposition nucleation is the only feasible mode of ice nucleation on *insoluble* particles like pristine mineral dust below the water saturation line. The threshold relative humidities for ice nucleation in AIDA chamber experiments on

uncoated ATD, SD, and AD in the cirrus cloud regime exhibit similar temperature dependencies, with the largest differences being observed at the highest temperature of 235 K where SD requires nearly water saturation to nucleate ice in the AIDA chamber, while the threshold relative humidity RH_i for ice nucleation on ATD was nearly a factor of two lower. The temperature of 235 K seems to mark a sharp reduction of the threshold RH_i, from close to water saturation (with a few exceptions, see above) to values in the order of 110% RH_i or less, below 225 K. There are unfortunately no experimental data between 225 K and 235 K (with the exception of AD which nucleates ice at an intermediate RH_i of about 120% at 233 K) to resolve the temperature dependence of this transition.

The conclusion drawn from numerous AIDA experiments that deposition nucleation occurs in the cirrus cloud regime on various kinds of mineral dust at much lower super-saturations than required by solution droplets to freeze homogeneously has important implications for the atmosphere: it implies that deposition freezing, whenever mineral dust particles are present in the upper troposphere, can lower the onset of ice nucleation from the "Koop threshold" for homogeneous freezing of solution droplets (green line in Figure 6.2) by as much as 50% to relative humidities with respect to ice which are in the order of only 110% or even less.

This result sheds new light on the interpretation of field observations in wave clouds (data from the WAVE90 experiment) by Heymsfield and Miloshevich (1995). These authors concluded that the peak relative humidities which were measured in November 1990 in the updraft regions of wave clouds along the front range of the Rocky Mountains in northern Colorado (red line in Figure 6.2 and equation (6.6) in Section 6.1.2), represented freezing thresholds of solution droplets. This interpretation is, however, incompatible with the now widely accepted parameterisation of the homogeneous nucleation thresholds of solution droplets by Koop et al. (2000), green line in Figure 6.2. The idea of relative humidities peaking at the green line in Figure 6.2 is also not supported by airborne humidity measurements in- and outside of cirrus clouds during the INCA campaign, Figure 6.1a, which seem to support the homogeneous freezing threshold parameterisation of Koop et al. (2000). We therefore speculate that the decrease of the peak relative humidities towards lower temperatures, red line in Figure 6.2 as well as data shown on Fig. 9b in the paper of Heymsfield and Miloshevich (1995), was due to the accidental presence of heterogeneous ice nuclei such as mineral dust particles. It is well known that large amounts of mineral dust from Asian deserts are transported across the Pacific to the US (D. Jaffe et al., 2003; VanCuren and Cahill, 2002) and further inland. Although desert dust events in Asia show a strong seasonality, being strongest in spring and weakest in winter, there is evidence that the advection of dust from Asia to the Western US is quasi-continuous for much of the year when anthropogenic particulate matter is included (VanCuren and Cahill, 2002; VanCuren et al., 2005). DeMott et al. (2003b) have conducted field measurements of ice nuclei with a continuous flow ice-thermal diffusion chamber in combination with a laser mass spectrometer for

single particle analysis in the Rockies at a high mountain site (elevation 3,200 m) in western Colorado during November 2001. Although they found less than 0.03 cm^{-3} heterogeneous ice nuclei[2] during the observation period (as expected in view of the seasonality of Asian dust episodes), they conclude that even these very low concentrations of heterogeneous ice nuclei can affect the formation of cirrus clouds at low or limited cooling rates.

Dual ice nucleation thresholds have indeed been observed at rapid cooling rates in AIDA chamber experiments with mineral dust in the cirrus cloud regime (Field et al., 2006): The first one at ice saturation ratios of 1.1 to 1.3 was attributed to deposition freezing on pristine dust particles, in agreement with this work, while the interpretation of the second ice nucleation threshold at significantly higher ice saturation ratios remained inconclusive. The most likely explanation was immersion freezing of partially soluble particles (probably impurities).

Very recently, an alternative (but likewise heterogeneous) ice nucleation mechanism has been proposed by Abbatt et al. (2006) to explain the field observations of Heymsfield and Miloshevich (1995) and their parameterisation of an ice nucleation threshold in the cirrus cloud regime, red line in figures 6.2 and 6.3, as well as results of DeMott et al. (2003b) from measurements on a mountain top in the Rockies in November 2001 (see above) who found that an extremely small fraction of presumably ammoniated sulphate particles can act as ice nuclei at low ice supersaturations. Abbatt et al. propose that very few *solid* ammonium sulphate particles may be present, acting as deposition freezing nuclei in a large excess of supercooled liquid haze particles. In fact, depending on the ammonium-to-sulphate ratio and the presence of other compounds including e.g. organic acids, the Gibbs phase rule predicts that the solid phase of a soluble compound (like ammonium sulphate) can be thermodynamically stable in contact with a solution which contains at least one other soluble compound. This implies that ammonium sulphate (like other soluble solids) can induce immersion freezing.

Only few AIDA simulation runs have been carried out in the cirrus cloud regime with sulphuric acid-coated ATD and SD particles. The results are summarised in Figure 6.3. They reveal that the coatings raise the nucleation thresholds above those of pristine dust particles. The threshold relative humidities are scattered between the red line (parameterisation of Heymsfield and Miloshevich, 1995) and the green line which represents the freezing threshold of solution droplets according to Koop et al. (2000). This can be expected if the nucleation thresholds depend on the type of mineral dust as well as on the amount of the sulphuric acid coating which is likely to react with the

[2] It is important to note that the sensitivity of the continuous flow diffusion chamber is limited to individual particles which nucleate ice crystals that grow to detectable sizes on a time scale of about 10 s.

solid substrate. As already mentioned in the previous paragraph, condensation freezing due to the soluble coatings is a likely explanation for this behaviour.

Polar stratospheric cloud conditions:

The results of many AIDA experiments with ATD and SD in the polar stratospheric cloud regime have been amalgamated into a red and a blue triangle at about 194 K in Figure 6.2. Note that the triangles are the means of several fairly reproducible nucleation thresholds which were measured at similar temperatures with either ATD or SD. The full data set can be found in Figures 5.20a and 5.26a. There is clearly a trend to somewhat higher deposition nucleation thresholds in the PSC regime than in the lower cirrus temperature regime. However, the trend is not dramatic, and the nucleation threshold for deposition freezing on pristine ATD and SD remains much lower than the homogeneous freezing threshold of solution droplets, green line in Figure 6.2. – Coating with sulphuric acid, which was only investigated once for SD, had no significant effect on the nucleation threshold.

6.3.2 Comparison with other Laboratory Studies

Generally, it is difficult to compare results of ice nucleation experiments in the AIDA chamber with those obtained in other laboratories. This is in part due to the heterogeneity of the investigated mineral dust particles which may differ in terms of chemical composition, size, shape, and surface morphology. In spite of all these difficulties, we have made an effort to explore the shape effect on the ice nucleation efficiency of mineral dusts, see section 6.2 of this chapter. Another difficulty arises from the vastly different experimental techniques. It is particularly problematic to compare heterogeneous ice nucleation thresholds $S_{ice,crit}(T)$ for deposition freezing on pristine particles, because these are functions of the active surface area, the observation time, and the sensitivity to detect ice which depend on the experimental technique. Wherever possible, heterogeneous nucleation rates $J(T,S_{ice})$ should be compared rather than nucleation thresholds. Rates $J(T,S_{ice})$ for deposition freezing, which can be derived on the basis of equation (5.7) in section 5.3, should ideally be independent of the experimental technique.

The results from AIDA chamber experiments will be compared with the following laboratory studies:

- Bailey and Hallett (2002) used a cylindrical static diffusion chamber which was capped with horizontal ice-coated surfaces to determine nucleation thresholds and study the habits of ice crystals formed on different substrates. The ice surfaces were held at slightly different temperatures to establish a well defined vertical ice supersaturation profile along the cylinder axis. The profile varied along a clean glass filament which was shown to be a poor substrate for ice nucleation, and thus could be used as a quasi inert substrate for other more active ice

nucleating materials. The nucleation of ice crystals on the surface of a clean glass filament, and alternatively on either micron-sized kaolinite or AgI particles adhering to the filament, was recorded with a video camera with microscope optics to determine threshold relative humidities $S_{ice,crit}(T)$.

- The second study was performed by Archuleta et al. (2005) with size-selected (D_p = 50, 100, and 200 nm) particles of various oxides and with genuine Asian dust, with and without sulphuric acid coatings. Threshold relative humidities $S_{ice,crit}(T)$ were determined by means of a continuous flow ice-thermal diffusion chamber. We have chosen their results with aluminium silicate ($3Al_2O_3$:$2SiO_2$) and Asian dust particles (D_p = 200 nm) for comparison because these materials are fairly similar to the materials investigated in the AIDA chamber studies.

Critical saturation ratios $S_{ice,crit}(T)$ for ice nucleation on various materials from the work of Bailey and Hallett (2002), and selected results from the work of Archuleta et al. (2005), can be directly compared with the results from AIDA chamber experiments in Figure 6.4. This leads us to the following conclusions:

Although the technique as well as the substrates studied by Bailey and Hallett (2002) differ in several respects from the AIDA chamber experiments, we can point out some striking similarities between the temperature dependencies of the ice nucleation thresholds, $S_{ice,crit}(T)$, for various materials in Figures 6.4a and 6.4b (= Figure 6.2, see above). There is a clear trend in the nucleation thresholds reported by Bailey and Hallett and those observed in AIDA chamber experiments to peak at the temperature where the green and the red lines (parameterisations of Koop et al., 2000, and of Heymsfield and Miloshevich, 1995, respectively) intersect with the black sloping line which marks liquid water saturation. This intersection occurs very close to the transition from the mixed cloud to the cirrus cloud regime. To the right of this singularity, i.e. essentially in the mixed cloud regime, two types of materials seem to exist:

1. Materials with very low ice nucleation activities (e.g. clean glass fibres in the work of Bailey and Hallett; Asian dust (AD) in the AIDA chamber studies), which require liquid water saturation to form droplets or liquid water films before nucleating ice by immersion freezing.

2. Materials which are very active (e.g. AgI and kaolinite particles in the work of Bailey and Hallett; CD and possibly ATD particles in AIDA studies) which act as ice nuclei at significantly less than 100% RH with respect to water, at least below about 250 K.

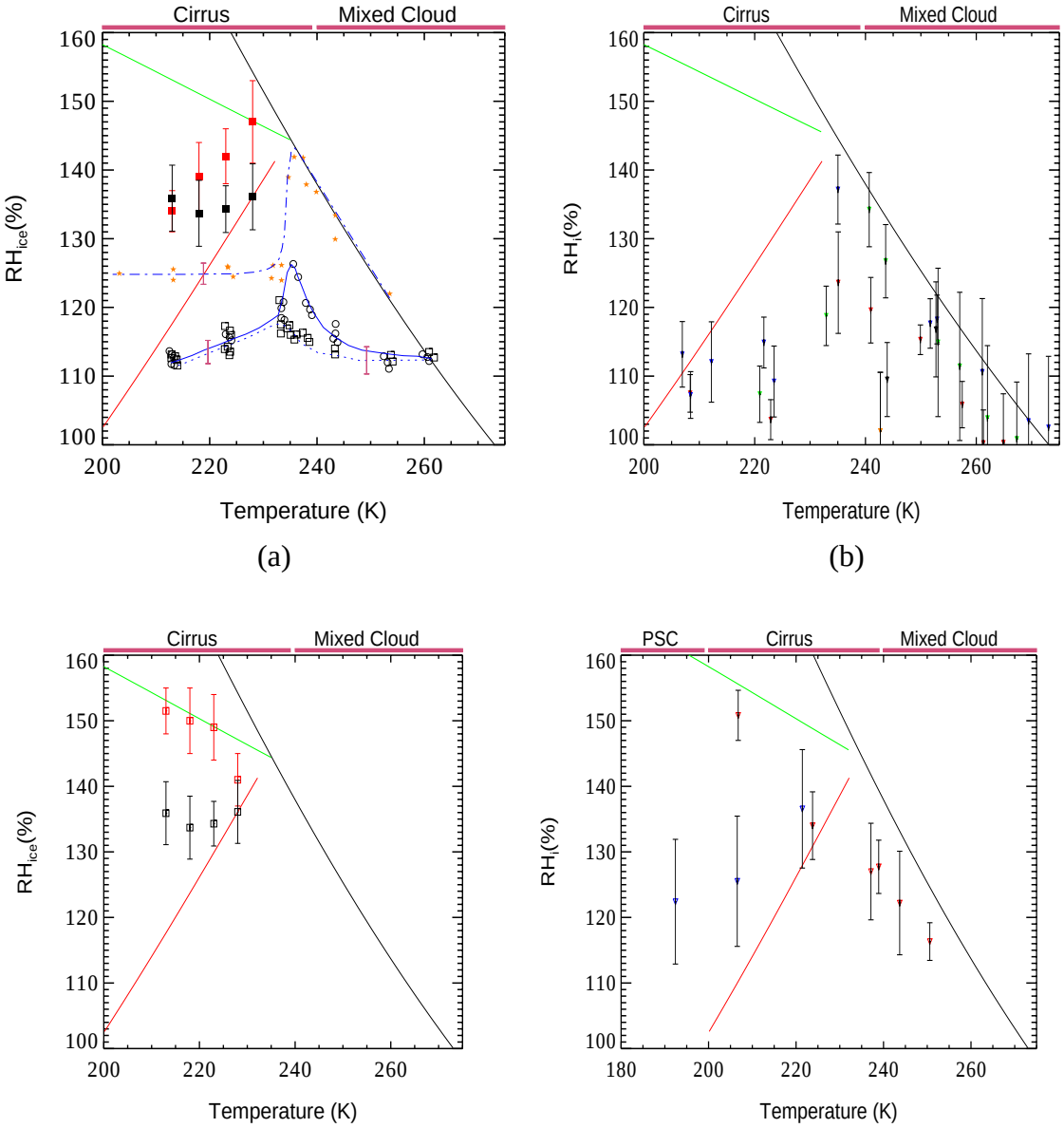

Figure 6.4:

(a) $S_{ice,crit}(T)$ after Bailey and Hallett (2002) for ice nucleation on the following materials: clean glass filament (★), µm-sized particles of AgI (○) and kaolinite (□). Also shown are $S_{ice,crit}(T)$ for monodispersed (D_p = 200 nm) aluminium silicate (■) and Asian dust particles (■), after Archuleta et al., 2005.

(b) $S_{ice,crit}(T)$ from AIDA experiments with ATD (▼), SD (▼), AD (▼), CD1 (▼), and CD1+CD2 particles (▼).

(c) $S_{ice,crit}(T)$ for H_2SO_4-coated aluminium silicate (□) and Asian dust particles (□), after Archuleta et al., 2005.

(d) $S_{ice,crit}(T)$ from AIDA experiments for H_2SO_4-coated ATD (▽) and SD (▽) particles.

To the left of the singularity, i.e. in the cirrus cloud regime, all solid substrates seem to act as ice nuclei, although with different efficiencies. Note, however, that for the reasons outlined in the introduction to section 6.3.2, it is dangerous to compare critical ice nucleation thresholds which have been measured by different techniques. E.g., particles with much larger surface areas were exposed by Bailey and Hallett than those used in AIDA chamber experiments: larger particles tend to induce ice nucleation at lower relative humidities. On the other hand, the detection limit of the static ice-diffusion chamber for ice nuclei (in terms of the fraction $\Delta n/n$ of all particles which yield ice crystals of a detectable size after spending Δt seconds at a given super-saturation) was significantly lower than in the AIDA chamber experiments.

Also shown in Figure 6.4a are nucleation thresholds for aluminium silicate particles and Asian dust particles from the work of Archuleta et al. (2005). Their results imply that commercial aluminium silicate ($3Al_2O_3{:}2SiO_2$) particles are poor ice nuclei, which is a surprising result. However, although the chemical composition of the artificial silicate is similar to that of natural clay minerals, it may differ in structure and surface properties. One is inclined to conclude, by comparing Figures 6.4a and 6.4b, that the Asian dust particles studied by Archuleta et al. are much poorer ice nuclei than the AD material used in our AIDA experiments. However, both materials turn out to be very similar in terms of their heterogeneous nucleation rates $J(T,S_{ice})$, as will be shown in section 6.5.

Figures 6.4c and 6.4d present some results for coated particles, both from the work of Archuleta et al. (2005) and from AIDA chamber experiments. Archuleta et al. present results for sulphuric acid-coated aluminium silicate particles, which have no direct counterpart in AIDA chamber experiments. Furthermore, they interpret their data for pristine Asian dust as being due to a soluble coating of unknown chemical composition (because the particles exhibited a significant growth factor at high relative humidities), and calculate a heterogeneous nucleation rate $J(T,S_{ice}) \approx 8\times10^5$ cm^{-2} s^{-1}, using the equivalent of our equation (6.9). However, they interpret their result as an ***immersion freezing rate***. Whether the derived nucleation rate $J(T,S_{ice}) \approx 8\times10^5$ cm^{-2} s^{-1} is due to deposition freezing, as was assumed in AIDA experiments with uncoated Asian dust, or must be interpreted as an immersion freezing rate due to the presence of a solution film of soluble impurities, remains an open question. Note that both nucleation mechanisms are fundamentally different according to current knowledge.

There is thus little basis for a direct inter-comparison between the nucleation thresholds of sulphuric acid-coated ATD and SD particles in AIDA chamber experiments, Figure 6.4d, and the results of Archuleta et al. (2005), Figure 6.4c, except that coatings with sulphuric acid tend to *increase* ice nucleation thresholds relative to those of pristine particles in most of the cases studied.

6.3.3 Comparison between Critical Ice Saturation Ratios $S_{ice,crit}(T)$ from AIDA Experiments and from INCA Flights

Although it is not possible (mainly due to the impact of the nearly isothermal chamber walls) to perfectly simulate with the AIDA chamber natural atmospheric processes like the formation of mixed clouds and cirrus clouds in rising and adiabatically cooling air masses, we make an attempt to compare AIDA chamber measurements of $S_{ice,crit}(T)$ for various pristine and sulphuric acid coated mineral dust particles with airborne field measurements of relative humidities over ice (RH_{ice}) in the upper troposphere / lower stratosphere. For this purpose we have analysed RH_{ice} data which were measured during the INCA campaign. Some salient features of this campaign have already been presented in section 6.1.3 and will not be repeated here. The RH_{ice} data are 1 min time averages, and include data from both the Northern and Southern hemispheres. The complete data set is plotted versus the air temperature in Figure 6.1a.

Our strategy was inspired by the approach of Heymsfield and Miloshevich (1995) in their analysis of relative humidity measurements from two aircraft campaigns: a series of wave cloud penetrations during the Wave90 experiment in November 1990, and cirrus cloud penetrations during the FIRE-II campaign, nearly exactly one year later in November 1991. These authors assumed that the envelope of the highest observed relative humidities over ice, RH_{ice}, is representative of $S_{ice,crit}$, the critical saturation ratio where ice nucleation takes place in adiabatically cooling updrafts. It appears reasonable to analyse the large number of INCA humidity measurements, Figure 6.1, in the same manner. In order to eliminate unreasonable outliers from Figure 6.1, cf. the discussion at the end section 6.1.3, we have calculated 98 percentiles of RH_{ice} data, binned in temperature intervals of ΔT = 3 K to improve the statistics. The 98 percentiles, open blue circles, are compared with the complete data set of critical saturation ratios $S_{ice,crit}$ for ice nucleation on different types of mineral dust which have been studied in the ADIA chamber (coloured triangles) in Figure 6.5a. Note that the 98 percentiles from RH_{ice} measurements in the upper troposphere and lower stratosphere are in fairly good agreement with AIDA measurements of $S_{ice,crit}$ for ice nucleation on inactive to moderately active types of mineral dust in the mixed cloud regime, where cloud and ice nucleation occurs when water saturation is reached, or where indications of deposition freezing on more active ice nuclei (e.g. ATD) have been found at somewhat less than water saturation.

The agreement becomes even better, and extends to temperatures well into the cirrus cloud regime, when sulphuric acid coated ATD and SD particles are compared with the 98 percentiles from the INCA campaign, Figure 6.5b. This is not surprising since it is known that the cirrus clouds during that part of the INCA campaign which started from Punta Arenas in the Southern hemisphere were

essentially due to homogeneous freezing of sulphuric acid aerosol. In the Northern hemisphere, where a large fraction of the sulphuric acid aerosol is partially neutralised by ammonia from anthropogenic sources (Colberg et al., 2003), the threshold relative humidities for cirrus formation were observed to be about 20 % lower than in the Southern hemisphere (Gayet et al., 2004). Neutralisation of sulphuric acid aerosol by ammonia can lead to the formation of solid inclusions like letovicite or ammonium sulphate crystals which act as immersion freezing nuclei in haze particles (Abbatt et al., 2006; Colberg et al., 2003).

Figure 6.5c shows a comparison between the ice nucleation thresholds from AIDA experiments with pristine mineral dust aerosols (coloured triangles) and 80 percentiles of the RH_{ice} data from the INCA campaign (blue open circles). Although the 80 % threshold is arbitrary, it is remarkable that the choice of a significantly lower percentile leads to a much better agreement between both data sets in the warmer cirrus cloud regime between 230 and 240 K, while the agreement in the mixed cloud regime is not much affected. This may indicate that deposition nucleation was also involved in cirrus cloud formation during the INCA campaign, although more likely on ammonium sulphate or other soluble solids than on mineral dust particles, as already discussed in the previous section.

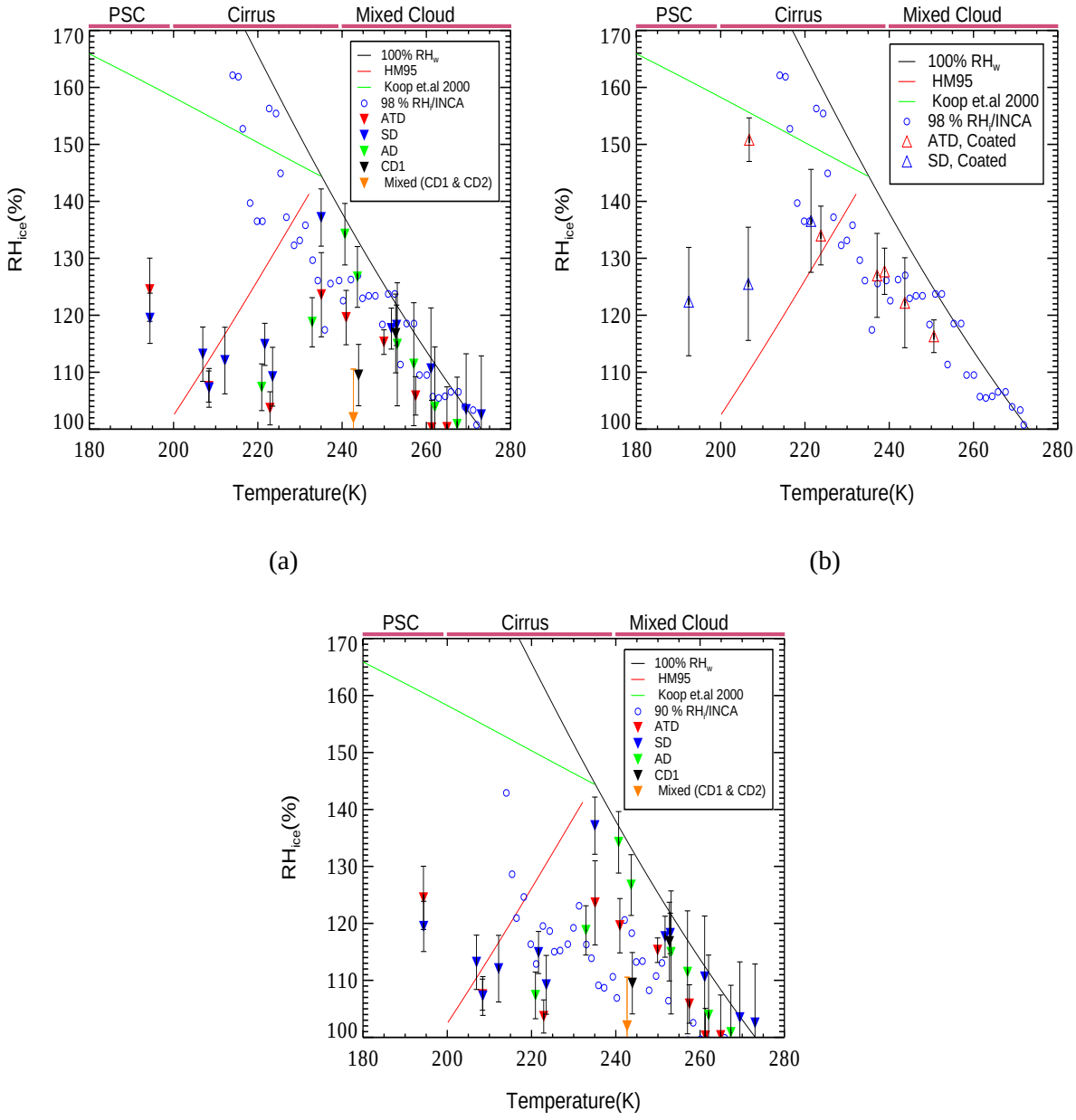

Figure 6.5:

(a) Solid triangles: $S_{ice,crit}(T)$ from AIDA experiments with pristine mineral dust particles; open circles: 98 percentiles of RH_{ice} for 1-K-intervals, INCA campaign data from Figure 6.1a.

(b) Open triangles: $S_{ice,crit}(T)$ from AIDA experiments with H_2SO_4-coated ATD and SD particles; open circles: 98 percentiles of RH_{ice} for 1-K-intervals, INCA campaign data from in Figure 6.1a.

(c) Solid triangles: $S_{ice,crit}(T)$ from AIDA experiments with pristine mineral dust particles; open circles: 90 percentiles of RH_{ice} for 1-K-intervals, INCA campaign data from Figure 6.1a.

6.4 Ice Water Content (IWC): Measurements in Cirrus Clouds versus AIDA Chamber Experiments

We have succeeded in section 6.3.3 to compare, at least qualitatively, AIDA chamber measurements of critical ice saturation ratios $S_{ice,crit}$ for mineral dust aerosols with field observations. We have already shown in section 5.4.2.1 that such a comparison is severely limited (if not impossible) with regards to maximum ice water contents in ADIA chamber experiments on the one hand, and measurements of the same parameter in real cirrus clouds on the other. The comparison data from cirrus clouds, Figure 6.1, were collected during the INCA campaign (Gayet et al., 2004; 2006). The problem is not due to the limited quality of the IWC data from the chamber experiments, because we could show in section 5.4 that the maximum ice water contents (IWC) in AIDA expansion experiments, which were retrieved from measurements of ice particle size distributions with optical particle counters, agreed well with FTIR-based retrievals. It was also shown that the agreement improved when the OPC data were corrected for evaporative losses in the warm sampling line of the PCS2000 instrument, as explained in Appendix B.

The *maximum* ice water content (IWC) observed in up-drafting cirrus clouds can be well understood on the basis of a simple thermodynamic parcel model. The model, which is summarised in equation (5.3), was introduced in section 5.4.2.1 where it was used to elucidate the impact of the ice-coated chamber walls on ice water yields in AIDA chamber experiments. However, while we noted in section 5.4.2.1 that equation (5.3) can be used to calculate ice water yields (IWY) for *any* combination of pressures and temperatures, we will now consider an air parcel which rises and cools adiabatically *in the atmosphere*. This implies that pressure and temperature cannot vary independently, since they are constrained by an adiabatic lapse rate. As an example, consider an air parcel which is initially sub-saturated with respect to ice, but rises and cools adiabatically until, at an altitude z = 8.15 km and a temperature of 323 K, the air becomes saturated with respect to ice, i.e. S_{ice}(T=232 K) = 1.000. We call the corresponding temperature the saturation temperature T_s. When the air parcel rises above the saturation level z(T_s) = 8.15 km (either due to buoyancy or by dynamic forcing), it continues to cool adiabatically until a critical saturation ratio $S_{ice,crit}$, > 1 is exceeded, where ice is formed. This may be due either to heterogeneous freezing on solid particles like mineral dust, or to homogeneous ice nucleation in haze droplets at the "Koop limit", if no solid ice nuclei are present. If we assume that thermodynamic equilibrium between the ice particles and the interstitial water vapour is immediately established, the ice water content would be given by the following equation:

$$\frac{m_{ice}}{V}\,[g\ m^{-3}] = 1000 \times \frac{0.018}{8.314\ T}\left(e_s(T_s)\frac{p(T)}{p(T_s)} - e_s(T) \right) \qquad (6.7)$$

Here, $e_s(T_s)$ denotes the partial pressure of water vapour at the saturation level $z(T_s)$, $p(T_s)$ is the corresponding air pressure, while T and $p(T)$ are the air parcel temperature and pressure at the altitude where the IWC is measured. We assume that the pressure profile $p(z)$ of the atmosphere is known. We can then use the adiabatic lapse rate Γ_s to relate the temperature $T < T_s$ of the air parcel with its altitude $z(T)$ and pressure $p(T)$. The situation is illustrated in Figure 6.6, which refers to the example given above. We have assumed for simplicity that the pressure profile $p(z)$ corresponds to the US standard atmosphere, but any other observed profile could be used.

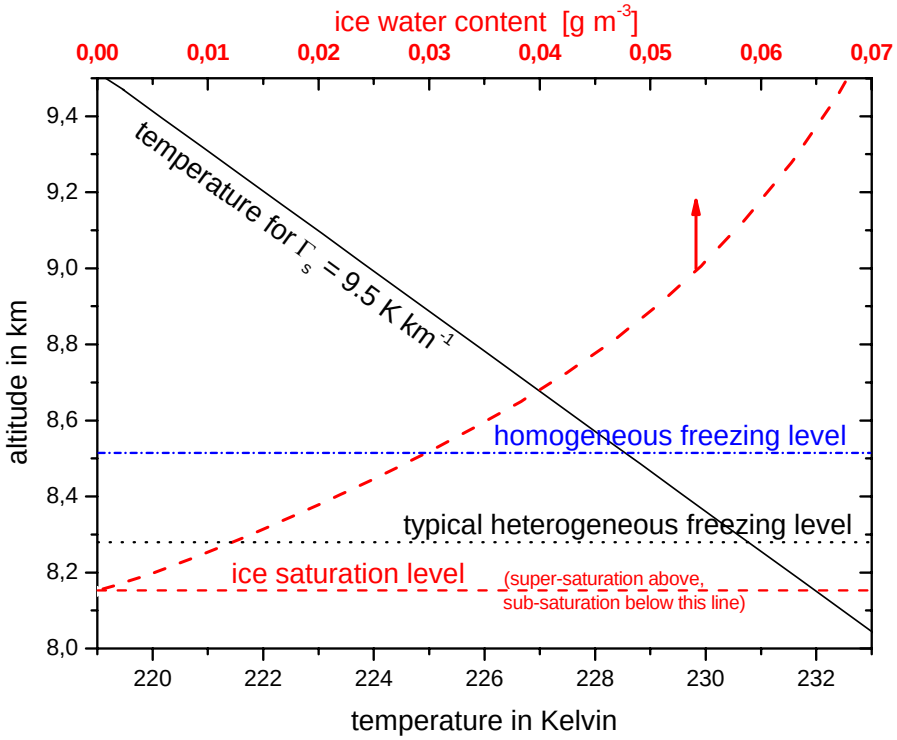

Figure 6.6: Example calculation showing the potential ice water yield IWY(z) (dashed red curved line) for an air parcel which rises adiabatically.

Note that we have assumed that the adiabatic lapse rate Γ_s for air in equilibrium with ice is 9.5 K km^{-1}, which is a good approximation for Γ_s which approaches the dry adiabatic lapse rate in the cirrus regime. The exact lapse rate, which is itself a function of the temperature, is given by

$$\Gamma_s = \Gamma \frac{1 + \frac{\Delta H}{RT} x_s}{1 + \frac{\Delta H}{RT} x_s \left(\frac{\Delta H}{c_p T} \right)} \tag{6.8}$$

Γ = 9.75 K km denotes the dry adiabatic lapse rate, ΔH is the sublimation enthalpy of ice, x_s is the molar mixing ratio of water vapour in equilibrium with ice, and c_p is the molar heat capacity of air at

constant pressure. The potential ice water content (dashed red sloping line) is of course limited by the mixing ratio of water vapour, which explains the upward curvature of the dashed red line. An ice-free zone exists between the ice saturation level and cirrus cloud base. The base is either at the heterogeneous freezing level (black dotted line) if refractory ice nuclei (e.g. mineral dust particles) are present, or significantly higher up at the homogeneous freezing level (Koop et al., 2000) if refractory ice nuclei are absent.

Very recently, Monier et al. (2006) have used a similar parcel model (but including detailed ice microphysics, which describes non-equilibrium effects between interstitial water vapour and ice particles, but ignores sedimentation effects) to simulate cirrus formation under INCA conditions. They have compared several parameterisations of homogeneous and heterogeneous ice nucleation rates. The ice water contents in their Figure 5 can be directly compared with our example calculation, Figure 6.6. The agreement at 800 m above the saturation level is surprisingly good, showing that the neglect of non-equilibrium effect is of minor importance for the conditions chosen.

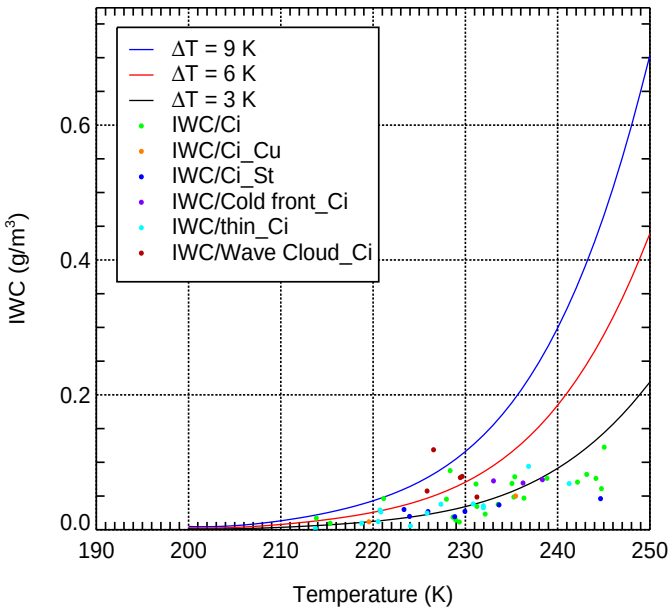

Figure 6.7: Maximal IWC from cirrus cloud measurements during the INCA campaign, plotted versus the temperature *T* where they were measured (data from Gayet er al., 2006). The black, red, and blue lines were calculated with the simple parcel model, equation (6.7), which assumes thermodynamic equilibrium between water vapour and ice once ice particles are formed, and neglects sedimentation.

We have used our extremely simple adiabatic parcel model to analyse maximal IWCs which were measured in cirrus clouds during the INCA campaign, data listed in Gayet et al. (2006). As

illustrated in Figure 6.6, the IWC given by the simple formula (6.7) depends on the height $z(T_s)$ and temperature T_s of the ice saturation level, and the height $z(T)$ above the ice saturation level where IWC is measured. The height difference Δz corresponds to a temperature difference $\Delta T = T_s - T$ between the saturation level and the measurement level. For a constant ΔT, the IWC is expected to decrease with altitude z, because the water vapour $e_s(T_s)$ at the altitude $z(T_s)$ (the "water capacity" of the air parcel, i.e. the amount of water available for freezing) decreases exponentially with temperature. The relation between z and p was taken from the US standard atmosphere, while a constant lapse rate in cirrus clouds of $\Gamma_s = 9.5$ K km^{-1} was adopted as an approximation. Figure 6.7 presents maximal IWCs which were measured in systematic flights through cirrus clouds during the INCA campaign (Gayet et al., 2006), plotted versus the temperature T where the maximum IWC of each cloud was measured, and compares the data with calculated IWCs. These were computed for our simple parcel model, equation (6.7), assuming temperature differences ΔT of 3 K, 6 K, and 9 K between the ice saturation level and the level where each measurement was made. Note that these ΔT values correspond with altitude differences Δz of about 315, 630, and 945 m above the ice saturation level. These Δz values are reasonably high above the saturation level of a young cirrus cloud in which sedimentation effects may still be neglected. Note that most of the measured IWCs are well described by the assumed range of ΔT (and of the corresponding Δz) above the saturation level. Only one IWC, measured at 227 K in a wave cloud, exceeds the blue line. Possible explanations are either $\Delta T > 9$ K, which is not unlikely in a strong wave cloud, and/or sedimentation effects, i.e. ice crystals which have grown large enough to settle below the nucleation level where they can grow by the seeder-feeder mechanism in the previously ice-free space between the nucleation level and the saturation level.

Note that cirrus ice nucleation above 240 K, i.e. above the homogeneous freezing temperature of pure cloud droplets and haze particles, is not very likely in the absence of efficient heterogeneous ice nuclei. This implies that at least some of the IWC data above this temperature were measured in sedimenting cirrus clouds, and should not be compared with our simple parcel model.

Although we have shown in section 5.4.2.1 that the IWC of an artificial cirrus cloud, forming in an AIDA chamber experiment with ice-covered walls, can significantly exceed the IWC which follows from equation (5.3), we have plotted the AIDA data in Figure 6.8 versus the temperature. The black, red, and blue lines have the same theoretical basis as in Figure 6.7, namely equation (6.7). However, this equation should *by no means* be applied to AIDA experiments, for the following reasons:

- AIDA experiments violate the assumption of constant H_2O (= total water) mixing ratio
- AIDA experiments violate the assumption of adiabaticity which was used to calculate the black, red, and blue lines in Figures 6.7 and 6.8.

Both violations are caused by the chamber walls. The consequences are not dramatic in the range 225 – 240 K where the IWC data measured in AIDA do not exceed the blue line. However, an increasing number of IWC data exceed the blue line at temperatures below 225 K. We emphasize that the temperature difference ΔT (which was defined above) is less, often *much* less than 9 K at low temperatures, see examples presented in section 5.4.2.1. This shows clearly that it is misleading to compare directly ice water content data from ADIA experiments with field measurements.

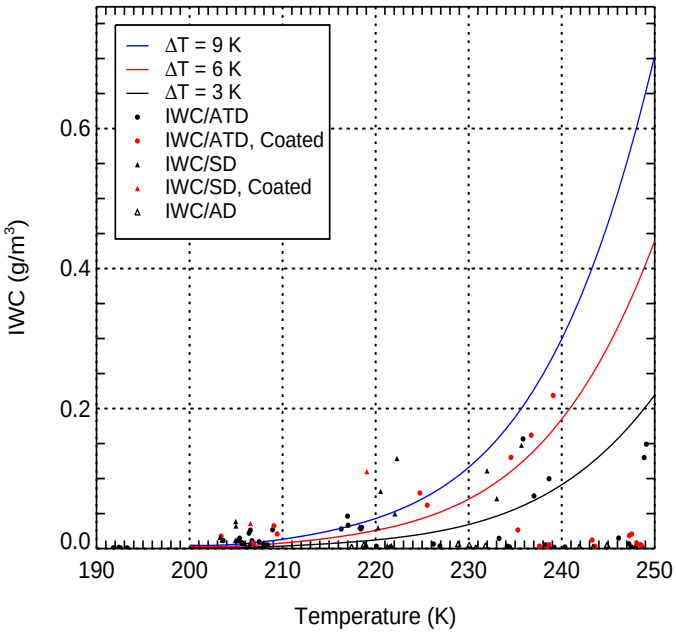

Figure 6.8: Maximal IWC measured in artificial cirrus, ADIA experiments with ice-coated chamber walls and various types of mineral dust as ice nuclei. Superimposed are the black, red, and blue lines which were calculated for air parcels rising and cooling adiabatically in the atmosphere, see text for discussion.

6.5 Heterogeneous Nucleation Rates, Comparison with Literature Data

Section 5.3 was devoted to the determination of heterogeneous nucleation rates for deposition freezing of water vapour on pristine mineral dust particles, results shown in Figure 5.44. In principle, these results could be compared with the theory of ice nucleation on the surface of smooth spherical particles (Pruppacher and Klett, 1997). However, this theory leaves a number of free parameters which are not accessible for mineral dust particles with rough surfaces. We will therefore compare our results with heterogeneous nucleation rate measurements from other laboratory studies.

A recent study of heterogeneous ice nucleation on surrogates of mineral dust and on Asian dust is due to Archuleta et al. (2005). These authors point out that: "If the nucleation mechanism in all untreated cases is presumed to be deposition, particles with diameters of 200 nm size display constant deposition nucleation rates (equal to 1×10^{-3} per particle per second […]) occurring at approximately constant or progressively lower ice supersaturations with decreasing temperature". Since the critical saturation ratio $S_{ice,crit} = 1.35$ for Asian dust particles with $D_p = 200$ nm was approximately independent of temperature in the range studied by Archuleta et al., we can calculate the heterogeneous nucleation rate $J(T,S_{ice})$ for this material using the following formula for monodispersed particles:

$$J_{depos.\,freez.} = \frac{1}{\pi D_p^2}\,\frac{\Delta n}{n}\,\frac{1}{\Delta t} \qquad [cm^{-2}\ s^{-1}] \tag{6.9}$$

Archuleta et al. have defined the nucleation threshold $S_{ice,crit}$ as that supersaturation which is needed to convert a fraction of $\Delta n/n = 0.01$ of all particles to ice crystals of detectable size within $\Delta t = 10$ s, which is the time spent by the particles in the supersaturated zone of their continuous flow ice-diffusion chamber. This yields a heterogeneous nucleation rate $J(T,S_{ice}) \approx 8\times10^5$ cm^{-2} s^{-1} for ice nucleation by deposition freezing of Asian dust particles at $T \approx 220$ K and $S_{ice} \approx 1.35$.

This result can be directly compared with our measurements in the AIDA chamber. However, Figure 5.44 in section 5.3 is extremely crowded, since it includes *all* heterogeneous nucleation rates determined from AIDA experiments, which makes the comparison difficult. We have therefore prepared three separate pseudo-3D-plots for ice nucleation on (a) ATD, (b) SD, and (c) AD. The plots are shown in Figure 6.9a-c. The heterogeneous ice nucleation rate $J(T,S_{ice}) \approx 8\times10^5$ cm^{-2} s^{-1}, which was determined by Archuleta et al. (2005) for Asian dust particles at $T \approx 220$ K and $S_{ice} \approx 1.35$, is in excellent agreement with nucleation rates from AIDA chamber experiments with Asian dust: a rate of about 1.5×10^6 cm^{-2} s^{-1} (average of two rate determinations with Asian dust) was found at ~ 216 K and $S_{ice} \sim 1.38$ in the AIDA chamber. Note that our experiments were done with polydisperse AD particles

of significantly larger size. The good agreement supports the interpretation that the nucleation rate measured by Archuleta with pristine Asian dust was indeed a deposition freezing rate, and should not be interpreted as an immersion freezing rate, as is the case with sulphuric acid-coated particles. Note that immersion freezing rates determined by Archuleta et al. (2005) and others (e.g., Hung et al., 2003) *increase* with decreasing temperature, while the opposite trend is observed in our deposition freezing rates, Figure 6.9a-c. However, we find that the deposition nucleation rate increases when the super-saturation ($S_{ice} - 1$) increases, as expected, although the data are too scattered to reveal a clear functional dependence.

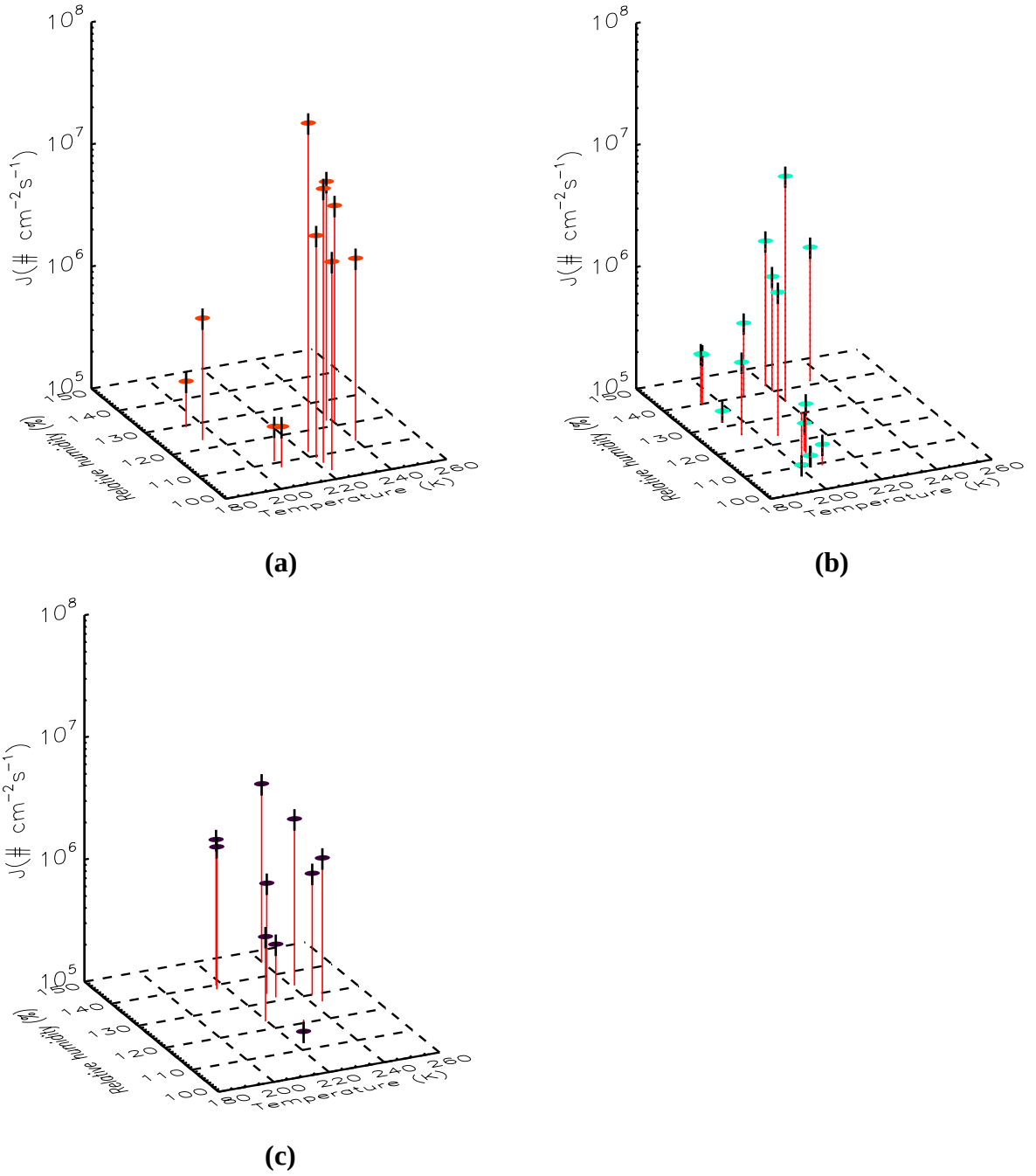

Figure 6.9: Heterogeneous nucleation rates for deposition freezing on mineral dust particles, derived from AIDA experiments, as described in section 5.3. The pseudo-3D plots represent nucleation rates on the following types of mineral dust:

(a) Arizona test dust (ATD, red symbols)

(b) Sahara dust (SD, turquoise symbols)

(c) Asian dust (AD, black symbols)

7 Summary and Recommendations

7.1 Summary

The large deserts of the northern hemisphere, in particular the Sahara, are abundant sources of coarse-mode mineral dust particles. Their source strength can only be compared to that of sea salt aerosol. The size distribution of desert dust also includes particles in the lower μm and sub-μm size range, which can be lifted to the middle and upper troposphere, where they affect climatically relevant properties of mixed clouds and cirrus clouds, mainly via their role as ice nuclei. This role is still poorly understood, although many laboratory and field studies have been undertaken to quantify the impact of mineral dust on cloud formation.

The large evacuable aerosol chamber AIDA, which can be cooled from ambient to stratospheric temperatures, has been used in recent years as a cloud expansion chamber in the temperature regimes of mixed, cirrus, and stratospheric clouds to investigate the cloud and ice nucleating properties of different μm-sized mineral dust samples: Two airborne Saharan dust samples (CD1 and CD2) were collected by gravitational settling on a flat surface during two dust storm events on 18 February and 19 March 2003, about 50 km north of Cairo city. A soil dust sample from the Egyptian Sahara (SD) was collected in the desert 70 km northeast of Cairo city. Asian soil dust (AD) was provided by the University of Mainz, which originated from the easterly part of the Takla Makan Desert in northwest China, east of the Dalimu Basin between Kuerle and Ruoquiang. Furthermore, numerous simulation experiments were done with so-called Arizona test dust. This is a commercially available standardised mineral dust which is frequently used reference material in laboratory experiments. All samples were carefully characterised in terms of chemical composition (core and soluble surface layer), size distribution, and shape (roundness) of the particles. The source regions of CD1 and CD2 were identified by altitude-resolved back-trajectory calculations. This includes a discussion of possible interactions with air pollutants during transport.

The AIDA experiments with mineral dusts were primarily aimed at determining temperature dependencies of critical saturation ratios ($S_{crit,ice}$) which, when exceeded, give rise to ice nucleation on different pristine or sulphuric acid coated mineral dust aerosols. Other parameters of interest were the freezing rate, the fraction of dust particles being activated, and the evolution of the ice water content. These parameters were measured as functions of the temperature and the saturation ratio. The main contribution of this thesis was the analysis of the raw data to provide consistent data sets, e.g. of critical saturation rations $S_{ice,crit}(T)$ and their uncertainty ranges, to determine correct numbers and size distributions of ice particles as function of time after pump start, and to develop correction algorithms.

We were also able to derive, for the first time, heterogeneous nucleation rates for deposition freezing on three different types of mineral dust for a wide range of temperatures and saturation ratios over ice. The nucleation thresholds were compared with parameterisations, derived either from field observations (Heymsfield and Miloshevich, 1995), or from laboratory studies (e.g., homogeneous nucleation thresholds of haze particles, Koop et al., 2000; immersion or deposition freezing rates, Archuleta et al., 2005). Important results of this work can be summarised as follows:

- It is likely that, in addition to the chemical composition, the surface morphology of the mineral dust particles has an impact on their ice nucleating ability. We have chosen the ratio of spherical to non-spherical particles as a suitable measure of surface morphology. This ratio was compared with the maximum frozen fraction of dust particles in simulation runs under otherwise comparable experimental conditions. It was found that spherical particles are slightly more efficient ice nuclei than non-spherical particles.

- All dust particles were found to form liquid water clouds in the temperature range 273 to about 250 K. Only very small fractions of ice crystals were formed simultaneously by condensation or immersion freezing. SD and AD particles give rise to the formation of supercooled liquid water clouds down to about 240 K. ATD particles are more efficient ice nuclei: they form ice by deposition freezing below the water saturation limit in the mixed cloud regime. Surprisingly, the airborne Saharan dust samples CD1 and CD2 are exceptionally efficient ice nuclei in the mixed cloud regime, with ice nucleation thresholds only a few % above ice saturation below 245 K. This may be due to the fact that the particles had been exposed to the polluted atmosphere before being collected by gravitational settling. Indeed, CD1 and CD2 contained the highest fraction of soluble ions. Coating of ATD particles with sulphuric acid, however, had no significant effect on their ice nucleating ability in the mixed cloud regime.

- ATD, SD and AD are powerful heterogeneous ice nuclei in the cirrus cloud regime. We find a sharp reduction of the critical saturation ratio from $S_{ice,crit}$ between ~1.25 for ATD and ~1.35 for SD at the upper temperature limit of the cirrus regime to critical saturation ratios in the order of 1.1 and less at lower temperatures. This behaviour resembles the temperature dependence of critical saturation ratios reported by Bailey and Hallett (2002): They observed a pronounced maximum close to the intersection of the homogeneous freezing limit of haze particles (Koop et al., 2000) and the saturation line. The $S_{ice,crit}$ data in this range are also reasonably well described by the parameterisation of Heymsfield and Miloshevich (1995), which hints at the possibility that their observations in cirrus clouds were affected by

heterogeneous ice nucleation on mineral dust or on solid ammonium sulphate, as recently proposed by Abbatt et al. (2006).

- Coating of ATD with sulphuric acid reduces the ice nucleation efficiency in the cirrus cloud regime significantly. The threshold approaches the high saturation ratio predicted for the freezing of haze particles (Koop et al., 2000). Coating of SD also reduces its ice nucleation efficiency, but the effect becomes less important at lower temperatures.

- The nucleation rates J_{dep} for deposition freezing in the cirrus cloud regime range between ~10^5 and ~10^7 cm^{-2} s^{-1}. They increase as function of the saturation ratio S_{ice}, but surprisingly decrease towards lower temperatures. This contrasts with measurements of J_{imm} for immersion freezing by Archuleta et al. (2005), who find an exponential *increase* of J_{imm} with decreasing temperature. To our knowledge, our measurements of J_{dep} are the first to cover such a wide range of temperatures and saturation ratios. The only comparison data reported by Archuleta et al. is in good agreement with our measurements.

- Superficially, the ice water contents (IWC) measured in the AIDA chamber are comparable with IWC measured in cirrus clouds during the INCA campaign (Gayet et al., 2006). However, as could be shown theoretically and by comparing careful measurements of interstitial water vapour and ice as well as total water mixing ratios in AIDA chamber experiments, both sets of measurements are basically different, because the AIDA experiments are neither adiabatic nor do they conserve the total water mixing ratio.

In conclusion, our data analysis based on AIDA chamber simulations of clouds in the mixed cloud regime, in the cirrus cloud regime, and in the PSC regime have resulted in qualitatively and quantitatively new data on the ice nucleating efficiencies of mineral dust aerosols. The results can be used to improve the description of cirrus cloud formation in microphysical cloud models in terms of ice particle number and size, which are climatically important properties.

7.2 Recommendations for Future Work.

The AIDA chamber experiments have closed a number of gaps, but there are many other unknowns, which should be studied in future experiments:

- Our finding that the airborne dust samples CD1 and CD2 are significantly more efficient ice nuclei in the mixed cloud regime than any other dust particles studied so far deserves further attention. An effort should be made to determine the properties, which are responsible (weathering?) for this exceptional activity.

- Our observation that particle shape may be important in controlling the ice nucleating ability of mineral dust has raised more questions than could be answered by this preliminary study.

- The impact of different coatings on the ice nucleating ability of mineral dust is not well understood.

- The temperature dependence of the deposition nucleation rate J_{dep}, which opposes the reported temperature dependence of J_{imm}, should be carefully checked in dedicated experiments.

Appendix A: Calculation of the Gas Temperature along the Sampling Tube of PCS-2000: Presentation of the Model

Generally, there are two models to represent the heat flow inside a circular tube under steady-state conditions. In our case, the pump downstream of the PCS-2000 causes laminar forced convection in the sampling tube. In the first model, the heat transfer from the tube wall into the gas starts as soon as the gas enters the tube, as shown in Figure A.1. According to the second model, the heat transfer to the gas starts with a significant delay downstream of an isothermal section, as shown in Figure A.2.

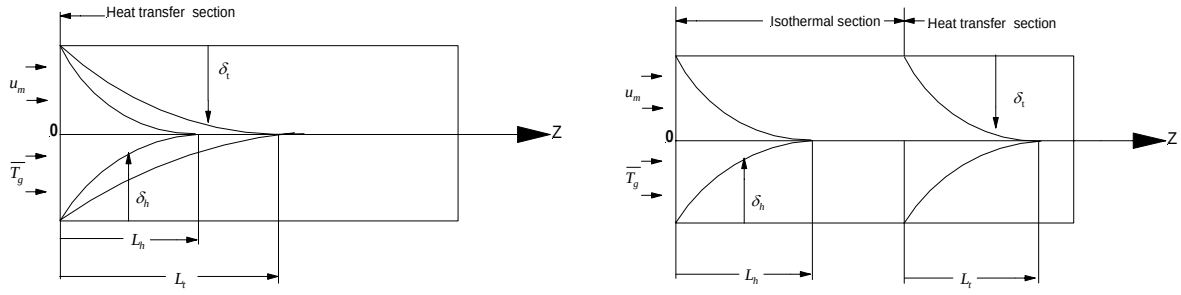

(1) (2)

Figure A: Sketches showing the development of the hydrodynamic and thermal boundary layer thicknesses δ_h and δ_t as well as the hydrodynamic and the thermal entrance lengths L_h and L_t according to two different models, (1) and (2):

(1) The heat transfer to the gas starts as soon as the gas enters the tube

(2) The heat transfer to the gas starts after an isothermal section. After Özişik, 1985

After comparing the models presented in Figure A with our problem, it is evident that the second model must be chosen to solve our heat flux problem for thermally developing, but hydrodynamically developed conditions. The solution of this problem in the case of laminar forced convection inside a circular tube with a uniform wall surface was given by Greatz and later quite independently by Nusselt (Özişik, 1985; Welty et al., 1984).

An IDL code was written based on the second model in order to calculate the distribution of the gas temperature in the connecting tube between the AIDA chamber and the PCS-2000 as follows: First, the physical properties of the gas in the chamber such as the gas density ρ, the dynamic viscosity μ, the thermal conductivity K_a, and the kinematic viscosity ν are calculated for the given conditions.

Then the volumetric gas flow across the measurement volume is calculated from the sampling flow under standard conditions, $F_{g,meas}$ which is prescribed by the flow controller, as follows,

$$F_{g,corr} = F_{g,meas} \times \frac{\overline{T_g}}{T_0} \times \frac{P_0}{P_{AIDA}} \tag{A.1}$$

where $T_o=273.15\ K$ and $P_o=1013.25\ mb$ refer to standard conditions. After that the IDL code calculates the mean gas velocity u_m from the corrected value of the gas flow: $F_{g,corr} = \pi R_{\text{tube}}^2 u_m$, where R_{tube} is the tube radius (Özişik, 1985; Welty et al., 1984). The effect of the pressure drop along the tube length *z* can be calculated according to the following formula (Özişik, 1985)

$$u_m = -\frac{R_{tube}^2}{8\mu}\frac{dP}{dz} \tag{A.2}$$

This equation can be integrated over the tube length from z_0 to *z* at which the pressure has changed from P_0 to P_z, so the pressure at the position z is equal to

$$P_z[i] = P_{z0}[i-1] - \frac{8\mu}{R_{tube}^2} u_m \Delta z \tag{A.3}$$

where *i* is an array over the tube length which is discretised in increments of 1 mm. The pressure at a position *i* , $P_z[i]$, differs from the pressure at a position *i*-1 by $-\frac{8\mu}{R_{tube}^2} u_m \Delta z$. The order of magnitude of this term is estimated by using the principle of scale analysis. The characteristic scales of the varibles are based on a calculated value of $\mu = 10^{-5}$ kg m^{-1} sec^{-1} (or Pa s), the square of the tube radius $R_{tube}^2 = 25\times10^{-6}$ m^2, the gas velocity = 2 m s^{-1} and $\Delta z = 10^{-3}$ m. So the order of magnitude of the second term in equation (A.3) is 0.1 Pa. This means that the pressure drops in the tube by a value of magnitude 0.1 Pa from the last calculated value. So the gas pressure drops by this value times the order of magnitude of the distance from the tube entrance. The gas pressure, measured at a distance of 10 m from the entrance, has changed from its value in the AIDA chamber by 1000 Pa as shown by the red line in Figure 4.2a chapter 4 sections 4.1 and accordingly by about 100 Pa from the AIDA chamber to the measuring volume of PCS-2000. So, the gas pressure along the tube length of interest may be assumed to be constant to a very good approximation.

The Reynolds number Re is then calculated to check whether the flow in the sampling tube is laminar or turbulent:

$$\text{Re} = \frac{\rho u_m D_T}{\mu} \tag{A.4}$$

where D_T is the tube diameter. Laminar flow is usually observed for Re < 2300. The IDL code also calculates the Prandtl number:

$$\mathrm{Pr} = \frac{C_p \, \mu}{K_a} \tag{A.5}$$

The hydrodynamic entrance length L_h and the thermal entrance length L_t in the case of fully developed laminar flow inside a circular tube at a constant wall temperature are calculated from the Reynolds and Prandtl numbers according to $L_h = 0.056 \, \mathrm{Re} \, D_T$ and $L_t = 0.033 \, \mathrm{Re} \, \mathrm{Pr} \, D_T$ (Özişik, 1985).

In the next step the mean Nusselt number is calculated for the case of laminar flow and a constant wall temperature (Özişik, 1985) according to the following equation

$$Nu_m = 3.66 + \frac{0.0668 \; Gz}{1 + 0.04 \left(Gz\right)^{2/3}} \tag{A.6}$$

where Gz is the Graetz number $Gz = Re \times Pr/(l \times D_T)$ and l is the axial distance along the tube measured from the beginning of the heat transfer section.

The heat transfer coefficient in the region of a hydrodynamically developed and thermally developing boundary layer is calculated according to the following equation

$$h_m = Nu_m \frac{K_a}{D_T} \tag{A.7}$$

where K_a is the thermal conductivity of the gas in J m^{-1} s^{-1} K^{-1}, calculated according to the equation given in Pruppacher and Klett, 1997, and converted to SI units.

Finally, the outlet temperature T_{out} at a distance l from the beginning of the heat transfer section is calculated according to the following equation

$$\frac{T_w - \overline{T_g}}{T_w - T_{out}} = \exp\left(\frac{4 \, l \, h_m}{D_T \, u_m \, \rho \, C_p} \right) \tag{A.8}$$

where $\overline{T}_g$ is the gas inlet temperature, T_w the tube wall temperature, and l is the length of the heat transfer section (Özişik, 1985; Welty et al., 1984).

The time spent by ice particles in the connecting tube between the ADIA chamber and PCS-2000 is only a fraction of a second, ~ 0.4 s, before they are optically detected by the PCS-2000. This time is short in comparison with the time until the next measurement of state variables in the AIDA

chamber occurs. The gas temperature every 1 mm along the tube aixs was calculated from the following equation.

$$T_{out}[i+1] = T_w + \left(T_w - \overline{T_g}[i]\right) e^{-\left(\frac{4 l h_m}{D_T u_m \rho C_p}\right)} \qquad \text{(A.9)}$$

where $T_{out}[i+1]$ is the exit gas temperature at the position of $i+1$ as a function of the inlet gas temperature at the position i, while the parameters h_m, u_m and ρ are calculated as explained above. Figure 4.3 in section 4.2.1 of chapter 2 shows the calculated profile of the gas temperature along the tube center line as a function of time for experiment N° 74 IN02. In the three dimensional plot the x-axis represents the running time of the experiment, the y-axis represents the distance from the tube entrance in mm, while the z-axis represents the gas temperature along the center line of the tube in K.

Appendix B: Calculation of Ice Particle Evaporation in the Sampling Line of PCS-2000

The growth (or evaporation) rate of ice crystals in the atmosphere depends upon the following environmental parameters: the air pressure and the super-saturation with respect to ice, $S_{i,v}$, which in turn is a function of the air temperature and the partial pressure of water vapour. General expressions from the literature have been used to calculate, by means of a numerical model, the change in ice crystal size while the particles travel from the cold AIDA chamber throught the sampling tube to the heated detection volume of the optical particle counter/sizer PCS-2000. The calculations are based on environmental factors which were introduced in chapter 4 sections 4.2.1 and 4.2.2.

The increase of the ice cyrstal mass with time by vapour diffusion to the particle surface is represented with the electrostatic analogy in many textbooks. For an immobile crystal (index 0) of mass *m* one finds for the mass change which is driven by the super-saturation

$$\left(\frac{dm}{dt}\right)_0 = \frac{4\pi C S_{i,v}}{\left(F_D + F_K\right)} \tag{B.1}$$

where $F_D = \frac{RT_\infty}{e_{sat,i} T_\infty D_v M_v}$ is a resistance associated with the diffusion of water vapour to the crystal surface, and $F_K = \frac{L_s}{K_a T_\infty}\left(\frac{L_s M_v}{RT_\infty} - 1\right)$ represents a resistance due to the combined effects of latent heat release and thermal conduction. *C* denotes the analogue of an electrical capacitance, in units of length, which is a function of the size and shape of the ice crystal. We have assumed “spherical crystals” which means $C = 1$ for our calculations.

The actual growth rate *dm*/*dt* of an ice crystal which is in motion relative to the surrounding air is enhanced by a ventilation coefficient f_v. It is defined as the ratio between the water mass flux to or from the ice crystal for the case of a moving ice crystal, and that of a motionless crystal:

$$\frac{dm}{dt} = f_v\left(\frac{dm}{dt}\right)_0 \tag{B.2}$$

The ventilation coefficient f_v depends upon the density and the dynamical viscosity of air, the diffusivity of water vapour in air, and the terminal fall velocity of the ice particle which is a function of particle mass and shape (Beard, 1976; Heymsfield and Iaquinta, 2000).

The ventilation coefficient f_v was calculated for hexagonal, broad-branched and columnar ice crystals by Wang and Ji (2000), and for spherical, columnar and plate-like ice crystals falling from

cirrus clouds with axis ratios of 0.05 and 0.2 in the case of forced convection by Hall and Pruppacher (1976). It has a general form of

$$f_v = \begin{cases} 1.00 + 0.14 X_1^2, & X_1^2 = N_{Sc,v}^{1/3} N_{\mathrm{Re},L^*}^{1/2} \prec 1.0 \\ 0.86 + 0.28 X_1, & X_1 \geq 1 \end{cases} \qquad \text{(B.3)}$$

where $N_{sc} = m/(r_a D_v)$ is ~0.63 in the atmosphere and $N_{\mathrm{Re}} = U_\infty D_P/n$. Ventilation coefficients f_v determined from equation (B.3) deviate by less than 10% from the ventilation coefficients f_v for any specific crystal shape when the value of X < 10, which is in the range for typical cirrus clouds (Hall and Pruppacher, 1976). The terminal velocity of the particles U_∞ was calculated for rigid spheres according to Beard (1976), eqs. 6 and 7.

An IDL code was written to integrate equation (B.3). It calculates the ventilation coefficient in time steps of one second during the experiment, and in increments of one millimeter along the tube axis for spherical particles with diameters from 0.25 µm to 19.55 µm, i.e. in the measuring range of the optical particle counter/sizer PCS-2000. As an example and for ease of presentation, the ventilation coefficient was calculated for spherical particles of 0.52 µm and 19.55 µm in diameter, i.e. at the minimum and the maximum values in the measuring range of PCS-2000, 250 s after the vacuum pumps were started in experiment N^o 74 IN02. The red line in Figure B.1a represents the ventilation coefficient which is unity for spherical particles of 0.52 µm diameter, while the blue line represents the ventilation coefficient for particles of 19.55 µm diameter. The latter has a constant value along the hydrostatic length and decreases in the heated section, i.e. with the increase of the gas temperature in the tube, as shown in Figure B.1. It turns out that all ventilation coefficients are sufficiently close to unity to be negligible for our conditions. We have plotted the ventilation coefficients of these spherical particles versus $N_{Sc,v}^{1/3} N_{\mathrm{Re},L^*}^{1/2}$ in Figure B.1b.

The IDL code then calculates the variation of super-saturation $S_{i,v}$ along the tube axis as explained chapter 4 section 4.2.2. The obtained super-saturation is shown in Figure 4.5 in the same chapter. The super-saturation is zero along the hydrostatic length and decreases with increasing mean gas temperature at the beginning of the heated section.

Substituting equation B.1 into B.2 yields

$$\frac{dm}{dt} = \frac{4\pi C S_{i,v} f_v}{\left(F_D + F_K\right)} \qquad \text{(B4)}$$

As noted above, the ventilation coefficient can be neglected. We have also assumed C = 1. So, the problem reduces to solving the following growth equation for a stationary ice crystal:

$$r\frac{dr}{dt} = \frac{S_{i,v}}{F_D + F_K} \tag{B.5}$$

The left hand side of equation (B.5) is calculated as a function of the gas temperature and the super-saturation along the tube axis every 1 mm.

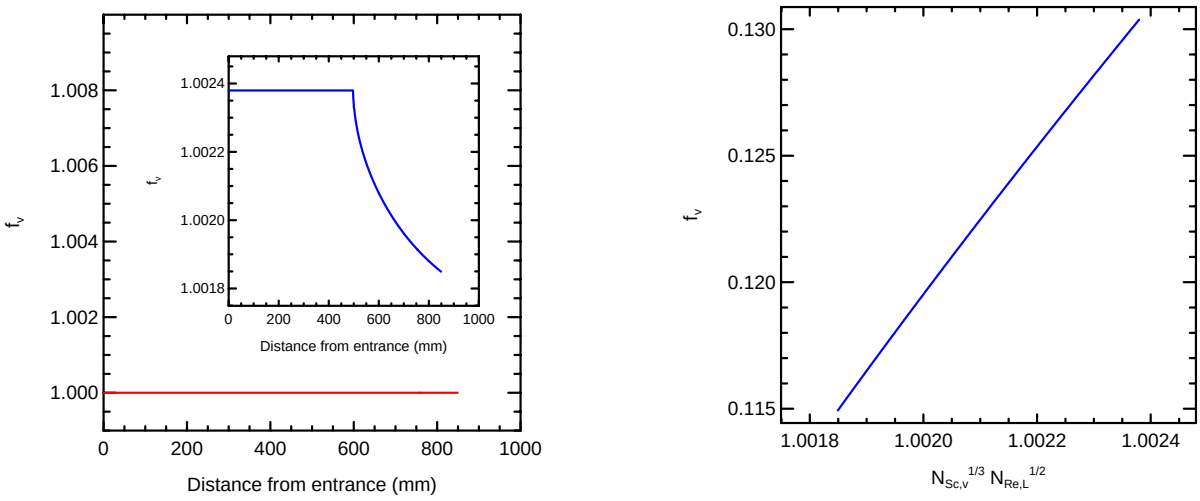

(a) (b)

Figure B.1: (a) Calculated ventilation coefficients f_v of spherical particles versus the tube length. The red and the blue lines represent f_v for particle diameters of 0.52 µm and 19.55 µm, respectively, 250 s after the principal pumps started. Activation N^o 74 IN02.

(b) As in (a) but f_v plotted versus $N_{Sc,v}^{1/3} N_{\mathrm{Re},L^*}^{1/2}$

Suppose an ice particle of initial radius r_0 is entrained in the sampling tube at time $t_0 = 0$, and moves along the tube axis at a uniform velocity, equal to the gas velocity u_m. The times after which the particle has moved 1, 2 …, n mm will be referred to as t_1, t_2,……, t_n. The radius of the ice particle at the end of the first step is calculated by integrating equation B.5 in this interval

$$\int_{r_0}^{r_1} r dr = C_0 \int_{t_0}^{t_1} dt \tag{B.6}$$

where C_o is constant along the first step

$$r_1^2 = r_o^2 + 2C_o(t_1 - t_0) = r_o^2 + 2C_o\left(\frac{l}{u_m} - 0\right) = r_o^2 + 2C_o\left(\frac{l}{u_m}\right) \tag{B.7}$$

Also the radius of the ice particle at the end of the second distance step is calculated by integrating equation (B.4) in the interval from t_1 to t_2 as follows

$$\int_{r_1}^{r_2} r dr = C_1 \int_{t_1}^{t_2} dt \tag{B.8}$$

where C_1 is constant along the second time step

$$r_2^2 = r_1^2 + 2C_1(t_2 - t_1) = r_1^2 + 2C_1\left(\frac{2 \times l}{u_m} - \frac{l}{u_m}\right) = r_1^2 + 2C_1\left(\frac{l}{u_m}\right) \tag{B.9}$$

Substituting (B.7) into (B.9), one obtains the ice particle radius at the second distance step as a function of the ice particle radius at the tube entrance

$$r_2^2 = \quad r_1^2 + 2C_1\left(\frac{l}{Vel}\right) = r_o^2 + 2C_o\left(\frac{l}{u_m}\right) + 2C_1\left(\frac{l}{u_m}\right) = \quad r_o^2 + \frac{2l}{u_m}\left[C_o + C_1\right] \tag{B.10}$$

In generalised form, (B.10) becomes

$$r_2^2 = \quad r_o^2 + \frac{2l}{u_m}\sum_{i=0}^{i=1} C_i \tag{B.11}$$

It follows that the radius of the ice particle at a position n as a function of its initial radius can be calculated according to the following equation

$$r_n^2 = r_o^2 + \frac{2l}{u_m}\sum_{i=0}^{n-1} C_i \tag{B.12}$$

where r_n is the calculated particle radius at a step n, r_0 is the initial radius in the AIDA chamber, l is an array referring to the tube length in increments of 1 mm, u_m is the particle velocity, C_i is the time dependent change of the particle mass, equal to the right-hand side of Equation (B.1) (not to be confused with the capacity factor C in the same equation). It varies as function of the temperature at the center line of the sampling tube along which the ice particles are assumed to travel from the AIDA chamber to the detection volume of the OPC. This equation was used to correct the ice crystal size measured by the optical particle counter/sizer PCS-2000 for evaporative losses in the sampling line to reconstruct the original ice crystal size distribution in the AIDA chamber.

Appendix C: Determination of the Threshold Relative Humidity of Ice Nucleation: Estimation of the Experimental Uncertainty

The threshold relative humidity with respect to ice which gives rise to heterogeneous ice nucleation in AIDA chamber experiments with mineral dust aerosol cannot be measured directly, but must be calculated from a combination of simultaneous measurements (e.g. from the partial pressure e_v of water vapour, the gas temperature T, and the total pressure p). Each of these individual measurements is more or less uncertain. These uncertainties propagate into the uncertainty of the calculated threshold relative humidity. An important error is introduced by the determination of the freezing onset time which is uncertain by an amount δt.

The relative error associated with the determination of the relative humidity with respect to ice, RH_i, at freezing threshold can be calculated by applying the law of error propagation after Gauss (Taylor, 1982). It is the square root of the sum of squares of the fractional errors in its parts,

$$\left.\frac{\delta RH_i}{RH_i}\right|_{t_f} = \sqrt{\left(\frac{\delta e_v|_{t_f}}{e_v|_f}\right)^2 + \left(\frac{\delta P|_{t_f}}{P|_f}\right)^2 + \left(\frac{\delta e_i|_{t_f}}{e_i|_f}\right)^2} \qquad \text{(C.1)}$$

where $e_v|_f$ is the measured vapour pressure at freezing threshold and $\delta e_v|_{t_f}$ the associated error, $P|_f$ is the measured absolute gas pressure at freezing threshold and δP the associated error (it is very small when compared with other errors and will therefore be neglected in the following), $e_i|_f$ is the calculated saturation vapour pressure of ice at freezing threshold based on measurements of Marti and Mauersberger (1993) and $\delta e_i|_{t_f}$ the associated error. The uncertainty in the calculated ice relative humidity due to these individual measurements can be then calculated according to

$$\frac{\delta RH_i}{RH_i} = \sqrt{\left(\frac{\delta e_v|_{t_f}}{e_v|_f}\right)^2 + \left(\frac{\delta e_i|_{t_f}}{e_i|_f}\right)^2} \qquad \text{(C.2)}$$

The saturation vapour pressure, $\delta e_i|_{t_f}$ and the error in the vapour pressure $\delta e_v|_{t_f}$ at freezing threshold can be calculated as a function of the uncertainty δt of the freezing onset time as follows:

$$\delta e_v|_{t_f} = \left.\frac{\partial e_v}{\partial t}\right|_{t_f} \delta t \qquad \text{(C.3)}$$

$$\begin{aligned}\delta e_i\big|_f &= \left.\frac{\partial e_i}{\partial T}\right|_{t_f} \delta T + \left.\frac{\partial e_i}{\partial t}\right|_{t_f} \delta t \\ &= \left.\frac{\partial e_i}{\partial T}\right|_{t_f} \delta T + \left.\frac{\partial e_i}{\partial T}\right|_{t_f} \left.\frac{\partial T}{\partial t}\right|_{t_f} \delta t \\ &= \left.\frac{\partial e_i}{\partial T}\right|_{t_f} \left(\delta T + \left.\frac{\partial T}{\partial t}\right|_{t_f} \delta t \right)\end{aligned} \tag{C.4}$$

where $\left.\frac{\partial e_v}{\partial t}\right|_{t_f}$ and $\left.\frac{\partial e_i}{\partial t}\right|_{t_f}$ are the partial derivatives with respect to time of the vapour pressure e_v and the vapour pressure of ice, e_i, at freezing threshold and $\left.\frac{\partial e_i}{\partial T}\right|_{t_f}$ is the partial derivative with respect to the gas temperature of the vapour pressure of ice at freezing onset. The fluctuation of the gas temperature around its mean value (cf. Figure 2.2b in chapter 2, section 2.1) will be taken as the error in the gas temperature δT, which amounts to 0.3 K. These terms can be calculated using a one dimensional Taylor expansion as follows

$$e_v\left(t_f \pm \delta t\right) = e_v\left(t_f\right) \pm \delta t \frac{\partial e_v}{\partial t} \tag{C.5}$$

or

$$\left.\frac{\partial e_v}{\partial t}\right|_{t_f} = \frac{e_v\left(t_f + \delta t\right) - e_v\left(t_f - \delta t\right)}{2\,\delta t} \tag{C.6}$$

So the error in the water vapour pressure at freezing onset can be then calculated by introducing equation (C.6) into (C.3). This yield

$$\delta e_v\big|_{t_f} = \frac{e_v\left(t_f + \delta t\right) - e_v\left(t_f - \delta t\right)}{2} \tag{C.7}$$

The partial derivative of the gas temperature with respect to time at freezing threshold, $\left.\frac{\partial T}{\partial t}\right|_{t_f}$, can be also calculated using a one dimensional Taylor expansion

$$\left.\frac{\partial T}{\partial t}\right|_{t_f} = \frac{T\left(t_f + \delta t\right) - T\left(t_f - \delta t\right)}{2\delta t} \tag{C.8}$$

The partial derivative of the vapour pressure over ice with respect to temperature, $\left.\frac{\partial e_i}{\partial T}\right|_{t_f}$, can be derived from the Clausius-Clapeyron equation with respect to the gas temperature

$$\frac{\partial e_i}{\partial T} = e_i\big|_{t_f} \frac{\Delta H}{RT^2} \tag{C.9}$$

where $e_i\big|_{t_f}$ is the vapour pressure over ice at the freezing threshold temperature *T*, and ΔH is the enthalpy of sublimation of ice, which was taken from the work of Marti and Mauersberger (1993). So the uncertainties in the saturation vapour pressure at the freezing onset can be then calculated by introducing equation (C.8) and (C.9) into (C.4). This yield

$$\begin{aligned} \delta e_i\big|_{t_f} &= e_i\big|_{t_f} \frac{\Delta H}{RT^2\big|_{t_f}} \left(0.3 + \frac{T\left(t_f + \delta t\right) - T\left(t_f - \delta t\right)}{2\delta t}\delta t\right) \\ &= e_i\big|_{t_f} \frac{\Delta H}{RT^2\big|_{t_f}} \left(0.3 + \frac{T\left(t_f + \delta t\right) - T\left(t_f - \delta t\right)}{2}\right) \end{aligned} \tag{C.10}$$

The fractional error in the calculated ice relative humidity at freezing onset can be calculated numerically as

$$\frac{\delta RH_i}{RH_i} = \sqrt{\left(\frac{e_v\left(t_f + \delta t\right) - e_v\left(t_f - \delta t\right)}{2e_v\big|_f}\right)^2 + \left(\frac{\Delta H}{RT^2\big|_{t_f}}\left(0.3 + \frac{T\left(t_f + \delta t\right) - T\left(t_f - \delta t\right)}{2}\right)\right)^2} \tag{C.11}$$

REFERENCES

Abbatt, J.P.D., S. Benz, D. J. Cziczo, Z. Kanji, U. Lohmann, and O. Möhler, Solid Ammonium Sulfate Aerosols as Ice nuclei: A pathway for Cirrus Cloud Formation, *Science* 313 (2006) 1770-1773

Ackerman, A. S., Toon, O. B., Taylor, J. P., Johnson, D. W., Hobbs, P. V., and Ferek, R. J., Effects of aerosols on cloud albedo: Evaluation of Twomey's parameterization of cloud susceptibility using measurements of ship tracks, *J. Atmos. Sci.* 57(16) (2000) 2684-2695.

Archuleta, C. M., P. D. DeMott, and S. M. Kreidenweis, Ice nucleation by surrogates for atmospheric mineral dust and mineral dust/sulfate particles at cirrus temperatures, *Atmos. Chem. Phys.* 5 (2005) 2617-2634.

Arnott, W. P., Y. Y. Dong, and J. Hallett, "Extinction efficiency in the infrared (2-18(m) of laboratory ice clouds: observations of scattering minima in the Christiansen bands of ice," *Appl. Opt.* 34 (1995) 541-551

Bailey, M., and J . Hallett, Nucleation effects on the habit of vapour grown ice crystals from -18 to -42 °C, *Q. J. R. Meteorol. Soc* 128A (2002) 1461-1483

Barkan, J., P. Alpert, H. Kutiel, and P. Kishcha, Synoptics of dust transportation days from Africa toward Italy and central Europe, *J. Geophys. Res.* 110 (2005) D07208, doi: 10.1029/2004JD005222

Beard, K. V., Terminal velocity and shape of cloud and precipitation drops aloft, *J. Atmos. Sci.* 33(5) (1976) 851-864.

Benz, St., K. Megahed, O. Möhler, H. Saathoff, R. Wagner, U. Schurath, T-dependent rate measurements of homogeneous ice nucleation in a large cloud chamber. *Journal of Photochemistry* A176 (2005) 208-217

Blanco, A., F. De Tomasi, E. Filippo, D. Manno, M.R. Perrone, A. Serra, A.M. Tafuro, and A. Tepore, Characterization of African dust over southern Italy, *Atmos. Chem. Phys.* 3 (2003) 2147-2159.

Bohren, C.F., D. Huffman, Absorption and scattering of light by small particles, John Wiley & Sons, Inc., p. 530, 1983.

References

Bruinties, R. T., A review of cloud seeding experiments to enhance precipitation and some new prospects, *Bull. Amer. Meteorol. Soc.* 80(5) (1999) 805-819.

Büttner, Simone, Diss.: Streulichtexperimente an asphärischen Aerosolpartikeln: Depolarisation und Vorwärtsstreuverhältnis von Mineralstaub und Eiskristallen. Wissenschaftliche Berichte FZKA 6989, April 2004

Busch, M., R. Bauer, H. Heer, M. Wagner, *Praxisbezogene IDL Programmierung*, Schriftenreihe des Forschungszentrums Jülich, Reihe Informationstechnik / Information Technology, Band 2, 2002. ISSN 1433-5514; ISBN 3-89336-308-4. Herausgeber und Vertrieb: Forschungszentrum Jülich GmbH, Zentralbibliothek, D-5245 Jülich. E-Mail-Adresse: zb-publikation@fz-juelich.de

Chiapello, I., and C. Moulin, TOMS and METEOSAT satellite records of the variability of Saharan dust transport over the Atlantic during the last two decades (1979-1997), *Geophys. Res. Lett.* 29(8) (2002) 1176, doi: 10.1029/ 2001GL013767.

Colarco, P.R., O.B. Toon, J.S. Reid, J.M. Livingston, P.B. Russell, J. Redemann, B. Schmid, H. B. Maring, D. Savoie, E.J Welton, J.R. Campbell, B.N Holben, and R. Levy, Saharan dust transport to the Caribbean during PRIDE: 2. Transport, vertical profiles, and deposition in dimulation of in situ and remote sensing observations, *J. Geophys. Res.* 108(D19) (2003) 8590, doi: 10.1029/2002JD002659.

Connolly, P. J., P. R. Field, O. Möhler, S. Büttner, H. Saathoff, A. J. Heymsfield, M. W. Gallagher, T. W. Choularton, Simulation of ice crystal nucleation and growth: Results from the AIDA cloud expansion chamber, 14th International Conference on Clouds and Precipitation 18-23 July 2004, Bologna, Italy.

DeMott, P. J., K. Sassen, M. R. Poellot, D. Baumgardner, D. C. Rogers, S. D. Brooks, and A. J. Prenni, and S. M. Kreidenweis, African dust aerosols as atmospheric ice nuclei, *Geophys. Res. Lett.* 30(14) (2003a) 1732, doi: 10.1029/ 2003GL017410.

DeMott, P.J., D.J. Cziczo, A.J. Prenni, D.M. Murphy, S.M. Kreidenweis, D.S. Thomson, R. Borys, D.C. Rogers, Measurements of the concentration and composition of nuclei for cirrus formation, *Proc. Natl. Acad. Sci. USA* 1000 (2003b) 14655-14660

Dennis, A.S. and M.R. Schock, Evidence of the dynamic effects in cloud seeding experiments in South Dakota, *J. Appl. Meteorol.* 10(6) (1971) 1180-1184.

Dentener, F., et al., Emissions of primary aerosol and precursor gases in the years 2000 and 1750, prescribed data-sets for AeroCom, *Atmos. Chem. Phys. Discuss*. 6 (2006) 2703-2763.

Duft, D. and T. Leisner, Laboratory evidence for volume-dominated nucleation of ice in supercooled water microdroplets. *Atmos. Chem. Phys.* 4 (2004) 1997-2000.

Ebert, V., H. Teichert, C. Giesemann, H. Saathoff, U. Schurath, Fasergekoppeltes In-situ-Laserspektrometer für den selektiven Nachweis von Wasserdampfspuren bis in den ppb-Bereich. *Tech. Messen* 1 (2005) 23-30.

Egyptian Environmental Affairs Agency (EEAA), Air Quality in Egypt, May 2001. pp 16

Eliassen, A., D. Blanchard, T. Bergeron, The life and science of Tor Bergeron, *Bull. Amer. Meteorol. Soc.* 59 (1978) 387-392

Escudero, M., S. Castillo, X. Querol, A. Avila, M. Alarcón, M. M. Viana, A. Alastuey, E. Cuevas, and S. Rodríguez, Wet and dry African dust episodes over eastern Spain, *J. Geophys. Res.* 110 (2005) D18S08, doi: 10.1029/2004JD004731.

Field, P. R., O. Möhler, P. Connolly, M. Krämer, R. Cotton, A. J. Heymsfield, H. Saathoff, and M. Schnaiter, Some ice nucleation characteristics of Asian and Saharan desert dust, *Atmos. Chem. Phys.* 6, 2991-3006, 2006

Gayet, J.F., Shcherbakov, V., Mannstein, H., Minikin, A., Schumann, U., Ström, J., Petzold, A., Ovarlez, J. and Immler, F., Microphysical and optical properties of high-altitude clouds observed in mid-latitudes of the southern hemisphere during INCA. *Q. J. R. Meteorol. Soc*. 132 (2006) 1-30

Gayet, J.-F., J. Ovarlez, V. Shcherbakov, J. Ström, U. Schumann, A. Minikin, F. Auriol, A. Petzold, and M. Monier, Cirrus cloud microphysical and optical properties at southern and northern midlatitudes during the INCA experiment, *J. Geophys. Res.* 109 (2004) D20206, doi:10.1029 /2004JD004803.

Giesemann, G., H. Teichert, V. Ebert, J. Wolfrum, H. Saathoff, R. Wagner, and U. Schurath, First setup of a Diode Laser based Absorption Spectrometer for H_2O-vapour measurement at the AIDA, Seminar at Physikalisch Chemische Institute, Universität Heidelberg, 2004.

Ginoux, P., and O. Torres, Empirical TOMS index for dust aerosol: Applications to model validation and source characterization, J. Geophys. Res., 108(D17), 4534, doi:10.1029/ 2003JD003470, 2003.

Gobbi, G. P., F. Barnabe, and L. Ammannato, The vertical distribution of aerosols, Saharan dust and cirrus clouds in Rome (Italy) in the year 2001, *Atmos. Chem. Phys.* 4 (2004) 351-359.

Grainger, R. G., J. Lucas, G. E. Thomas, and G. B. L. Ewen, Calculation of Mie derivatives, *Appl. Opt.* 43(28) (2004) 5386-5393.

Haag, W., B. Kärcher, S. Schaefers, O. Stetzer, O. Möhler, U. Schurath, M. Krämer and C. Schiller, Numerical simulations of homogeneous freezing processes in the aerosol chamber AIDA. *Atmos. Chem. Phys.* 3 (2003) 195-210

Hall, W. D., H. R. Pruppacher, The survival of Ice particles falling from cirrus cloud in subsaturated air, *J. Atmos. Sci*. 33 (1976) 1995-2006.

Hansen J., M. Sato, and R. Ruedy, Radiative forcing and climate response, *Journal of Geophysical Research*, 102, 6831-6846, 1997.

Haywood J. M., P. N. Francis, M. D. Glew, and J. P. Taylor, Optical properties and direct radiative effect of Saharan dust: A case study of two Saharan outbreaks using data from the U. K. Met. Office C-130, *J. Geophys. Res.*106 (2001) 18417-18430.

Heintzenberg, J., K. Okada, and J. Stöm, on the composition of non-volatile material in upper tropospheric aerosols and cirrus crystals, *Atmos. Res.* 41 (1996) 81-88.

Heymsfield, A., and J. Iaquinta, Cirrus crystal terminal velocities, *J. Atmos. Sci.* 57, (2000) 916–938.

Heymsfield, A., and Larry M. Miloshevich, Relative Humidity and Temperature Influences on Cirrus Formation and Evolution: Observations from Wave Clouds and FIRE II, *J. Atmos. Sci*. 52 (1995) 4302–4326.

Hung, H.-M, A. Malinowski, and S. T. Martin, Kinetics of heterogeneous ice nucleation on the surfaces of mineral dust cores inserted into aqueous ammonium sulphate particles, *J. Phys. Chem.* A107 (2003) 1296-1306.

Husar, R. B., J. M. Prospero, and L. L. Stowe, Characterization of tropospheric aerosols over the oceans with the NOAA advanced very high resolution radiometer optical thickness operational product, *J. Geophys. Res*. 102 (1997) 16889-16909.

Intergovernmental Panel on Climate Change (IPCC). *Climate Change 2001*: *The Scientific Basis*. Cambridge University Press, New York, 2001. Note that a draft version of the next IPCC report, to be published in 2007 and not to be cited before publication, has been made available on the internet in spring 2006 by the US Government

Israelevich P. L., E. Ganor, Z. Levin, and J. H. Joseph, Annual variations of physical properties of desert dust over Israel, *J. Geophys. Res.* 108(D13) (2003) 4381, doi: 10.1029/2002JD003163.

Jaffe D., J. Snow, and O. Cooper, The 2001 Asian Dust Events: Transport and Impact on Surface Aerosol Concentrations in the U.S., *EOS* 84 (2003) 501-504.

Kärcher, B. and Lohmann, U., A parameterization of cirrus cloud formation: Homogeneous freezing including effects of aerosol size, *J. Geophys. Res.* 107(D23) (2002) 4698, doi: 10.1029/2001JD001429.

Kishcha, P., F. Barnaba, G. P. Gobbi, P. Alpert, A. Shtivelman, S. O. Krichak, and J. H. Joseph, Vertical distribution of Saharan dust over Rome (Italy): Comparison between 3-year model predictions and lidar soundings, *J. Geophys. Res.* 110 (2005) D06208, doi:10.1029/2004 JD 005480.

Koop, T., B. Luo, A. Tsias, and T. Peter, Water activity as the determinant for homogeneous ice nucleation in aqueous solutions, *Nature* 406 (2000) 611-614.

Larson, B.H. and Swanson, B.D., Experimental investigation of the homogeneous freezing of aqueous ammonium sulphate droplets. J. Phys. Chem. A110 (2006) 1907-1916

Laskin, A., M. J. Idema, A. Ichkovich, E. R. Graker, I. Taraniuk, and Y. Rudich, Direct observation of completely processed calcium carbonate dust particles, *Faraday Discuss.* 130 (2005) 453-468.

Laurent, B., B. Marticorena, G. Bergametti, P. Chazette, F. Maignan, and C. Schmechtig, Simulation of the mineral dust emission frequencies from desert areas of China and Mongolia using an aerodynamic roughness length map derived from the POLDER/ADEOS 1 surface products, *J. Geophys. Res.* 110 (2005) D18S04, doi:10.1029/2004JD005013.

Levin, Z., J. H. Joseph, and Y. Mekler, Properties of Sharav (Khamsin) Dust–Comparison of Optical and Direct Sampling Data, *J. Atmos. Sci.*, 37(4) (1980) 882–891.

Levin Z., E. Ganor, and V. Gladstein, The effects of desert particles coated with sulphate on rain formation in the eastern Mediterranean, *J. Appl. Meteorol.* 35(9) (1996) 1511-1523.

Levi, Y., and D. Rosenfeld, Ice nuclei, rainwater chemical composition, and static cloud seeding effects in Israel, *J. Appl. Meteorol.* 35(9) (1996) 1494-1501.

Li, X., H., Maring, D. Savoie, K., Voss, and J. M. Prospero, Dominance of mineral dust in aerosol light scattering in the North Atlantic trade winds, *Nature* 380 (1996) 416-419.

Lide D.R., Editor-in-Chief of "Handbook of Chemistry and Physics", 79th Edition 1998-1999, CRC Press 1998, U.S. Standard Atmosphere (1976).

Lohmann, U., A glaciation indirect aerosol effect caused by soot aerosols, *Geophys. Res. Lett.* 29(4) (2002) 1052, doi: 10.1029/2001GL014357.

Mahowald, N. M., and L. M. Kiehl, Mineral aerosol and cloud interactions, *Geophys. Res. Lett.* 30(9) (2003) 1475, doi: 10.1029/2002GL016762.

Mangold, A., R. Wagner, H. Saathoff, U. Schurath, C. Giesemann, V. Ebert, M. Krämer, and O. Möhler, Experimental investigation of ice nucleation by different of aerosols in the aerosol chamber AIDA: implications to microphysics of cirrus clouds. *Meteorol. Z.* 14 (2005) 485-497

Marti, J., and K. Mauersberger, A survey and new measurements of ice vapour pressure at temperatures between 170 and 250 K, *Geophys. Res. Lett.* 20(5) (1993) 363-366.

Middleton, N.J., A.S. Goudie, Saharan dust: sources and trajectories. *Trans. Inst. Br. Geogr. NS* 26 (2001) 165-181

Miller R., and I. Tegen, Climate response to soil dust aerosols, *J. Climate* 11 (1998) 3247-3267.

Miloshevich, L. M., H. Vömel, D. N. Whiteman, B. M. Lesht, and F. J. Schmidlin (2006), Absolute accuracy of water vapor measurements from six operational radiosonde types launched during A WEX and implications for AIRS validation, *J. Geophys. Res.*, 10.1029/2005JD006083

Mishchenko, M. I., L. D. Travis, and A. A. Lacis, Scattering, *Absorption, and Emission of Light by Small Particles*, Cambridge University Press, p. 445, 2002.

Moulin, C., and I. Chiapello, Evidence of the control of summer atmospheric transport of African dust over the Atlantic by Sahel sources from TOMS satellites (1979-2000), *Geophys. Res. Lett.* 31 (2004) L02107, doi: 10.1029/2003GL018931.

Möhler, O., S. Büttner, C. Linke, M. Schnaiter, H. Saathoff, O. Stetzer, R. Wagner, M. Krämer, A. Mangold, V. Ebert, and U. Schurath, Effect of sulphuric Acid Coating on Heterogeneous Ice Nucleation by Soot Aerosol Particles. *J. Geophys. Res.* 110 (2005) D11210, doi:10.1029/2004JD005169.

Möhler, O., O. Stetzer, S. Schaefers, C. Linke, M. Schnaiter, R. Tiede, H. Saathoff, M. Krämer, A. Mangold, P. Bundz, P. Zink, J. Schreiner, K. Mauersberger, W. Haag, B. Kärcher, and U. Schurath, Experimental investigation of homogeneous freezing of sulphuric acid particles in the aerosol chamber AIDA, *Atmos. Chem. Phys.* 3 (2003) 211-223.

Möhler, O., C. Linke, H. Saathoff, M. Schnaiter, R. Wagner, A. Mangold, M. Krämer, and U. Schurath, Ice nucleation on flame soot aerosol of different organic carbon content. Accepted for publication in *Meteorol. Z.*, 2004

Möhler, O., H. Bunz, A. Nink, and U. Schurath, Laboratory studies on the potential of tropospheric insoluble aerosol components for heterogeneous ice nucleation, AIP Conference Proceedings Vol 534(1), pp. 475-478, August 2, 2000

Monier, M., W. Wobrock, J.-F. Gayet, A. Flossmann, Development of a micropysical cirrus model tracking aerosol particles' histories for interpretation of the recent INCA campaign. *J. Atmos. Sci*. 63 (2006) 504-525

Murayama T. N., S. J. Masonis, J. Redemann, T. L. Anderson, B. Schmid, J. M. Livingston, P. B. Russell, B. Huebert, S. G. Howell, C. S. McNaughton, A. Clarke, M. Abo, A. Shimizu, N. Sugimoto, M. Yabuki, H. Kuze, S. Fukagawa, K. L. Maxwell, R. J. Weber, D. A. Orsini, B. Blomquist, A. Bandy, and D. Thornton. Ground-based network observation of Asian dust events of April 1998 in East Asia, *J. Geophys. Res.* 106 (2001) 18345-18360.

Murphy, D.M. and T. Koop, Review of the vapour pressure of ice and supercooled water for atmospheric applications. *Quart. J. Roy. Meteorol. Soc.* 131 N°608 (2005) 1539-1565, doi: 10.1256/qj.04.94.

Murray, B.J., D.A. Knopf, A.K. Bertram, The formation of cubic ice under conditions relevant to the Earth's atmosphere. *Nature* 434 (2005) 202-205

Noble, C. A., and K. A. Prather, Real-time measurement of correlated size and composition profiles of individual atmospheric aerosol particles, *Environ. Sci. Technol.* 30(9) (1996) 2667-2680.

Noone, K., J., Johnson, D. W., Taylor, J. P., Ferek, R. J., Garrett, T. C., Smith, M. H., Russell, L. M., Flagan, R. C., Seinfeld, J. H., DeBock, L., Van Grieken, R. E., Hudson, J. G., Brooks, I., Gasparovic, R. F., and Pockalny, R. A., A case study of ship track formation in a polluted marine boundary layer, *J. Atmos. Sci.* 57(16) (2000) 2748-2764.

Özişik, M. N., Heat transfer, A Basic Approach, McGraw-Hill, Inc, p. 780, 1985.

Palas GmbH, Operating Manual Particle Counter Sizer PCS-2000 under licence of University of Karlsruhe, MVM, 1997

Palas GmbH, Operating Manual Aerosol Spectrometer Welas Series 2000, 2003

Perry, K., S. S. Cliff, and M. P. Jimenez-Cruz, Evidence for hygroscopic mineral dust particles from intercontinental transport and chemical transformation experiment, *J. Geophys. Res.* 109 (2004) D23S28, doi:10.1029/2004JD004979.

Petit, R.H, M. Legrand, I. Jankowiak, J. Molinié, C. Asselin de Beauville, G. Marion, and J. L. Mansot, Transport of Saharan dust over the Caribbean Islands, *J. Geophys. Res.* 110 (2005) D18S09, doi:10.1029/2004JD004749.

Pruppacher, H., and J. D. Klett, Microphysics of Clouds and Precipitation. D. Reidel, 714 pp, 1997.

Ramaswamy, V., o. Boucher, J. Haigh, D. Hauglustaine, J. M. Haywood, G. Myhre, T. Nakajima, G. Y. shi, and S. Solomon, *Radiative forcing of climate change, in climate change 2001: The Scientific basis,* Contribution of working Group I to the third Assessment report of the Intergovernmental Panel on Climate Change, edit by J. T. Houghton J. T., Y. Ding, D. J. ,Griggs,

M. Noguer, P.J. van der Linden, X. Dai, K. Maskell, C.A. Johnson, pp. 349-416, Cambridge Univ. Press, New York, 2001.

Reid, J. S., D. L. Westphal, J. M. Livingston, D. L. Savoie, H. B. Maring, H. H. Jonsson, D. P. Eleuterio, J. E. Kinney, and E. A. Reid, Dust vertical distribution in the Caribbean during the Puerto Rico Dust Experiment, *Geophys. Res. Lett.* 29(7) (2002) 1151, doi: 10.1029/2001GL014092.

Rosenfeld D., Comments on "A New Look at the Israeli Cloud Seeding Experiments". *J. Appl. Meteorol.* 36(3) (1997) 260–271.

Rosenfeld, D., and H. Farbstein, Possible influence of desert dust on seedability of clouds in Israel, *J. Appl. Meteorol.* 31(7) (1992) 722–731.

Rosenfeld, D., and R. Nirel, Seeding effectiveness – the interaction of desert dust and the southern margins of rain cloud systems in Israel, *J. Appl. Meteorol.* 35(9) (1996) 1502-1510.

Rosenfeld D., Y. Rudich, and R. Lahav, Desert dust suppressing precipitation: A possible desertification feedback loop, *Proc. Natl. Acad. Sci. USA* 98(11) (2001) 5957-5980.

Rosenfeld D. and W. L. Woodley, 1993: Effect of cloud seeding in West Texas: additional results and new insights. *J. Appl. Meteorol.* 32, 1848-1866.

Rudich, Y., O. Khersonsky, and D. Rosenfeld, Treating clouds with a grain of salt, *Geophys. Res. Lett.* 29(22) (2002) 2060, doi: 10.1029/2002GL016055.

Sassen, K., Indirect climate forcing over the western US from Asian dust storm, *Geophys. Res. Lett.* 29(10) (2002) 1465, doi: 10.1029/2001GL014051.

Sassen, K., P. J. DeMott, J. M. Prospero, and M. R. Poellot, Saharan dust storms and indirect aerosol effects on clouds: CRYSTAL-FACE results, *Geophys. Res. Lett* 30(12) (2003) 1633, doi: 10.1029/2003GL017371.

Saathoff, H., O. Möhler, U. Schurath, S. Kamm, B. Dippel, and D. Mihelcic, The AIDA soot aerosol characterisation campain 1999, *J. Aerosol Sci.* 34 (2003) 1277-1296, doi:10.1016/S0021-8502(03)00363-X.

References

Schäfers, S., A. Nink, and M. Schnaiter, Optical detection of particle growth and ice nucleation in H_2SO_4/H_2O and $H_2SO_4/H_2O/HNO_3$ aerosol in simulated stratospheric leewaves, *J. Aerosol Sci.* 32 (2001) S281-S282.

Schwartz, S.E., Harshvardhan, C.M. Benkovitz, Influence of anthropogenic aerosol on cloud optical depth and albedo shown by satellite measurements and chemical transport modelling. *Proc. Natl. Acad. Sci. USA* 99 (2002) 1784-1789.

Seifert, M., J. Ström, R. Krejci, A. Minikin, A. Petzold, J.-F.Gayet, H. Schlager, H. Ziereis, U. Schumann, and J. Ovarlez, Aerosol-cirrus interactions: a number based phenomenon at all?, *Atmos. Chem. Phys.* 4 (2004) 293-305.

Shaw, R.A., A.J. Durant and Y. Mi, Heterogeneous surface crystallization observed in undercooled water. *J. Phys. Chem.* B109 (2005) 9865-9868

Sodemann, H., A.S. Palmer, C. Schwierz, M. Schwikowski, H. Wernli, The transport history of two Saharan dust events archieved in an Alpine ice core. *Atmos. Chem. Phys.* 6 (2006) 667-688

Sokolik I. N., and O. B. Toon, Direct radiative forcing by anthropogenic airborne mineral aerosols, *Nature* 381 (1996) 681-683.

Stöckel, P., I.M. Weidinger, H. Baumgärtel, Th. Leisner, Rates of homogeneous ice nucleation in levitated H_2O and D_2O droplets. *J. Phys. Chem.* 109 (2005) 2540-2546

Sugimoto, N., I. Matsui, A. Shimizu, I. Uno, K. Asai, T. Endoh, and T. Nakajima, Observation of dust and anthropogenic aerosol plumes in the Northwest Pacific with a two-wavelength polarization lidar on board the research vessel Mirai, *Geophys. Res. Lett.* 29(19) (2002) 1901, doi: 10.1029/2002GL015112.

Szakáll, M., Z. Bozóki, M. Krämer, N. Spelten, O. Möhler, and U. Schurath, Evaluation of a photoacoustic detector for water vapour measurements under simulated tropospheric/ lower stratospheric conditions, *Environ. Sci. Technol.* 35 (2001) 4882-4885.

Szakáll, M., Z. Bozóki, A. Mohácsi, A. Varga, G. Szábo, Diode laser based photoacoustic water vapor detection system for atmospheric research. *Appl. Spectrosc.* 58 (2004) 792-798

Takemi, T., and N. Seino, Dust storms and cyclone tracks over the arid regions in east Asia in spring, *J. Geophys. Res.* 110 (2005) D18S11, doi: 10.029/2004JD004698.

Takemura, T., I. Uno, T. Nakajima, A. Higurashi, and I. Sano, Modelling study of long-range transport of Asian dust and anthropogenic aerosols from East Asia, *Geophys. Res. Lett.* 29(24) (2002) 2158, doi: 10.1029/2002GL016251.

Talbot, R. W., R. C., Harris, E. V. Browell, G. L., Gregory, D. L., Sebacher, and S. M. Beck, Distribution and geochemistry of aerosols in the tropical North Atlantic troposphere: Relationship to Saharan dust, *J. Geophys. Res.* 91 (1986) 5173-5182.

Tanré D., J. Haywood, J. Pelon, J. F. Léon, B. Chatenet, P.Formenti, P. Francis, P. Goloub, E. J. Highwood, and G. Myhre, Measurement and modelling of the Saharan dust radiative impact: Overview of the Saharan Dust Experiment (SHADE), *J. Geophys. Res.* 108(D18) (2003) 8574, doi: 10.1029/2002JD003273.

Taylor, John R., An introduction to error analysis, 270pp, 1982

Tegen I., and I. Fung, Contribution to the atmospheric mineral aerosol load from the land surface modification. *J. Geophys. Res.* 100 (1995) 18707-18726.

Tegen I., A. A. Lacis, and I. Fung, The influence on climate forcing of mineral Aerosols from disturbed soils, *Nature* 380 (1996) 419-422.

Thomas, G. (2004), "light scattering routines, http://www.atm.ox.ac.uk/code/mie/index.html .

Thulasiraman, S., N. T. O'Neill, A. Royer, B. N. Holben, D. L. Westphal, and L. J. B. McArthur, Sunpotometric observations of the 2001 Asian dust storm over Canada and the U.S., *Geophys. Res. Lett.* 29(8) (2002) 1255, doi: 10.1029/ 2002GL016251.

Tomasi, F. De, A. Blanci, M.R. Perrone, Raman lidar monitoring of extinction and backscattering of African dust layers and dust characterization. *Appl. Optics* 42 (2003) 1699-1709

Umhauer, H., Particle size distribution analysis by scattered light measurements using an optically defined measuring volume, *J. Aerosol Sci.* 14(6) (1983) 765-770.

Vali, G., Ice Nucleation-Theory, A. Tutorial, presentation at the NCAR/ASP 1999 Summer Colloquium; see also G. Vali, *J. Aerosol Sci.* 16 (1985) 575-576.

VanCuren, R., and T. Cahill, Asian aerosols in North America: Frequency and concentration of fine dust, *J. Geophys. Res.* 107(D24) (2002) 4804, doi: 10.1029/2002JD002204, 2002.

VanCuren, R.A., S.S. Cliff, K.D. Perry, M. Jimenez-Cruz, Asian continental aerosol persistence above the marine boundary layer over the eastern North Pacific: Continuous aerosol measurements from Intercontinental Transport and Chemical Transformation 2002 (ITCT 2K2). *J. Geophys. Res.* 110 (2005) D09S90

Vrbka, L., and P. Jungwirth, Homogenous Freezing of Water Starts in the Subsurface, *J. Phys. Chem*. B110 (2006) 18126-18129

Wagner, R., H. Bunz, C. Linke, O. Möhler, K.-H. Naumann, H. Saathoff, M. Schnaiter, U. Schurath, Chamber Simulations of Cloud Chemistry: The AIDA Chamber, in "Environmental Simulation Chambers: Application to Atmospheric Chemical Processes", I. Barnes, K. Rudzinki (Eds.), Springer 2005a

Wagner, R., S. Benz, O. Möhler, H. Saathoff, M. Schnaiter and U. Schurath, Mid-infrared extinction spectra and optical constants of supercooled water droplets. *J. Phys. Chem.*109 (2005b) 7099-7112

Wagner, R., A. Mangold, O. Möhler, H. Saathoff, M. Schnaiter, and U. Schurath, A quantitative test of infrared optical constants for supercooled sulphuric and nitric acid droplet aerosols, *Atmos. Chem. Phys.* 3 (2003) 1147-1164.

Wang, P.K, and W. Ji, Collision efficiencies of ice crystals at low-intermediate Reynolds Number colliding with supercooled cloud droplets: a numerical study. *J. Atmos. Sci.* 57 (2000) 1001-1009.

Waquet, F., J.-F. Léon, P. Goloub, J. Pelon, D. Tanré, and J.-L. Deuzé, Maritime and dust aerosol retrieval from polarized and multispectral active and passive sensors, *J. Geophys. Res.* 110 (2005) D10S10, doi:10.1029/2004JD004839.

Welty, J. R., C. E. Wicks, R. E. Wilson, Fundamentals of Momentum, Heat, and Mass Transfer, John Wiley & Sons, pp. 803, 1984.

Wurtele, Z. S, Analysis of the Israeli cloud seeding experiment by means of concomitant meteorological variables, *J. Appl. Meteorol.* 10(6) (1971) 1185–1192.

Wurzler S., T. G. Reisin, and Z. Levin, Modification of mineral dust particles by cloud processing and subsequent effects on drop size distribution, *J. Geophys. Res.* 105 (2000) 4501-4512.

Yin Y., S. Wurzler, Z. Levin, and T. Reisin, Interactions of mineral dust particles and clouds: Effects on precipitation and cloud optical properties, *J. Geophys. Res.* 107(D23) (2002) 4724, doi: 10.1029/2001JD001544.

Yoshioka, M., N. Mahowald, J. Dufresne, and C. Luo, Simulation of absorbing aerosol indices for African dust, *J. Geophys. Res.* 110 (2004) D18S17, doi:10.1029/2004JD005276.

Young, K. C., *Microphysical Processes in Clouds*. New York Oxford, 427pp, 1993.

Zhang, R., R. Arimoto, J. An, S. Yabuki, and J. Sun, Ground observations of a strong dust storm in Beijing in March 2002, *J. Geophys. Res*. 110 (2005) D18S06, doi:10.1029 / 2004 JD 004589.

Zhang Y. , and G. R. Carmichael, The role of mineral aerosol in tropospheric chemistry in East Asia – a model study, *J. Appl. Meteorol.* 38(3) (1999) 353-366.

Zhang, J., and S. A. Christopher, Long wave radiative forcing of Saharan dust aerosols estimated from MODIS, MISR, and CERES observations on Terra, *Geophys. Res. Lett.* 30(23) (2003) 2188, doi: 10.1029/2003GL018479.

Zöger, M., A. Engel, D.S. Mckenna, C. Schiller, U. Schmidt, and T. Woyke, Ballon-borne in situ measurements of stratospheric H_2O, CH_4 and H_2 at midlatitudes, *J. Geophys. Res.* 104 (1999) 1817-1825.

Zuberi, B., A. K. Bertram, C. A. Cassa, L. T. Molina, and M. J. Molina, Heterogeneous nucleation of ice in $(NH_4)_2SO_4$-H_2O particles with mineral dust immersions, *Geophys. Res. Lett.* 29 (2002) 1504, doi: 10.1029/2001GL014289.

Zuberi, B., A. K. Bertram, Th. Koop, L. T. Molina, and M. J. Molina, Heterogeneous Freezing of Aqueous Particles Induced by Crystallized $(NH_4)_2SO_4$, Ice, and Letovicite, *J. Phys. Chem.* 105 (2001) 6458-6464